



HAL
open science

K-space analysis of complex large-scale periodic structures

Giovanni Tufano

► **To cite this version:**

Giovanni Tufano. K-space analysis of complex large-scale periodic structures. Other. Université de Lyon; KU Leuven (1970-..), 2020. English. NNT : 2020LYSEC008 . tel-02870030

HAL Id: tel-02870030

<https://theses.hal.science/tel-02870030>

Submitted on 16 Jun 2020

HAL is a multi-disciplinary open access archive for the deposit and dissemination of scientific research documents, whether they are published or not. The documents may come from teaching and research institutions in France or abroad, or from public or private research centers.

L'archive ouverte pluridisciplinaire **HAL**, est destinée au dépôt et à la diffusion de documents scientifiques de niveau recherche, publiés ou non, émanant des établissements d'enseignement et de recherche français ou étrangers, des laboratoires publics ou privés.

N° d'ordre NNT : 2020LYSEC08



THÈSE DE DOCTORAT DE L'UNIVERSITÉ DE LYON

opérée au sein de l' **École Centrale de Lyon**

École Doctorale ED162

Mécanique - Énergétique - Génie Civil - Acoustique

Spécialité : Génie Mécanique

en co-tutelle avec **KU Leuven**

Arenberg Doctoral School

Faculty of Engineering Science - Faculteit Ingenieurswetenschappen

Mechanical Engineering - Werktuigkunde

pour obtenir le grade de

Doctor of Mechanical Engineering

par :

Giovanni TUFANO

K-SPACE ANALYSIS OF COMPLEX LARGE-SCALE PERIODIC STRUCTURES

Présentée et soutenue publiquement le 20 février 2020, devant le jury composé de :

| | |
|---|-------------------------|
| M-A. HAMDI, Professeur, Univ. de Technologie de Compiègne, France, | Président et Rapporteur |
| E. DECKERS, Professeure, KU Leuven, Belgique, | Examinatrice |
| J-R. ARRUDA, Professeur, Université de Campinas, Brésil, | Rapporteur |
| B. PLUYMERS, Chercheur, Industrial research fund, KU Leuven Belgique, | Examineur |
| M. ICHCHOU, Professeur, École Centrale de Lyon, France, | Directeur |
| O. BAREILLE, Maître de Conférences HDR, École Centrale de Lyon, France, | Co-Directeur |
| N. ATALLA, Professeur, Université de Sherbrooke, Canada, | Invité |
| A-M. ZINE, Maître de Conférences HDR, École Centrale de Lyon, France, | Invité |



ÉCOLE CENTRALE DE LYON

École Doctorale ED162

Mécanique - Énergétique - Génie Civil - Acoustique

Spécialité : Génie Mécanique



KU LEUVEN

Arenberg Doctoral School

Faculty of Engineering Science - Faculteit Ingenieurswetenschappen

Mechanical Engineering - Werktuigkunde

K-SPACE ANALYSIS OF COMPLEX LARGE-SCALE PERIODIC STRUCTURES

by

Giovanni TUFANO

in partial fulfillment of the requirements for the degree of

Doctor of Mechanical Engineering

and

Doctor of Engineering Science (PhD): Mechanical Engineering

Supervisors:

Prof. Mohamed ICHCHOU, École Centrale de Lyon

Prof. Wim DESMET, KU Leuven

Co-Supervisor:

Prof. Olivier BAREILLE, École Centrale de Lyon

Acknowledgment

First of all, I would like to express my sincere thanks to my Supervisors, Professor Mohamed ICHCHOU, Professor Wim DESMET and Professor Olivier BAREILLE, for their continued human, scientific and technical support, for their patience, their guidance and motivation. I could not ask for better guidance in completing my research and education. I would also like to thank Professor Abdel-Malek ZINE, Dr Bert PLUYMERS and Professor Elke DECKERS for their valuable contributions.

I would like to express particular thanks to the European Union for having fully funded the research activity through the programme *Horizon 2020 - Marie Skłodowska-Curie Innovative Training Networks (MSCA-ITN-EJD)* under the project VIPER (*Vibroacoustic of PERiodic media*, GA 675441). A big thank you goes to the coordinators of the project and to all the participants, both academic and industrial. I would also like to thank the European Union for its continued funding of research and development activities and for giving the opportunity to young researchers to complete their education in a very stimulating framework.

A thank you to my family, for having supported with every means, material and not, to my human and professional education, for having supported me throughout these years.

I would also like to thank Barbara, for her love, her patience and her support during these three years, for being present throughout all the bad and the good times.

A warm thank you to the 12 (now 11) colleagues of the VIPER project, for sharing these years together. In particular, Fabrizio, *frate fidate*, for spending more than six years together and with which I shared more than a simple formative path; Dario, the lion, even if he has the flaw of being a supporter of Juventus FC..., and finally Nassardin, with whom I shared every single moment of this journey.

A heartfelt thanks goes to all the people met during these years, professors, staff and colleagues from both École Centrale de Lyon and KU Leuven, to Université de Sherbrooke and *VibraTec SA* for having warmly welcomed me and having contributed to the realization of this work.

Last but not least, a heartfelt thanks to the Facebook page *Napoli VHS* for having ripped more than a laugh in the long office days.

Remerciements

Tout d'abord, je voudrais exprimer mes remerciements les plus sincères à mes *Supervisors*, Professeur Mohamed ICHCHOU, Professeur Wim DESMET et Professeur Olivier BAREILLE, pour leur constant soutien humain, scientifique et technique, pour leur patience, leur conduite et leur motivation. Je ne pouvais pas demander de meilleur guide dans l'achèvement de mon chemin de recherche et de formation. Je voudrais également remercier le Professeur Abdel-Malek ZINE, le Docteur Bert PLUYMERS et le Professeur Elke DECKERS pour leur précieuse contribution.

Je tiens à remercier tout particulièrement l'Union européenne pour avoir entièrement financé l'activité de recherche à travers le programme *Horizon 2020 - Marie Skłodowska-Curie Innovative Training Networks (MSCA-ITN-EJD)* avec le projet VIPER (*Vibroacoustic of PERiodic media*, GA 675441). Un grand merci est adressé aux coordinateurs du projet et à tous les participants, qu'ils soient universitaires ou industriels. Je voudrais également remercier l'Union européenne pour le financement continu des activités de recherche et développement et pour permettre un haut niveau de formation aux jeunes chercheurs.

Un remerciement à ma famille, pour avoir soutenu par tous les moyens, matériel ou non, mon parcours de formation, pour m'avoir soutenu dans toutes les années à l'étranger.

Je voudrais ensuite remercier Barbara, pour son amour, sa patience et son soutien durant ces trois années, pour être là dans les bons et dans les mauvais moments.

Un chaleureux merci aux 12 (puis 11) collègues du projet VIPER, pour avoir partagé ce parcours ensemble. En particulier, Fabrizio, *frate fidate*, depuis maintenant six ans ensemble et avec qui j'ai partagé plus qu'un simple parcours de formation ; Dario, le lion, même si malheureusement il est supporter de la Juventus FC... et enfin Nassardin, avec lequel j'ai partagé chaque instant de ce parcours.

Un grand merci est adressé à toutes les personnes rencontrées pendant le parcours, professeurs, personnel et collègues soit au sein de l'École Centrale de Lyon soit de KU Leuven, à l'Université de Sherbrooke et à *VibraTec SA* pour m'avoir accueilli chaleureusement et contribué à la réalisation de ce travail.

Enfin, mais pour cela pas moins important, un ressenti merci à la page Facebook *Napoli VHS* pour avoir arraché plus d'un rire dans les longues journées au bureau.

Ringraziamenti

Prima di tutto, vorrei esprimere i più sinceri ringraziamenti ai miei *supervisors*, Professor Mohamed ICHCHOU, Professor Wim DESMET e Professor Olivier BAREILLE, per il loro continuo supporto umano, scientifico e tecnico, per la loro pazienza, la loro guida e motivazione. Non potevo chiedere guida migliore nel completamento del mio percorso di ricerca e formazione. Vorrei inoltre ringraziare Professor Abdel-Malek ZINE, Dottor Bert PLUYMERS e Professoressa Elke DECKERS per il loro prezioso contributo.

Vorrei esprimere un particolare ringraziamento all'Unione Europea per aver finanziato completamente l'attività di ricerca attraverso il programma *Horizon 2020 - Marie Skłodowska-Curie Innovative Training Networks (MSCA-ITN-EJD)* con il progetto VIPER (*Vibroacoustic of PERiodic media*, GA 675441). Un grande ringraziamento è rivolto ai coordinatori del progetto e a tutti i partecipanti, sia accademici che industriali. Vorrei ulteriormente ringraziare l'Unione Europea per il continuo finanziamento alle attività di ricerca e sviluppo e per permettere un elevato grado di formazione a giovani ricercatori.

Un ringraziamento alla mia famiglia, per aver supportato con ogni mezzo, materiale e non, al mio percorso formativo, per essermi stati vicini nella scelta di questo percorso all'estero.

Vorrei poi ringraziare Barbara, per il suo amore, la sua pazienza ed il suo supporto durante questi tre anni, per esserci sia nei momenti belli che nei momenti negativi.

Un caloroso grazie ai 12 (poi 11) colleghi del progetto VIPER, per aver condiviso questo percorso insieme. In particolare, Fabrizio, *frate fidate*, da ormai sei anni insieme e con il quale ho condiviso più di un semplice percorso formativo; Dario, il leone, anche se purtroppo ha il difetto di essere juventino..., ed infine Nassardin, con il quale ho condiviso ogni singolo momento di questo percorso.

Un sentito ringraziamento è rivolto a tutte le persone incontrate durante il percorso, professori, staff e colleghi sia in École Centrale de Lyon sia in KU Leuven, all'Université de Sherbrooke e a *VibraTec SA* per avermi calorosamente ospitato e aver contribuito alla realizzazione di questo lavoro.

Per ultimo, ma per questo non meno importante, un sentito grazie alla pagina Facebook *Napoli VHS* per aver strappato più di una risata nelle lunghe giornate in ufficio.

Abstract

During its operational mission, a transportation mean is subject to broadband acoustic, aerodynamic and structure-borne excitations. The transportation means, such as aircrafts, space launchers, ships, cars, trains, etc., are designed to accomplish a primary goal, usually to transfer a payload (passengers, goods, satellites, for example) from a point to another, always keeping a high level of comfort, safety and survivability of the payload. National and international regulations about noise pollution are more and more stringent; scientists and industrial players are facing with these challenges developing new materials and new design choices.

Composite materials, complex geometries and new design concepts are investigated, making the analysis and the prediction of the vibroacoustic response of these structures a huge challenge. The complexity makes the derivation of analytical models harder to obtain; the use of numerical tools is of crucial importance. One of the most employed methods is the Finite Element (FE) modeling, but the huge amount of degrees of freedom together with a high computational cost limits its use to the low frequency range. In the last decades, different methods are derived to obtain the dispersion characteristics of the structures; one of the most common is the Wave Finite Element Method (WFEM), that is based on the wave propagation. This method has been applied on various simple and complex structures, deriving both 1D and 2D formulations, extended also to curved structures.

Recently, an energetic approach has been derived starting from the Prony's method, the Inhomogeneous Wave Correlation (IWC) method. This approach has its applicability in the mid-high frequency range, where the modal overlap is quite high. The IWC method is based on the projection of the wavefield on an inhomogeneous traveling wave. The dominant wavenumber, at each frequency, is obtained by maximization of the correlation function between the projected wavefield and the inhomogeneous wave.

In this context, an extended version of the IWC method is derived, allowing to describe the dispersion curves of complex structures: periodic narrow plates, composite plates, ribbed panels, composite curved shells and curved stiffened structures. The method has the advantage to be applied in an operational environment, making use of sparse acquisition locations. A complete dispersion characteristics analysis is conducted, even in presence of periodic elements and vibration-control devices, describing the directly correlated band-gaps in certain frequency regions and general vibration level attenuation. A numerical and experimental estimation of the structural damping loss factor is computed. A description of the local dynamics in presence of small-scale resonators, of the periodicity effect and the identification of the multi-modal behavior are also captured.

All the results of the numerical simulations are experimentally validated on complex large-scale meta-structures, such as a 3D-printed sandwich panel, a curved composite laminated sandwich panel and a aluminum aircraft sidewall panel. The effect of industrially-oriented 3D-printed small-scale resonators on the vibro-acoustic response of the considered structures is conducted, taking in account both diffuse acoustic field and mechanical excitations.

Keywords: Wavenumber, k -space, periodic structures, dispersion curve, damping loss factor, stiffened curved structures, resonators, meta-structures

Résumé

Pendant sa mission opérationnelle, un moyen de transport est soumis à des excitations acoustiques, aérodynamiques et structurales à large bande. Les moyens de transport, tels que les avions, les lanceurs spatiaux, les bateaux, les voitures, les trains, etc., sont conçus pour accomplir un objectif principal, généralement de transférer une charge utile (passagers, marchandises, satellites, par exemple) d'un point à un autre, en maintenant toujours un niveau élevé de confort, de sécurité et de capacité de survie de la charge utile. Les réglementations nationales et internationales en matière de pollution sonore sont de plus en plus strictes ; les scientifiques et les acteurs industriels sont confrontés à ces défis de développement de nouveaux matériaux et de nouveaux choix de conception.

Les matériaux composites, les géométries complexes et les nouvelles conceptions sont étudiés, ce qui rend l'étude et la prédiction de la réponse vibro-acoustique de ces structures un défi énorme. La complexité rend la dérivation des modèles analytiques plus difficile à obtenir ; l'utilisation d'outils numériques est d'une importance cruciale. L'une des méthodes les plus utilisées est la modélisation par éléments finis (FE), mais l'énorme quantité de degrés de liberté associée à un coût de calcul élevé limite son utilisation dans la gamme de basses fréquences. Au cours des dernières décennies, différentes méthodes sont dérivées pour obtenir les caractéristiques de dispersion des structures ; l'une des plus courantes est la méthode des éléments finis ondulatoire (WFEM), qui est basée sur la propagation des ondes. Cette méthode a été appliquée sur diverses structures simples et complexes, dérivant une formulation soit 1D que 2D, également étendu à des structures courbes.

Récemment, une approche énergétique a été dérivée à partir de la méthode de Prony : la méthode de corrélation d'onde inhomogène (IWC). Cette approche trouve son applicabilité dans la gamme de fréquence moyenne et haute, où le chevauchement modal est assez élevé. La méthode IWC est basée sur la projection du champ d'onde sur une onde itinérante inhomogène. Le nombre d'onde dominant, à chaque fréquence, est obtenu par maximisation de la fonction de corrélation entre le champ d'onde projeté et l'onde inhomogène.

Dans ce contexte, une version étendue de la méthode IWC est dérivée, permettant de décrire les courbes de dispersion des structures complexes : plaques étroites périodiques, plaques composites, panneaux raidis, panneaux composites courbes et panneaux raidis courbes. La méthode a l'avantage d'être applicable dans un environnement opérationnel, en utilisant des emplacements d'acquisition clairsemés. Une analyse complète des caractéristiques de dispersion est effectuée, même en présence d'éléments périodiques et de dispositifs de contrôle des vibrations, décrivant les écarts de bande directement corrélés dans certaines régions de fréquence et l'atténuation du niveau de vibration. Une

estimation numérique et expérimentale du facteur de perte d'amortissement structurel est calculée. Une description de la dynamique locale en présence de résonateurs à petite échelle, de l'effet de la périodicité et de l'identification du comportement multi-modal sont également capturés.

Tous les résultats des simulations numériques sont validés expérimentalement sur des meta-structures complexes à grande échelle, comme un panneau sandwich imprimé en 3D, un panneau courbé sandwich en composite et un panneau d'avion en aluminium. L'effet des résonateurs à petite échelle imprimés en 3D à orientation industrielle sur la réponse vibro-acoustique des structures considérées est réalisé en tenant compte soit de l'excitation champ acoustique diffus et de l'excitations mécaniques.

Mots-clés : Nombre d'onde, *k-space*, structures périodiques, courbes de dispersion, facteur de perte d'amortissement, structures courbées raidies, résonateurs, meta-structures

Samenvatting

Tijdens zijn operationele opdracht, is een vervoersgemiddelde onderworpen aan breedband akoestische, aërodynamische en structuur - gedragen excitaties. De transportmiddelen, zoals vliegtuigen, ruimtelanceerders, schepen, auto's, treinen, enz., zijn ontworpen om een primair doel te verwezenlijken, gewoonlijk om een lading (passagiers, goederen, satellieten, bijvoorbeeld) van een punt naar een andere over te brengen, altijd houdend een hoog niveau van comfort, veiligheid en overleefbaarheid van de lading. De nationale en internationale regelgeving inzake geluidshinder is steeds strenger; wetenschappers en industriële spelers worden geconfronteerd met deze uitdagingen bij de ontwikkeling van nieuwe materialen en nieuwe ontwerpkeuzes.

Samengestelde materialen, complexe geometrieën en nieuwe ontwerpconcepten worden onderzocht, waardoor de studie en de voorspelling van de vibroakoestische respons van deze structuren een enorme uitdaging. De complexiteit maakt de afleiding van analytische modellen moeilijker te verkrijgen; het gebruik van numerieke tools is van cruciaal belang. Een van de meest gebruikte methoden is de FE-modellering (Finite Element), maar de enorme hoeveelheid vrijheidsgraden in combinatie met hoge computerkosten beperkt het gebruik ervan in het lage frequentiebereik. In de afgelopen decennia zijn verschillende methoden afgeleid om de verspreidingskenmerken van de structuren te verkrijgen; een van de meest voorkomende methoden is de Wave Finite element Method (WFEM), die gebaseerd is op de golfvoortplanting. Deze methode is toegepast op verschillende eenvoudige en complexe structuren, die een 1D- en 2D-formulering afleiden, ook uitgebreid tot gebogen structuren.

Onlangs is een energieke benadering afgeleid van de methode van Prony, de Inhomogeneous Wave Correlation (IWC) methode. Deze benadering heeft haar toepasbaarheid in het middenhoge frequentiebereik, waar de modale overlapping vrij hoog is. De IWC-methode is gebaseerd op de projectie van het golfveld op een inhomogene golf. De dominante golvenummer wordt bij elke frequentie verkregen door maximalisatie van de correlatiefunctie tussen het geprojecteerde golfveld en de inhomogene golf.

In dit verband wordt een uitgebreide versie van de IWC-methode afgeleid, waarmee de verspreidingscurves van complexe structuren kunnen worden beschreven: Periodieke smalle platen, samengestelde platen, geribde panelen, samengestelde gebogen schalen en gebogen geribbelde panelen. De methode heeft het voordeel om te worden toegepast in een operationele omgeving, waarbij gebruik wordt gemaakt van sparse acquisitielocaties. Er wordt een volledige analyse van de verspreidingskenmerken uitgevoerd, zelfs in aanwezigheid van periodieke elementen en apparatuur voor trillingscontrole, die de direct met elkaar verband houdende bandhiaten in bepaalde frequentiegebieden en de verzwakking van het trillingsniveau beschrijven. Er wordt een numerieke en expe-

rimentele schatting van de verliesfactor van de structurele demping berekend. Een beschrijving van de lokale dynamiek in aanwezigheid van kleinschalige resonatoren, van het periodiciteitseffect en de identificatie van het multimodale gedrag worden ook vastgelegd.

Alle resultaten van de numerieke simulaties worden experimenteel gevalideerd op complexe grootschalige meta-structuren, zoals een 3D-gedrukt sandwichpaneel, een gebogen samengesteld gelamineerd sandwichpaneel en een aluminium zijpaneel aan de zijkant van het vliegtuig. Het effect van industrieel georiënteerde 3D-gedrukte kleinschalige resonatoren op de trillings-akoestische respons van de overwogen structuren wordt uitgevoerd, waarbij rekening wordt gehouden met zowel diffuus akoestisch veld als mechanische excitaties.

Trefwoord: *Wavenumber, k-space*, periodieke structuren, dispersiecurve, demping verliesfactor, verstevigde gebogen structuren, resonatoren, meta-structuren

Contents

| | |
|--|-----------|
| Contents | xv |
| Introduction | 1 |
| 1 Literature review and <i>state of the art</i> | 7 |
| 1.1 Introduction | 7 |
| 1.2 Wavenumber identification techniques | 8 |
| 1.2.1 Space-wavenumber Fourier transform | 9 |
| 1.2.2 <i>McDaniel's</i> method | 11 |
| 1.2.3 The <i>Inhomogeneous Wave Correlation</i> (IWC) method | 14 |
| 1.2.4 <i>Spatial Laplace Transform for COmplex Wavenumber recovery</i> (SLaTCoW) method | 22 |
| 1.2.5 <i>High-Resolution Wavenumber Analysis</i> (HRWA) method | 23 |
| 1.2.6 Image source method | 28 |
| 1.3 <i>Force Analysis Technique</i> (FAT) | 37 |
| 1.4 <i>Wave Finite Element Method</i> (WFEM) | 40 |
| 1.5 Damping Loss Factor estimation | 44 |
| I Structural characterization of flat structures | 47 |
| 2 New formulation of the IWC method based on Green's and Hankel's functions | 49 |
| 2.1 Introduction | 50 |
| 2.2 Methodology | 51 |
| 2.3 Narrow plate structures: numerical models and result discussion | 52 |
| 2.3.1 Isotropic narrow plate | 53 |
| 2.3.2 Periodic narrow plate | 53 |
| 2.3.3 Isotropic narrow plate with distributed TMDs | 55 |
| 2.4 Two-dimensional flat structures: numerical models and result discussion | 60 |
| 2.4.1 Homogeneous plate | 60 |
| 2.4.2 Laminated composite plate | 61 |
| 2.4.3 Homogeneous plate with distributed TMDs | 62 |
| 2.5 Concluding remarks | 64 |
| 3 Wavenumber analysis of flat orthotropic structures | 67 |
| 3.1 Introduction | 67 |
| 3.2 Overview of the IWC method | 68 |
| 3.3 Numerical investigation of homogeneous panels | 68 |

| | | |
|-----------|---|------------|
| 3.3.1 | Isotropic panels | 69 |
| 3.3.2 | Orthotropic panel | 69 |
| 3.4 | Orthotropic sandwich panels | 73 |
| 3.4.1 | Double-wall panel with 1 cm of inter-spacing: numerical results and experimental validation | 73 |
| 3.4.2 | Double-wall panel with 2 cm of inter-spacing: numerical investigation | 74 |
| 3.5 | Concluding remarks | 77 |
| II | Large-scale meta-structures and stiffened shells | 79 |
| 4 | K-space analysis of complex large-scale meta-structures | 81 |
| 4.1 | Introduction | 81 |
| 4.2 | <i>Inhomogeneous Wave Correlation</i> method for curved structures | 83 |
| 4.3 | Experimental sets-up | 85 |
| 4.3.1 | Isotropic plate | 86 |
| 4.3.2 | Curved composite sandwich panel | 87 |
| 4.3.3 | Aluminum aircraft sidewall panel | 88 |
| 4.4 | Numerical validations and experimental results | 92 |
| 4.4.1 | Steel plate: experimental results and validation | 92 |
| 4.4.2 | Isotropic curved panel: numerical simulation and validation | 94 |
| 4.4.3 | Curved composite laminated sandwich panel: experimental results and validation | 95 |
| 4.4.4 | Aluminum aircraft sidewall panel: experimental results and validation | 97 |
| 4.5 | Conclusions | 103 |
| 5 | Vibro-acoustic response of axially and ring stiffened curved structures | 105 |
| 5.1 | Introduction | 105 |
| 5.2 | Overview of the methodologies | 107 |
| 5.2.1 | Donnell-Mushtary theory for thin cylindrical shells | 107 |
| 5.2.2 | IWC method for curved structures | 109 |
| 5.3 | Numerical models of the considered configurations | 110 |
| 5.4 | Wavenumber analysis | 112 |
| 5.4.1 | Bare test case configuration | 113 |
| 5.4.2 | Stiffened panels with T shaped stiffeners: inter-spacing effect | 113 |
| 5.4.3 | Effect of the stiffener cross-section shape on the dispersion curves | 114 |
| 5.5 | Sound transmission Loss calculations | 118 |
| 5.5.1 | The effect of pitch distance on sound radiation | 119 |
| 5.6 | Conclusions | 122 |
| | Concluding remarks and perspectives | 125 |
| | Bibliography | 127 |
| | List of Publications | 139 |
| | List of Figures | 141 |

List of Tables

147

Introduction

Industrial and scientific context

In transportation engineering, the vibro-acoustic and dynamic behaviors of the main structures are of fundamental interest. The transportation means, such as aircrafts, space launchers, ships, cars, trains, etc., are designed to accomplish a primary goal, usually to transfer a payload (passengers, goods, satellites, for example) from a point to another, always keeping a high level of comfort, safety and survivability of the payload. During their missions, transportation means are subject to different transient and dynamic loads, such as acoustic, aerodynamic and structure-born excitations, which are transferred to the payload and to the structures themselves.

National and international regulations about noise pollution are more and more stringent, imposing to the constructors and industrial players a strong reduction of the radiated noise and an high level of acoustic comfort. This aspect is more and more used as quality indicator, pushing the authorities and the industrial players to invest resources into this sector. To face these challenges, the transportation industries are focusing their attention on new structural designs and new materials, such as composites and sandwich panels.

Composite and sandwich materials are more and more used, to fulfill the requirements of reduced structural weight and high mechanical performances. Concerning the composite materials, one of the main drawbacks is the exhibition of bad vibro-acoustic performances compared to an equivalent structure made of a common metal alloy. In this context, the vibro-acoustic response and the dynamical behavior of laminated composite sandwich shells are of fundamental relevance for the industry, even at a preliminary stage of the design process, where the design rules are in evolution. An example of laminated honeycomb sandwich composite panel is shown in Fig. 0.1, in which a lightweight thick core is bonded by two thin stiff skins. The identification of the energy propagation, of the waves attenuation, with the related damping informations, and of the waves dispersion characteristics are relevant aspects to fully describe the vibro-acoustic behavior of a system. The anisotropic behavior and the complexity related to their composite nature make the development of an analytical theory and/or of a predictive model very hard to obtain.

The presence of stringers and frames in the longitudinal and circumferential directions of aircraft fuselages, space launchers fairings, ship hulls and submarines, for example, is a very common design choice. These stiffening elements are usually periodically distributed on the main structures, allowing to assume a certain degree of structural periodicity which, if properly designed, can give some advantages in the vibro-acoustic



Figure 0.1 – Honeycomb sandwich panel



Figure 0.2 – Periodic structures: part of the fuselage of an AIRBUS A350 aircraft (a) and a rail (b).

response. Many methods were developed based on the spatial repetition of a unit cell; the unit cell modeling approach allows to reduce the computational effort working on a small geometrical part of the structure and applying periodic boundary conditions at the edges, and it is widely used to simulate infinite media. Periodic structures can be designed and employed to attenuate the wave propagation in certain frequency regions, originating the so-called band gaps. Examples of periodic structures for aerospace and rail applications are shown in Fig. 0.2.

Many noise control treatments are proposed to reduce the noise inside the vehicle. Amongst them, the most employed are the sound-absorbing materials, usually attached to the structure or introduced in the sandwich panels, and damping materials usually stick between two different structural layers.

To mitigate structural vibrations, some devices can be designed and included in the structure. In civil engineering, tuned mass dampers are used in the skyscrapers to mitigate the vibrations induced by earthquakes and wind gusts (see Fig. 0.3). These resonant systems are used to attenuate the vibrations induced at a known frequency. The application field is enlarged also to mechanical engineering, where a distributed pattern of small-scale resonators is used to attenuate the vibration levels in specified frequency regions, introducing the so-called band-gaps, and leading to meta-structures.

Research objectives and Thesis outline

The scope of this dissertation is to develop a tool to investigate the vibro-acoustic performances of complex periodic structures in industrial environment. The idea is to conduct the analysis in the wavenumber domain (also called k -space), in order to



Figure 0.3 – Tuned mass damper used in the *Taipei 101* skyscraper.

identify the dispersion relations, the damping loss factor information, to investigate the preferred directions of wave/energy propagation and to estimate the equivalent mechanical properties of complex structures by an inverse approach.

The k-space investigation is conducted using an *Inhomogeneous Wave Correlation* (IWC) method based approach, extending the IWC method to periodic curved structures and avoiding some limitations related to plane wave assumption. The IWC method is also compared to standard k-space techniques, such as *Fast Fourier Transform* (FFT) function, *McDaniel's* approach and the *Wave Finite Element Method* (WFEM).

The IWC method is here proposed as a preliminary design tool for a fast vibro-acoustic characterization of a complex structure, making a comparison in the wavenumber domain between different design choices. The flowchart of the proposed approach is presented in Fig. 0.4.

In the flowchart, a bare test structure is considered and investigated in the wavenumber domain, under a frequency-dependent excitation. Then, the structure is equipped with periodic add-on, such as stiffeners, frames, distributed small-scale resonators, etc., and subject to the same excitation. The k-space informations are obtained for the new configuration and compared to the bare test case. An optimization process can be reached by these comparisons.

The present work is organized following a step-by-step process, moving from some relatively simple *in-plane* structures to complex large-scale curved structures, equipped with both industrially-oriented 3D-printed small-scale resonators and periodic patterns of stringers and frames. Experimental validations are also provided, testing the structures under both diffuse acoustic field and mechanical excitations.

A literature survey is conducted in chapter 1. An overview of the k-space methods available in literature is provided, reporting also the most important achievements and results.

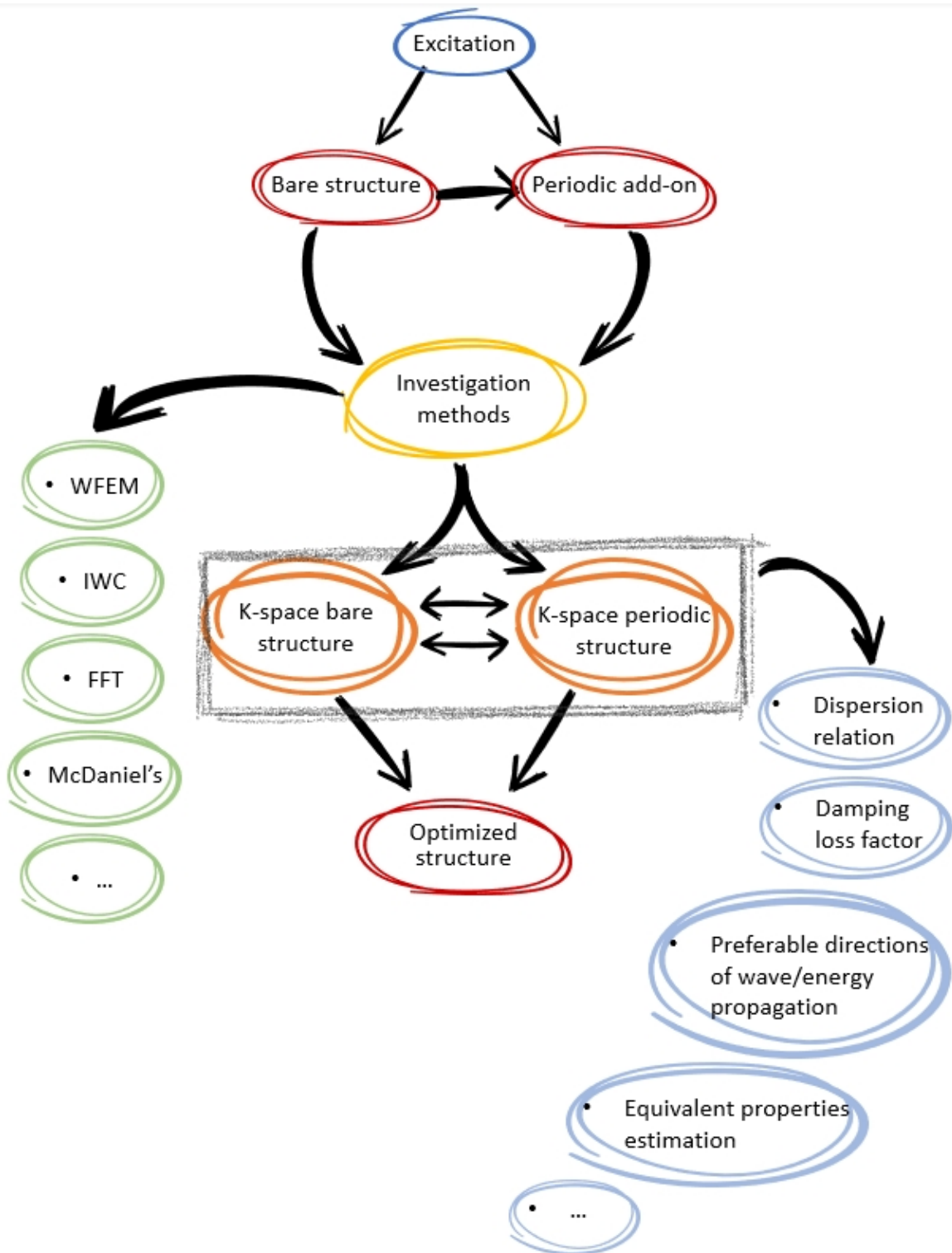


Figure 0.4 – Flowchart of the optimization process.

In chapter 2, a modified formulation of the IWC method is proposed, using a combination of Green's and Hankel's functions. Numerical investigations are conducted on both 1D beam-like and 2D in-plane structures. The dispersion relations are identified, with the related damping loss factor information. Both geometric periodicity and resonators band-gaps occurrence are discussed.

An experimental validation on a 3D-printed sandwich panel is proposed in chapter 3. The angle-dependent dispersion relation is described for both isotropic and orthotropic panels. Two different sandwich panels are investigated, focusing on the effect of the spacing between the vertical mechanical links of the double-wall panels. The geometric periodicity band-gap is also captured in the wavenumber domain.

Chapter 4 is devoted to the development of the IWC method for curved structures. In this chapter, complex large-scale meta-structures are experimentally investigated: an isotropic panel, a laminated composite honeycomb sandwich shell and an aluminum aircraft sidewall panel. The industrially-oriented concept of 3D-printed small-scale resonators is experimentally investigated. The multi-modal behavior and the band-gaps occurrence are described and compared to the bare test structures, under both diffuse acoustic field and shaker excitations.

In chapter 5, an investigation about the effect of the stiffeners cross-section shape and of their inter-spacing on the vibro-acoustic response of axially and ring stiffened curved structures is conducted. Two different stiffeners pitches are investigated. For what concerns the stiffener cross-section, three different shapes are taken in account, keeping constant the cross-sectional inertia properties. The effect of both cross-section shape and pitch are analyzed in terms of dispersion relations and sound transmission losses.

Finally, some concluding remarks and future perspectives are presented in a concluding section.

Chapter 1

Literature review and *state of the art*

1.1 Introduction

The identification of wave propagation and dispersion characteristics of a vibrating structure are of fundamental importance and a highly discussed topic in the vibro-acoustic domain. Dispersion is a physical phenomenon which can be easily explained as a dependency of the phase-velocity from the frequency, mainly related to the inhomogeneous structure of the material and to the geometrical shape of the structure.

Waveguide dispersion, phase velocity dispersion, group velocity dispersion play a key role in understanding how the energy flows in a structure and to highlight if there are some preferable directions of waves propagation. Usually, in the dispersion relation the most important parameters are the wavenumber k and the angular velocity ω . The wavenumber k is defined as the total number of complete wave cycles per unit length; in other words, it can be considered as the spatial frequency of a wave: $k = 2\pi/\lambda$, where λ is the wavelength of the wave. Usually, the wavenumber is a complex number; its imaginary part contains information about the attenuation factor per unit distance. Its estimation is very helpful in the determination of the evanescent field and in the identification of wave spatial decay.

Structural identification, equivalent material properties of complex structures and damping estimation are of great interest in engineering applications, such as vibro-acoustics [1–5]. Some semi-analytical approaches have been developed in order to estimate the mechanical properties of sandwich composite structures [2, 6, 7]. Numerical simulations become more and more important to reduce the cost of experimental identification processes and to describe the damping phenomenon on which any vibration problem is directly dependent.

The most employed methods for wavenumber identification, wave propagation and damping loss factor estimation are discussed in this chapter. In literature, many works can be found on these topics, giving a large overview of the vibro-acoustic related problems. In this chapter, a general overview of the methods is given, showing also the main results and applications.

1.2 Wavenumber identification techniques

The wavenumber domain is also known as *k-space* and it is largely used in various sciences, from medicine, where this technique is used to rebuild the magnetic resonance image from the acquired data, to mechanical engineering, to study the vibration of the structures, for example.

To introduce the idea of wavenumber, a two-dimensional time-harmonic wave propagation is considered. Assuming a constant amplitude U_0 along the propagation direction, the wave is called *plane wave*, and can be expressed as:

$$U(\vec{r}) = U_0 e^{ik(ct - \vec{d} \cdot \vec{r})}, \quad (1.1)$$

in which k is the wavenumber, i is the imaginary unit, \vec{r} is the spatial vector, c is the phase velocity, t is the time variable and \vec{d} is the propagation direction vector. From the previous definition of wavenumber, defined as the number of complete oscillation per unit length, $k = 2\pi/\lambda$, Eq. (1.1) can be rewritten as:

$$U(\vec{r}) = U_0 e^{i(\omega t - k_x x - k_y y)}, \quad (1.2)$$

where $k_x = k \cos \theta$ and $k_y = k \sin \theta$ are the wave-vector ($\vec{k} = k\vec{d}$) components in the x and y directions.

In general, a positive wavenumber represents a rightward traveling wave, while a negative wavenumber denotes a left going wave. By definition, when k_x and k_y are real valued, the wave is defined to be *propagative* and free to propagate without attenuation. If the wavenumber components are purely imaginary valued, the wave is defined to be *evanescent*. When the wavenumber is complex valued, the propagating wave is defined to be *attenuated*. The wave propagation is strictly dependent on the wavenumber, being the relation between wavenumber and frequency defined as the dispersion relation: $\omega = kc$, with $c = 1/\lambda$.

In the field of structural vibrations many different methods are employed to obtain information from/about the k -space; the most common is the Fourier transform analysis, which directly gives the k -space from the vibrational field acquisition. Some others inverse methods were developed in the last decades; these methods allow to predict several quantities, such as the material properties, the structure-borne sound transmission coefficients, the radiated power, the attenuation, applying an inverse approach based on the estimated complex wavenumbers.

In literature, most works focus on the modal-based numerical approaches; these approaches reach their limits in mid- and high-frequency ranges where great wave modes density exists. This disadvantage makes their use of limited interest. As alternatives, in a wave propagation framework, for parameter identification other methods based on the wavenumber domain analysis [8–12] or based on the Statistical Energy Analysis (SEA) [13–15] are introduced.

The most employed technique in the wavenumber domain analysis is the spatial Fourier Transform, with the associated Discrete Fourier Transform (DFT) in the discrete domain. This approach is very simple and very fast, but it is affected by some limitations

in terms of resolution (directly dependent on the geometrical dimensions of the structure and its discretization) and of the indirect estimation of the complex wavenumbers. This latter aspect has been solved using different approaches based on Prony's method. Prony's method offers high resolution along with the capability of identifying the unknown complex wavenumbers and their amplitudes. The Prony's technique is a means of identifying the constituent wavenumbers and their corresponding amplitudes in an exponential model of the spatial response. The Prony's method is a two-stage process. In the first stage, the wavenumbers are found and, in the second stage, the amplitudes for these wavenumbers are found from a linear least-squares fit of the model to the data. A modified extended technique based on Prony's method to estimate the complex wavenumbers is shown in [16].

1.2.1 Space-wavenumber Fourier transform

The basic idea of the Fourier transform is to determine the constitutive waves of any signal, giving back information about the frequency and the amplitude.

The space-wavenumber Fourier transform is analogous to the well known time-frequency Fourier transform; the main difference is the operating variables that have changed from ωt to kr . A very basic tutorial on how to calculate the wavenumber and its transforms from a structural vibration field can be found in [17]. The expressions of the spatial Fourier transform and its inverse are, respectively:

$$F(k) = \int_{-\infty}^{\infty} f(\vec{r}) e^{i\vec{k}\vec{r}} d\vec{r}, \quad (1.3a)$$

$$f(\vec{r}) = \frac{1}{2\pi} \int_{-\infty}^{\infty} F(k) e^{-i\vec{k}\vec{r}} dk. \quad (1.3b)$$

One of the main difference between time-frequency and space-wavenumber Fourier transforms is the presence of right and left traveling waves in the spatial vibrational field. Considering a single wave propagating in the rightward direction at a fixed frequency f , this wave is defined by a single wavenumber k , showing a single peak in the wavenumber domain.

One of the most simple application of this technique is on a 2D plane structure. A harmonic displacement field can be considered as primary input, usually defined in the (x, y) plane (see Eq. (1.4), in which the symbol \hat{w} indicates that the displacement field is frequency-dependent):

$$w(x, y, t) = \int_0^{+\infty} \hat{w}(x, y) e^{i\omega t} d\omega. \quad (1.4)$$

An application of the spatial-wavenumber Fourier transform is shown in Fig. 1.1, in which the classical $(4, 2)$ structural mode shape is shown for an isotropic plate, together with the correlated wavenumber transform.

In the following part the main advantages and the main drawbacks of the Discrete Fourier Transform (DFT) are investigated [12]. The DFT assumes two hypothesis:

1. the displacement field \hat{w} is given in an uniform grid $(x_i = idx, y_j = jdy)$ with $1 \leq i \leq N_1 - 1$ and $1 \leq j \leq N_2 - 1$, in which N_1 and N_2 are the meshgrid dimensions

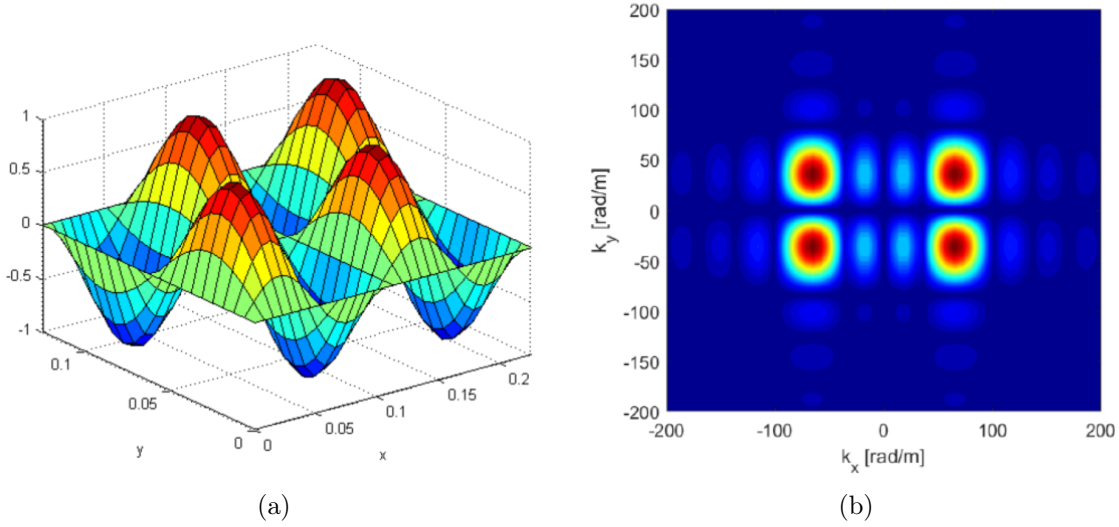


Figure 1.1 – Structural mode shape (a) and wavenumber transform (b) [17].

along x and y directions, respectively, dx and dy are the space increments along the axes x and y , respectively;

2. the field is assumed to be 2D-*periodic*:

$$\forall i, j \in \mathbb{N}^2, \hat{w}(idx, jdy) = \hat{w}((i/N_1)dx, (j/N_2)dy). \quad (1.5)$$

The spatial mesh has to be small enough to satisfy the Nyquist criterion, at the least half of the smallest wavelength of interest; on the other hand, the span of the measurement has to be large enough to have an acceptable resolution in the wavenumber domain.

In the discrete domain, we can assume $\Delta k_x = 2\pi/N_1 dx$ and $\Delta k_y = 2\pi/N_2 dy$ as a basis for the complex functions space; the family of exponential functions with discrete wavenumbers can be written as $(k_{xp} = p\Delta k_x, k_{yq} = q\Delta k_y)_{(1 \leq p \leq N_1-1, 1 \leq q \leq N_2-1)}$. Consequently, the displacement field can be written as follows:

$$\hat{w}(x_i, y_j) = \sum_{p=0}^{N_1-1} \sum_{q=0}^{N_2-1} \hat{w}(k_{xp}, k_{yq}) e^{i(k_{xp}x_i + k_{yq}y_j)}. \quad (1.6)$$

The DFT $\hat{w} \rightarrow \hat{\hat{w}}$ assumes the following expression:

$$\hat{\hat{w}}(k_{xp}, k_{yq}) = \frac{1}{N_1 N_2} \sum_{i=0}^{N_1-1} \sum_{j=0}^{N_2-1} \hat{w}(x_i, y_j) e^{-i(k_{xp}x_i + k_{yq}y_j)}. \quad (1.7)$$

Two main advantages are bijectivity and rapidity; the first one, bijectivity, means that the inverse of the DFT (IDFT) exists, that is useful to rebuild the displacement field from the k -space or to introduce a filter in the wavenumber domain. Rapidity is related to the possibility to use the Fast Fourier Transform (FFT) to process the data very fast [12].

The drawbacks connected to the use of the DFT are aliasing, leakage and poor resolution. The aliasing effect is related to field discretization and to the fact that the DFT is $(2\pi/\Delta x)$ -periodic; the periodicity condition is expressed in Eq. (1.8):

$$\widehat{w}(k_x, k_y) = \widehat{w}\left(k_x + \frac{2\pi}{dx}, k_y\right) = \widehat{w}\left(k_x, k_y + \frac{2\pi}{dy}\right). \quad (1.8)$$

This means erroneous DFT treatments for wavenumbers k_x and k_y outside the domains $[-\pi/\Delta x, \pi/\Delta x]$, $[-\pi/\Delta y, \pi/\Delta y]$, respectively. Leakage is due to the finite size of the field \widehat{w} , because a singular wave (k_x, k_y) appears as a cardinal sine shape, while it should appear in the k -space as a Dirac distribution. The k -space resolution allows to obtain a poor estimation of the wave vectors, because the wave content of a given field \widehat{w} is only known in a k -space grid [12].

1.2.2 *McDaniel's method*

A method for estimating the complex wavenumbers and amplitudes of waves that propagate in damped structures was proposed by McDaniel [8]. The idea is to compare the response measurements of a vibrating structure with a wave field that approximates its behavior; in other words, re-constructing the wave field from the spatially response data. A harmonic time-dependent expression of the displacement field is assumed, in the form: $w = \Re\{We^{-i\omega t}\}$. In a steady-state condition, the governing differential equation that describes the motion of the neutral surface of the structure (the neutral axis in case of beam-like structures) assumes the following expression:

$$-\omega^2 W + \mathcal{L}\{W\} = 0, \quad (1.9)$$

where W is the displacement amplitude, ω^2 is the angular frequency and \mathcal{L} is a linear operator that involves derivatives with respect to x and structural parameters. To solve the differential equation expressed in Eq. (1.9), a mathematical expression of the boundary conditions has to be defined, based on the order of differentiation of the operator \mathcal{L} . The boundary conditions equations can be expressed as follows:

$$\mathcal{L}_b\{w\}|_{x=x_b} = \Re\{Be^{-i\omega t}\}, \quad (1.10)$$

where x_b represents the spatial coordinate at the boundaries and B is a complex valued amplitude. The steady-state solution of Eq. (1.9) subject to a set of boundary conditions of the form given in Eq. (1.10) is a summation of damped waves [8]:

$$W(x) = \sum_{n=1}^N \left(F_n e^{ik_n x} + B_n e^{ik_n(L-x)} \right). \quad (1.11)$$

Each value of n represents a distinct wave type that propagates on the structure with a complex-valued wavenumber, k_n . The two terms F_n and B_n are the amplitudes of the forward and backward propagating waves, respectively; their values are boundary conditions-dependent.

The proposed method uses an iterative process for the wavenumbers estimation; the iterative process consists in adjusting the wavenumber and waves amplitudes in Eq. (1.11) so that the measured data are approximated by the wave-field. The algorithm starts assuming a value of the propagating wavenumbers at a fixed frequency; a way to

obtain a first estimation of the wavenumber is to use analytical expressions (if the cross-section is homogeneous) for the bending k_f , longitudinal k_l and shear k_s wavenumbers, respectively:

$$\begin{aligned} k_f^4 &= \sqrt{\frac{\rho A \omega^2}{E(\omega)[1 - i\eta(\omega)]I}} \\ k_l &= \sqrt{\frac{\rho \omega^2}{E(\omega)[1 - i\eta(\omega)]}} , \\ k_s &= \sqrt{\frac{\rho \omega^2}{G(\omega)[1 - i\eta(\omega)]}} \end{aligned} \quad (1.12)$$

where ρ is the mass density, A is the cross-sectional area, I is the area moment of inertia, E is the real part of the Young's modulus, η is the material loss factor and $G = E/[2(1 + \nu)]$ is the shear modulus.

The waves amplitudes are found imposing that the wave-field in Eq. (1.11) approximates the measured data at each location:

$$W_m \approx \widetilde{W}_m, \quad \text{for } m = 1, 2, \dots, M \quad , \quad (1.13)$$

where M is the total number of acquisition points. Each amplitude W_m can be expressed as the sum of all the individual wave-fields evaluated at the m -th measurement position, as follows:

$$W_m = \sum_{n=1}^N \left(F_n e^{ik_n x_m} + B_n e^{ik_n(L-x_m)} \right), \quad (1.14)$$

in which $N = 2$ when flexural modeling is required, and $N = 1$ in case of longitudinal or torsional motions.

Writing the approximations of Eq. (1.13) in matrix form gives:

$$[[\Phi][\beta]] \begin{Bmatrix} \{F\} \\ \{B\} \end{Bmatrix} \approx \widetilde{W}_m, \quad (1.15)$$

where the forward and backward propagation matrices, respectively $[\Phi]$ and $[\beta]$, are given by:

$$\Phi_{mn} = e^{ik_n x_m} \quad \text{and} \quad \beta_{mn} = e^{ik_n(L-x_m)}. \quad (1.16)$$

The waves amplitudes are found by satisfying Eq. (1.15) in a least-squares sense; the number of required measurement locations depends on the the number of waves that propagate in the structure [8]. An estimation error can be then calculated, making the difference between the wave-field and the measurements. The normalized error assumes the following expression:

$$\varepsilon = \sqrt{\left(\sum_{m=1}^M |W_m - \widetilde{W}_m|^2 / \sum_{m=1}^M |\widetilde{W}_m|^2 \right)}. \quad (1.17)$$

Based on the error norm in Eq. (1.17), the wavenumber estimates are refined and the process repeats until the error norm is below a given tolerance.

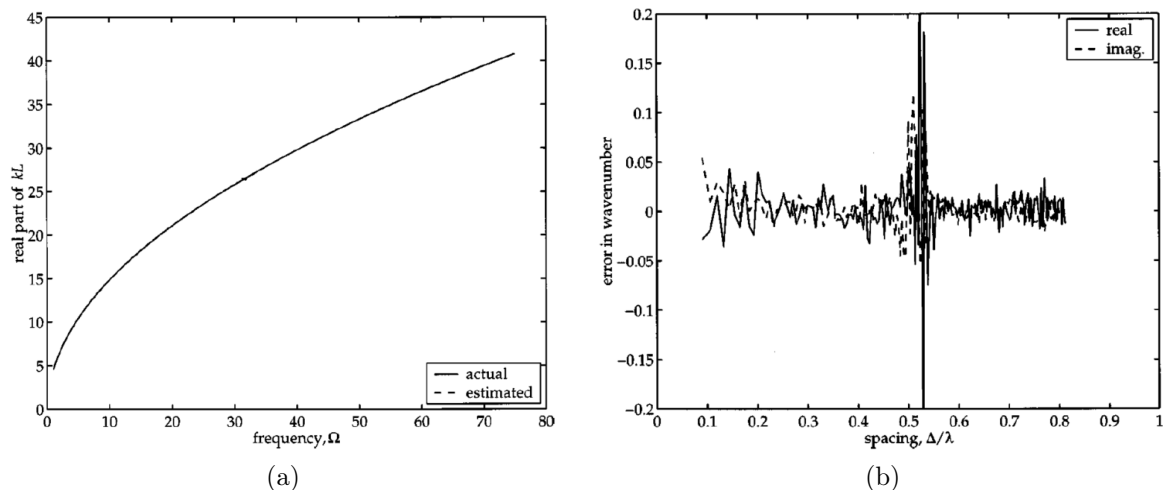


Figure 1.2 – Normalized dispersion curve (a) and estimation error in the real and imaginary parts of the normalized wavenumbers (b) [8] .

The presented method is then applied to a vibrating beam and compared to an analytical solution. The real part of the dispersion curve is shown in Fig. 1.2a, in which both wavenumber and frequency are normalized. The estimation of the errors in the real and imaginary parts of the normalized wavenumbers are shown in Fig. 1.2b.

A similar approach is presented in [9], in which a wave approach is used to estimate the damping loss factor under transient loading condition. To obtain the forced response of the beam, the global solution $y(x, t)$ is assumed to be given by a sum of wave and modal solutions, as follows:

$$y(x, t) = y_w(x, t) + y_m(x, t), \quad (1.18)$$

where y_w represents the wave solution (needed to satisfy homogeneous initial conditions and non-homogeneous boundary conditions) and y_m is the modal solution (required to satisfy non-homogeneous initial conditions and homogeneous boundary conditions). Both wave and modal solutions have to satisfy the following differential equation:

$$\rho \frac{d^2 y}{dt^2} + \mathcal{L}\{y\} = 0, \quad (1.19)$$

where \mathcal{L} is the time-invariant linear operator involving derivatives with respect to the spatial coordinate x . The boundary conditions assume the following expression:

$$\mathcal{L}_b\{y\}|_{x=x_b} = \begin{cases} f(t), & \text{wave solution} \\ 0, & \text{modal solution} \end{cases}, \quad (1.20)$$

in which $x_b = \{0, L\}$ and \mathcal{L}_b is time-invariant and involves spatial derivatives of y [9]. By solving the differential equation expressed in Eq. (1.19), imposing the appropriate boundary and initial conditions for both wave and modal solutions, the complex wavenumbers can be estimated (with the related damping loss factor information).

An example of damping loss factor estimation for the finite element model of a vibrating beam is shown in Fig. 1.3a; the normalized error of the noise-free and noisy-simulated data are shown in Fig. 1.3b.

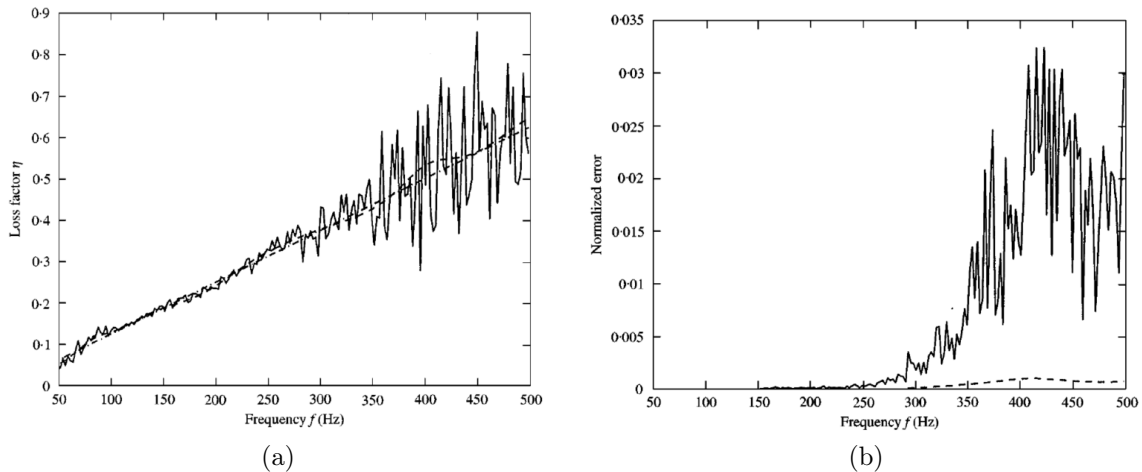


Figure 1.3 – Damping loss factor estimation for the finite element model: exact solution \cdots , noise-free simulated data $---$, noisy-simulated data $—$ (a) and normalized error: noise-free simulated data $---$, noisy-simulated data $—$ (b). [9]

McDaniel’s method provides an estimation of the dispersion curves and of the damping loss factor in damped structures from a small number of acquisition points. The steady-state condition is assumed constituted of a sum of forward and backward propagating waves. The main advantages are the absence of any hypotheses about the boundary conditions, the material properties or the cross-sectional dimensions of the structures [8].

1.2.3 The *Inhomogeneous Wave Correlation (IWC)* method

In the mid-high-frequency domain classical normal modes-based methods cannot be used due to high modal overlap and high modal density, making the identification of the modes hard to obtain. In this context, a method based on plane wave propagation was developed: the Inhomogeneous Wave Correlation (IWC) method [11, 18]. The aim of this approach is the estimation of the damping information of a vibrating structure and the identification of the angle-dependent dispersion curves for orthotropic plane structures [12, 19, 20]. The idea is to correlate the total energy of a vibrating structure and the energy carried on by an inhomogeneous damped plane wave, traveling with a incidence angle θ . The IWC method can be considered the equivalent, in the wavenumber domain, of the Modal Assurance Criterion (MAC), in the modal domain [21]. The basic assumptions of the IWC method can be summarized as follows:

- comparison between the displacement field of the vibrating plane structure and the inhomogeneous plane wave;
- possibility to use coherence signals of the experimental measured points;
- separation of the near field from the far field by the introduction of the attenuation factor;
- assumption of a single plane wave traveling in the specific direction θ .

The inhomogeneous wave assumes the following expression:

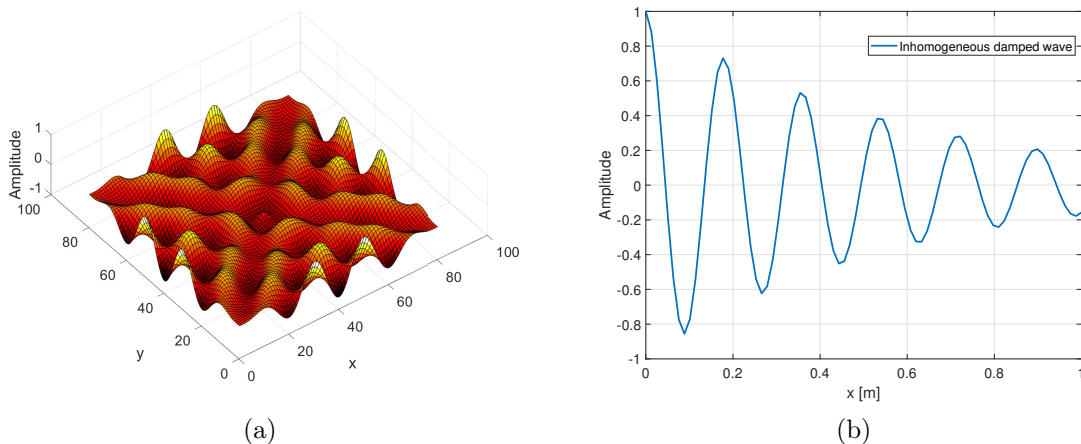


Figure 1.4 – Schematic representation of the basis of the IWC method: vibrational field of a plane structure (a) and the representation of an inhomogeneous damped wave (b).

$$\hat{\sigma}_{k,\gamma,\theta}(x, y) = e^{-ik(\theta)(1+i\gamma(\theta))(x \cos \theta + y \sin \theta)}, \quad (1.21)$$

where θ is the heading angle of the traveling wave, γ is the attenuation factor ($\gamma = \eta c_\varphi / 2c_g$, with η, c_φ, c_g being the damping loss factor, the phase velocity and the group velocity, respectively [13]), $i^2 = -1$ is the imaginary unit and (x, y) are the spatial coordinates. A schematic representation of the vibrational field of a plane structure subjected to a harmonic unit force and of a one-dimensional inhomogeneous damped wave is shown in Fig. 1.4.

For a fixed frequency f_0 , the correlation between the inhomogeneous wave expressed in Eq. (1.21) and the complete wave field is calculated by the following relationship:

$$IWC(k, \gamma, \theta) = \frac{|\iint_S \hat{w} \cdot \hat{\sigma}_{k,\gamma,\theta}^* dx dy|}{\sqrt{\iint_S |\hat{w}|^2 dx dy \cdot \iint_S |\hat{\sigma}_{k,\gamma,\theta}|^2 dx dy}}, \quad (1.22)$$

where $*$ denotes the complex conjugate and S is the surface of the vibrating structure. The identification of the unknown complex wavenumber $k = k_{\mathbb{R}e} + ik_{\mathbb{I}m}$, for a given direction θ , leads to the maximization of the function $(k, \gamma) \rightarrow IWC(k, \gamma, \theta)$. For very simple structures, the IWC function has a well-defined maximum, identifying the point where the inhomogeneous wave $\hat{\sigma}_{k,\gamma,\theta}(x, y)$ correlates best with the displacement field [18]. An example of the identified maximum values of the real part of the wavenumber and of the attenuation factor are shown in Fig. 1.5a and Fig. 1.5b, respectively.

In practical applications, the wave field is measurable in some discrete points, becoming the integration over the entire surface S in Eq. (1.22) a finite weighted sum:

$$\iint_S dx dy \implies \sum_{i=1}^N \rho_i S_i, \quad (1.23)$$

where ρ_i are the coherence values of the measured data at each point ($\rho_i = 1$ if the coherence is not available), S_i is an estimation of the surface around the point i and

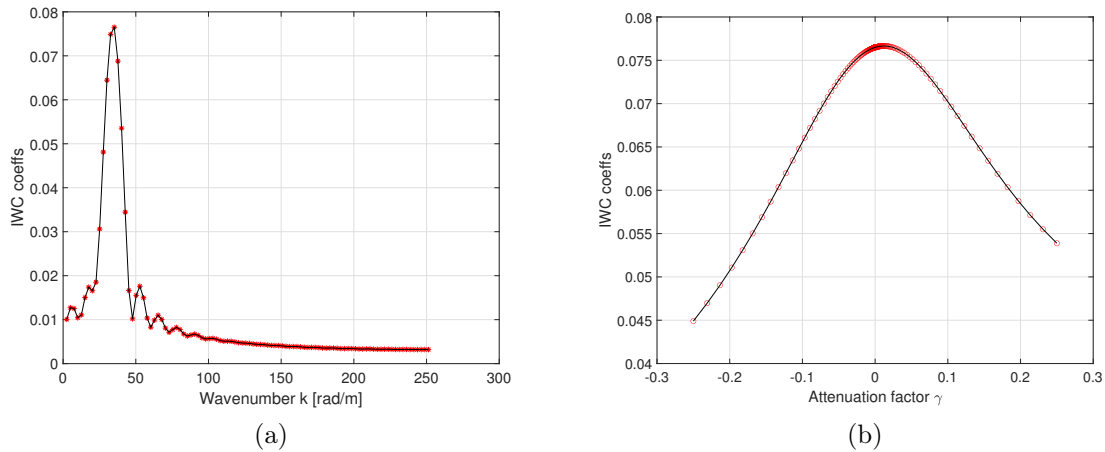


Figure 1.5 – Identified maximum values of the wavenumber (a) and of the attenuation factor γ (b) for a fixed frequency f_0 .

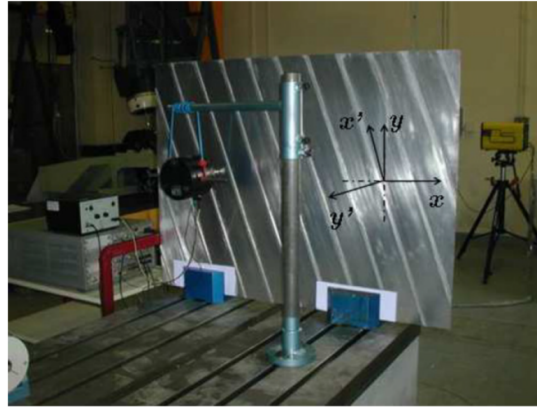


Figure 1.6 – Set-up of the one-side clamped ribbed panel [12].

N is the total number of discrete points. Introducing Eq. (1.23) into Eq. (1.22), the correlation function becomes:

$$\text{IWC}(k, \gamma, \theta) = \frac{|\sum_{i=1}^N \hat{w}(x_i, y_i) \cdot \hat{\sigma}_{k, \gamma, \theta}^*(x_i, y_i) \rho_i S_i|}{\sqrt{\sum_{i=1}^N |\hat{w}(x_i, y_i)|^2 \rho_i S_i \cdot \sum_{i=1}^N |\hat{\sigma}_{k, \gamma, \theta}(x_i, y_i)|^2 \rho_i S_i}}. \quad (1.24)$$

The algorithm first discretizes the angle θ into (θ_j) ; for each of these angles, the maximum of IWC is located at a value (k_j, γ_j) ; thus the method creates two functions $\theta \rightarrow k(\theta)$ and $\theta \rightarrow \gamma(\theta)$ defined on the set of discrete values (θ_j) . Finally, the trio $(\theta_{j_0}, k_{j_0}, \gamma_{j_0})$ is removed from the list if γ_{j_0} is greater than 1. The introduction of a loss factor makes it possible to distinguish the near-field from the far-field: the near-field corresponds to a high apparent loss factor (imaginary part of the identified wavenumber greater than its real part [12]).

Ichchou et al. [12, 19] applied the IWC method to a ribbed plate to identify the orthotropic behavior (i.e. the angle-dependent wavenumbers) and the multi-modal propagation. The set-up of their experimental investigation is shown in Fig. 1.6.

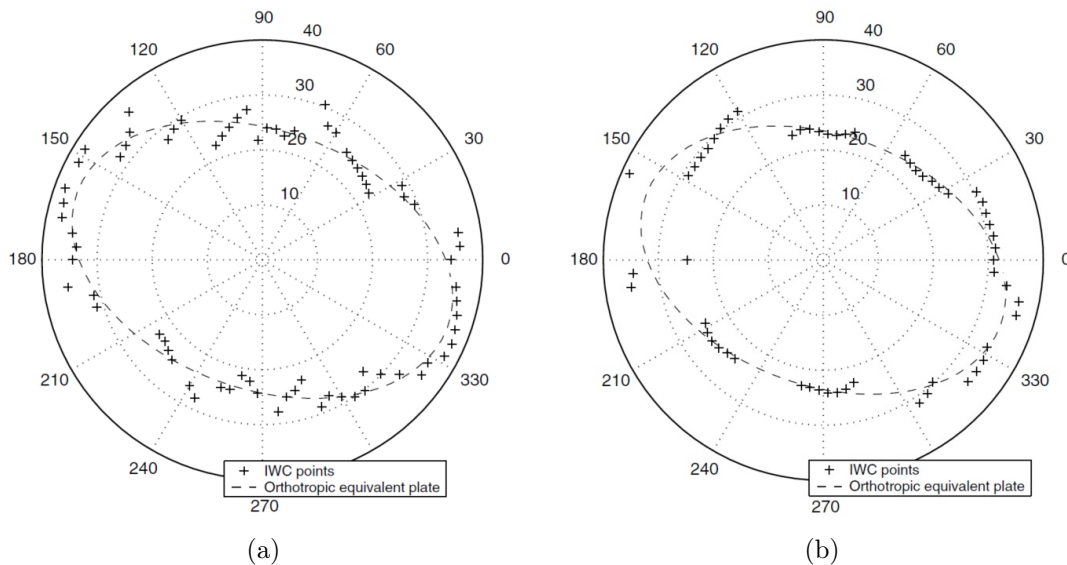


Figure 1.7 – IWC results for a ribbed panel with different boundary conditions: free (a) and one-side clamped (b) [12].

The independence of the wavenumber from the boundary conditions have been also demonstrated, describing the orthotropic behavior and the classical elliptic shape in the wavenumber domain (see Fig. 1.7).

The uncoupled flexural plate and stiffeners wavenumbers are captured and shown in Fig. 1.8. In this case, the correlation function is characterized by the presence of a maximum value (see Fig. 1.5) and some other local maxima, denoting several wavenumbers propagating at the same frequency. In the low-frequency range the global bending mode of the plate is dominated by the motion of the skin; increasing the frequency, two straight segments appear in the k -space domain, as shown in Fig. 1.9, denoting a wave propagation along the stiffeners direction.

Based on the estimated flexural wavenumbers with the IWC method, an inverse approach is presented in [22], obtaining an evaluation of the equivalent material properties of a composite sandwich honeycomb beam and plate. The dispersion curve of the composite sandwich honeycomb beam is shown in Fig. 1.10, in which a comparison with the Timoshenko's beam theory and the McDaniel formulation (described in section 1.2.2) is proposed.

The estimation of the orthotropic behavior of the composite sandwich honeycomb panel is shown in Fig. 1.11a; an inverse estimation of the dynamic stiffness is proposed in Fig. 1.11b.

A slightly different formulation for the inhomogeneous traveling wave is proposed in [23]. This variant of the method is proposed to avoid some limitations of the classical IWC approach related to the damping estimation and the plane wave assumption in the region close to the excitation point. A sum of inhomogeneous waves is considered, dealing with the following expression:

$$\hat{\sigma}_{k,\gamma,\theta}(x, y) = e^{-ik(\theta)(1+i\gamma(\theta))(x \cos \theta + y \sin \theta)} + e^{ik(\theta)(1+i\gamma(\theta))(x \cos \theta + y \sin \theta)}, \quad (1.25)$$

which accounts for both right $e^{-ik(\theta)}$ and left $e^{ik(\theta)}$ traveling waves. The two ways trav-

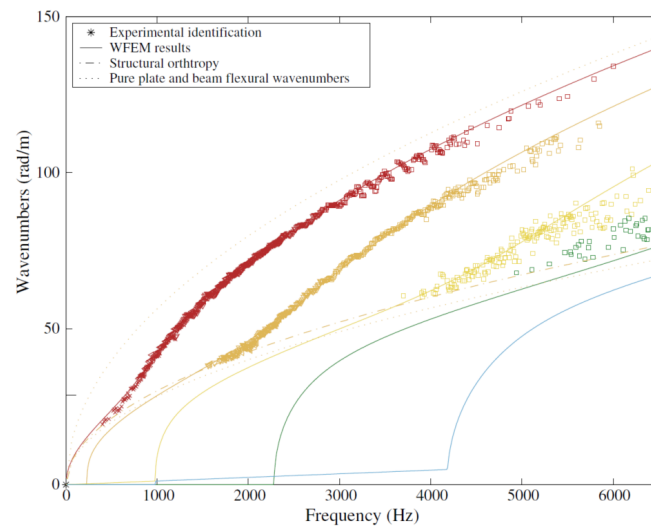


Figure 1.8 – Multi-modal dispersion curves [19].

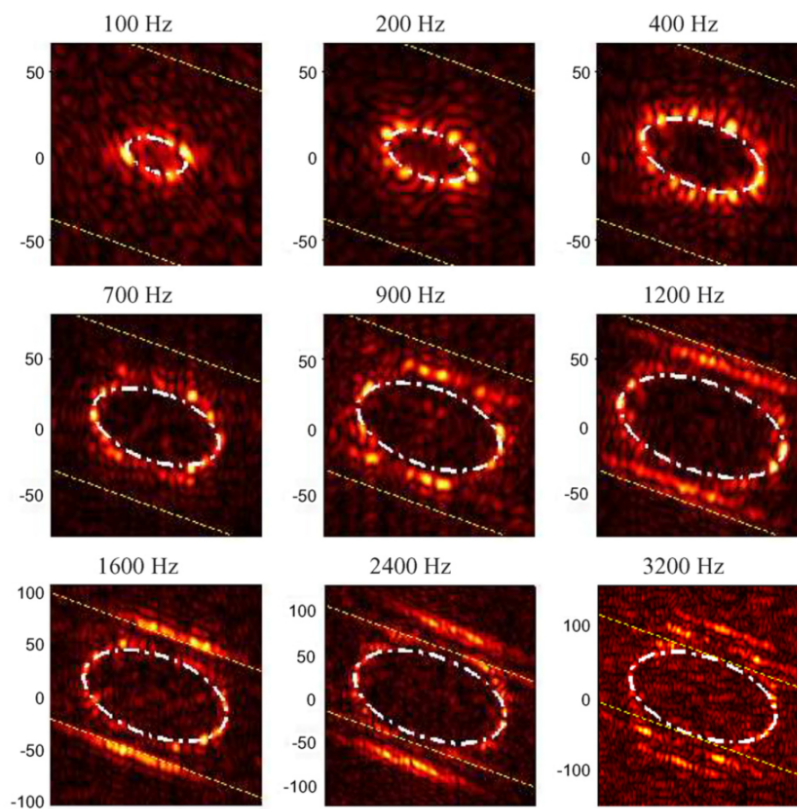


Figure 1.9 – Multi-modal propagation at different frequencies [12].

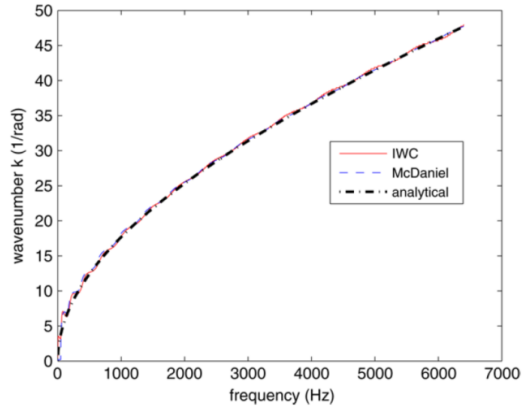


Figure 1.10 – Dispersion curve for the composite beam [22].

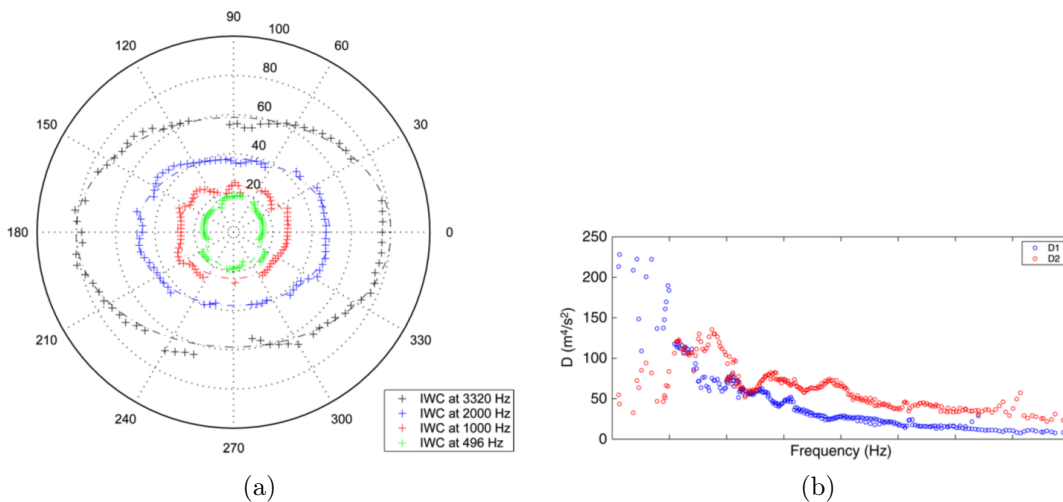


Figure 1.11 – Angle-dependent wavenumbers at fixed frequencies (a) and inverse estimation of the dynamic stiffness (b) [22].

eling waves is the main difference with the classical IWC method, which considers only the forward propagating (incident) wave $e^{-ik(\theta)}$ and neglects the term corresponding to backward propagating wave $e^{ik(\theta)}$ and two other terms corresponding to evanescent waves.

1.2.3.1 Extended IWC formulation

An application of the IWC method on a locally resonant meta-material plate is proposed in [24], using a so called "extended" IWC approach. In this work, experimental dispersion curves are retrieved from harmonic out-of-plane displacement field measurements $w(x, y)$ of a vibrating locally resonant meta-material plate (see Fig. 1.12), built attaching a periodic pattern of resonators (a schematic representation of the resonator is given in Fig. 1.12a). To obtain a better estimate of the attenuation around the band-gap frequency region, a different expression of the inhomogeneous wave is proposed, taking in account the location of the punctual excitation, (x_0, y_0) , as follows:

$$\hat{\sigma}_{k,\gamma,\theta}(x, y) = e^{-ik(\theta)(1+i\gamma(\theta))((x-x_0)\cos\theta+(y-y_0)\sin\theta)}. \quad (1.26)$$

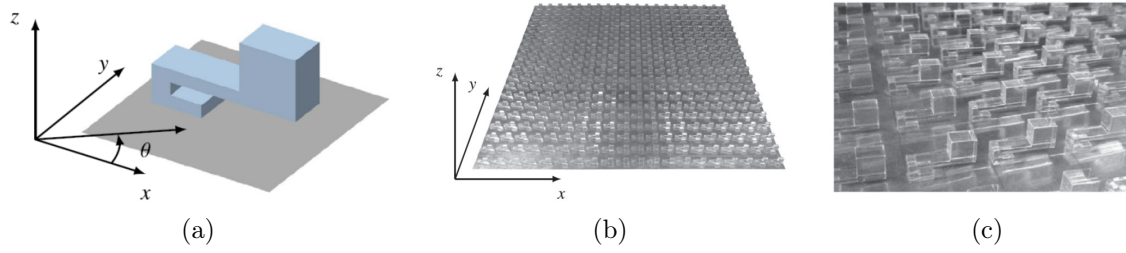


Figure 1.12 – Unit cell of the locally resonant meta-structure (a), full-scale resonant plate (b) and close-up view (c) [24].

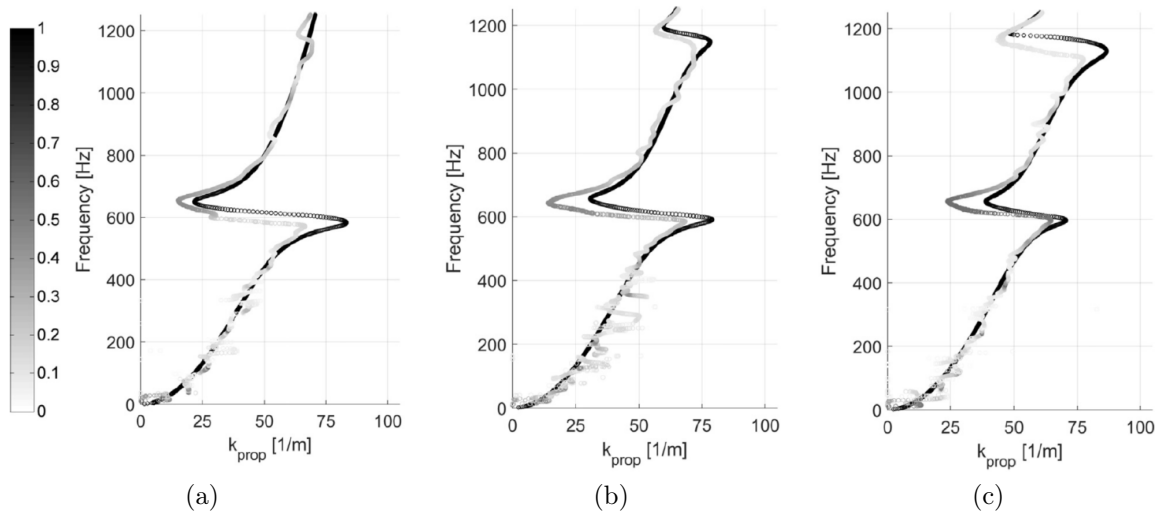


Figure 1.13 – Numerically predicted dispersion curves compared with the measured one by using the extended IWC method: $\theta = 0$ deg (a), $\theta = 45$ deg (b) and $\theta = 90$ deg (c)[24].

The inhomogeneous wave in Eq. (1.26) is then correlated in the same way showed in Eq. (1.24). The damped unit cell technique is applied to the unit cell presented in Fig. 1.12a, in order to obtain the numerical dispersion curves in three different directions: $\theta = 0$ deg, $\theta = 45$ deg and $\theta = 90$ deg. The resonators are tuned at 600 Hz; the resonance is characterized by an increase of the amplitude of the wavenumber in the frequency region just before the tuning frequency, then a strong attenuation around that value of the frequency (with an increase of the imaginary part of the wavenumber) and followed by a gradual increment of the real part after the resonance region (see Fig. 1.13). The experimental dispersion curves are obtained exciting the meta-structure by a mechanical shaker and scanning the out-of-plane displacement using a Laser Doppler Velocimeter; the displacement field is then post-processed with the extended IWC method. From the dispersion curves analysis, a directional effect of the resonators can be observed.

1.2.3.2 1D variant of the IWC method

The IWC method is also valid for one-dimensional structures [25, 26]. In this case, a wave propagation in the form e^{kx} is assumed; the inhomogeneous wave has the following expression:

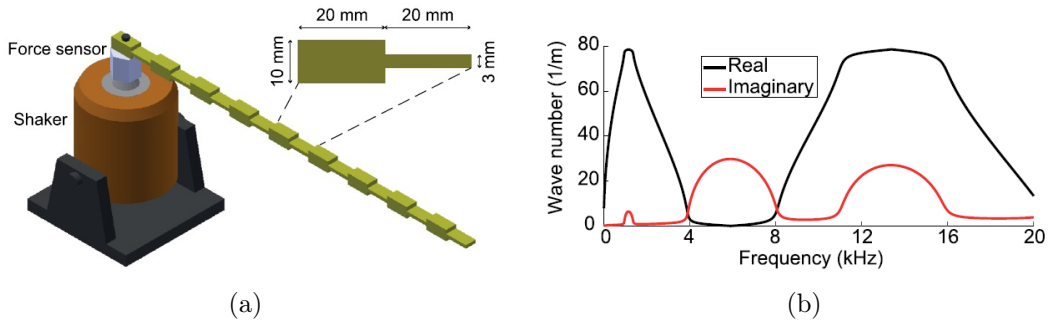


Figure 1.14 – Experimental set-up of the beam with varying cross-section (a) and analytical dispersion curves in the first Brillouin zone (b) [26].

$$\hat{\sigma}_{k,\gamma,\theta}(x) = e^{-ik(\theta)(1+i\gamma(\theta))x}. \quad (1.27)$$

Moving from the 2D domain to the 1D one and assuming L the length of the structure, Eq. (1.22) becomes:

$$\text{IWC}(k, \gamma, \theta) = \frac{|\int_L \hat{w} \cdot \hat{\sigma}_{k,\gamma,\theta}^* dx|}{\sqrt{\int_L |\hat{w}|^2 dx \cdot \int_L |\hat{\sigma}_{k,\gamma,\theta}|^2 dx}}. \quad (1.28)$$

As in the 2D case, the maximization of the correlation function in terms of k and γ defines the point of best agreement between \hat{w} and $\hat{\sigma}_{k,\gamma,\theta}$. In order to reconstruct the full spatial spectrum of the wave pattern, an iterative process is proposed in [26], and it can be summarized as follows:

1. find the location (k_1, γ_1) of the absolute maximum using the *fmincon* function of MATLAB[®] (the *fmincon* function is used to estimate the imaginary part of the wavenumber within given boundaries, i.e. ranges of possible values of k and γ);
2. calculate the complex amplitude of this component of the total deflection, by projecting the inhomogeneous wave onto the measured vibration pattern, and normalizing it to the norm of $\hat{\sigma}$

$$A_1 = \frac{\sum_i \hat{\sigma}(k_1, \gamma_1, x_i) \hat{w}(x_i)}{\sum_i \hat{\sigma}(k_1, \gamma_1, x_i) \hat{\sigma}^*(k_1, \gamma_1, x_i)};$$

3. subtract the scaled inhomogeneous wave $A_1 \hat{\sigma}(k_1, \gamma_1, x)$ from the measured vibration pattern and go back to step 1 .

The IWC method is successfully implemented to obtain the real and the imaginary parts of the wavenumbers for a beam with a varying cross-section and for a cross laminated timber beam. The experimental set-up and the beam dimensions are very similar for both cases; a schematic representation of the periodic beam and of the set-up is illustrated in Fig. 1.14a. The analytical solution is derived using the transfer-matrix formulation [27] using a thick-beam model, described as follows:

$$EI \frac{\partial^4 w}{\partial x^4} + \rho A \frac{\partial^2 w}{\partial t^2} - \left(\rho I + \frac{EI\rho}{KAG} \right) \frac{\partial^4 w}{\partial x^2 \partial t^2} + \frac{\rho^2 I}{KG} \frac{\partial^4 w}{\partial t^4} = 0, \quad (1.29)$$

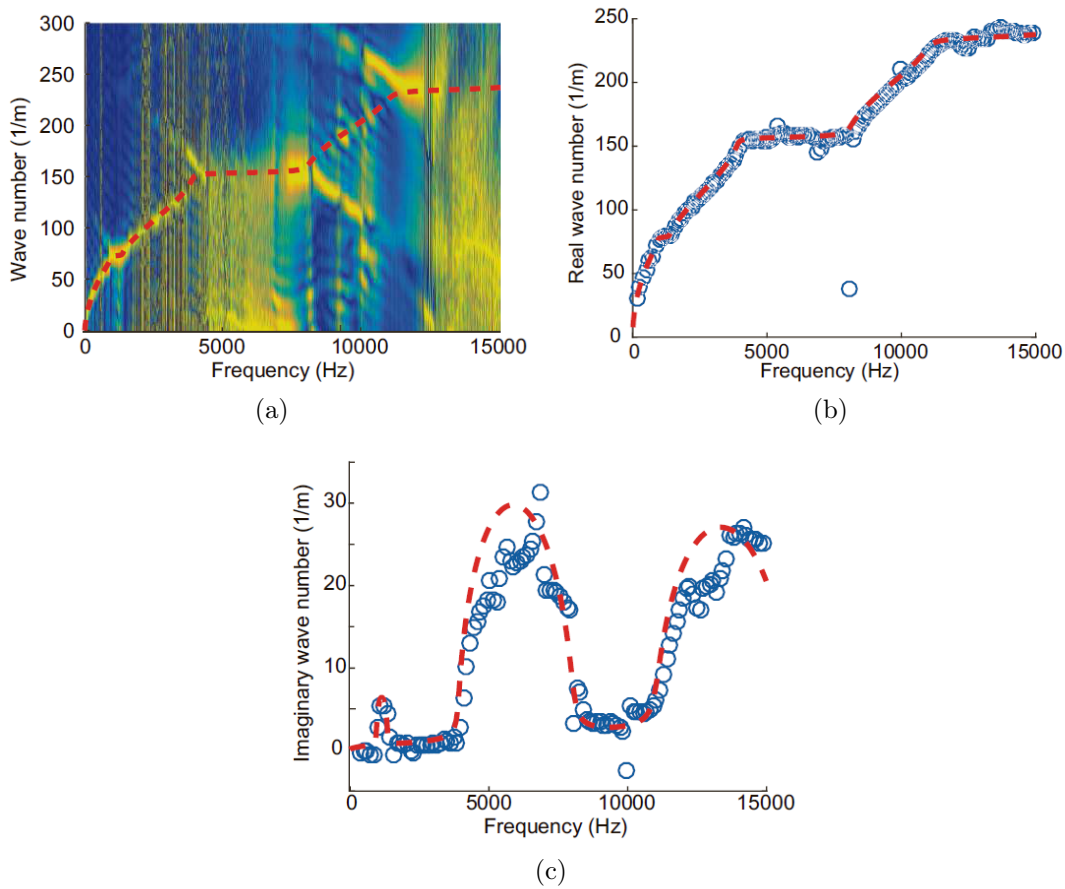


Figure 1.15 – Dispersion curves of the polyamid beam with periodically varying thickness with the spatial Fourier transform (a) and the IWC method (real part (b) and imaginary part (c)) [25].

where E is the Young's modulus, I is the moment of area, G is the shear modulus, ρ is the mass density, w is the transverse displacement, x is the spatial coordinate, A is the beam cross-section area, t is the time dependence and $K = 5/6$ is a constant value to take in account the shear-force variation in the thickness direction. The dispersion curves obtained solving Eq. (1.29) are shown in Fig. 1.14. The IWC method is then applied to the harmonic displacement field, estimating the complex dispersion curves shown in Fig. 1.15, where a comparison with a 1D spatial Fourier transform is also made (see Fig. 1.15a).

1.2.4 *Spatial Laplace Transform for COMplex Wavenumber recovery (SLaTCoW) method*

A method very similar to the IWC method is proposed in [28] and applied in [29, 30]; this method is called *SLaTCoW*, which is an acronym for Spatial Laplace Transform for COMplex Wavenumber recovery. The main difference between the proposed approach and the IWC method is the use of the Laplace transform instead of the Fourier transform, in order to recover both the real and imaginary parts of the wavenumber.

Following the formulation of Geslain et al. [28], the *SLaTCoW* method can be sum-

marized as follows. Assuming a general wave-field discretely recorded along a line of length L with a time dependence of $e^{-i\omega t}$, the complete wave-field can be reconstructed by a sum of modal contributions, as follows:

$$\xi(x) = \sum_{m \in M} \tilde{\xi}^m e^{iK^m x} \Pi(x, L), \quad (1.30)$$

where x is the spatial coordinate, $\tilde{\xi}^m$ is the complex amplitude of the m -th mode, K^m is the complex wavenumber of the m -th mode, M is the set of modes and $\Pi(x, L)$ is the gate function equal to 1 when $x \in [0, L]$ and equal to 0 elsewhere. The expression of Eq. (1.30) takes into account only forward propagating modes, having both real and imaginary parts of the complex wavenumber a positive value. Denoting with $\Xi(s) = \int_{-\infty}^{\infty} \xi(x) e^{-sx} dx$ (s being the complex wavenumber parameter $s = s_{\mathbb{I}m} + i s_{\mathbb{R}e}$, with real valued $s_{\mathbb{I}m}$ and $s_{\mathbb{R}e}$) the spatial Laplace transform of the wave field $\xi(x)$. This spatial Laplace transform is expressed as follows:

$$\begin{aligned} \Xi(s) &= \sum_{m \in M} \tilde{\xi}^m \int_0^L e^{[(iK^m - s)x]} dx \\ &= L \sum_{m \in M} \tilde{\xi}^m e^{[(iK^m - s)L/2]} \frac{\sinh [(iK^m - s)L/2]}{(iK^m - s)L/2}. \end{aligned} \quad (1.31)$$

The complex wavenumber can be found for each frequency by minimizing the following cost function (similarly to what is described in [31]):

$$\begin{aligned} F(|\tilde{\xi}^m|, \phi^m, k_r^m, k_i^m, M) &= \\ &= \sum_{s_r} \sum_{s_i} \left| \Xi^{\text{mes}}(s) - L \sum_{m \in M} |\tilde{\xi}^m| e^{i\phi^m} \cdot \right. \\ &\quad \left. e^{[i(k_r^m + ik_i^m) - s_i - is_r]L/2} \frac{\sinh [i(k_r^m + ik_i^m) - s_i - is_r]L/2}{[i(k_r^m + ik_i^m) - s_i - is_r]L/2} \right|, \end{aligned} \quad (1.32)$$

where Ξ^{mes} is the spatial Laplace transform of the measured field $\xi(x)$, $|\tilde{\xi}^m|$ and ϕ^m are, respectively, the theoretical amplitude and phase of the m -th mode.

The method is then applied to a porous material to determine the frequency-wavenumber relation, as shown in Fig. 1.16.

The proposed approach seems to be robust, efficient and versatile; it is possible to recover the complex wavenumber in a very large frequency band and to take in account several modes, which may overlap. Some limitations are related to the choice of the appropriate cost function and to the treatment of noisy data [28].

1.2.5 High-Resolution Wavenumber Analysis (HRWA) method

The High-Resolution Wavenumber Analysis (HRWA) method [32, 33] identifies complex wavenumbers and amplitudes of waves composing the harmonic response of vibrating structures. The HRWA method is developed to overcome some limitations related to complex poles identification from measured signals and to extend the approach to

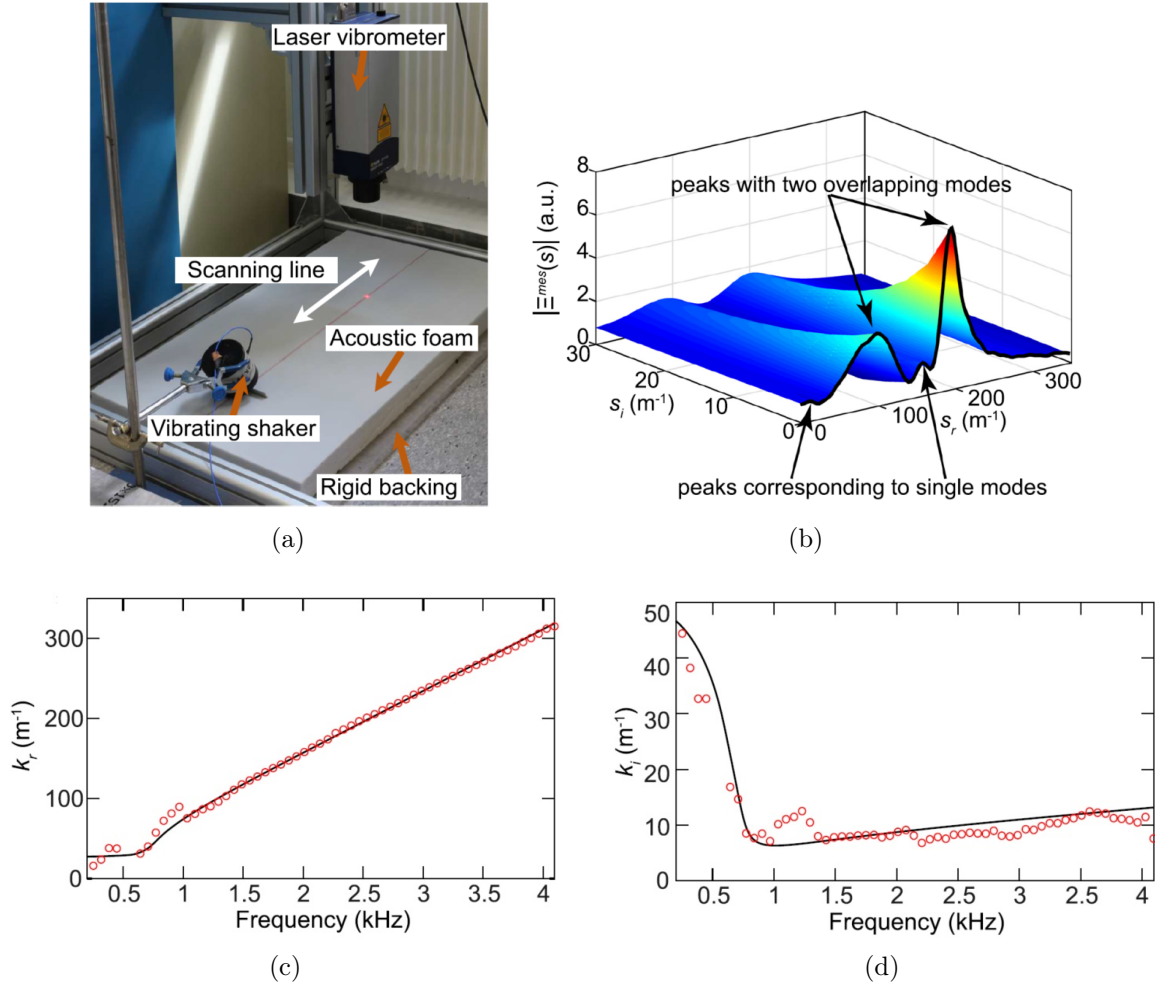


Figure 1.16 – Set-up of the experimental test (a), Laplace transform at 2453 Hz (b), real part (c) and imaginary part (d) of the estimated wavenumbers [28].

full-field measurements. Complex poles identification techniques were widely developed and applied in many engineering applications, starting from Prony’s approach [34]. Other methods directly related to Prony’s approach are Matrix Pencil [35], Pisarenko method [36], MUSIC (Multiple Signal Classification) algorithm [37] and ESPRIT algorithm based methods [16, 38–45].

The HRWA method has been firstly developed for unidimensional structures [32]. In these beam-like structures, the wavenumbers are dependent of the local structural behavior, considering the beams as waveguides. The HRWA method makes use of the subspace-based identification algorithm ESPRIT (Estimation of Signal Parameters via Rotational Invariance Techniques, [46]). The main advantages of the use of the ESPRIT algorithm are:

- high resolution, as it uses a recurrence property of the signal to identify the wave parameters;
- by using the subspace decomposition, the number of waves contained in the signal can be estimated automatically with the ESTER (ESTimation or ERror) criterion ([47]);

- the complex wavenumbers are the solution of an optimization-free problem thus the computational cost is lightened.

The analytical formulation here described is taken from [32], which makes use of Euler's and Timoshenko's beam models.

The harmonic response of the beam, far from sources and boundaries, is measured along the beam x axis, assuming a discrete model of a beam, with N points along the x axis and with a regular spacing Δ , as follows:

$$x_u = x_1 + (u - 1)\Delta \quad \text{with } u \in [1, N]. \quad (1.33)$$

In a linear formulation framework, the measurement of a component of $u(x, y, z)$ along the mesh x can be expressed as a sum of R damped exponentials, \mathbf{p} , and noise, \mathbf{n} :

$$s_u = u_i(x_u, y_0, z_0) + n_u = p_u + n_u = \sum_{r=1}^R a_r z_r^u + n_u, \quad (1.34)$$

where a_r are the amplitudes corresponding to the poles $z_r = e^{ik_r\Delta}$, with $k_r = k_r(1 - i\gamma_r)$.

The \mathbf{p} part of the signal can be expressed as $\mathbf{p} = \mathbf{V}_N(\mathbf{z}_R) \cdot \mathbf{a}_R$, where $\mathbf{a}_R = [a_1 \cdots a_R]^T$, $\mathbf{z}_R = [z_1 \cdots z_R]^T$ and $\mathbf{V}_N(\mathbf{z}_R)$ is the Vandermonde matrix. The main problem is to find the poles \mathbf{z}_R . Once the poles are known, the complex amplitudes \mathbf{a}_R can be estimated in the measured noisy signal \mathbf{s} in the least-square sense:

$$\mathbf{a}_R = (\mathbf{V}_N^*(\mathbf{z}_R) \cdot \mathbf{V}_N(\mathbf{z}_R))^{-1} (\mathbf{V}_N^*(\mathbf{z}_R) \cdot \mathbf{s}). \quad (1.35)$$

where $*$ denotes complex conjugate or hermitian transpose.

The ESPRIT algorithm is applied in order to obtain the subspace decomposition to improve the resistance to noise and it is here reported to the sake of clarity (the following formulation is taken from [32]). In addition, the ESTER criterion is used to estimate the signal order (number of poles contained in the signal). The first step of the algorithm consists in the decomposition of the signal between signal and noise subspaces. First, a Hankel matrix \mathbf{H} is formed with the measured signal \mathbf{s} of length N :

$$\begin{bmatrix} s_1 & s_2 & \cdots & s_{N-K} \\ s_2 & s_3 & \cdots & s_{N-K+1} \\ \vdots & & \ddots & \vdots \\ s_K & \cdots & & s_N \end{bmatrix}, \quad (1.36)$$

where the integer parameter K corresponds to the sum of the dimensions of signal and noise subspaces. The HRWA method makes use of the auto-covariance matrix \mathbf{R}_{ss} , expressed as follows:

$$\mathbf{R}_{ss} = \mathbf{H}\mathbf{H}^* = \mathbf{W}^*\mathbf{D}\mathbf{W}, \quad (1.37)$$

which eigenvectors \mathbf{W} span the same subspace as the Hankel matrix singular vectors, and has the advantage to be an asymptotically non-biased estimator of the signal autocovariance, in presence of white gaussian noise. The eigenvector matrix \mathbf{W} spans

the entire subspace of the noisy signal s . This total subspace can be decomposed into signal subspace \mathbf{W}_p and noise subspace \mathbf{W}_n , with \mathbf{W}_p built with the eigenvectors corresponding to the R dominant eigenvalues.

The ESPRIT algorithm strategy consists in estimating the signal poles z_R via the signal subspace matrix \mathbf{W}_p . As this last matrix and the Vandermonde matrix spans close subspaces, they are related by a transformation matrix \mathbf{T} : $\mathbf{V}_N(\mathbf{z}_R) = \mathbf{W}_p \mathbf{T}$. The rotational invariance property is then expressed as a function of the signal subspace matrix $\mathbf{W}_p^\downarrow = \mathbf{W}_p^\uparrow \mathbf{F}$, in which \downarrow and \uparrow respectively correspond to the $(N - 1)$ first and last samples of the signal and $\mathbf{F} = \mathbf{T} \mathbf{Z} \mathbf{T}^{-1}$ and:

$$\begin{aligned}\mathbf{W}_p^\uparrow &= \begin{bmatrix} \mathbf{I}_{(K-1)} & \mathbf{0}_{(K-1) \times 1} \end{bmatrix} \mathbf{W}_p, \\ \mathbf{W}_p^\downarrow &= \begin{bmatrix} \mathbf{0}_{(K-1) \times 1} & \mathbf{I}_{(K-1)} \end{bmatrix} \mathbf{W}_p.\end{aligned}\tag{1.38}$$

The matrix \mathbf{F} is estimated in the Least-Square sense: $\mathbf{F} = (\mathbf{W}_p^\uparrow)^{-1} \mathbf{W}_p^\downarrow$; then, the poles \mathbf{z}_R are extracted from the diagonalization of \mathbf{F} .

Usually, the number of dominant waves is unknown; the HRWA method uses the ESTER criterion, which can estimate the signal order R that minimizes the \mathbf{F} estimation residuals, in a given range $r \in [r_{\min}, r_{\max}]$:

$$R = \min_{r \in [r_{\min}, r_{\max}]} \|\mathbf{W}_p^\uparrow(r) \mathbf{F}(r) - \mathbf{W}_p^\downarrow(r)\|_2.\tag{1.39}$$

The HRWA procedure consists in applying the following steps to each obtained harmonic response $\mathbf{s}(\omega_i) = \mathbf{S}(\mathbf{x}, \omega_i)$, where $\mathbf{S}(\mathbf{x}, \omega)$ is the time domain Fourier transform of the measured displacement, velocity or acceleration:

1. based on the array $\mathbf{s}(\omega_i)$, the Hankel matrix is built (see Eq. (1.36));
2. the covariance matrix \mathbf{R}_{ss} is computed and diagonalized yielding the matrix of eigenvectors \mathbf{W} (see Eq. (1.37));
3. the ESTER method is applied to estimate the number of detectable waves in the noisy signal. Then, for each $r \in [r_{\min}, r_{\max}]$:
 - the r eigenvectors corresponding to the r dominant eigenvalues are extracted to form the approximated signal subspace matrix \mathbf{W}_p ;
 - the truncated signal subspace matrices \mathbf{W}_p^\uparrow and \mathbf{W}_p^\downarrow are built (see Eq. (1.38));
 - the least-squares estimation of \mathbf{F} is computed;
 - the ESTER criterion as function of r is evaluated (see Eq. (1.39));
4. the eigenvalues of matrix \mathbf{F} are computed, yielding the wavenumbers k_r of all the waves which can be detected with the HRWA at the angular frequency ω_i :

$$k_r(\omega_i) = \frac{\ln(i z_r(\omega_i))}{\Delta};$$

5. if a signal reconstruction is needed, the Vandermonde matrix $\mathbf{V}_N(\mathbf{z}_R)$ is computed, and the complex amplitudes \mathbf{a}_R are estimated (see Eq. (1.35)).

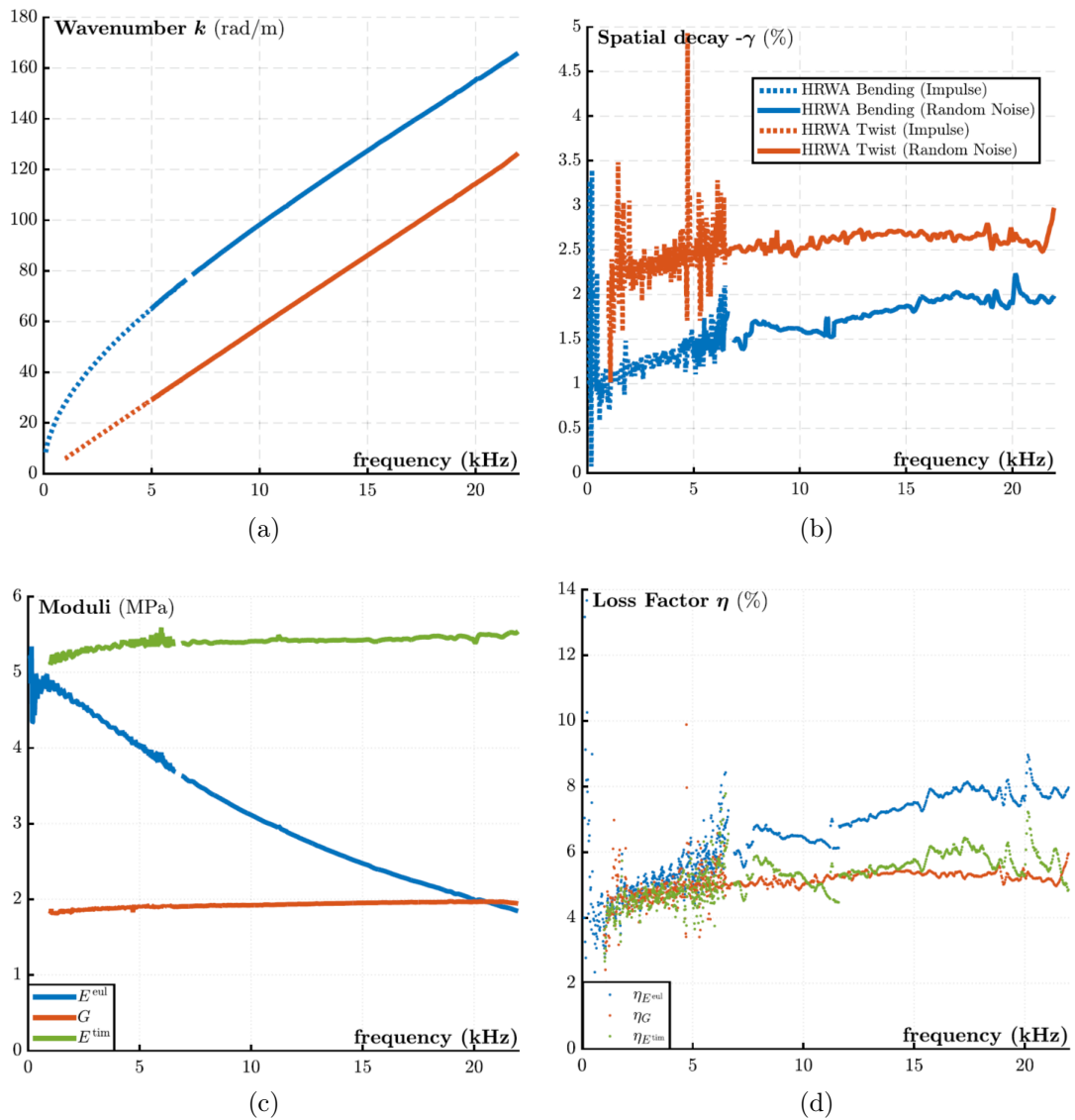


Figure 1.17 – HRWA method on a PVC beam: torsional and bending wavenumbers (a), spatial decay γ (b), apparent complex moduli (c) and damping loss factor (d) [32].

The HRWA method is applied on a polyvinyl chloride (PVC) beam in [32], exciting the beam with impulse and random noise excitations in the range $[0 \text{ Hz} - 22 \text{ kHz}]$. The real part of the dispersion curves is shown in Fig. 1.17a, where both torsional and flexural wavenumbers are estimated. The decay for both torsional and flexural waves is captured and shown in Fig. 1.17b. From the estimated complex wavenumbers, the equivalent material properties (see Fig. 1.17c) and the damping loss factor (see Fig. 1.17d) have been estimated.

A 2D version of the HRWA method is developed and presented in [33]. The fundamental equations are basically the same of the 1D approach, except for the 2D formulation of the ESTER criterion [48–50]. The experimental results on two different sandwich plates with carbon fiber reinforced polymer (CFRP) skins and different core materials (PVC foam and honeycomb) are shown in Fig. 1.19 and Fig. 1.20, respectively; both plates have dimensions $60 \text{ cm} \times 60 \text{ cm}$. The excitation is provided by a mechan-

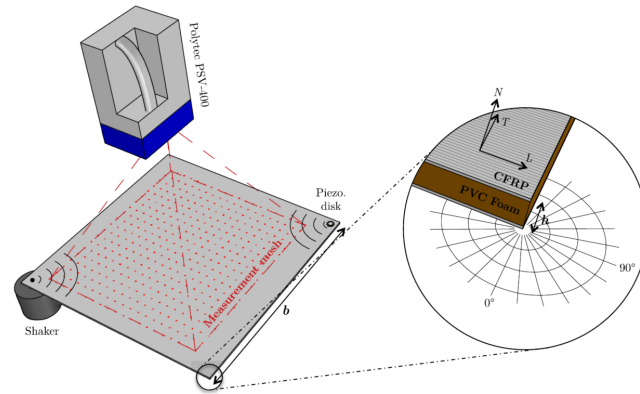


Figure 1.18 – Set-up of the experimental tests, with excitation and acquisition systems, for the 2D application of the HRWA method [33].

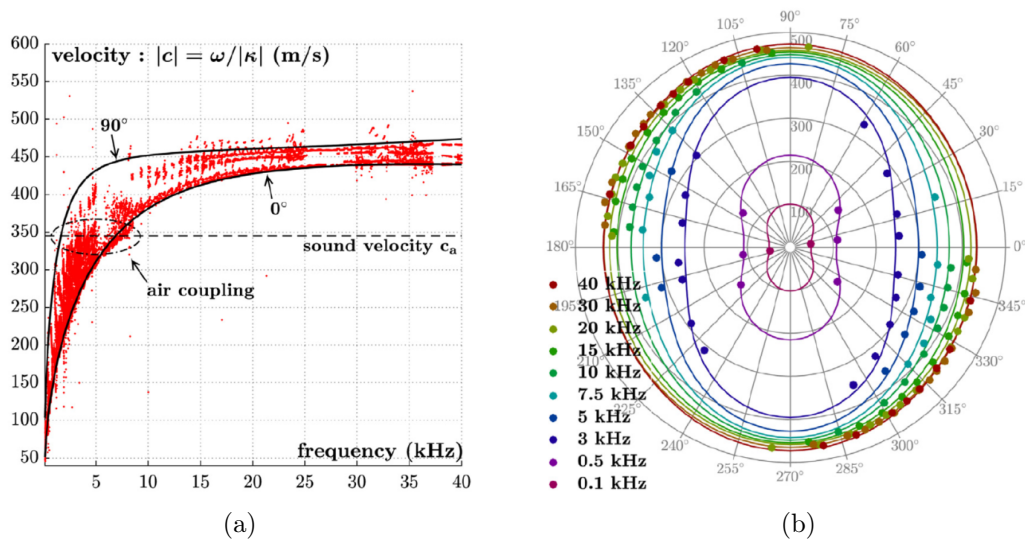


Figure 1.19 – 2D application of the HRWA method on a sandwich plate with CFRP skins and PVC core: phase velocity-frequency relation (a) and phase velocity angle dependency (b) [33].

ical shaker in the frequency range [100 Hz - 40 kHz]; the vibrational field is acquired by a scanning laser vibrometer (see Fig. 1.18). The results are compared with the results obtained with the Spectral Finite Elements Method (SFEM) scheme [51–53]. The frequency-dependent phase velocities for the orthotropic sandwich plate with PVC core are shown in Fig. 1.19; the solid lines are estimated by using the SFEM scheme [52], while the dot markers are the HRWA method estimations. The angle-dependent dispersion curves for the sandwich plate with honeycomb core are shown in Fig. 1.20. A singularity is observed around 34 kHz; at this frequency, the half-wavelength $\pi/|k|$ approaches the cell-size of the honeycomb core, resulting in a resonance effect.

1.2.6 Image source method

All the methods based on plane waves propagation are valid only if some assumptions are verified. In these methods the measure of the steady state response is needed and

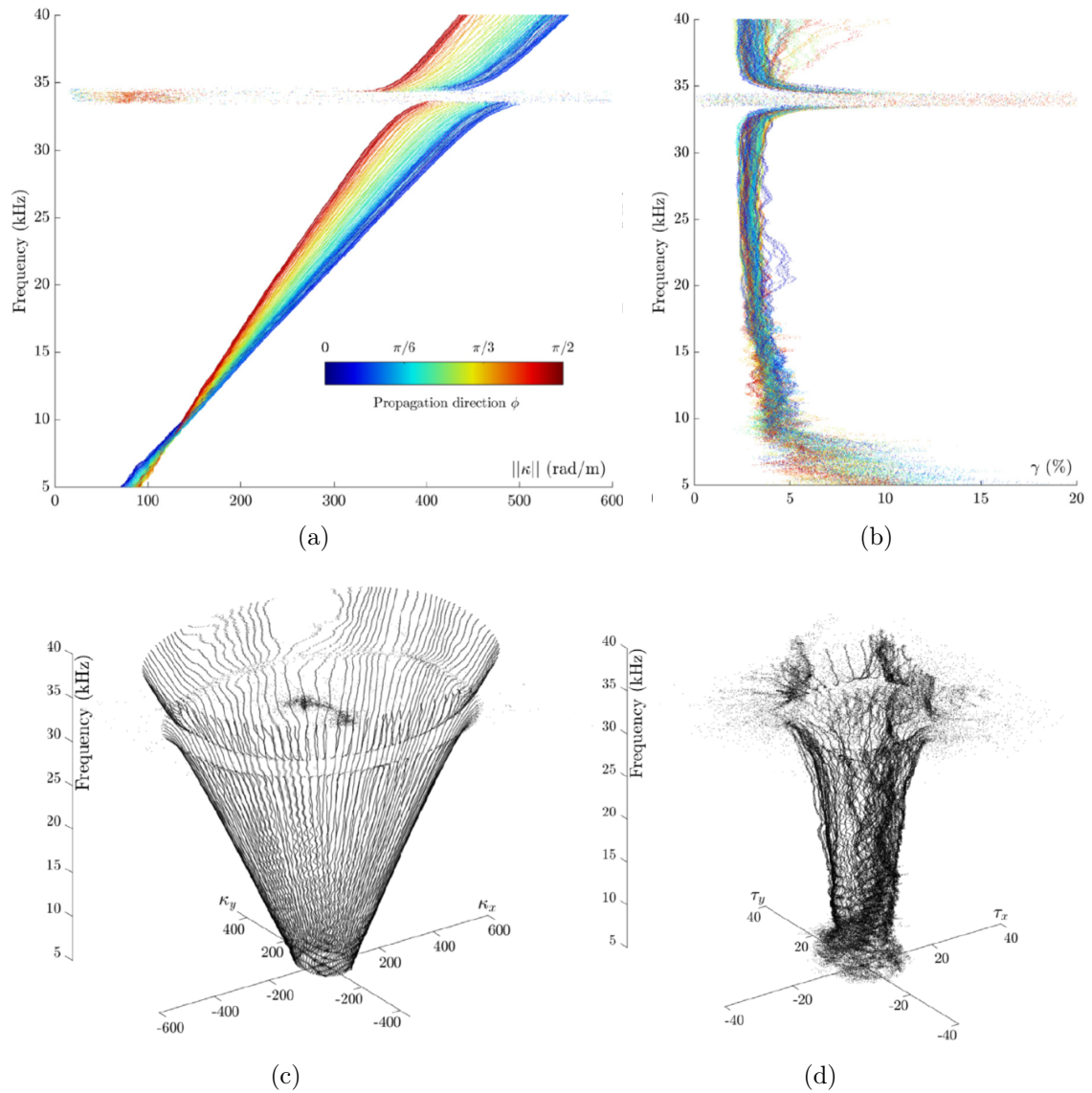


Figure 1.20 – 2D application of the HRWA method on a sandwich plate with CFRP skins and honeycomb core: frequency and angle dependency of the real (a) and imaginary (b) parts of the estimated wavenumbers; real (c) and imaginary (d) discrete dispersion surfaces [33].

the acquisition region should be far from the excitation points, due to the singularities introduced in the formulation. In fact, the basic problem with plane waves of the type $e^{\pm ik_x x \pm ik_y y}$ is that the vibrational field of a structure deviates from a plane wave field near the excitation points. The image source method, based on the Green's function of a point excited plate, is not affected by these problems. The image source method replaces the boundaries of the considered domain by mirror sources of the original source. The weights and the locations of image sources are calculated in order to satisfy the boundary conditions [54].

The image source method can be used for both electrostatics and acoustics problems [55]. Starting from the time-dependent solution of the wave equation $\nabla^2 \Psi = (1/c^2)(\partial^2 \Psi / \partial t^2)$, the solution of the Helmholtz equation by specifying a simple-harmonic dependence on time of the solution of the wave equation is given by $\psi e^{-i\omega t} = \psi e^{-ikct}$ [55]. Substituting the Helmholtz solution ψ with the Green's one G , the complete solution is given by Ge^{-ikct} . The expression of the waves going outward from the source point is given by:

$$G_k(r|r_0) = g_k(R) = e^{ikR}/R, \quad \text{with boundary at infinity.} \quad (1.40)$$

In case of incoming wave the term e^{-ikR}/R should be considered in Eq. (1.40). A combination of outgoing and incoming waves has to be assumed when the boundaries are at a finite distance r_0 from the source; in this case, the energy might not be completely dissipated at the surface and might be reflected back to the source.

As said before, an analogy between electrostatics and acoustics can be made; without any boundaries, $g_k(R)$ is the classical Green's function. In electrostatics, when a surface is introduced a potential is developed, due to the induced charge on the boundary surface, which in turn is caused by the applied electric field $g_k(R)$. In acoustics, the presence of boundaries causes the reflections which contribute to the total pressure [55]; Eq. (1.40) modifies in:

$$G_k(r|r_0) = g_k(R) + F_k(r|r_0), \quad (1.41)$$

where $F_k(r|r_0)$ represents the boundary effects.

In [55] a detailed discussion about Eq. (1.41) and the term $F_k(r|r_0)$ is provided and here reported for clearness purpose.

The image source method can be employed to determine $F_k(r|r_0)$ since it describes the reflected waves contribution. A schematic representation of the image source method is shown in Fig. 1.21, applied to an electrostatics problem. An infinitely conducting metal plane is considered with a unit line charge placed in (x_0, y_0) . On the surface at $x = 0$ the potential must be zero, imposing to the Green's function to satisfy the Dirichlet boundary conditions. In this method, a line charge of opposite sign is considered at the image point $(-x_0, y_0)$. The total potential for $x > 0$ is:

$$G_0(r|r_0) = -2 \ln(R/R_0), \quad x \geq 0. \quad (1.42)$$

The boundary conditions are satisfied at the equipotential plane, where $R = R_0$ and $G_0 = 0$; as consequence, since $g_k(R) = -2 \ln R$, we obtain $F_0 = 2 \ln R_0$. By the generalization of Eq. (1.42), the expression of G_k can be found:

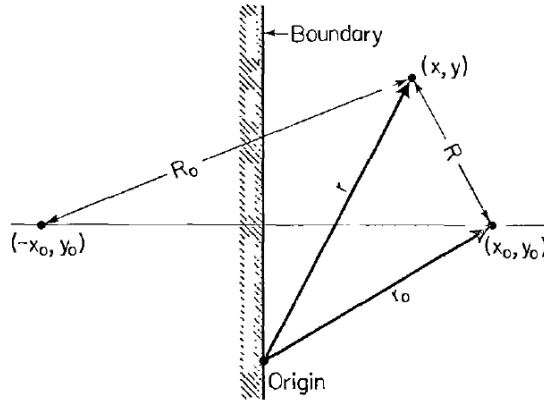


Figure 1.21 – Image of a source point (x_0, y_0) in the plane $x = 0$ [55].

$$G_k(r|r_0) = i\pi[H_0^{(1)}(kR) - H_0^{(1)}(kR_0)], \quad (1.43)$$

where $H_0^{(1)}$ is the cylindrical Hankel's function of the first kind of order 0.

One of the first application of the image source method on polygonal plates is shown in Gunda et al. [56], in which the feasibility of calculating the frequency-dependent response of thin plates and beams has been demonstrated. The image source method has been successfully applied to describe the structural vibrations of a plane structure. Cuenca et al. [54] derived the formulation of the image source method in case of simply supported convex polygonal plates (see Fig. 1.22). The plate has an interior domain Ω , boundaries $\partial\Omega$ and it is excited by a point source at location r_0 . To obtain an expression of the flexural vibrations of the plate, the Kirchhoff's theory is adopted [57]. The solution of the system of equations listed in Eq. (1.44) represents the Green's function G_Ω associated to the flexural vibrations of the considered structure.

$$\begin{cases} D(\nabla^4 - k_f^4)G_\Omega(\mathbf{r}, \mathbf{r}_0) = \delta(\mathbf{r} - \mathbf{r}_0) & \text{in } \Omega \\ G_\Omega(\mathbf{r}, \mathbf{r}_0) = 0 & \text{on } \partial\Omega, \\ \frac{\partial^2 G_\Omega}{\partial n^2}(\mathbf{r}, \mathbf{r}_0) + \nu \frac{\partial^2 G_\Omega}{\partial t^2}(\mathbf{r}, \mathbf{r}_0) = 0 & \text{on } \partial\Omega \end{cases} \quad (1.44)$$

where $D(\nabla^4 - k_f^4)$ is the differential operator governing flexural wave propagation, δ is the Dirac delta function, ν is the Poisson's coefficient and n and t are the normal and tangent to the boundary, respectively [54, 58]. The term D is the flexural rigidity of the plate and is given by $D = Eh^3/[12(1 - \nu^2)]$, being E the Young's modulus and h the thickness of the plate. The flexural wavenumber is defined as $k_f^4 = \omega^2 \rho h / D$, where ρ is the mass density.

To obtain the solution of the finite plate, the image source method considers an infinite plate containing the original source and a sum of image sources whose locations and weighted amplitudes in order to satisfy the boundary conditions [59]. Denoting with $\mathcal{D}_\Omega(\mathbf{r}, \mathbf{r}_0)$ the sum of Dirac delta functions, the vibrational field is obtained as the superposition of elementary contributions from all the sources; as consequence, Eq. (1.44) can be express as follows:

$$D(\nabla^4 - k_f^4)G_\Omega(\mathbf{r}, \mathbf{r}_0) = \mathcal{D}_\Omega(\mathbf{r}, \mathbf{r}_0). \quad (1.45)$$

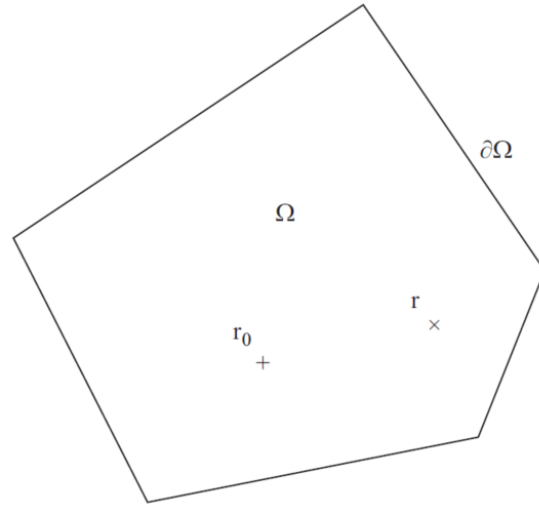


Figure 1.22 – Polygonal plate with inside domain Ω and boundaries $\partial\Omega$, with source (+) and receiver (x) locations [54].

For a point source located at $\mathbf{0}$, G_∞ (the Green's function of the infinite plate [56]) is the solution of the following equation:

$$D(\nabla^4 - k_f^4)G_\infty(\mathbf{r}, \mathbf{0}) = \delta(\mathbf{r}), \quad (1.46)$$

where G_∞ is defined as:

$$G_\infty(\mathbf{r}, \mathbf{0}) = \frac{i}{8k_f^2 D} [H_0^{(1)}(k_f |\mathbf{r}|) - H_0^{(1)}(ik_f |\mathbf{r}|)], \quad (1.47)$$

Finally, the Green's function of the finite plate is defined by the convolution product of the infinite Green's function (in Eq. (1.47)) and the contribution of all the sources:

$$G_\Omega(\mathbf{r}, \mathbf{r}_0) = \mathcal{D}_\Omega(\mathbf{r}, \mathbf{r}_0) * G_\infty(\mathbf{r}, \mathbf{0}). \quad (1.48)$$

An experimental validation of the proposed approach is presented by Cuenca et al. [60]; the image source method is here applied on a flat panel covered with viscoelastic layer in order to obtain the equivalent Young's modulus and the structural damping loss factor. The schematic representation of the panel and of the excitation is shown in Fig. 1.23. Based on [61], the displacement field at the input point of an infinite plate is given by the asymptotic limit of the Green's function, as follows:

$$\lim_{\mathbf{r} \rightarrow \mathbf{r}_0} G_\infty(\mathbf{r}, \mathbf{r}_0; k_f) = \frac{i}{8k_f^2 D}. \quad (1.49)$$

The bending stiffness can be then estimated by an inverse approach based on the driving point mobility:

$$|Y|(\mathbf{r}, \mathbf{r}_0; k_f) = |i\omega \lim_{\mathbf{r} \rightarrow \mathbf{r}_0} G_\infty(\mathbf{r}, \mathbf{r}_0; k_f)| = \frac{1}{8\sqrt{\rho h}(D^{1/2})}. \quad (1.50)$$

The Young's modulus can be estimated from the bending stiffness modulus of Eq. (1.50), as a function of the damping loss factor:

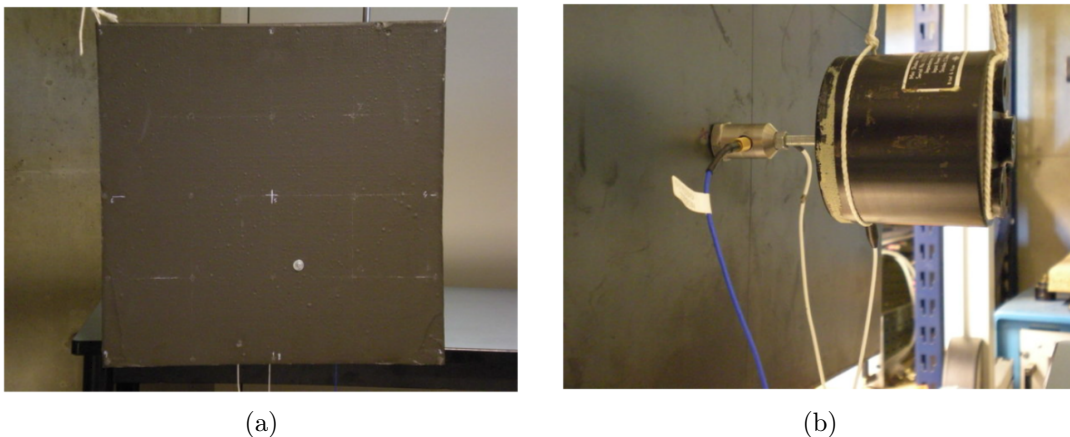


Figure 1.23 – Experimental set-up of the plate with viscoelastic layer (a) and shaker excitation (b) [60].

$$E = \frac{|D|12(1 - \nu^2)}{h^3\sqrt{1 + \nu^2}}. \quad (1.51)$$

The couple (E, η) is iteratively estimated by using the standard deviation of the driving point mobility as a criterion for comparison between simulated and measured mobilities. The estimations of the bending stiffness D , the Young's modulus E and the damping loss factor are shown in Fig. (1.24).

A 1D formulation of the image source method is developed in [62] and applied to beam-like structures in presence of uncertainties. Assuming a homogeneous rectangular cross-section for a beam structure, the longitudinal and flexural displacements are given, respectively, by the following expressions [58]:

$$EA \left(\frac{\partial^2}{\partial x^2} + k_{l0}^2 \right) G_l(x, x_0; k_{l0}) = \delta(x - x_0), \quad (1.52a)$$

$$EI \left(\frac{\partial^4}{\partial x^4} + k_{f0}^4 \right) G_f(x, x_0; k_{f0}) = \delta(x - x_0), \quad (1.52b)$$

where E is the Young's modulus, $A = hb$ is the cross-section area, with h and b the thickness and width, respectively, $I = bh^3/12$ is the second moment of area, G_l and G_f are respectively the Green's functions of longitudinal (along the x axis) and flexural motion (along the z axis) with corresponding wavenumbers $k_{l0} = \omega\sqrt{\rho/E}$ and $k_{f0} = (\omega^2\rho A/EI)^{1/4}$, x_0 is location of the source and ρ is the mass density. The Green's function of the longitudinal motion in Eq. (1.52a) is given by:

$$G_l(x, x_0; k_{l0}) = \frac{e^{ik_{l0}|x-x_0|}}{2ik_{l0}EA}, \quad (1.53)$$

while the Green's function of the flexural motion in Eq. (1.52b) is equal to:

$$G_f(x, x_0; k_{f0}) = \frac{e^{ik_{f0}|x-x_0|}}{-4ik_{f0}^3EI} + \frac{e^{-k_{f0}|x-x_0|}}{-4k_{f0}^3EI}. \quad (1.54)$$

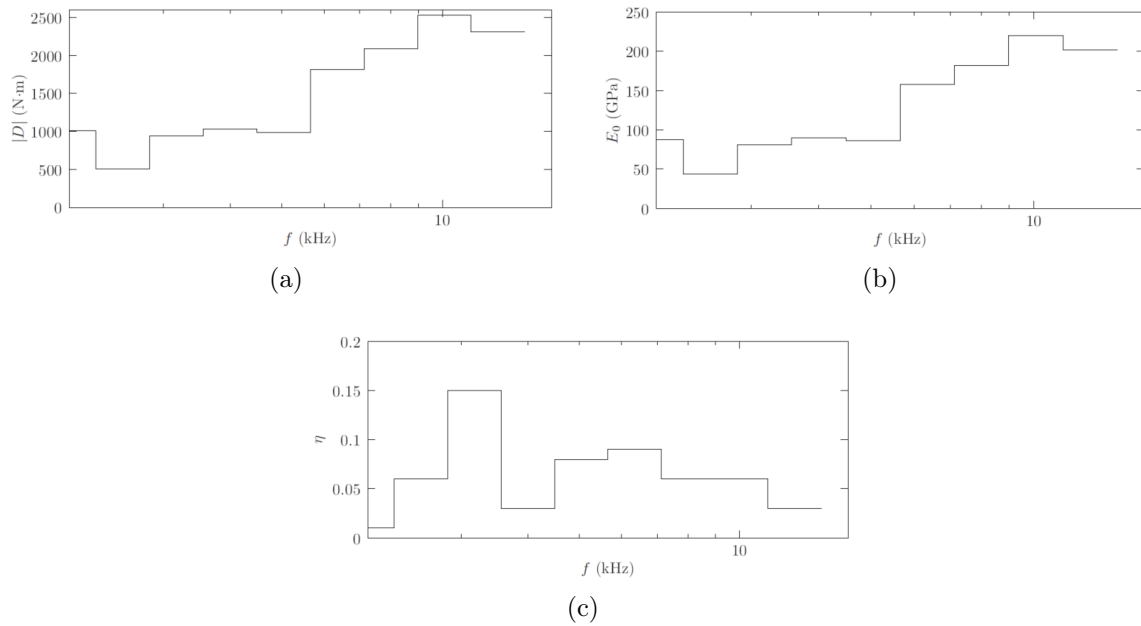


Figure 1.24 – Experimental estimation of the bending stiffness D (a), the Young's modulus E (b) and the damping loss factor (c) [60].

The first terms in both Eq. (1.53) and Eq. (1.54) are representative of the propagative waves, while the second term in Eq. (1.54) represents the evanescent wave.

Recently, Roozen et al. [5] developed an approach based on a combination of image source method and a set of Hankel's functions to retrieve the vibrational field of a point excited plate. The equation of motion of the isotropic plate is given by the Kirchhoff's thin plate theory [57], similarly to Eq. (1.45):

$$D(\nabla^4 - k_f^4)w(x, y) = \delta(x - x_0, y - y_0), \quad (1.55)$$

where $w(x, y)$ is the out-of-plane displacement of the plate and (x_0, y_0) is the location of the point force. The solution of Eq. (1.55) can be obtained in a similar manner of Eq. (1.43):

$$G_\infty(x - x_0, y - y_0) = \frac{1}{8k_f^2 D} \left(H_0^{(1)}(k_f r) - H_0^{(1)}(ik_f r) \right), \quad (1.56)$$

where:

- $k_f = \left(\omega^2 \frac{\rho h}{D} \right)^{1/4}$, flexural wavenumber;
- $D = \frac{Eh^3}{12(1-\nu^2)}$, bending stiffness;
- $H_0^{(1)}$, Hankel's function of order zero and first kind;
- $r = \|x - x_0, y - y_0\|$, source-to-receiver distance.

The response of the finite plate can be calculated by a linear combination of image sources contributions. Considering the transverse displacements in the form $w(x_j, y_j, \omega)$

and a discrete number M of acquisition points (x_j, y_j) , with $j = 1, \dots, M$, the vibrational field can be built as follows:

$$\tilde{w}(x_j, y_j, \omega) = \sum_{n=1}^N \alpha_n(\omega) \phi_n(x_j, y_j), \quad (1.57)$$

where:

- $\alpha_n(\omega)$, is the strength of each image source;
- $\phi_n(x_j, y_j) = G_\infty(x_j - x_0(n), y_j - y_0(n))$, Green's function of the infinite plate at the location $(x_0(n), y_0(n))$ of the n -th image source.

Considering a matrix notation and all the M measured points, Eq. (1.57) can be written as:

$$\tilde{\mathbf{w}} = \Phi \alpha, \quad (1.58)$$

where $\tilde{\mathbf{w}}$ is a vector containing the projected displacements $w(x_j, y_j, \omega)$, Φ is a matrix containing the vectors of the image source Green's functions and α is a vector containing the contribution strengths [5]. The vector of contribution strengths α needs to be determined by means of a generalized inverse approach; different methods are proposed in [5, 63–65].

The projected vibrational field and the normalized reconstruction error between the matrix Φ and measurements w are expressed, respectively, by:

$$\tilde{w} = \Phi \Phi^{+\lambda} w \quad \text{and} \quad e = \frac{\|w - \tilde{w}\|^2}{\|w\|^2}. \quad (1.59)$$

The error e also depends upon the complex valued flexural wavenumber k_f used to build the test wave fitting function Φ . The optimal value for k_f , from a set of candidate values for k_f sampled in complex plane, is obtained by the minimization of the reconstructed error e . Assuming that a single flexural wave is propagating, a single wavenumber k_f is found for each angular frequency ω .

The method is then applied to a thin isotropic plate in order to estimate the material properties and the damping loss factor information. The experimental set-up is shown in Fig. 1.25. The real part of the dispersion curve is shown in Fig. 1.26a; the damping loss factor is also estimated and reported in Fig. 1.26b. Using an inverse approach based on the estimated flexural wavenumbers, the equivalent stiffness D and Young's E moduli are determined and shown in Fig. 1.26.

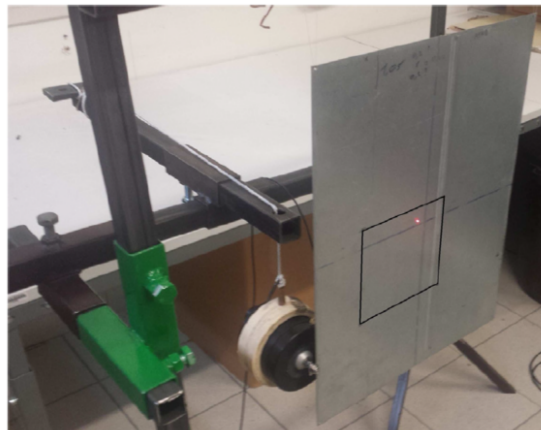


Figure 1.25 – Isotropic plate and measurement area [5].

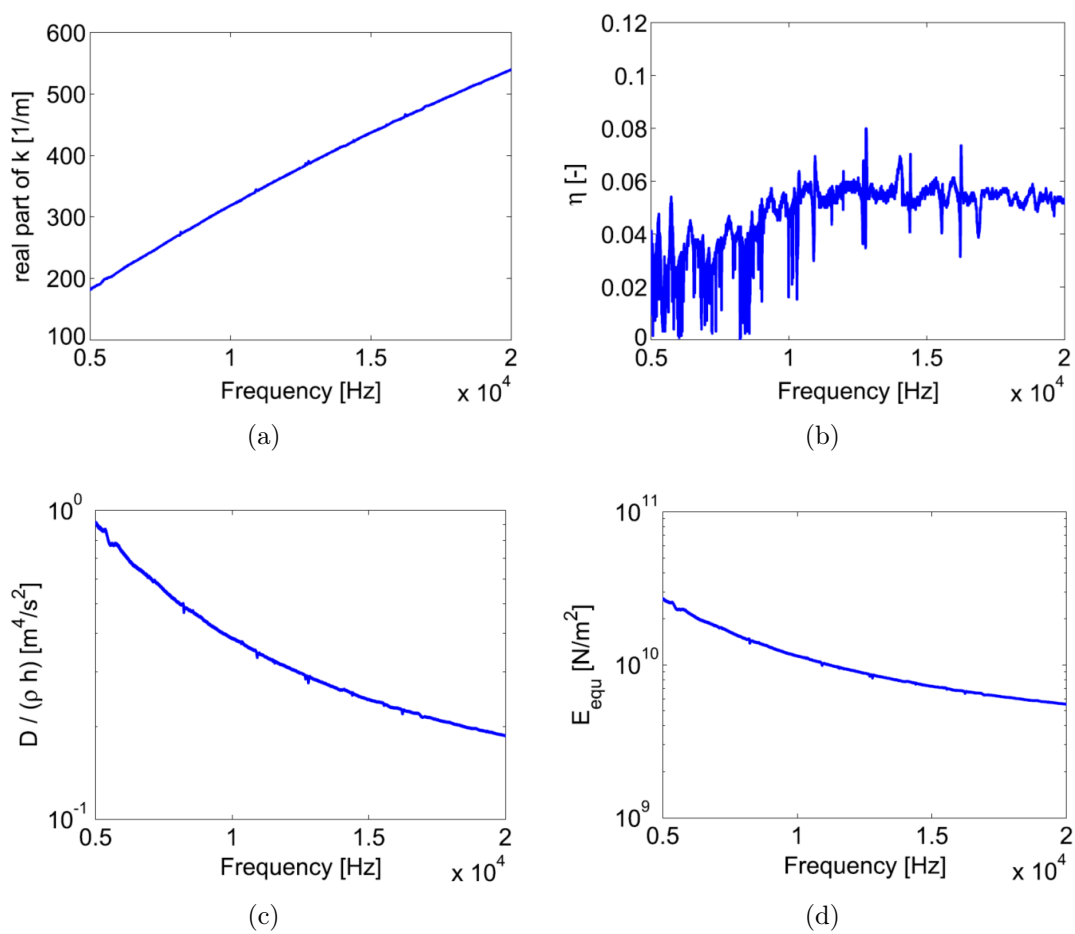


Figure 1.26 – Real part of the dispersion curve (a), damping loss factor estimation (b), equivalent stiffness modulus (c) and equivalent Young's modulus (d) [5].

1.3 Force Analysis Technique (FAT)

The Force Analysis Technique (FAT), also known with the French acronym RIFF (*Régularisation Inverse Filtrée et Fenêtrée*), is an inverse method for the localization of the external excitation from displacement field information. This method was introduced by Pézerat et al. [66] in one-dimensional formulation and applied for the first time to a beam-like structure and then extended to 2D structures [67]. Further development of the FAT are presented by Pézerat's research group and extended to more complex cases [68–74].

The method allows to identify stationary force distribution from the knowledge of the measured flexural displacement fields, using a finite difference scheme to discretize the local equation of motion. When dealing with experimental data, the acquired data may be affected by noise; to avoid this problem and to mitigate the uncertainties related to the data, two different approaches are used: Singular Value Decomposition (SVD), which consists in the elimination of the singular values of the operator applied to the displacements, and a high wavenumber filter [67].

The force distribution can be calculated at each point where the displacement and its fourth derivatives are known. Considering a simple isotropic plate, the equation of motion, under point harmonic excitation, is given by the following relationship:

$$\frac{Eh^3}{12(1-\nu^2)} \left(\frac{\partial^4 w}{\partial x^4} + \frac{\partial^4 w}{\partial y^4} + \frac{2\partial^4 w}{\partial^2 x \partial^2 y} \right) - \rho h \omega^2 w = F(x, y, \omega), \quad (1.60)$$

where E is the Young's modulus, h is the plate thickness, ν is the Poisson's coefficient, ρ is the mass density, ω is the frequency, w is the normal displacement, (x, y) are the spatial coordinates and F is the distribution of external forces.

In practical applications, the displacements can be measured, but the derivatives have to be obtained in a different manner. One of the most employed technique to estimate the derivatives is the use of the finite difference scheme. Following a classical centered scheme, the first derivatives can be approximated as follows:

$$\frac{\partial w}{\partial x} \Rightarrow \delta_{i,j}^{1x} = \frac{1}{\Delta x} (w_{i+1/2,j} - w_{i-1/2,j}), \quad (1.61a)$$

$$\frac{\partial w}{\partial y} \Rightarrow \delta_{i,j}^{1y} = \frac{1}{\Delta y} (w_{i,j+1/2} - w_{i,j-1/2}), \quad (1.61b)$$

where Δx and Δy are the distance between two consecutive points in the directions x and y , i and j are the indexes of the meshgrid point and $w_{i,j}$ is the transverse displacement at the point (i, j) . From equations (1.61a) and (1.61b), the fourth derivatives can be obtained:

$$\frac{\partial^4 w}{\partial x^4} \Rightarrow \delta_{i,j}^{4x} = \frac{1}{\Delta x^4} (w_{i+2,j} - 4w_{i+1,j} + 6w_{i,j} - 4w_{i-1,j} + w_{i-2,j}), \quad (1.62)$$

$$\frac{\partial^4 w}{\partial y^4} \Rightarrow \delta_{i,j}^{4y} = \frac{1}{\Delta y^4} (w_{i,j+2} - 4w_{i,j+1} + 6w_{i,j} - 4w_{i,j-1} + w_{i,j-2}), \quad (1.63)$$

$$\frac{\partial^4 w}{\partial x^2 \partial y^2} \Rightarrow \delta_{i,j}^{2x2y} = \frac{1}{\Delta x^2 \Delta y^2} (w_{i+1,j+1} - 2w_{i+1,j} + w_{i+1,j-1} - 2w_{i,j+1} + 4w_{i,j} - 2w_{i,j-1} + w_{i-1,j+1} - 2w_{i-1,j} + w_{i-1,j-1}). \quad (1.64)$$

Substituting equations (1.62), (1.63) and (1.64) in the equation of motion (see Eq. (1.60)), the force distribution can be calculated as:

$$F_{i,j} = \frac{Eh^3}{12(1-\nu^2)} \left(\delta_{i,j}^{4x} + \delta_{i,j}^{4y} + \delta_{i,j}^{2x2y} \right) - \rho h \omega^2 w_{i,j}. \quad (1.65)$$

From Eq. (1.65) can be noted that the calculation of the force at one point requires the measurements of the displacements in 13 different points (around the considered one, see Fig. 1.28).

An example of force distribution identification is shown in Fig. 1.27. Firstly, the force distribution is reconstructed using the finite difference scheme, starting from the exact values of the displacement (see Fig. 1.27a, in which the iso-lines also are plotted). A random noise distribution is then applied to the displacement field; in this case, the estimated force distribution is irregular and shown in Fig. 1.27b. Three different filtering approaches are used to mitigate the uncertainties and to de-noise the displacement field. The first technique is the SVD; the identified force distribution is shown in Fig. 1.27c. The second filtering technique that can be used to de-noise the displacement field is the low-pass wavenumbers filter; the reconstructed force distribution is shown in Fig. 1.27d. To avoid the singularities introduced by the boundaries (as shown in Fig. 1.27d), a spatial multiplicative window can be introduced (see Fig. 1.27e). After the application of the three filtering technique, the identified force distribution is shown in Fig. 1.27f; the obtained results are very close to the exact case.

The Force Analysis Technique is used in [72] to identify the flexural dispersion curve of a plate in fluid-structure coupling condition. The FAT is applied to a plate without singularities, as shown in Fig. 1.29a. The equation of motion of one-side fluid-loaded plate, in case of fluid-structure coupling, can be written as:

$$\nabla^4 w(x, y, \omega) - k_f^4 w(x, y, \omega) = \frac{p(x, y, \omega)}{D} + \frac{p_{\text{coupling}}(x, y, \omega)}{D}, \quad (1.66)$$

in which k_f is the flexural wavenumber of the plate, p is the fluid pressure and D is the bending stiffness modulus. Introducing the effective flexural wavenumber γ , which takes in account the fluid-structure coupling:

$$\gamma^4 = k_f^4 + \frac{p_{\text{coupling}}(x, y, \omega)}{D}, \quad (1.67)$$

the motion equation expressed by Eq. (1.66) can be rewritten as:

$$\nabla^4 w(x, y, \omega) - \gamma^4 w(x, y, \omega) = \frac{p(x, y, \omega)}{D}. \quad (1.68)$$

The dispersion curve is shown in Fig. 1.29b and compared to the one of the plate without fluid-structure coupling and to the analytical solution.

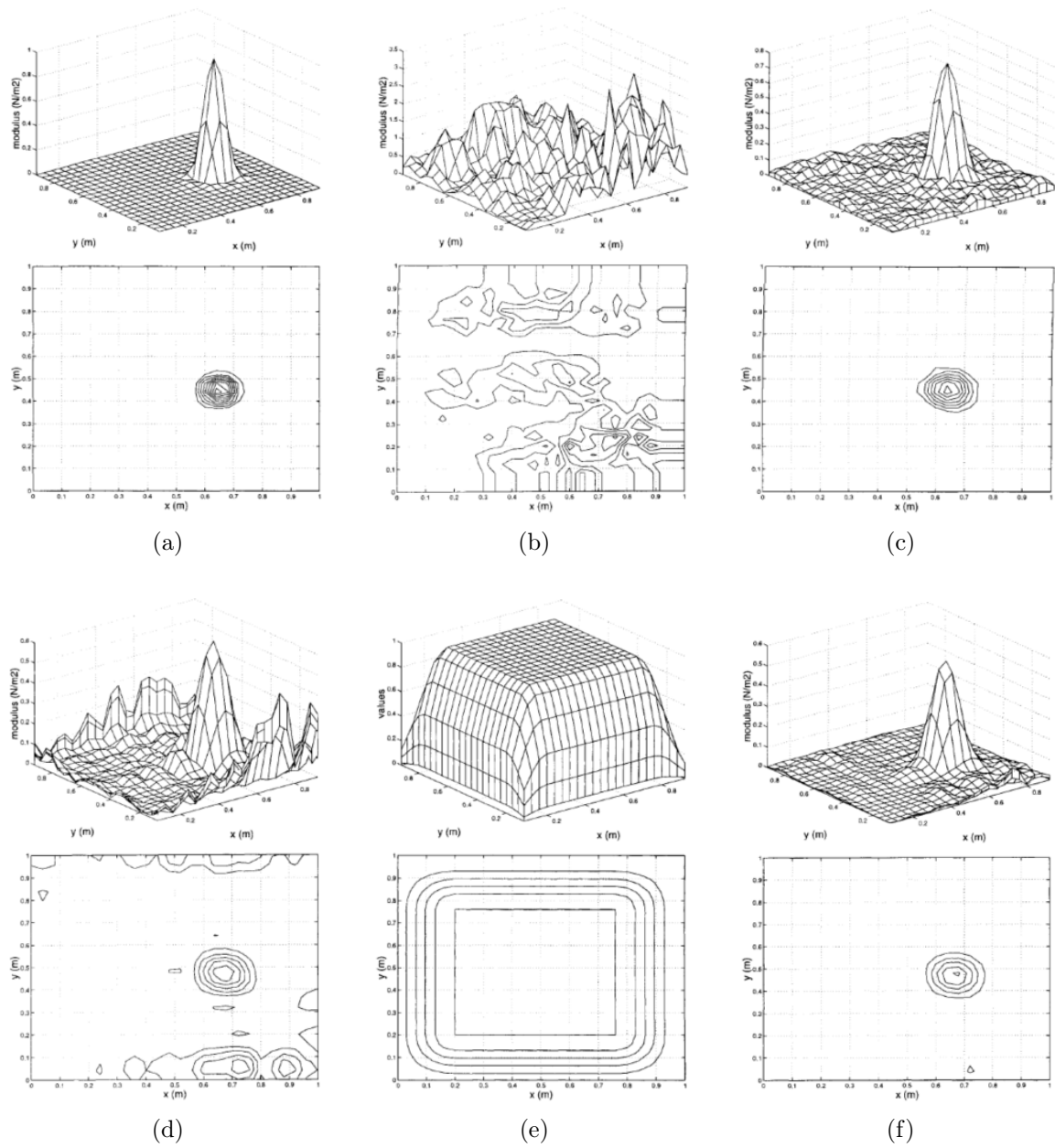


Figure 1.27 – FAT on isotropic plate: exact motion (a), noisy displacement (b), SVD filtering (c), low-pass wavenumber filtering (d), spatial windowing (e) and filtered force distribution (f) [67].

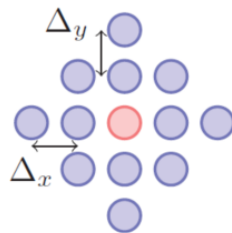


Figure 1.28 – Points needed to estimate the fourth derivatives with the finite difference scheme [72].

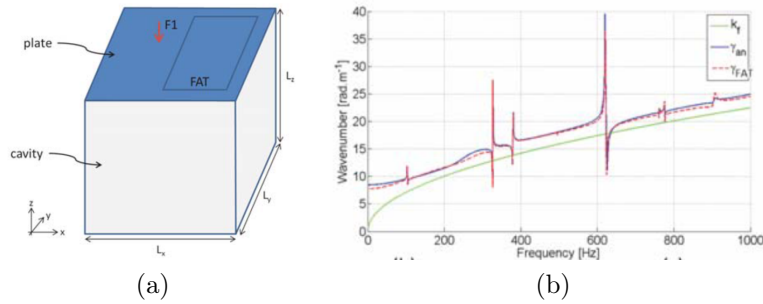


Figure 1.29 – Fluid-loaded plate (a) and dispersion curves (b) [72].

1.4 Wave Finite Element Method (WFEM)

The Wave Finite Element Method (WFEM) is a technique developed to investigate wave motion and wave propagation in periodic structures, assumed as assembled by elementary cells, which are modeled using conventional FE techniques. The method starts from a short section of a waveguide or a small part of a 2D structure; the governing equation for time-harmonic motion is expressed in terms of discrete nodal degrees of freedom (DOF) and forces of the FE model, assuming the following expression (similarly to what described in [75, 76]):

$$(\mathbf{K} + i\omega\mathbf{C} - \omega^2\mathbf{M})\mathbf{q} = \mathbf{f}, \quad (1.69)$$

where \mathbf{K} , \mathbf{C} and \mathbf{M} are the stiffness, damping and mass matrices, respectively, \mathbf{q} and \mathbf{f} are the nodal DOFs and forces vectors, respectively. In the WFEM for waveguides [77, 78], the FE dynamic matrix of Eq. (1.69) assumes the role of transfer matrix, leading to an eigenvalue problem after applying periodicity conditions [79].

The basis of the WFE method can be found in [80], in which the dispersion curves of periodic structures are estimated using a combination of FE approach and receptance method. An extended application of the proposed approach to 1D, 2D and 3D periodic structures is presented in [81]. An application of the method to railway tracks is presented in [82–85], in which both free wave propagation and dynamic behavior have been analyzed. An application of the wave FE method to structures that are geometrically periodic along one main dimension is proposed in Silva et al. [86].

In the last years, several contributions to the WFEM were given by Ichchou’s and Mencik’s research groups [87–93]; in their works, waveguides propagation, multi-modal behavior and fluid-structure interaction problems for straight and curved structures have been analyzed.

Another research group which gave an important contribution to the development of the WFE method is the one of Mace [77, 78, 94–107]. Their approach started from a commercial FE package for the modeling of the unit cell and using free wave propagation in simple waveguides to obtain the forced response of different structures.

The WFE method is applied to periodic structures, assumed to be constituted by unit cells each of which coupled to its neighbors on all sides and corners. Following the

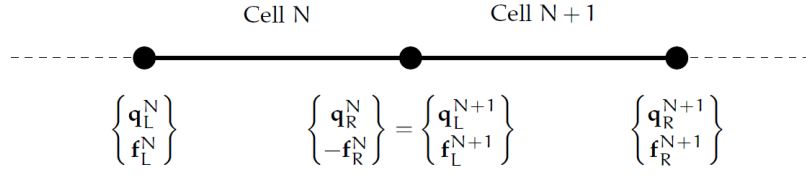


Figure 1.30 – Periodicity conditions between two adjacent cells [108].

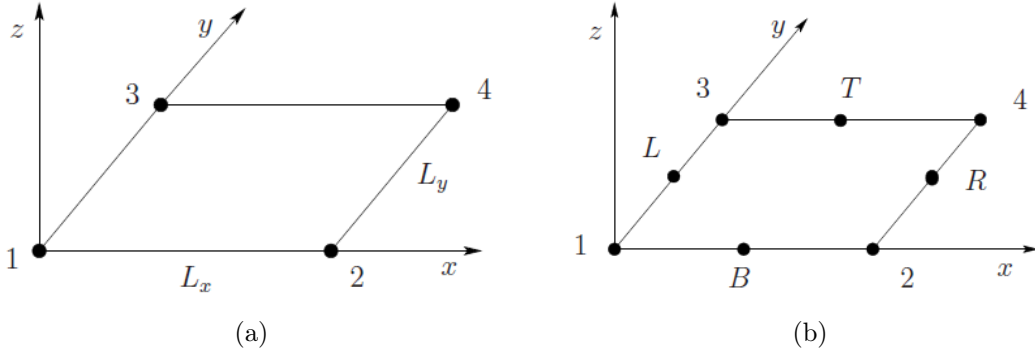


Figure 1.31 – FE models of the 2D unit cells with corners nodes (a) and mid-side nodes (b) [99].

same notation of Eq. (1.69), the continuity of nodal displacements and the equilibrium of nodal forces between two adjacent cells can be expressed as shown in Fig. 1.30.

Considering a unit periodic element modeled in commercial FE package, as shown in Fig. 1.31a, the vector of the nodal DOFs can be expressed as:

$$\mathbf{q} = \left[\mathbf{q}_1^T \quad \mathbf{q}_2^T \quad \mathbf{q}_3^T \quad \mathbf{q}_4^T \right]^T, \quad (1.70)$$

where the superscript T represents the transpose and \mathbf{q}_i is the vector of the DOFs of the i -th node. In general, if multiple elements are present in the thickness direction, the i -th node becomes an hypernode, obtained concatenating all the nodes through the thickness. Similarly, the vector of the nodal forces can be obtained:

$$\mathbf{f} = \left[\mathbf{f}_1^T \quad \mathbf{f}_2^T \quad \mathbf{f}_3^T \quad \mathbf{f}_4^T \right]^T. \quad (1.71)$$

Being k_x and k_y the wavenumber components in two orthogonal directions, L_x and L_y the dimensions of the unit element (see Fig. 1.31a), the propagation of the free wave [109, 110] can be derived starting from the propagation constants in the two orthogonal directions, $\mu_x = k_x L_x$ and $\mu_y = k_y L_y$; the nodal displacements \mathbf{q} at a corner can be related to the other one by the following relationships:

$$\mathbf{q}_2 = \lambda_x \mathbf{q}_1; \quad \mathbf{q}_3 = \lambda_y \mathbf{q}_1; \quad \mathbf{q}_4 = \lambda_x \lambda_y \mathbf{q}_1, \quad (1.72)$$

where $\lambda_x = e^{-i\mu_x}$ and $\lambda_y = e^{-i\mu_y}$. Substituting Eq. (1.72) into Eq. (1.70), we obtain:

$$\mathbf{q} = \Lambda_R \mathbf{q}_1, \quad \text{with} \quad \Lambda_R = \left[\mathbf{I} \quad \lambda_x \mathbf{I} \quad \lambda_y \mathbf{I} \quad \lambda_x \lambda_y \mathbf{I} \right]^T. \quad (1.73)$$

If no external forces are applied, from the equilibrium condition at node 1, the following expression is obtained:

$$\Lambda_L \mathbf{f} = 0, \quad \text{with} \quad \Lambda_L = [\mathbf{I} \quad \lambda_x^{-1} \mathbf{I} \quad \lambda_y^{-1} \mathbf{I} \quad (\lambda_x \lambda_y)^{-1} \mathbf{I}]. \quad (1.74)$$

Pre-multiplying both sides of Eq. (1.69) and taking in account Eq. (1.73), the expression of free wave motion is given by:

$$[\bar{\mathbf{K}}(\mu_x, \mu_y) + i\omega \bar{\mathbf{C}}(\mu_x, \mu_y) - \omega^2 \bar{\mathbf{M}}(\mu_x, \mu_y)] \mathbf{q}_1 = 0, \quad (1.75)$$

in which:

$$\bar{\mathbf{K}} = \Lambda_L \mathbf{K} \Lambda_R, \quad (1.76a)$$

$$\bar{\mathbf{C}} = \Lambda_L \mathbf{C} \Lambda_R, \quad (1.76b)$$

$$\bar{\mathbf{M}} = \Lambda_L \mathbf{M} \Lambda_R \quad (1.76c)$$

are the element stiffness, damping and mass matrices projected onto the DOFs of node 1. Denoting with \mathbf{D} the element dynamic matrix projected onto the DOFs of node 1, the eigenvalue problem can be expressed as:

$$\bar{\mathbf{D}}(\omega, \lambda_x, \lambda_y) = 0. \quad (1.77)$$

The dimensions of the dynamic stiffness matrix are dependent on the number of nodal DOFs; assuming to have n DOFs per node, nodal displacements and force vectors are of $n \times 1$, the element matrices are $4n \times 4n$ and the reduced matrix is $n \times n$.

In some cases, the unit periodic cell doesn't coincide with the single discrete element employed to model the structure in the FE package; a certain number of mid-side nodes can be present, as shown in Fig. 1.31b. The nodal DOFs vector expressed in Eq. (1.70) becomes:

$$\mathbf{q} = [\mathbf{q}_1^T \quad \mathbf{q}_2^T \quad \mathbf{q}_3^T \quad \mathbf{q}_4^T \quad \mathbf{q}_L^T \quad \mathbf{q}_R^T \quad \mathbf{q}_B^T \quad \mathbf{q}_T^T]^T, \quad (1.78)$$

while the periodicity condition in Eq. (1.73) is now expressed by:

$$\mathbf{q} = \Lambda_R \begin{bmatrix} \mathbf{q}_1 \\ \mathbf{q}_L \\ \mathbf{q}_B \end{bmatrix}, \quad \text{with} \quad \Lambda_R = \begin{bmatrix} \mathbf{I} & \lambda_x \mathbf{I} & \lambda_y \mathbf{I} & \lambda_x \lambda_y \mathbf{I} & \mathbf{0} & \mathbf{0} & \mathbf{0} & \mathbf{0} \\ \mathbf{0} & \mathbf{0} & \mathbf{0} & \mathbf{0} & \mathbf{I} & \lambda_x \mathbf{I} & \mathbf{0} & \mathbf{0} \\ \mathbf{0} & \mathbf{0} & \mathbf{0} & \mathbf{0} & \mathbf{0} & \mathbf{0} & \mathbf{I} & \lambda_y \mathbf{I} \end{bmatrix}. \quad (1.79)$$

The set of relationship between the DOFs of the node 1 and the others are completed as follows:

$$\mathbf{q}_L = \lambda_y^{1/2} \mathbf{q}_1; \quad \mathbf{q}_B = \lambda_x^{1/2} \mathbf{q}_1. \quad (1.80)$$

Considering Eq. (1.70), the dynamic stiffness matrix of the element in Eq. (1.69) can be partitioned as follows:

$$\mathbf{D} = \begin{bmatrix} \mathbf{D}_{11} & \mathbf{D}_{12} & \mathbf{D}_{14} & \mathbf{D}_{14} \\ \mathbf{D}_{21} & \mathbf{D}_{22} & \mathbf{D}_{23} & \mathbf{D}_{24} \\ \mathbf{D}_{31} & \mathbf{D}_{32} & \mathbf{D}_{33} & \mathbf{D}_{34} \\ \mathbf{D}_{41} & \mathbf{D}_{42} & \mathbf{D}_{43} & \mathbf{D}_{44} \end{bmatrix}, \quad (1.81)$$

giving the following reduced eigenvalue problem:

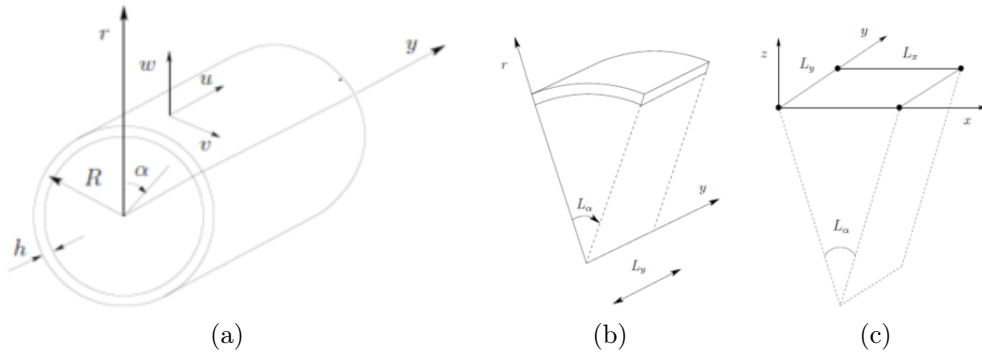


Figure 1.32 – Wave Finite Element method for curved structures: cylindrical coordinates (a), curved element (b) and FE model of the unit periodic cell (c) [99].

$$\begin{aligned} & [(\mathbf{D}_{11} + \mathbf{D}_{22} + \mathbf{D}_{33} + \mathbf{D}_{44})\lambda_x\lambda_y + (\mathbf{D}_{12} + \mathbf{D}_{34})\lambda_x^2\lambda_y + \\ & \quad + (\mathbf{D}_{13} + \mathbf{D}_{24})\lambda_x\lambda_y^2 + \mathbf{D}_{32}\lambda_x^2 + \mathbf{D}_{23}\lambda_y^2 + (\mathbf{D}_{21} + \mathbf{D}_{43})\lambda_y + \\ & \quad + (\mathbf{D}_{31} + \mathbf{D}_{42})\lambda_x + \mathbf{D}_{14}\lambda_x^2\lambda_y^2 + \mathbf{D}_{41}] \mathbf{q} = 0. \end{aligned} \quad (1.82)$$

In general, four kind of eigenvalue problems are possible:

- linear algebraic for real propagation constants, in which the dispersion relations for free wave propagation are obtained by fixing the real propagation constants μ_x and μ_y and calculating the corresponding frequency ω ;
- quadratic polynomial for complex propagation constant, in which the frequency ω and one wavenumber component k_x or k_y are given and all the possible solutions for the other wavenumber component are found;
- polynomial for complex propagation constant, in which the frequency ω and the propagation direction θ are given, while the propagation constants have to be found (but their ratio is known, $\mu_x/\mu_y = (L_x/L_y) \tan \theta$);
- transcendental, if the ratio μ_x/μ_y is not rational.

The WFE method can be extended to curved structures [99]. Considering the cylindrical coordinates in Fig. 1.32a the circumferential wavenumber can be defined: $k_x = k_\alpha/R$, with $x = R\alpha$ the axis along the circumference.

To apply the periodicity condition, the local reference system must be rotated to model the curvature. The stiffness, damping and mass matrices of the curved element can be obtained by the support of a transformation matrix $\bar{\mathbf{R}}$, as follows:

$$\mathbf{K} = \bar{\mathbf{R}}^T \mathbf{K}_{\text{LOC}} \bar{\mathbf{R}}, \quad (1.83a)$$

$$\mathbf{C} = \bar{\mathbf{R}}^T \mathbf{C}_{\text{LOC}} \bar{\mathbf{R}}, \quad (1.83b)$$

$$\mathbf{M} = \bar{\mathbf{R}}^T \mathbf{M}_{\text{LOC}} \bar{\mathbf{R}}, \quad (1.83c)$$

being the transformation matrix defined as:

$$\bar{\mathbf{R}} = \begin{bmatrix} \mathbf{I} & \mathbf{0} & \mathbf{0} & \mathbf{0} \\ \mathbf{0} & \mathbf{R} & \mathbf{0} & \mathbf{0} \\ \mathbf{0} & \mathbf{0} & \mathbf{I} & \mathbf{0} \\ \mathbf{0} & \mathbf{0} & \mathbf{0} & \mathbf{R} \end{bmatrix}. \quad (1.84)$$

The rotation matrix \mathbf{R} is defined as follows:

$$\mathbf{R} = \begin{bmatrix} \mathbf{r} & \mathbf{0} \\ \mathbf{0} & \mathbf{r} \end{bmatrix}, \quad \text{with} \quad \mathbf{r} = \begin{bmatrix} \cos \alpha & 0 & -\sin \alpha \\ 0 & 1 & 0 \\ \sin \alpha & 0 & \cos \alpha \end{bmatrix}. \quad (1.85)$$

After introducing the rotation matrix and after the calculation of the stiffness, damping and mass matrices of the curved element (see Eq. (1.83a), 1.83b and 1.83c), the WFE method becomes the same of flat structures.

1.5 Damping Loss Factor estimation

The experimental investigation of the damping loss factor is an highly debated topic. Oberst [111, 112] developed a technique to estimate the damping loss factor of multi-layer cantilever beams from non-contact measurement, making a comparison between the FRF of the bare beam (usually lightly damped) and the one of the damped beam. Thwaites et al. [113] proposed a technique based on the Time-of-Flight method, calculating the wave decay between consecutive measurement points. McDaniel et al. [9] proposed an approach based on the estimated complex wavenumbers. Depending on which kind of wavenumber is estimated (flexural k_f or longitudinal k_l), the damping loss factor is determined at each frequency with the following relationships [9]:

$$\eta = \left| \frac{\text{Im}(k_f^4)}{\text{Re}(k_f^4)} \right| \quad \text{or} \quad \eta = \left| \frac{\text{Im}(k_l^2)}{\text{Re}(k_l^2)} \right|. \quad (1.86)$$

An experimental estimation of the damping loss factor based on bending wavenumbers of a beam-like structure is shown in Fig. 1.33.

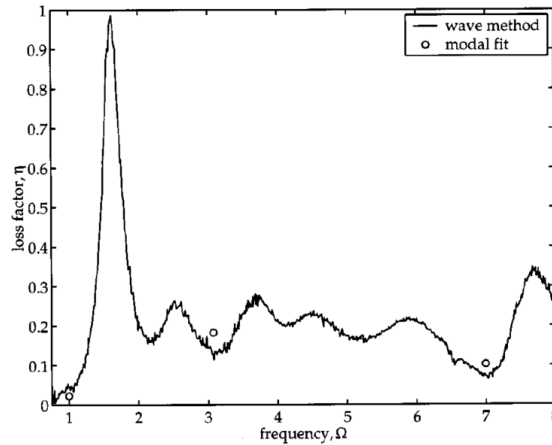


Figure 1.33 – Experimental estimation of the damping loss factor [8].

Cherif et al. [1] proposed an experimental vibro-acoustic investigation and damping estimation for complex flat panels. The damping loss factor calculated by Eq. (1.86) is then compared with some classical methods: the half-power bandwidth method (3 dB method) [114], the decay rate method [115] and the power injection method [116]. The previous methods are here briefly summarized for the sake of clarity:

- Half-power bandwidth method: this technique is largely used in the low frequency range or when the modal overlap is very low. With this approach it is possible to estimate the modal damping at each resonance, adopting the following formula:

$$\eta_n = \frac{\Delta f}{f_n}, \quad (1.87)$$

where f_n is the resonance frequency of the mode and Δf the half-power bandwidth of the mode (-3 dB).

- Decay rate method: this method is based on the logarithmic decrement of the transient structural response. Usually, some accelerometers are placed on the structure to measure the decay of the vibrations after the excitation is cut off. The damping is assumed to have an exponential decay and the same damping is assumed for all the modes in the same frequency band. Assuming a third-octave band and a decay rate DR (in dB/s), the damping loss factor is given by:

$$\eta_i = \frac{\text{DR}}{27.3f}. \quad (1.88)$$

- Power injection method: this method is directly derived from the Statistical Energy Analysis (SEA) power balance equation. The damping loss factor is obtained from the spatially averaged square velocities produced by the power injected to the structure. In steady-state condition, the space and frequency averaged input power is equal to the average dissipated power; the average loss factor is given by the following relationship:

$$\eta_i = \frac{P_i}{\omega E_i}, \quad (1.89)$$

where:

$$P_i = 0.5\mathbb{R}e\{F^*v\} = 0.5\mathbb{R}e\left\{\int_{\omega_1}^{\omega_2} G_{Fv}(\omega) d\omega\right\}, \quad (1.90)$$

is the input power obtained from the real part of the cross-spectral density $G_{Fv}(\omega)$ between the force F and the velocity v and

$$E_i = M_i v_i^2 = M_i \int_{\omega_1}^{\omega_2} G_{vv}(\omega) d\omega, \quad (1.91)$$

is the space and frequency averaged total energy, with M_i the mass related to the measurement area.

The previous methods are applied to four different panels: an isotropic aluminum panel, an isotropic aluminum panel with viscoelastic layer, a thin and a thick composite sandwich honeycomb panels. The structures were freely suspended and subject to point harmonic excitation, using a mechanical shaker generating a white noise excitation in the range [100 Hz - 10 000 Hz]. The results are shown in Fig. 1.34.

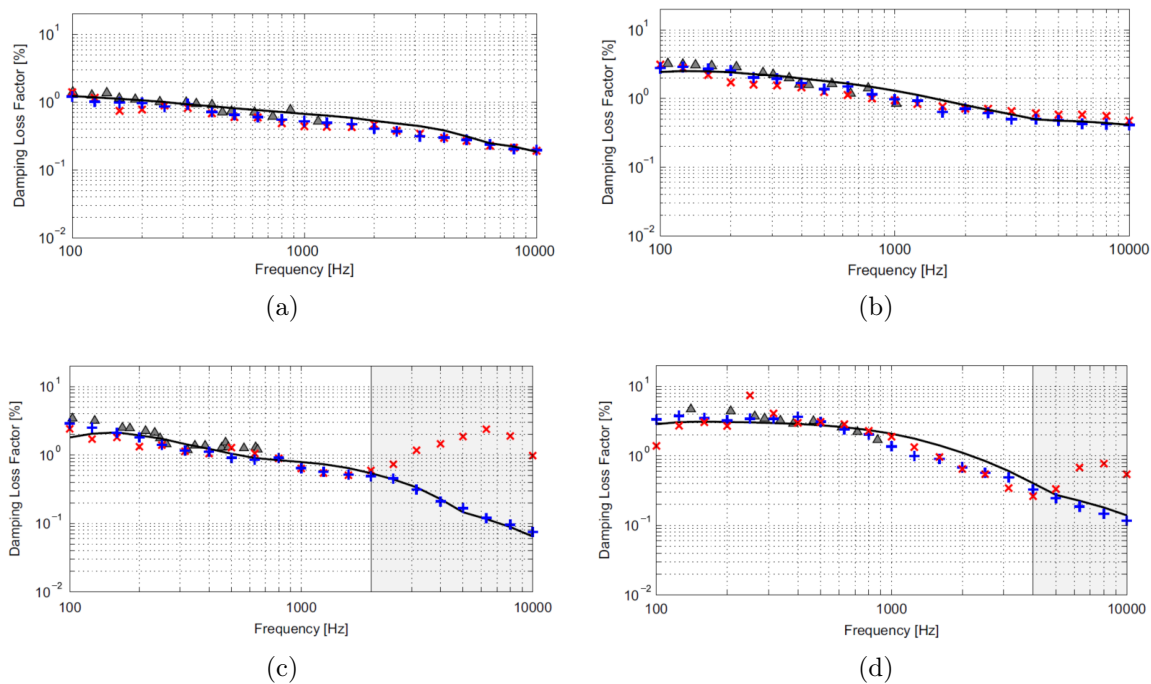


Figure 1.34 – Damping loss factor estimation for flat panels: isotropic aluminum (a), isotropic aluminum with viscoelastic layer (b), thin composite (c) and thick composite (d), with 3 dB method (Δ), decay rate method (+), power injected method (\times) and IWC method (—) [1].

Part I

Structural characterization of flat structures

Chapter 2

New formulation of the IWC method based on Green's and Hankel's functions

Part of this Chapter has already been published as "G. Tufano, C. Droz, M. Ichchou, O. Bareille, A.-M. Zine, B. Pluymers and W. Desmet, *On the structural characterization through k-space methods: assessments and validations*, *Book of Proceeding of 9th ECCOMAS Thematic Conference on Smart Structures and Materials, SMART 2019*, Paris, France".

Abstract

Periodic structures are very common and widely used in many engineering fields. Many methods were developed based on the spatial repetition of a unit cell; the unit cell modeling approach allows to reduce the computational effort working on a small geometrical part of the structure and applying periodic boundary conditions at the edges, and it is widely used to simulate infinite media. Periodic structures can be designed and employed to attenuate the wave propagation in certain frequency bands, originating the so-called band-gaps. This physical behavior can be obtained in two different ways, which are: resonant meta-materials (usually spatially distributed resonators) and phononic crystals. The band-gaps generated by phononic crystal are related to the Bragg's effect; a band-gap occurs when the incoming waves are scattered by a periodic structure, giving rise a destructive interference. This physical effect occurs when the distance between the two scatters is of the same order of magnitude of the wavelength of the propagating waves. K-space methods are widely employed to determine the dispersion characteristics, to identify the direction of propagation and to estimate the equivalent material properties of complex structures through an inverse approach, when the analytical models are not available or too complex to be derived. In addition to the classical Fourier-transform based methods, other approaches were developed, such as the Inhomogeneous Wave Correlation (IWC) method. In this chapter, the physical characteristics of periodic structures are employed to analyze the vibro-acoustic response of several complex structures in the wavenumber domain. The idea is to investigate a mechanical system with a certain degree of periodicity to control and attenuate the vibration levels of the structure subjected to a harmonic excitation. The proposed technique shows an accurate description of the band-gaps and of the wave

attenuation, giving some interesting information about the physics of the problem and the structural damping of the system. The optimal wavenumber, at each frequency, is obtained by a maximization function, making a comparison between the vibrational field (usually calculated in a finite element framework) and the one generated by a set of Green's and Hankel's functions.

2.1 Introduction

In literature, several methods are available to correctly extract the real part of the wavenumber, but the estimation of the related damping information is still an open challenge. In the domain of punctual harmonic excited structures, McDaniel et al. [8, 9] developed a semi-analytical approach based on damped plane wave propagation (1D guided waves), using an expression of the plane wave of type $e^{\pm ikx}$, where i is the imaginary unit, k is the complex wavenumber and x is the spatial coordinate (see section 1.2.2).

To describe the vibrational field of a structure subjected to punctual harmonic excitation, the Green's functions and the related image source method are widely used in literature (see section 1.2.6). An application of the method of images is shown in Gunda et al. [56]; the authors used this approach to describe the harmonic response of beams and rectangular plates. Based on the method of the images, Cuenca et al. [54] described the vibrational field of a finite plate with simply supported boundary conditions by the reconstruction of the Green's function of a point excited plate. The same method has been applied by Cuenca et al. [60] to estimate the equivalent material properties of a plate covered by a viscoelastic layer. Recently, Roozen et al. [5] used the Green's function of a point excited plate, by using a set of Hankel's functions, into a complex wavenumber fit procedure, making a comparison between the acquired vibrational field and the Green's function; the procedure here described allows to retrieve the complex wavenumber and the equivalent material properties.

All the methods based on plane wave assumption are affected by some limitations due to the nature of the plane wave itself. The vibrational field should be acquired in a steady-state condition, sufficiently far from the excitation location (this is a singularity point where the plane wave hypothesis is not valid) and trying to distinguish between the direct, reflected and evanescent fields.

When dealing with harmonic excitation, the need to mitigate some specific structural modes allows to develop vibration control devices, such as the tuned mass dampers (TMDs). The TMD devices are widely used in civil engineering to attenuate wind and earthquake effects on tall buildings. Most of the TMDs are tuned at a specific frequency, playing on different values of mass and stiffness properties in order to obtain a resonance frequency equal to the excitation frequency [117–120].

In this chapter, a method is proposed to combine advantages of the IWC method and of the image source method, which uses a set of Hankel's functions to obtain the vibrational field of a point excited structure. The main advantage of this approach is the possibility to be close to the excitation region, avoiding the problems related to the plane wave assumption. The proposed approach estimates the complex wavenum-

ber and the dispersion relation of several complex structures, showing a description of the periodicity effect (Bragg's band-gaps); the damping loss factor is also estimated. The local dynamics is also well described on narrow plates and isotropic panels with distributed tuned mass-damper elements.

For what concerns the numerical simulations, the out-of-plane component of the displacement is taken in account and used as primary input for the proposed IWC approach. The boundary conditions are of kind *free* on each edge of the considered structure. The full vibrational field is acquired and considered for the estimation of the complex wavenumbers.

2.2 Methodology

The complex dispersion relation of different structures is here estimated by a wave correlation method. The presented approach estimates, at each frequency f_0 , the complex wavenumber as the point of best agreement between the acquired vibrational field and the Green's function of the point excited structure. The Green's function is derived from the classical Kirchhoff's thin plate theory [57]; according to this theory, for an isotropic, homogeneous plate with a constant thickness h , the flexural vibration, in terms of transverse displacement w , is expressed by:

$$D\nabla^4 w(\vec{x}, t) + \rho h \frac{\partial^2 w(\vec{x}, t)}{\partial t^2} = F(\vec{x}_0, t), \quad (2.1)$$

where $D = Eh^3/12(1-\nu^2)$ is the bending stiffness, E is the Young's modulus, ν is the Poisson's coefficient, ρ is the mass density, $\nabla^4 = \nabla^2 \nabla^2$ is the biharmonic operator, ∇^2 is the Laplacian operator, t is the time variable, F is the force per unit area and \vec{x} , \vec{x}_0 are the position vectors of the acquisition and excitation points, respectively. The Laplacian operator is defined as follows:

$$\nabla^2 \nabla^2 = \frac{\partial^4}{\partial x_1^4} + 2 \frac{\partial^4}{\partial x_1^2 \partial x_2^2} + \frac{\partial^4}{\partial x_2^4}. \quad (2.2)$$

Assuming a harmonic point excitation, the expression of the force becomes $P(\vec{x}_0, t) = F(\vec{x}_0)e^{i\omega t}$, ω being the angular frequency; consequently, the steady state response of the transversal vibrational field is $w(\vec{x}, t) = u(\vec{x})e^{i\omega t}$. Substituting these two expressions in Eq. (2.1), the governing equation assumes the following form:

$$D\nabla^4 u(\vec{x}) - k^4 u(\vec{x}) = F(\vec{x}_0), \quad (2.3)$$

where $k^4 = \rho h \omega^2 / D$ is the flexural wavenumber.

For a plate of infinite dimensions, the solution of Eq. (2.3) is given by:

$$G_\infty(x, y) = \frac{1}{8k^2 D} \left[H_0^1(kr) - H_0^1(ikr) \right], \quad (2.4)$$

with G_∞ the Green's function of the infinite plate, H_0^1 the Hankel's function of first kind and order 0 and $r = \|x - x_0, y - y_0\|$ is the distance between the acquisition (x, y) and excitation (x_0, y_0) points.

At each frequency f_0 , the complex flexural wavenumber is found as the point of best agreement between the measured vibrational field and the Green's function expressed in Eq. (2.4). Considering an acquisition region of area S in the plane (x, y) , indicating with \tilde{w} and w the measured vibrational field and the one described by Eq. (2.4), respectively, the normalized correlation function assumes the following expression:

$$\mathcal{F}(k_{\mathbb{R}e}, k_{\mathbb{I}m}) = \frac{\left| \iint_S \tilde{w} \cdot w_{k_{\mathbb{R}e}, k_{\mathbb{I}m}}^* dx dy \right|}{\sqrt{\iint_S |\tilde{w}|^2 dx dy \cdot \iint_S |w_{k_{\mathbb{R}e}, k_{\mathbb{I}m}}|^2 dx dy}}, \quad (2.5)$$

where $*$ denotes the complex conjugate. For discrete point measurements, the integrals in Eq. (2.5) are replaced by summations over the entire domain, as follows:

$$\mathcal{F}(k_{\mathbb{R}e}, k_{\mathbb{I}m}) = \frac{\left| \sum_{j=1}^N \tilde{w}(x_j, y_j) \cdot w_{k_{\mathbb{R}e}, k_{\mathbb{I}m}}^*(x_j, y_j) \rho_j S_j \right|}{\sqrt{\sum_{j=1}^N |\tilde{w}(x_j, y_j)|^2 \rho_j S_j \cdot \sum_{j=1}^N |w_{k_{\mathbb{R}e}, k_{\mathbb{I}m}}(x_j, y_j)|^2 \rho_j S_j}}, \quad (2.6)$$

where j denotes the j -th discrete point, N is the total number of points, ρ_j is the coherence of the measured signal at the j -th point and S_j is the estimation of the nodal surface around the point (x_j, y_j) .

The complex wavenumber is identified as the location of the maximum of the correlation function. From the estimated wavenumber, an estimation of the damping loss factor can be obtained, at each frequency, by the well-known relationship between the real and imaginary parts of the flexural wavenumber, expressed in Eq. (1.86):

$$\eta = \left| \frac{\mathbb{I}m(k^4)}{\mathbb{R}e(k^4)} \right|.$$

By choosing a proper direction of propagation, Eq. (2.4) can be applied to a narrow plate subjected to punctual harmonic excitation. Keeping the same notation and indicating as L the length of the acquisition region, the correlation function showed in Eq. (2.5) becomes:

$$\mathcal{F}(k_{\mathbb{R}e}, k_{\mathbb{I}m}) = \frac{\left| \int_L \tilde{w} \cdot w_{k_{\mathbb{R}e}, k_{\mathbb{I}m}}^* dx \right|}{\sqrt{\int_L |\tilde{w}|^2 dx \cdot \int_L |w_{k_{\mathbb{R}e}, k_{\mathbb{I}m}}|^2 dx}}. \quad (2.7)$$

Similarly to what done in Eq. (2.5), in the discrete domain Eq. (2.7) becomes:

$$\mathcal{F}(k_{\mathbb{R}e}, k_{\mathbb{I}m}) = \frac{\left| \sum_{j=1}^N \tilde{w}(x_j) \cdot w_{k_{\mathbb{R}e}, k_{\mathbb{I}m}}^*(x_j) \rho_j L_j \right|}{\sqrt{\sum_{j=1}^N |\tilde{w}(x_j)|^2 \rho_j L_j \cdot \sum_{j=1}^N |w_{k_{\mathbb{R}e}, k_{\mathbb{I}m}}(x_j)|^2 \rho_j L_j}}. \quad (2.8)$$

The dispersion curves of the different structures have been validated using the Wave Finite Element Method (WFEM), in both one- and two-dimensional formulations (see section 1.4).

2.3 Narrow plate structures: numerical models and result discussion

The proposed approach is applied to several structures. Firstly, different narrow plates are taken in account: isotropic, periodic (with varying material and cross-section along

the length) and with distributed TMDs narrow plates. For all the analyzed configurations, the vibrational field is obtained by a FE analysis; the dynamic matrices of the structures are obtained using a commercial FE package, while the full-FEM analysis is done using a *in-home* MATLAB[®] code script. A harmonic unit force is applied in the center of the considered structures.

2.3.1 Isotropic narrow plate

The first application of the proposed approach is on a simple homogeneous narrow plate. The total length of the narrow plate is 1.0 m (see Fig. 2.1a); a periodic unit cell of 5 mm length can be identified, with cross-sectional dimensions of 10 mm × 1 mm, as shown in Fig. 2.1b; the finite element models of the narrow plate and of the periodic unit cell are shown in Fig. 2.1. The FE model of the structure is built using 200 structural beam elements (ANSYS BEAM44), resulting in a total number of 1206 degrees of freedom.

The employed material is a general thermoplastic polymer (ABS) with Young's modulus $E = 1.0$ GPa, density $\rho = 980.0$ kg m⁻³ and Poisson's coefficient $\nu = 0.35$; two constant values of structural damping η are assumed: 2% and 4%. The FE analysis is conducted in the frequency range [100 Hz - 10 000 Hz], with a frequency step of 5 Hz.

The propagative part of the dispersion curve for the isotropic homogeneous narrow plate is shown in Fig. 2.2a. The proposed approach is compared to the WFE method and to the analytical dispersion relation that can be derived from Timoshenko's model for vibrating beams, as follows:

$$EI k^4 - \rho A \omega^2 - \left(\rho I + \frac{EI \rho}{KG} \right) k^2 \omega^2 + \frac{\rho^2 I}{KG} \omega^4 = 0, \quad (2.9)$$

where G is the shear modulus, $I = bh^3/12$ is the second moment of area, A is the narrow plate's cross-section area and $K = 5/6$ is a constant to take in account the shear force variation.

The proposed IWC approach exhibits a very good agreement with the analytical model (expressed by Eq. (2.9)) and the WFE method, in the whole frequency range. In Fig. 2.2b the damping loss factor estimations are shown; in both cases, the identified complex wavenumbers give a reasonable estimation of the structural damping introduced in the model. In the low frequency range, the estimated damping loss factor exhibits an oscillating behavior; on the contrary, when the excitation frequency increases the damping loss factor value reaches asymptotically the exact value of structural damping introduced in the FE model.

2.3.2 Periodic narrow plate

A periodic narrow plate is also investigated, to prove the feasibility of the proposed approach in describing the band-gaps due to the geometric periodicity of the structure. The finite element models of both the periodic unit cell and the full-scale structure are shown in Fig. 2.3. The unit cell has total length of 0.04 m and it's characterized by a double periodicity: material and cross-section. The employed materials are a standard aluminum alloy, with Young's modulus $E = 70.0$ GPa, density $\rho = 2700.0$ kg m⁻³ and

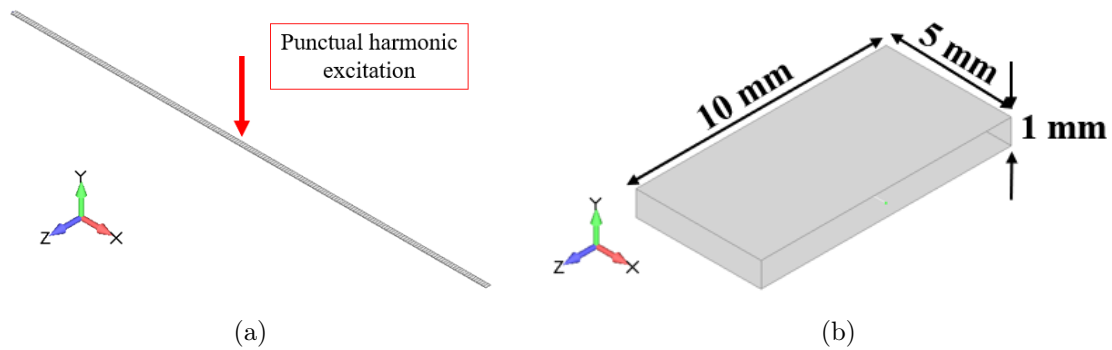


Figure 2.1 – Finite element models of the isotropic narrow plate: full-scale (a) and periodic unit cell (b).

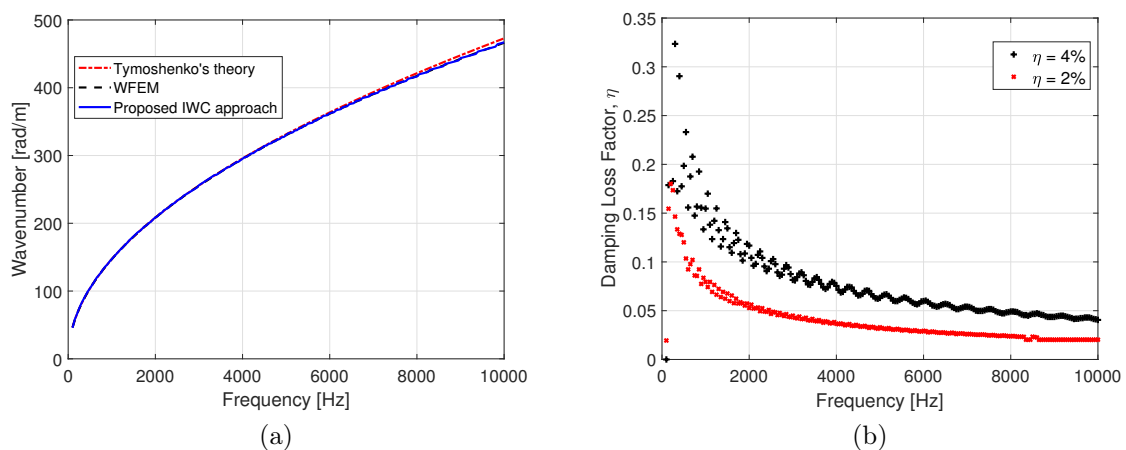


Figure 2.2 – Isotropic beam: propagative part of the dispersion curve calculated with proposed approach compared with the analytical model and the WFE method (a) and damping loss factor estimation (b).

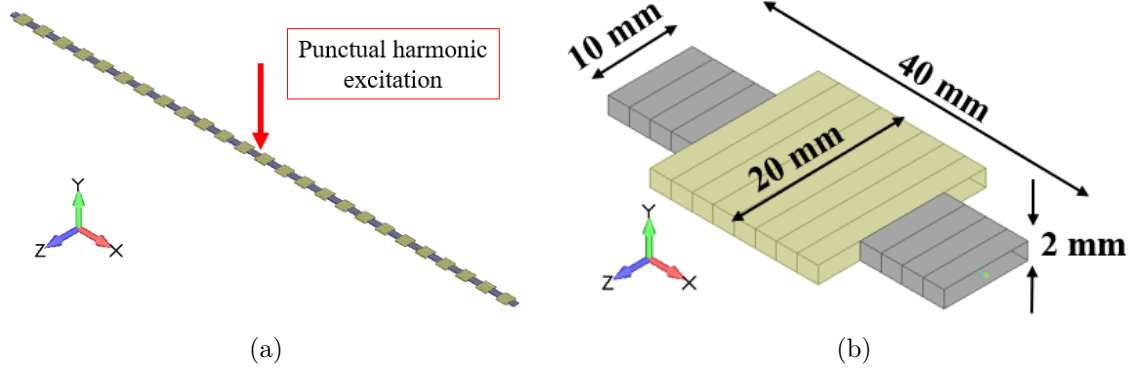


Figure 2.3 – Finite element models of the periodic narrow plate: full-scale (a) and periodic unit cell (b).

Poisson’s coefficient $\nu = 0.33$, and the ABS material already employed for the homogeneous narrow plate described in section 2.3.1. The aluminum part has a cross-section of dimensions $10 \text{ mm} \times 2 \text{ mm}$; the ABS part has dimensions $20 \text{ mm} \times 2 \text{ mm}$. The FE model of the structure is built using 400 structural beam elements (ANSYS BEAM44), resulting in a total number of 2406 degrees of freedom. The FE analysis is conducted in the frequency range $[100 \text{ Hz} - 20\,000 \text{ Hz}]$, with a frequency step of 5 Hz.

The dispersion curves of the periodic narrow plate are shown in Fig. 2.4; the dispersion curves calculated with the WFE method are limited to the first Brillouin zone, where the wavelengths are longer than one period of the structure (see Fig. 2.4a). The real part of the wavenumber has periodicity π/Δ , with Δ the length of the unit cell, showing multiples band-gaps, but always with $k_{\mathbb{R}e} \in [0, \pi/\Delta]$. The dispersion curves estimated with the proposed approach are shown in Fig. 2.4b, being in good agreement with the one calculated with the WFE method, identifying the same wide band-gaps zone. The proposed IWC approach takes in account the whole structure, avoiding the periodicity issue previously described in the wavenumbers estimation.

As shown in Fig. 2.4, from the dispersion curves four different resonance zones can be identified. The first band-gap, corresponding to the first Brillouin zone, appears in the frequency range $[700 \text{ Hz} - 1100 \text{ Hz}]$; the second band-gap opens at 2900 Hz and closes at 4900 Hz. The widest band-gap is the third, which is approximately of 3 kHz, from 8.2 kHz to 11 kHz; the last band-gap occurs in the frequency range $[15.4 \text{ kHz} - 16.6 \text{ kHz}]$. Each band-gap is characterized by a constant value of the propagative part of the wavenumber and an increase of the evanescent one; this effect is related to the physical phenomenon called scattering, in which the wave is reflected between two consecutive scatterers.

2.3.3 Isotropic narrow plate with distributed TMDs

The considered narrow plate has the same geometric characteristics of the isotropic beam analyzed in section 2.3.1; the total length is 1.0 m, with cross-sectional dimensions of $10 \text{ mm} \times 1 \text{ mm}$, as shown in Fig. 2.1b. For the host structure, the employed material is a classical aluminum alloy with Young’s modulus $E = 70.0 \text{ GPa}$, density $\rho = 2700.0 \text{ kg m}^{-3}$ and Poisson’s coefficient $\nu = 0.33$; a constant value of structural damping $\eta = 5\%$ is introduced in the model. The narrow plate is equipped with dis-

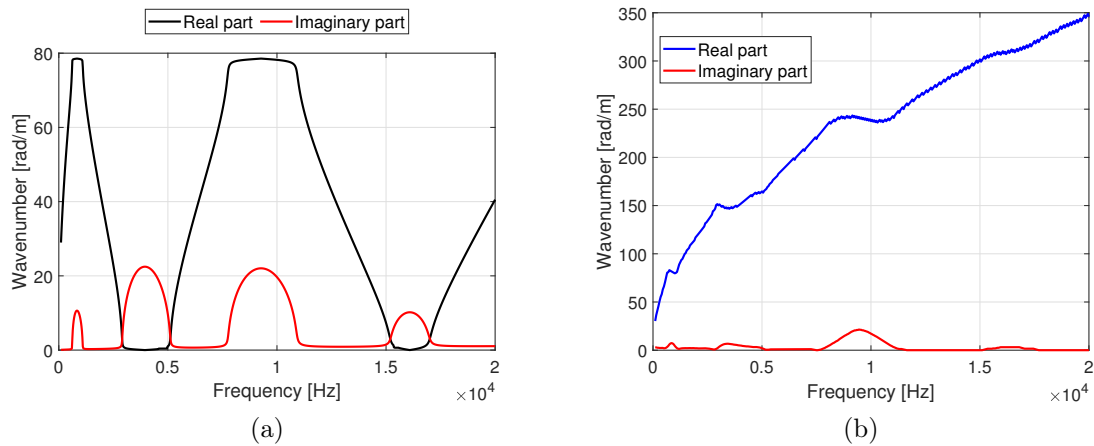


Figure 2.4 – Periodic beam: WFE method (a) and proposed approach (b) complex dispersion curve estimation.

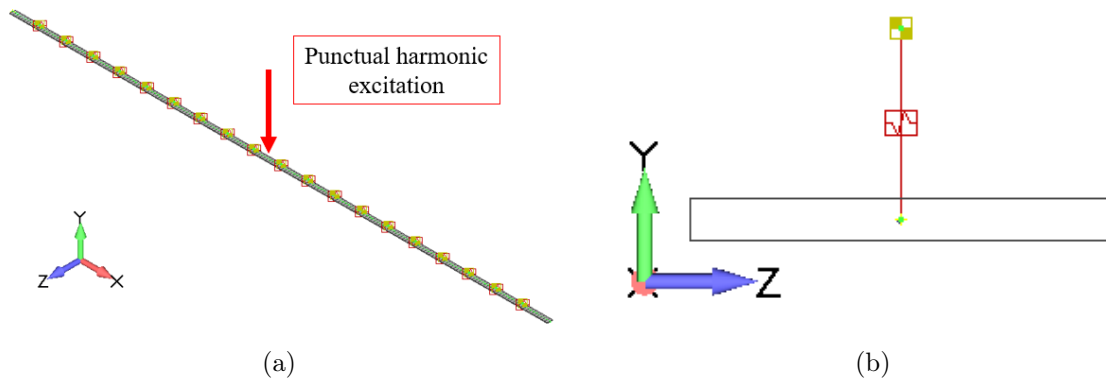


Figure 2.5 – FE models of the isotropic narrow plate with distributed TMDs: full-size (a) and front view of the unit periodic cell (b).

tributed TMD devices, modeled as mass-spring systems. The distance between each TMD is of 10 cm, resulting in a total number of 19 TMDs. The FE model of the structure is built using 200 structural beam elements (ANSYS BEAM44) for the host structure, 19 linear spring elements (ANSYS COMBIN14) and 19 point mass element (ANSYS MASS21), resulting in a total number of 1263 degrees of freedom. The finite element model of the resonating narrow plate is shown in Fig. 2.5; a front view of the narrow plate cross-section and of the TMD model is shown in Fig. 2.5b. The FE analysis is conducted in the frequency range [100 Hz - 7000 Hz], with a frequency step of 5 Hz.

A preliminary analysis is conducted on the bare test base narrow plate, to obtain the FRF and to identify the natural modes of the structure (as shown in Fig. 2.6a). Then the TMD devices are tuned following a three steps process:

1. identification of the natural frequency of the mode to attenuate, ω_n ;
2. definition of the percentage of added mass and, as a consequence, of the mass of each TMD, m_i ;

3. from the values of the natural frequency and of the mass of each TMD, the stiffness value k_i to be assigned at each spring element can be found: $\omega_n = \sqrt{k_i/m_i}$.

A first study is conducted using mass-spring systems, introducing a null value of damping. The mode to attenuate is chosen to be the one at 1500 Hz and two different percentages of added mass are chosen: 5% and 10%; the FRF comparison is shown in Fig. 2.6a, showing an attenuation of the considered mode. The associated dispersion curves are shown in Fig. 2.7; around the tuning frequency of the mass-spring systems a band-gap occurs. The depth of the band-gap and the attenuation in the wavenumber amplitude become more evident increasing the added-mass value.

Introducing the damping in the mass-spring system, the three-step process becomes a four-step one:

4. the damping coefficient c_i to introduce in each spring element is calculated as follows: $c_i = 2\zeta\omega_n m_i$, in which ζ is the structural damping ratio of the main mass.

A value of 5% of added mass is considered for the TMDs with the damping effect; a second mode to attenuate is chosen at 3500 Hz, and the related FRFs are plotted in Fig. 2.6b.

In Fig. 2.8a there are the dispersion curves of the bare narrow plate and of the resonating one with damping coefficient; this figure can be compared to Fig. 2.7, in which the damping coefficient was imposed equal to zero: the band-gap is wider and the amplitude of the propagative wavenumber is strongly attenuated. In Fig. 2.8b the global structural damping loss factor is calculated based on the estimated complex wavenumbers; in the region around the tuning frequency of the resonators, the equivalent damping coefficient is higher than 1, denoting a region in which the evanescent part of the wavenumber is much higher of its propagative part. After the tuning frequency of the TMDs, the estimated damping loss factor reach asymptotically the structural damping of the FE model.

The same behavior is obtained when the TMDs are tuned at 3500 Hz, as shown in Fig. 2.9; in this case, the band-gap is approximately of 1.5 kHz and associated with a strong attenuation of the propagative wavenumber. The same behavior observed in Fig. 2.8b is obtained in Fig. 2.9b for the estimation of the damping loss factor.

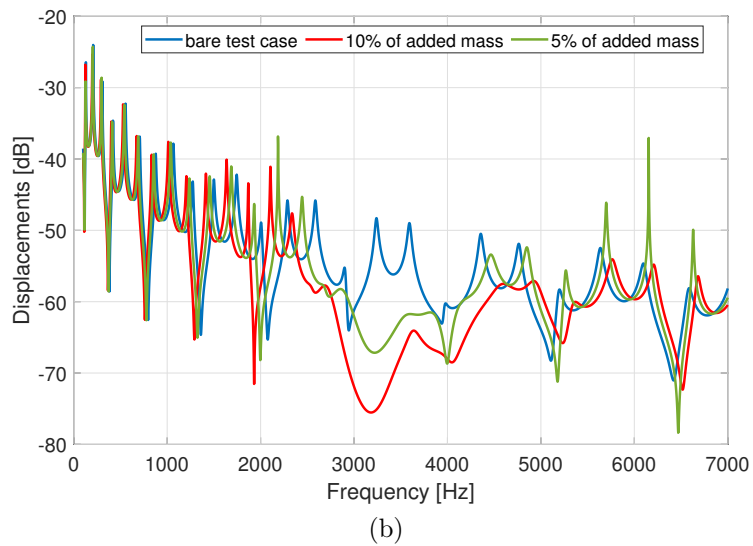
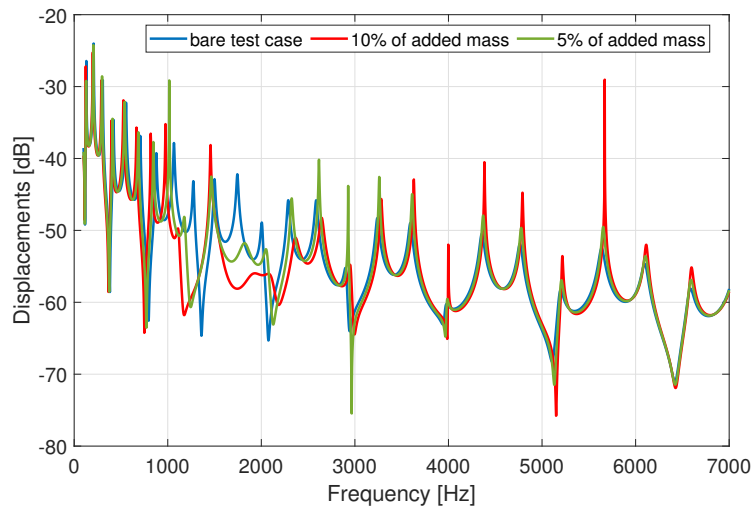


Figure 2.6 – FRFs comparison of the isotropic narrow plate with distributed TMDs: resonators tuned at 1500 Hz (a) and at 3500 Hz (b).

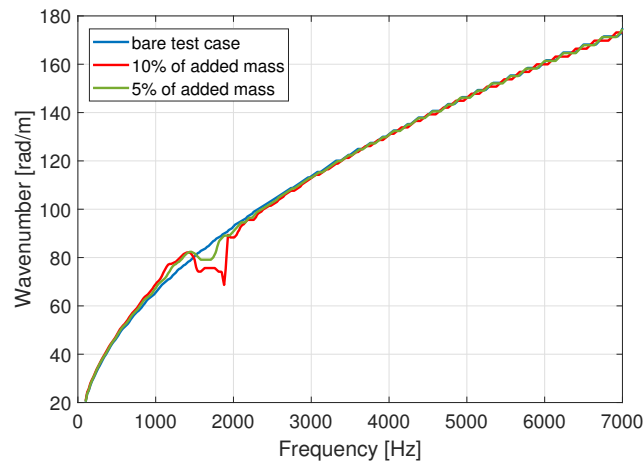


Figure 2.7 – Dispersion curves of the isotropic narrow plate with distributed TMDs.

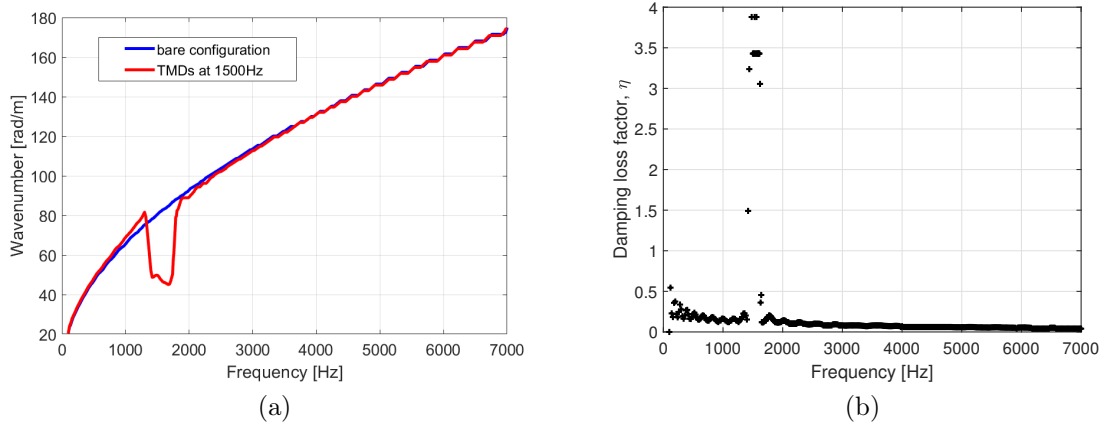


Figure 2.8 – Dispersion curve (a) and damping loss factor estimation (b) for the isotropic narrow plate with distributed TMDs tuned at 1500 Hz.

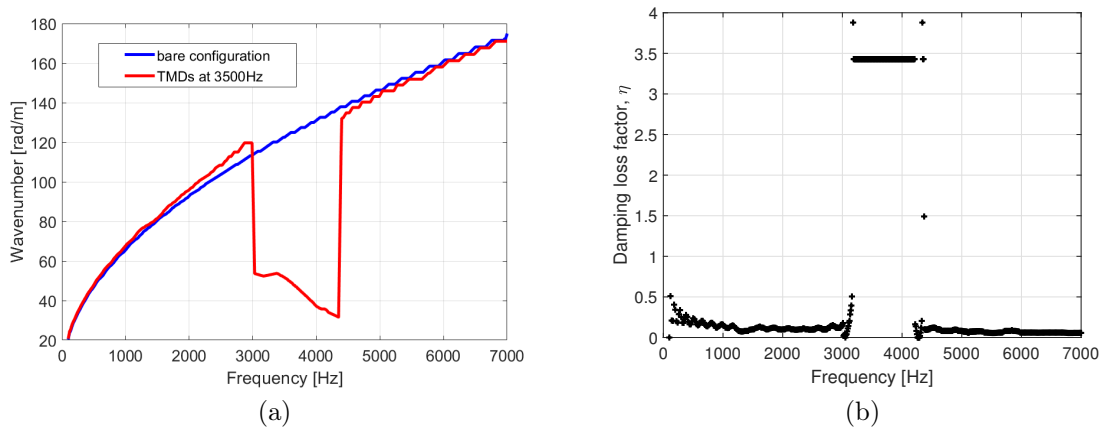


Figure 2.9 – Dispersion curve (a) and damping loss factor estimation (b) for the isotropic narrow plate with distributed TMDs tuned at 3500 Hz.

2.4 Two-dimensional flat structures: numerical models and result discussion

The proposed approach has been applied to two-dimensional flat structures, taking in account an homogeneous plate, a composite one, sticking together three different layers in the thickness direction, and an homogeneous plate with distributed TMD devices.

2.4.1 Homogeneous plate

An homogeneous plate has been investigated to demonstrate the feasibility of the proposed approach to two-dimensional structures. The plate has dimensions $1.0 \text{ m} \times 0.6 \text{ m}$ and thickness $h = 0.01 \text{ m}$; the employed material is the ABS already described in section 2.3.1. The FE model is built using solid structural elements (ANSYS SOLID45) in order to have a sufficient number of elements in the thickness direction; a total number of 30000 elements is used for the FE model, resulting in 221796 degrees of freedom. The FE models of the full-size panel and of the periodic unit cell are shown in Fig. 2.10. Two different constant values of structural damping η are assumed and introduced in the FE model: 2% and 5%. The harmonic displacement fields are obtained by an FE analysis in the frequency range [100 Hz - 5000 Hz], with a frequency step of 10 Hz.

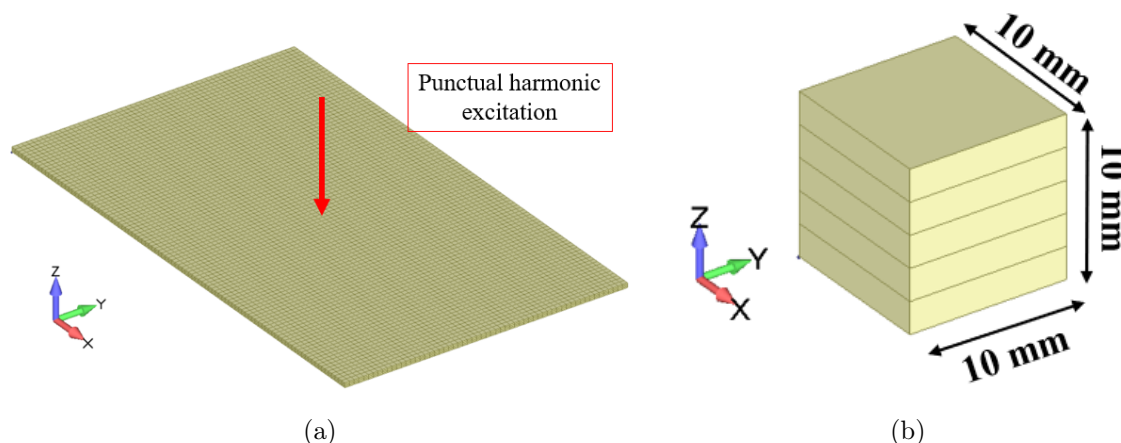


Figure 2.10 – Finite element models of the full-size (a) and of the periodic unit cell (b) of the homogeneous plate.

The propagative part of the dispersion curve is plotted in Fig. 2.11a; the proposed approach is compared with the WFE method (see section 1.4), which makes use of the periodic unit cell shown in Fig. 2.10b, and with the analytical expression of the dispersion relation derived from Kirchhoff's thin plate theory, expressed as follows:

$$k = \sqrt{\omega} \left(\frac{\rho h}{D} \right)^{1/4}. \quad (2.10)$$

A good agreement between the three methods is observed in the low frequency range, while in the high-frequency region the proposed approach exhibits an overestimation. The damping loss factor is estimated using Eq. (1.86) and the estimated values are plotted in Fig. 2.11b. As already discussed for the narrow plates in the previous

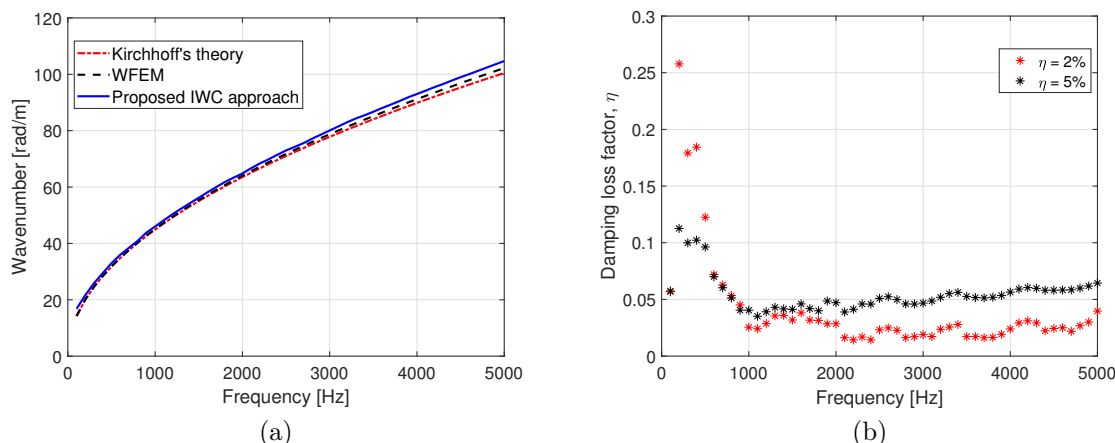


Figure 2.11 – Homogeneous plate: dispersion curve comparison (a) and damping loss factor estimation (b).

section, the damping loss factor reaches asymptotically the value of the structural damping introduced in the FE model.

2.4.2 Laminated composite plate

The proposed approach has been applied to a laminated composite plate, constituted of three layers of different materials: aluminum - ABS - aluminum (the material properties have been already described in the previous sections), of thickness 1 mm - 8 mm - 1 mm, respectively. The global dimensions of the plate are 1.0 m × 0.6 m and thickness $h = 0.01$ m. The FE model is built using solid structural elements (ANSYS SOLID45) in order to have a sufficient number of elements in the thickness direction; a total number of 30000 elements is used for the FE model, resulting in 221796 degrees of freedom. The FE models of the full-size panel and of the periodic unit cell are shown in Fig. 2.12. Two different constant values of structural damping η are assumed and introduced in the FE model: 2% and 5%. The harmonic displacement fields are obtained by an FE analysis in the frequency range [100 Hz - 5000 Hz], with a frequency step of 10 Hz.

The propagative part of the dispersion curve of the laminated composite plate is shown in Fig. 2.13a; a good agreement between the proposed approach and the WFE method is obtained in the whole frequency band of interest. A good identification of the damping loss factor is performed and shown in Fig. 2.13b. From the analysis of the dispersion curves and from the comparison between Fig. 2.13a and Fig. 2.11a, it can be observed how the laminated composite plate is stiffer than the homogeneous one, due to the presence of the two thin aluminum skins. Using an inverse approach based on the estimated wavenumber, the equivalent bending stiffness and the equivalent Young's modulus of the structure have been calculated by the following formulas, directly derived from Eq. (2.3):

$$D_{eq} = \frac{\omega^2 \rho h}{k^4} \quad \text{and} \quad E_{eq} = \frac{D_{eq} 12(1 - \nu^2)}{h^3}. \quad (2.11)$$

The equivalent plate properties are shown in Fig. 2.14.

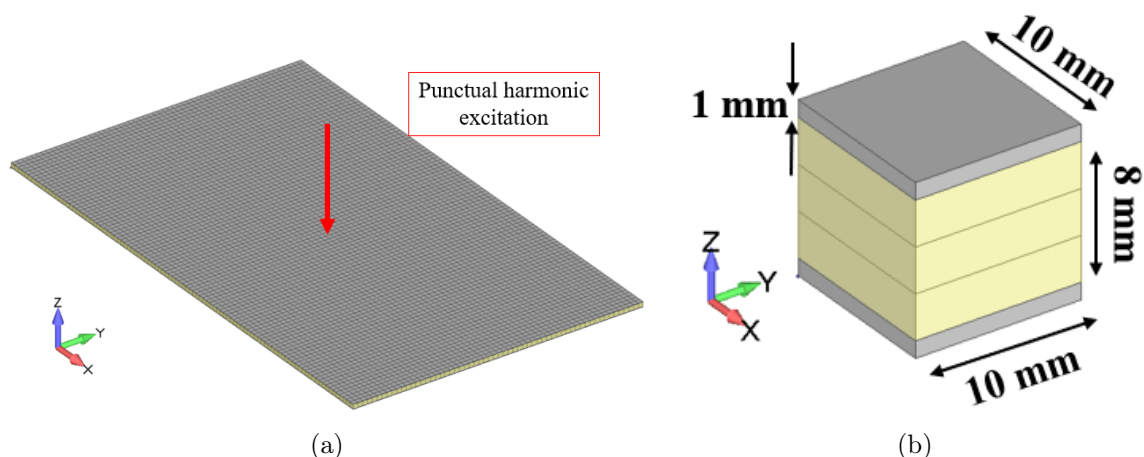


Figure 2.12 – Finite element models of the full-size (a) and of the periodic unit cell (b) of the laminated composite plate.

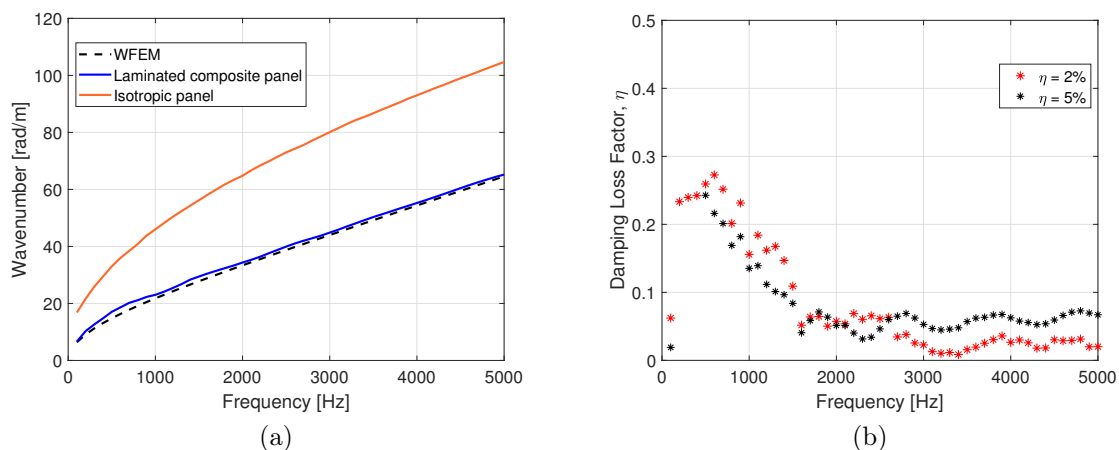


Figure 2.13 – Dispersion curve (a) and damping loss factor estimation (b) for the laminated composite plate.

2.4.3 Homogeneous plate with distributed TMDs

The proposed IWC approach is then applied to an homogeneous panel with distributed TMDs on the external surface. The plate has global dimensions equal to $1.0\text{ m} \times 1.0\text{ m}$ and thickness $h = 0.002\text{ m}$. The employed material is a standard aluminum alloy, with the following material properties: Young's modulus $E = 70.0\text{ GPa}$, density $\rho = 2700.0\text{ kg m}^{-3}$ and Poisson's coefficient $\nu = 0.33$; a constant value of structural damping $\eta = 5\%$ is introduced in the model. The FE model is built using solid structural elements (ANSYS SOLID45); a total number of 6400 elements is used for the FE model of the host panel, resulting in 39366 degrees of freedom. A total number of 100 TMDs is spatially distributed on the surface of the panel; the TMD devices are modeled using mass-spring elements: linear spring element (ANSYS COMBIN14) and point mass element (ANSYS MASS21). The distance between each TMD is 10.0 cm , identifying a periodic unit cell of dimensions $10.0\text{ cm} \times 10.0\text{ cm}$. The TMDs are tuned following the process described in section 2.3.3, with a null damping coefficient. The

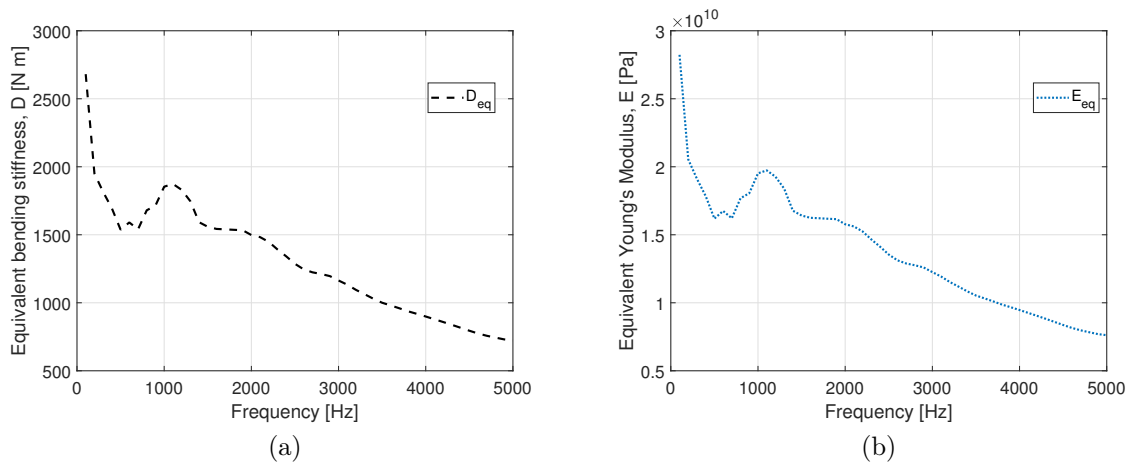


Figure 2.14 – Equivalent mechanical properties of the laminated composite panel: bending stiffness modulus (a) and Young's modulus (b).

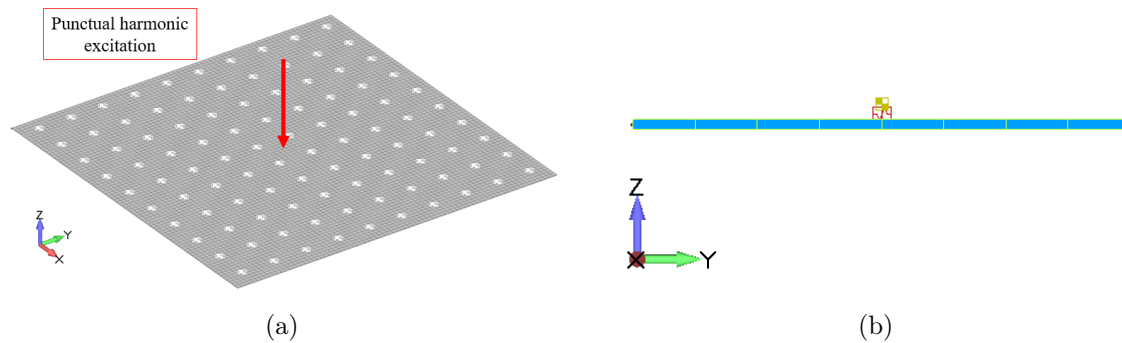


Figure 2.15 – FE models of the homogeneous panel with distributed TMDs: full-size (a) and front view of the unit periodic cell (b).

FE models of the full-size panel and of the periodic unit cell are shown in Fig. 2.15. The harmonic displacement fields are obtained by an FE analysis in the frequency range [50 Hz - 1000 Hz], with a frequency step of 2 Hz.

A preliminary investigation of the FRF of the bare panel is conducted to identify the mode to attenuate; the natural mode at $f_n = 350.0$ Hz is then chosen to tune the TMDs. Two different values of percentage of added mass are investigated: 3% and 5%. The comparison between the FRFs is shown in Fig. 2.16.

In Fig. 2.17a the dispersion curve of the homogeneous panel is calculated using the Kirchhoff's thin plate theory of Eq. (2.10); the analytical dispersion curve is compared to the ones obtained using the proposed IWC approach on the resonating plates. The band-gap is well captured and its width is added-mass-dependent, as already described in section 2.3.3. The damping loss factor is also estimated, showing a fast convergence to the value of the structural damping introduced in FE model; of course, around the tuning frequency of the TMDs, the damping coefficient estimation is affected by the dominance of the evanescent waves.

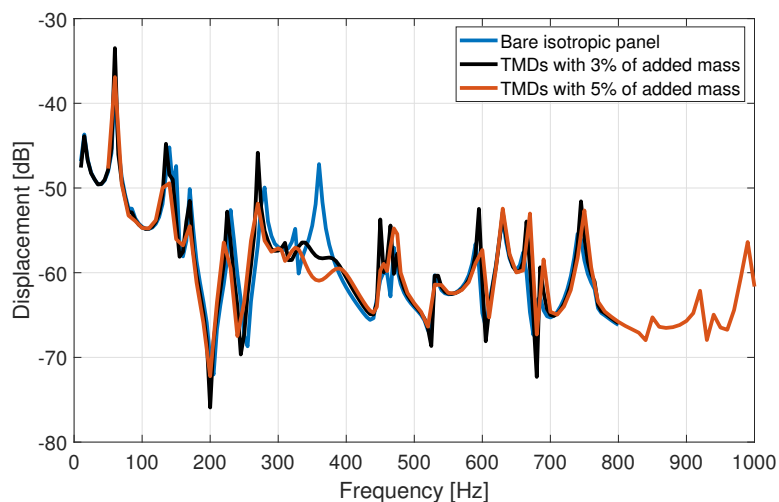


Figure 2.16 – FRFs comparison of the homogeneous panel with distributed TMDs.

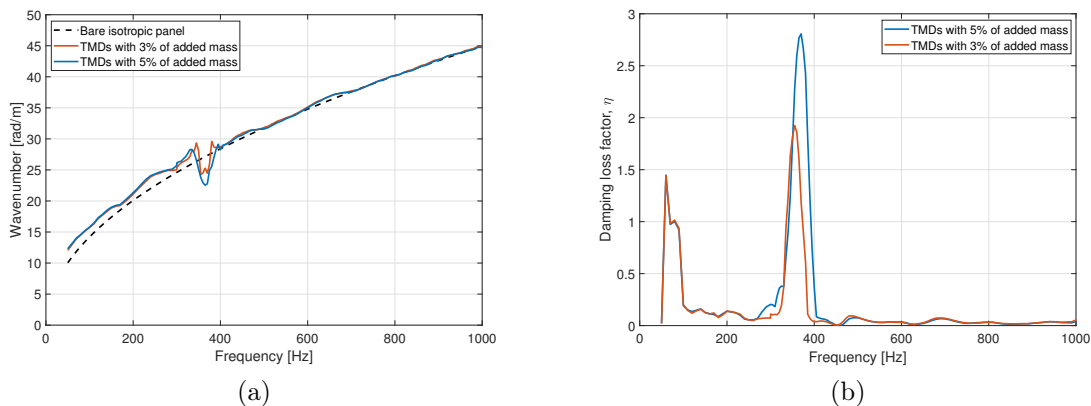


Figure 2.17 – Dispersion curve (a) and damping loss factor estimation (b) for the homogeneous panel with distributed TMDs.

2.5 Concluding remarks

In this chapter, different ideas are successfully implemented in this modified IWC approach, showing a very good prediction of the complex dispersion relations of periodic narrow plates and laminated structures. An estimation of the damping loss factor is obtained; the calculated values of η fast converge to the structural damping introduced in the FE models. The feasibility of this method in estimating the wave attenuation in the structures is successfully demonstrated.

The proposed approach allows to identify the resonance regions (stop-bands) due to the geometrical periodicity of the structure, showing a good agreement with the WFE method, based on the unit cell theory.

The proposed approach can be used in an inverse way to estimate the frequency dependent equivalent material properties of complex structures, when analytical models are not available or difficult to obtain.

Both global bending behavior and local dynamics are captured by the proposed approach; the dynamics of the TMD devices is well described, in both propagative and evanescent parts.

Chapter 3

Wavenumber analysis of flat orthotropic structures

Abstract

Two double-wall panels are investigated in this chapter, based on the unit cell modeling. The idea is to identify the angle-dependent dispersion curves, due to the orthotropic behavior of the analyzed structures. In case of isotropic behavior, the dispersion curves are the same in all directions, while in case of orthotropic materials, the wavenumber may be different in each direction. Two different double wall panels are investigated, with two different inter-spacings between the vertical mechanical links, to identify band-gaps occurrence.

One of the considered panels was 3D printed and experimentally tested under punctual harmonic excitation.

3.1 Introduction

The aim to combine lightness and good vibro-acoustic and mechanical properties of engineering structures allows to design new shapes and new materials. Composite, non-isotropic skins, sandwich cores of different shapes are widely used in transportation engineering. With the introduction of numerical tools, such as the Wave Finite Element Method (WFEM) (see section 1.4), the Finite Element (FE) analysis and some k -space methods, sandwich panels are widely investigated changing the design of the core, always keeping a high stiffness-to-mass ratio [121–123].

Among the vibro-acoustic indicators, one of the most important is the wavenumber. For relatively simple structures, some analytical methods are made available in literature [10, 58, 124]. An analytical formulation for the prediction of the core transverse shear and bending matrices for orthotropic sandwich panels has been introduced by Renji et al. [125]. The acoustic indicators and the dispersion characteristics are obtained using an analytical model based on Discrete Laminate Theory by Ghinet et al. [126, 127]. In the low-to-mid-frequency range, Guillaumie [128] proposed an analytical solution for the identification of the modal density and the eigenmodes.

Analytical and semi-analytical theories are limited to low- and mid-frequencies analy-

sis, where the wave modes are well defined (normally there aren't intersections between the different propagating modes) and in the case of relatively simple structures. Increasing the frequency and/or the complexity of the structures, numerical models and approaches become more and more important. Some application of the WFEM method in the estimation of the dispersion curves for flat and curved structures can be found in [99, 129, 130]. Chronopoulos et al. [6, 7, 15] estimated the vibro-acoustic properties of complex composite sandwich structures deriving a dynamic stiffness matrix based approach.

This chapter is structured as follows: a short recall of the IWC method in section 3.2; calculation of the angle-dependent dispersion curves on a simple isotropic panel and on an orthotropic plate is presented in section 3.3. In section 3.4 the IWC method is applied to two sandwich panels with different spacing values between the mechanical links: numerical and experimental investigations are conducted. Some concluding remarks are presented in section 3.5.

3.2 Overview of the IWC method

In this section, an overview of the Inhomogeneous Wave Correlation method is presented, based on what described in section 1.2.3. The IWC method estimates the damping information of a vibrating structure and the angle-dependent dispersion curves for orthotropic plane structures. The idea is to correlate the total energy of a vibrating structure and the energy carried by an inhomogeneous damped plane wave, traveling with a incidence angle θ . The inhomogeneous wave is expressed in Eq. (1.26):

$$\hat{\sigma}_{k,\gamma,\theta}(x, y) = e^{-ik(\theta)(1+i\gamma(\theta))((x-x_0)\cos\theta+(y-y_0)\sin\theta)}.$$

For a fixed frequency f_0 , the correlation between the inhomogeneous wave expressed in Eq. (1.26) and the complete wave field is calculated by Eq. (1.22):

$$\text{IWC}(k, \gamma, \theta) = \frac{|\iint_S \hat{w} \cdot \hat{\sigma}_{k,\gamma,\theta}^* dx dy|}{\sqrt{\iint_S |\hat{w}|^2 dx dy \cdot \iint_S |\hat{\sigma}_{k,\gamma,\theta}|^2 dx dy}}.$$

Moving from the continuous domain to the discrete one, the integrals in Eq. (1.22) become sums, as expressed in Eq. (1.24):

$$\text{IWC}(k, \gamma, \theta) = \frac{|\sum_{i=1}^N \hat{w}(x_i, y_i) \cdot \hat{\sigma}_{k,\gamma,\theta}^*(x_i, y_i) \rho_i S_i|}{\sqrt{\sum_{i=1}^N |\hat{w}(x_i, y_i)|^2 \rho_i S_i \cdot \sum_{i=1}^N |\hat{\sigma}_{k,\gamma,\theta}(x_i, y_i)|^2 \rho_i S_i}}.$$

The harmonic displacement field of the vibrating structures is introduced in Eq. (1.24) to extract the propagating wavenumber at each frequency and for a fixed propagation angle θ .

3.3 Numerical investigation of homogeneous panels

The IWC method is firstly applied to two homogeneous structures: an isotropic and orthotropic panels. The angle-dependent dispersion curves are numerically estimated

and compared, for some specific frequencies, with the Fourier-based methods results (see section 1.2.1 for the theoretic background).

3.3.1 Isotropic panels

An isotropic homogeneous panel is firstly investigated. The panel dimensions are $1.0\text{ m} \times 1.0\text{ m}$ and thickness $h = 0.001\text{ m}$. The employed material is a standard aluminum alloy, with the following material properties: Young's modulus $E = 70.0\text{ GPa}$, density $\rho = 2700.0\text{ kg m}^{-3}$ and Poisson's coefficient $\nu = 0.33$; a constant value of structural damping $\eta = 1\%$ is introduced in the model. The FE model of the considered structure is shown in Fig. 3.1. A punctual harmonic unit force is applied in the middle of the panel, as shown in Fig. 3.1. The FE analysis is conducted at three different frequencies: 500 Hz, 700 Hz and 1100 Hz. The IWC method is computed with a heading angle varying in the range $[0\text{ deg} - 360\text{ deg}]$, with a resolution of 5 deg.

For each frequency value, the IWC method is computed on a set of discrete values of the angle θ (heading angle of the inhomogeneous wave, see Eq. (1.26)), obtaining the complete θ -dependent dispersion relation. The results are shown in Fig. 3.2; in the polar plots (see Fig. 3.2a, 3.2c and 3.2e), the IWC results are compared with the Kirchhoff's thin plate theory (see Eq. (2.10)), showing a good agreement for the three considered frequencies and for all the heading angles. The IWC results are then compared to the FFT analysis; in Fig. 3.2b, 3.2d and 3.2f the IWC correctly estimates the dominant wavenumber in each direction.

The same isotropic panel made of ABS and described in section 2.4.1 is also analyzed in this section. Using the symmetry and isotropy properties, the angle-dependent dispersion curves are analyzed in one-fourth of the circle. In particular, the dispersion curves are estimated using the following values for the heading angle of the inhomogeneous wave: $[0, 30, 45, 60, 90\text{ deg}]$. A punctual harmonic force is applied to the structure, as shown in Fig. 3.1; the excitation is applied in the frequency range $[50\text{ Hz} - 3000\text{ Hz}]$, with a frequency step of 10 Hz.

The dispersion curves are shown in Fig. 3.3a; a superposition of the curves was expected and obtained, due to the isotropic material. The damping loss factor is also calculated using Eq. (1.86), based on the estimated complex wavenumbers. In this case, a perfect agreement is observed in Fig. 3.3b, estimating the same damping coefficient in each considered direction.

3.3.2 Orthotropic panel

An orthotropic panel is analysed in this section. The panel dimensions are $1.0\text{ m} \times 0.6\text{ m}$ and thickness $h = 0.01\text{ m}$. The employed material has properties: Young's moduli $E_x = 1.0\text{ GPa}$ and $E_y = 0.5\text{ GPa}$, density $\rho = 980.0\text{ kg m}^{-3}$ and Poisson's coefficient $\nu = 0.35$; a constant value of structural damping $\eta = 5\%$ is introduced in the model. The FE model is built using solid structural elements (ANSYS SOLID45) in order to have a sufficient number of elements in the thickness direction; a total number of 30000 elements is used for the FE model, resulting in 221796 degrees of freedom. A punctual harmonic unit force is applied in the middle of the panel, as shown in Fig. 3.4. The FE analysis is conducted in the frequency range $[50\text{ Hz} - 5000\text{ Hz}]$, with a frequency step

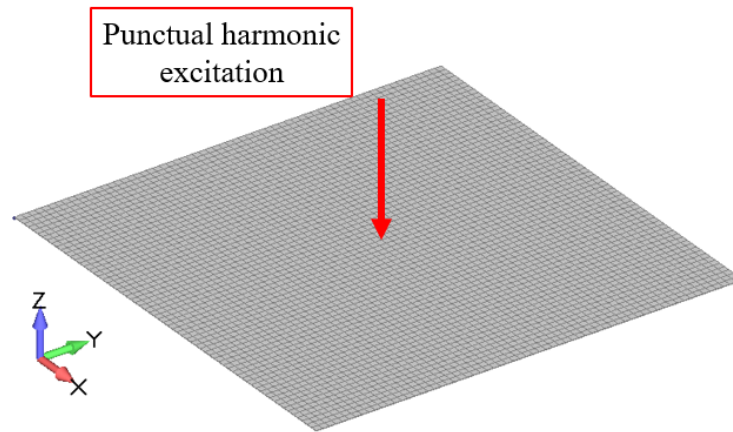


Figure 3.1 – FE model of the isotropic panel with the punctual harmonic excitation.

of 10 Hz. Two different values of the heading angles are chosen in this case: $\theta = 0$ deg and $\theta = 90$ deg.

The estimations of the dispersion curves and of the damping loss factor are shown in Fig. 3.5. Both quantities are calculated in the two orthogonal directions, as shown in Fig. 3.4. The propagative part of the dispersion curves is shown in Fig. 3.5a, in which a comparison with the WFE method is presented. The IWC results are in agreement with the WFEM estimations, highlighting the orthotropic behavior of the panel. The damping loss factor estimations are slightly different in the two directions, but they asymptotically converge to the value of structural damping introduced in the FE model.

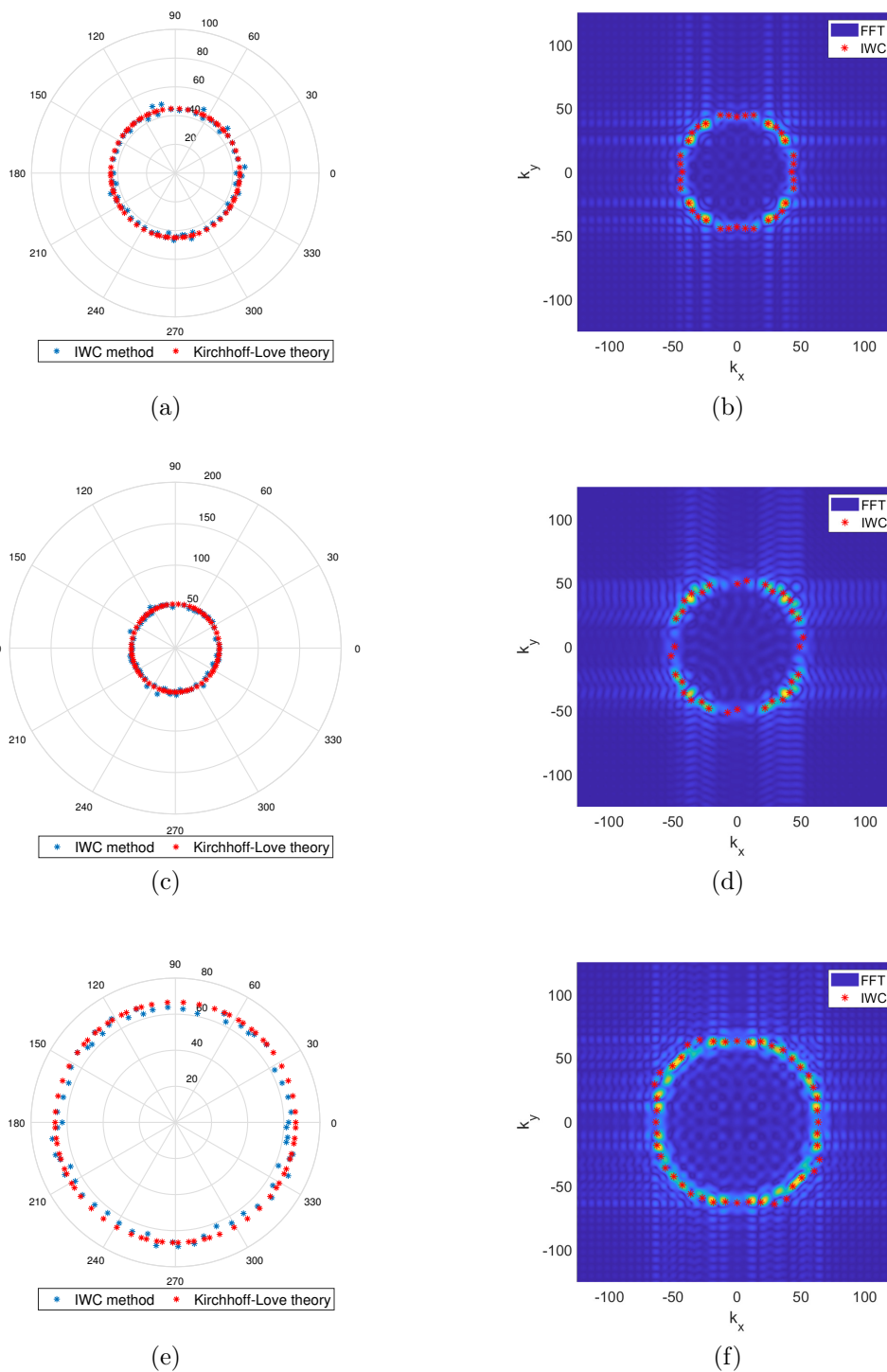


Figure 3.2 – Angle-dependent dispersion curves for the isotropic panel. Comparison with the Kirchhoff’s theory and the FFT at three different frequencies: at 500 Hz (a-b), at 700 Hz (c-d) and at 1100 Hz (e-f).

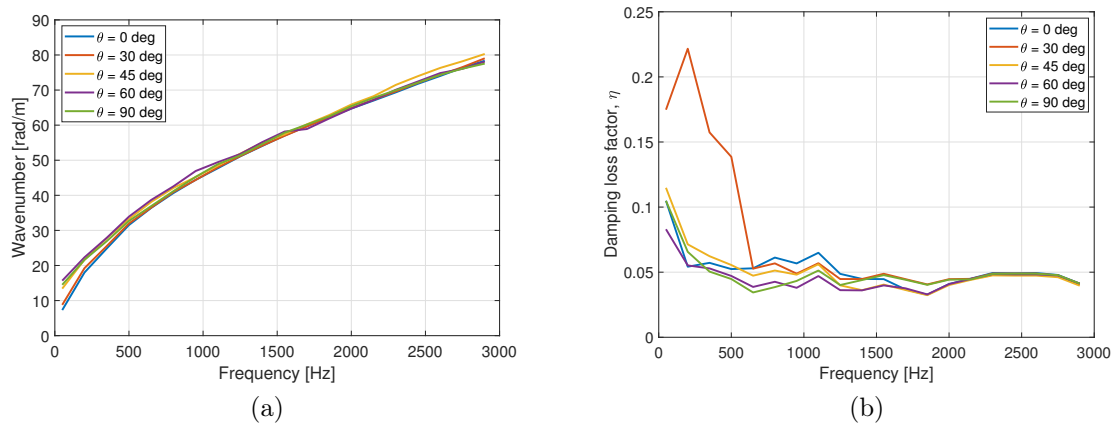


Figure 3.3 – Isotropic panel: angle-dependent dispersion curves (a) and damping loss factor estimation (b).

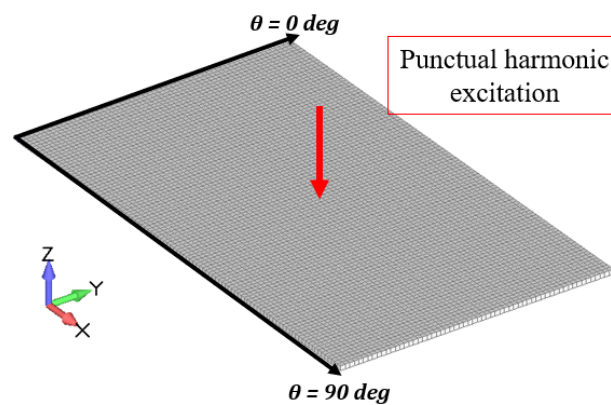


Figure 3.4 – FE model of the orthotropic panel with the punctual harmonic excitation.

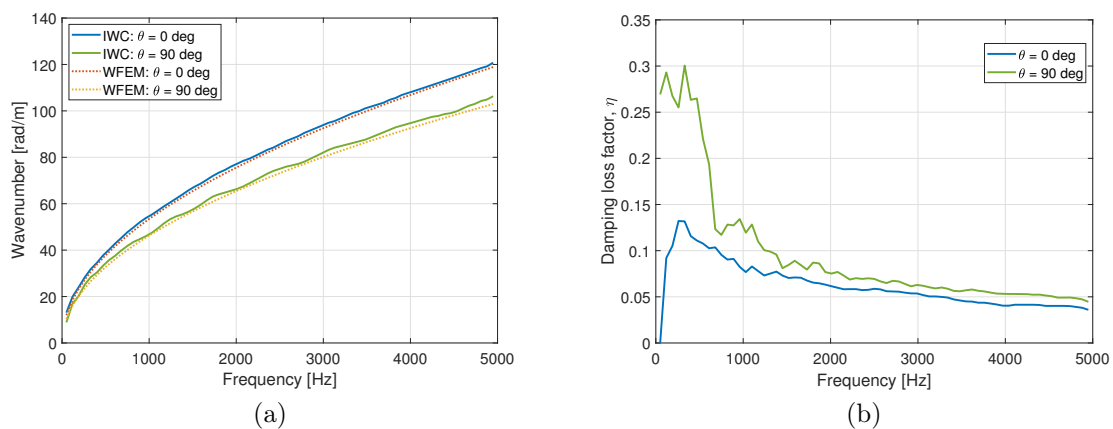


Figure 3.5 – Orthotropic panel: angle-dependent dispersion curves (a) and damping loss factor estimation (b).

3.4 Orthotropic sandwich panels

This section is devoted to numerical simulations and experimental validations of two sandwich panels, constituted by two skins separated by vertical mechanical links; two different inter-spacings between the mechanical links are considered: 1.0 cm and 2.0 cm. The first panel only is experimentally tested.

3.4.1 Double-wall panel with 1 cm of inter-spacing: numerical results and experimental validation

For what concerns the first panel, the FE models of the full-size panel and of the periodic unit cell are shown in Fig. 3.6. The panel has dimensions $0.40\text{ m} \times 0.35\text{ m}$ and thickness $h = 0.0106\text{ m}$; the thickness of both skins and vertical links is 0.6 mm. The FE model is built using shell structural elements (ANSYS SHELL181); a total number of 19200 elements is used, resulting in 98172 degrees of freedom. The employed material is the ABS already described in the previous sections (Young's modulus $E = 1.0\text{ GPa}$, density $\rho = 980.0\text{ kg m}^{-3}$ and Poisson's coefficient $\nu = 0.35$). The panel is 3D-printed using a Stratasys *Fortus 450mc* industrial 3D printer which has a maximum printable volume of $40 \times 35 \times 40\text{ cm}^3$. The 3D-printed panel is shown in Fig. 3.7.

The 3D-printed panel has been experimentally investigated under mechanical excitation. To simulate free boundary conditions, the panel was freely suspended using Polylactic Acid filaments, as shown in Fig. 3.8b. The panel was excited by a point mechanical force using a Brüel & Kjær shaker attached to the structure using an impedance head. The out of plane vibrational field was acquired using a Polytec PSV-500 Scanning Vibrometer. An acquisition window of $0.36\text{ m} \times 0.31\text{ m}$ was scanned, using a mesh of 19×17 along length and width, respectively, with a total number of 323 acquisition points. To acquire the vibrational field by the Laser Doppler Velocimeter, some stripes of reflective tape were attached on the external surface of the 3D-printed panel (see Fig. 3.8). The shaker was mounted on the rear surface while the front one was scanned by the Laser Doppler Velocimeter. The excitation was generated using a white noise signal from 10 Hz to 2000 Hz. The acquisition was made with a frequency resolution of 0.625 Hz, resulting in 3185 acquisition frequencies; for each measured point, the signal was averaged over 10 acquisitions.

The considered panel is also numerically investigated. A punctual harmonic unit force is applied to the panel, as shown in Fig. 3.6. The FE analysis is conducted in the frequency range [10 Hz - 2000 Hz], with a frequency step of 5 Hz. The IWC method is applied on a set of discrete values of the heading angle θ , with a resolution of 5 deg. For a fixed frequency, the IWC results are compared to the one obtained using the FFT method, as shown in Fig. 3.9. For each considered angle of propagation of the inhomogeneous wave, the IWC correlation functions are plotted considering not only the dominant wavenumber but also the local maxima, obtaining a full k -space description, as shown in Fig. 3.9b. The orthotropic property is highlighted in the k -space plot, as shown in Fig. 3.9c, in which an elliptic-shaped plot is obtained.

The comparison between numerical and experimental dispersion curves is shown in Fig. 3.10. The dispersion curves are calculated along two orthogonal directions: $\theta = 0\text{ deg}$ and $\theta = 90\text{ deg}$; the magnitude of the estimated wavenumbers is strongly different in

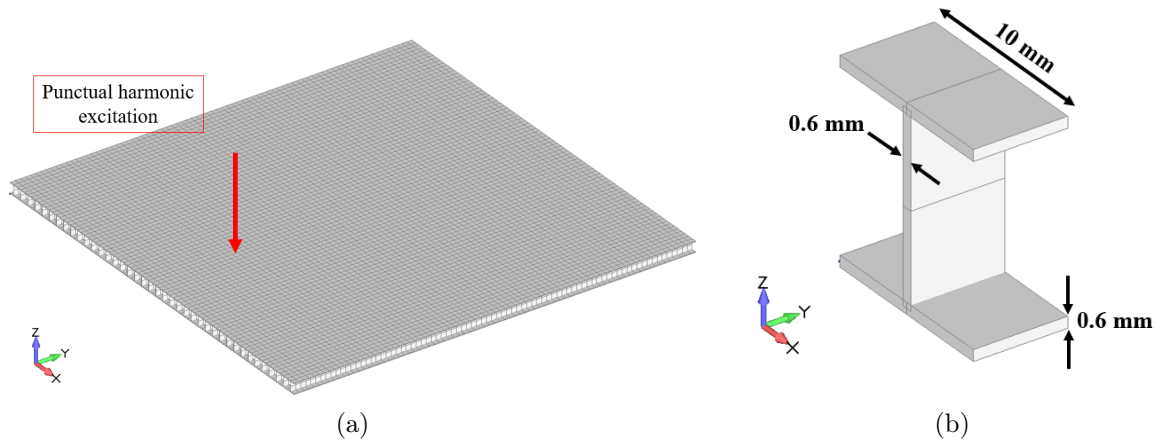


Figure 3.6 – Double-wall panel with 1.0 cm of inter-spacing between the mechanical links: full view (a) and periodic unit cell (b).

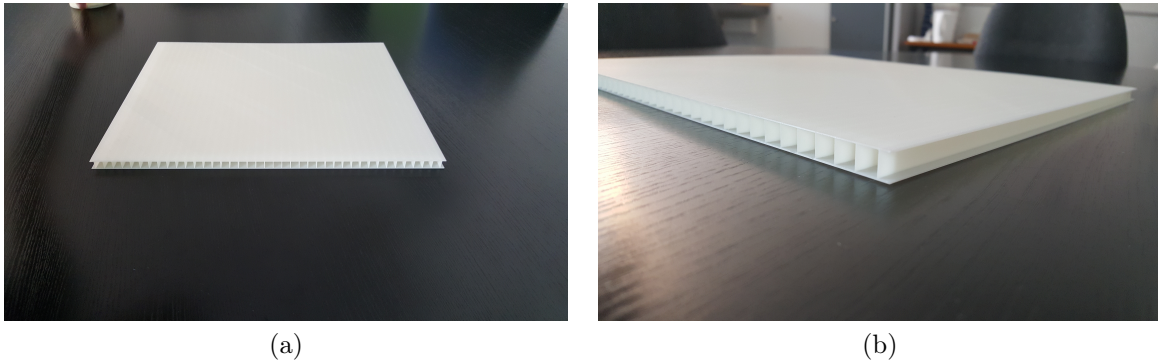


Figure 3.7 – 3D-printed sandwich panel: full-size (a) and close up (b) views.

the two considered directions, in agreement with the orthotropic behavior. The global behavior of the panel in the x direction is dominated by the bending motion of the skins and it is representative of an apparent softness of the structure (higher wavenumber amplitude). When the dispersion curve is evaluated in the stiffeners direction (y direction in this case), the global behavior is dominated by the bending motion of the stiffeners; there is an apparent increase of the stiffness of the structure, characterized by a lower amplitude of the estimated wavenumbers (see Fig. 3.10).

3.4.2 Double-wall panel with 2 cm of inter-spacing: numerical investigation

In this section, a double-wall panel with 2 cm of inter-spacing between the mechanical links is numerically investigated. This stiffeners pitch is chosen in order to open a geometric periodicity related band-gap in the frequency range [10 Hz - 2000 Hz]. The panel dimensions are $0.40 \text{ m} \times 0.35 \text{ m}$ and thickness $h = 0.0106 \text{ m}$; the thickness of both skins and vertical links is 0.6 mm. The FE model is built using shell structural elements (ANSYS SHELL181); a total number of 14000 elements is used, resulting in 77532 degrees of freedom. The employed material is the ABS already described in the previous sections (Young's modulus $E = 1.0 \text{ GPa}$, density $\rho = 980.0 \text{ kg m}^{-3}$ and

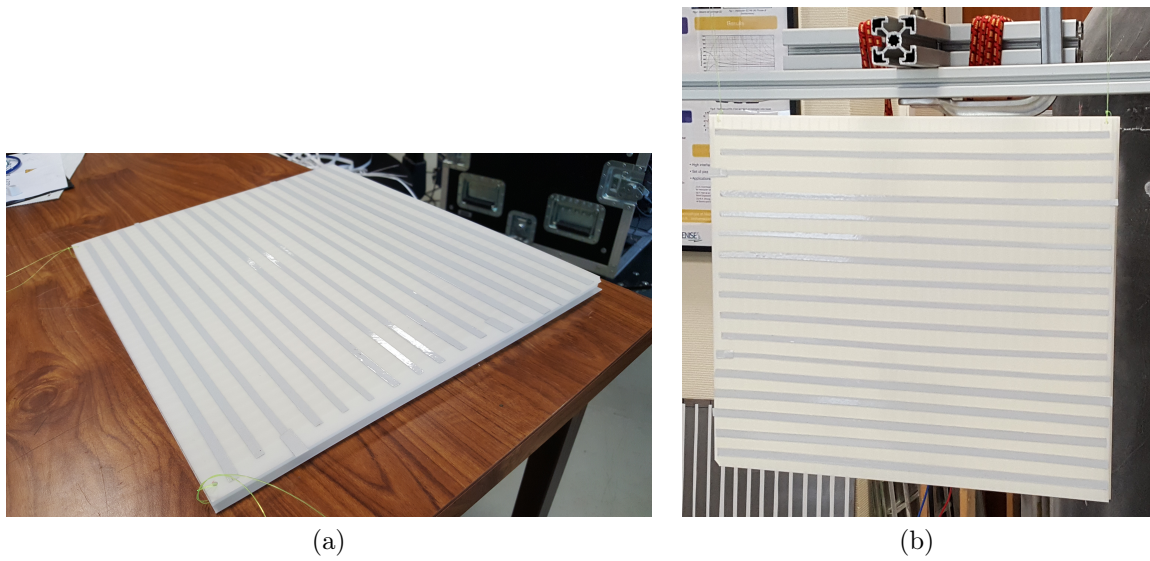


Figure 3.8 – 3D-printed sandwich panel: reflective tape (a) and installation for shaker excitation (b).

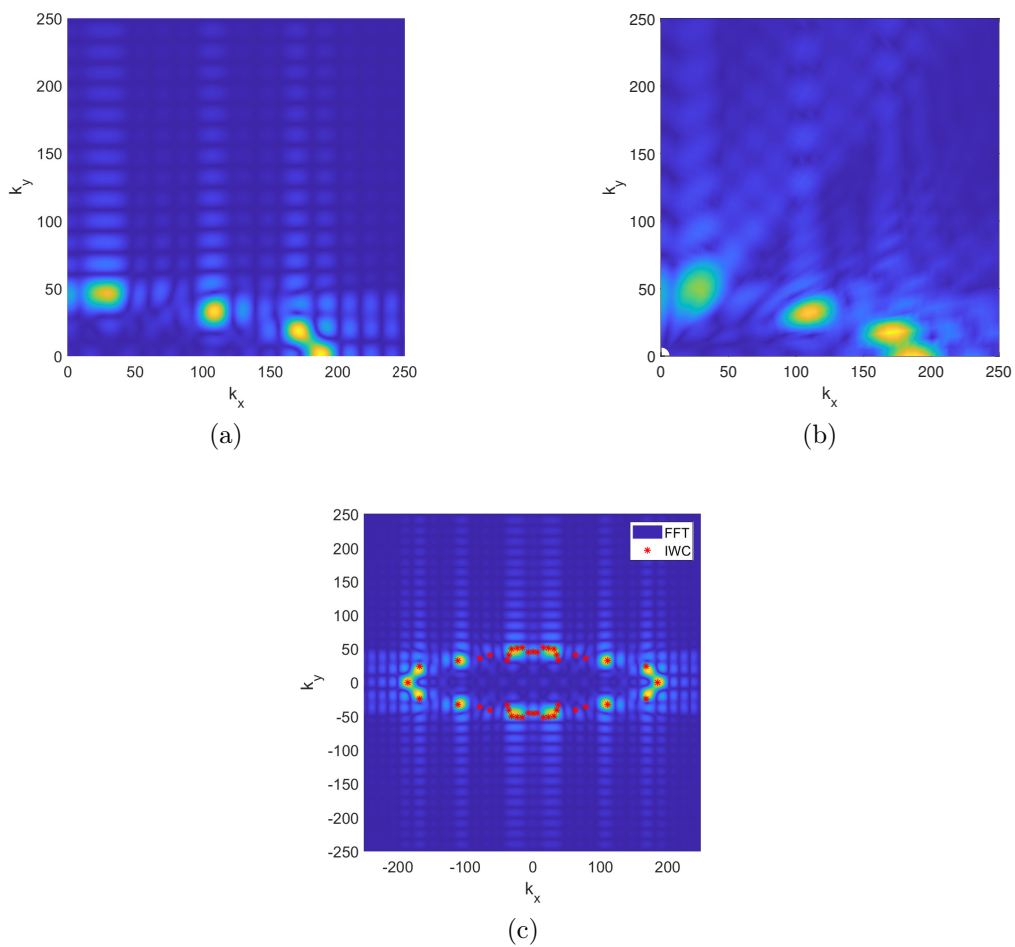


Figure 3.9 – Double-wall panel with 1.0 cm of inter-spacing. K-space obtained using the FFT (a) and the IWC (b) methods, and angle-dependent wavenumbers (c) at 1500 Hz.

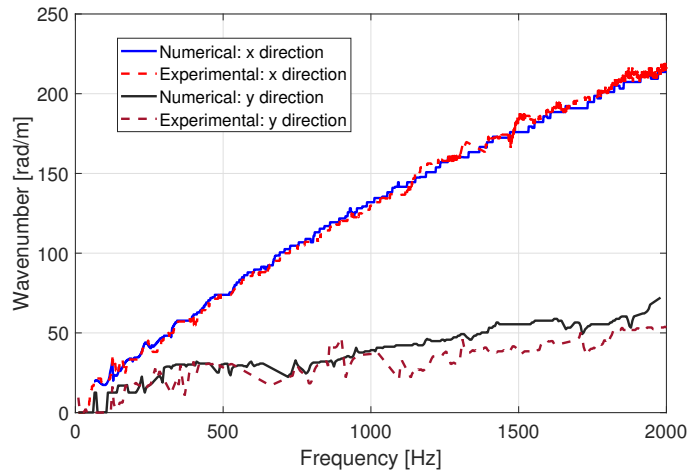


Figure 3.10 – Numerical-experimental dispersion curves of the double-wall panel with 1.0 cm of inter-spacing between the mechanical links.

Poisson’s coefficient $\nu = 0.35$). The FE models of both full-size panel and periodic unit cell are shown in Fig. 3.11.

A punctual harmonic unit force is applied to the panel, as shown in Fig. 3.11. The FE analysis is conducted in the frequency range [10 Hz - 2000 Hz], with a frequency step of 5 Hz.

The dispersion curves are calculated along two orthogonal directions: $\theta = 0$ deg and $\theta = 90$ deg; the magnitude of the estimated wavenumbers is strongly different in the two considered directions, in agreement with the orthotropic behavior. The global behavior of the panel in the x direction is dominated by the bending motion of the skins and it is representative of an apparent softness of the structure (higher wavenumber amplitude). When the dispersion curve is evaluated in the stiffeners direction (z direction in this case), the global behavior is dominated by the bending motion of the stiffeners; there is an apparent increase of the stiffness of the structure, characterized by a lower amplitude of the estimated wavenumbers (see Fig. 3.12).

Evaluating the dispersion curve in the x direction, the periodic distribution of stiffeners opens a band-gap width of approximatively 400 Hz, starting from 760 Hz. The band-gap opens when the wavenumber assumes the value $k = \pi/\Delta$, where Δ is the length of the unit cell (or, in other words, the distance between two scatterers); when this condition is reached, the scattered waves interfere destructively.

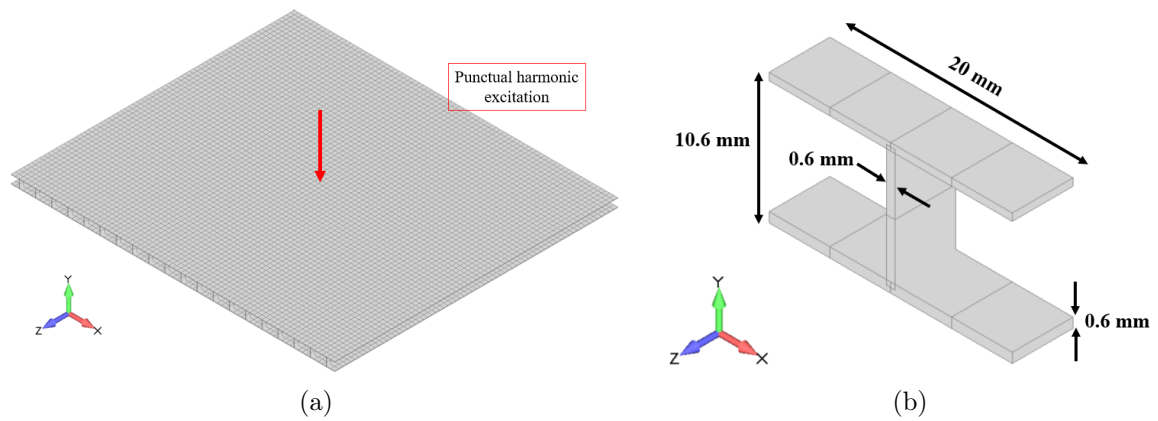


Figure 3.11 – Double-wall panel with 2.0 cm of inter-spacing between the mechanical links: full view (a) and periodic unit cell (b).

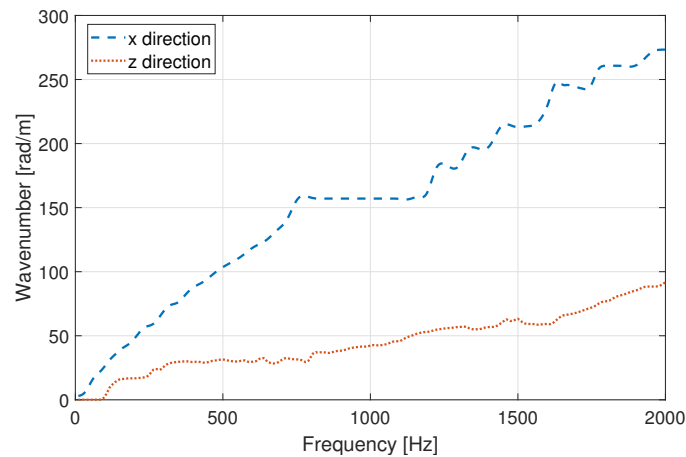


Figure 3.12 – Numerical dispersion curves of the double-wall panel with 2.0 cm of inter-spacing between the mechanical links.

3.5 Concluding remarks

In this chapter, the IWC method is successfully implemented to obtain the angle-dependent dispersion curves. The orthotropic behavior is described in both dispersion curves and k -space plots at fixed frequencies. The estimated complex wavenumber allows also to estimate the damping loss factor for both isotropic and orthotropic structures.

The proposed approach allows to identify the resonance zones (stop-bands) due to the geometrical periodicity of the structure, including the apparent stiffening or softening behavior of the structures in presence of mechanical stiffeners.

The numerical results are experimentally validated using a 3D-printed sandwich panel. A good agreement between the numerical simulation and the experimental results is observed in the whole frequency range and for the two orthogonal directions of wave propagation.

Part II

Large-scale meta-structures and stiffened shells

Chapter 4

K-space analysis of complex large-scale meta-structures

This chapter is mainly based on "G. Tufano, F. Errico, O. Robin, C. Droz, M. Ichchou, B. Pluymers, W. Desmet and N. Atalla, *K-space analysis of complex large-scale meta-structures using the Inhomogeneous Wave Correlation method*, Mechanical System and Signal Processing 135, 106407, 2020".

Abstract

A new formulation of the Inhomogeneous Wave Correlation method for curved structures is developed in this chapter and it is used to characterize the vibration behavior of three structures and meta-structures with different complexity levels: a plane steel panel, a curved thick composite sandwich shell and a stiffened aluminum aircraft sidewall panel. Bare structures are first studied and then equipped with spatially distributed small-scale resonators, leading to meta-structures. For the two curved panels, tests are conducted under diffuse acoustic field and point mechanical excitations.

For each studied case, the effect of the industrially-oriented small-scale resonators is highlighted using frequency and wavenumber analysis, showing general attenuation of the vibration level and even band-gaps occurrence. The complex wavenumber identification allows also estimating the structural loss factor in the composite sandwich panel, while the multi-modal behavior is captured in the aluminum aircraft sidewall panel.

4.1 Introduction

In the aerospace sector, curved shells and axial-symmetric structures are widely used. The presence of stringers and frames in the longitudinal and circumferential directions of aircraft fuselages lets assume a certain degree of structural periodicity which, if properly designed, can give some advantages in the vibroacoustic response.

Composite materials are more and more used in this sector, to fulfill the requirements of reduced structural weight and high mechanical performances. The anisotropic behavior and the complexity related to their composite nature make the development of an analytical theory or of a predictive model very hard to obtain. The vibro-acoustic

response and the dynamical behavior of laminated composite sandwich shells are of fundamental relevance for the industry. The identification of the energy propagation, of the wave attenuation, with the related damping informations, and of the wave dispersion characteristics are relevant aspects to fully describe the vibro-acoustic behavior of a system [1].

Some semi-analytical approaches have been developed in order to estimate the mechanical properties of sandwich composite structures [2, 6, 7, 10]. These formulations are limited to the low-frequency domain, in which the wave modes are well defined; in the mid-high-frequency range, classical analytical approaches do not give a good estimation of the waves dispersion characteristics, due to an high wave modes density. As alternatives, in a wave propagation framework, for the parameter identification other methods based on the wavenumber domain (k -space) analysis [8, 9, 11, 12] or based on the Statistical Energy Analysis (SEA) [13–15] are introduced.

Some applications of the Prony's method for the wavenumber analysis of one- and two-dimensional structures have been proposed [131?]. The Prony's technique is a mean of identifying the constituent complex wavenumbers and their corresponding amplitudes in an exponential model of the spatial response. It is a two-step process: the wavenumbers are first found and the amplitudes for these wavenumbers are then obtained from a linear least-squares fit of the model to the data. A modified extended technique based on Prony's method to estimate the complex wavenumbers is shown in Grosh et al. [16]. Ferguson et al. [132] proposed a technique to identify the dominant wavenumber in a considered area, using a windowed field of the displacement of the structure, computing the correlation between the normal velocities measurement and a harmonic wave-field. An algorithm for the identification of the complex wavenumber and of the damping loss factor was developed by Berthaut et al. [11, 12, 19]; the proposed method is called Inhomogeneous Wave Correlation (IWC) method and it allows to identify the complex flexural wavenumber in a large frequency range.

In order to increase the wave attenuation in certain frequency bands and to generate some band-gaps, periodic adds-on and locally resonant devices are widely used. The effect of wave propagation in rib-stiffened plate structures is investigated in [19, 133], showing the multi-modal behavior in the wavenumber domain, in terms of uncoupled plate and stringer flexural wavenumbers. A vibroacoustic study of a fluid-loaded ribbed plate is shown by Maxit [134], in which the response is investigated in the wavenumber domain using a discrete Fourier Transform based approach. A numerical investigation of the IWC method on curved shells and axial-symmetric structures is presented in [135], showing a good prediction of the angle-dependent wavenumber at different excitation frequencies and compared with the Discrete Fourier Transform technique. For what concerns the stop-band behavior of tuned resonators, Claeys et al. [136, 137] have demonstrated their potential use to reduce the vibrational response of panels, spatially distributing them over the panel surface. An application of the IWC method on a meta-material plate with distributed resonators is given by Van Belle et al. [24].

An experimental investigation on the vibro-acoustic response of cylindrical shells is presented in Williams et al. [138], in which the dominant wavenumbers are identified in the regions close to the natural frequencies of the structure. An analysis in the wavenumber domain is conducted in Photiadis et al. [139] to investigate the acoustic

response of a ribbed shell, demonstrating the dominant flexural behavior in the mid-frequency range. Photiadis et al. [140] investigated the effect of distributed internal oscillators on the acoustic response of a complex ribbed shell, showing their influence in the wavenumber domain compared to the bare configuration. The effect of the internal frames on the vibro-acoustic response of an aluminum cylinder is performed by Meyer et al. [141], providing a better understanding of frames influence in the wavenumber domain and on the dispersion curves, mainly based on the numbers and the spatial distribution of the internal frames.

Nateghi et al. [142, 143] have discussed and experimentally validated that by adding locally resonating structures to cylindrically curved panels and pipes, improved noise and vibration behavior can be obtained in a targeted and tunable frequency band. This concept was applied on an aircraft sidewall panel by Droz et al. [144], improving the acoustic properties of the panel in the ring frequency region, showing how a smart design of meta-material structures can be adopted to improve the vibro-acoustic performance.

This work is fully devoted to the experimental identification of the dispersion characteristics of these complex structures, subjected to either a diffuse acoustic field or point mechanical excitations. Each considered structure is first tested alone, and then with the addition of spatially-distributed small-scale resonators. The method used in this work is an extended version of the IWC method, capturing the effect of the local dynamics of the resonators and applied under diffuse acoustic excitation, in presence of periodic adds-on. The main advantages of this method are the possibility to investigate both flat and curved structures, the identification of the resonator-related band-gaps and the use of the experimental measured data, without any restriction related to an ordered mesh-grid for the acquisition points.

In section 4.2, an overview of the IWC method is presented and an extended formulation to take in account the curvature effect is developed. The experimental set-up for each studied case is fully described in section 4.3, showing how the experimental tests were performed and giving information about the tuning frequencies of the resonators. Section 4.4 is fully devoted to the result discussion; an isotropic steel panel is first considered, then all the results concerning the curved structures are discussed. A numerical simulation of an isotropic curved panel is performed to validate the feasibility of the proposed IWC formulation for curved structures, followed by experimental results on the two considered curved structures for tests.

4.2 *Inhomogeneous Wave Correlation* method for curved structures

The *Inhomogeneous Wave Correlation* (IWC) method here proposed is extended to complex curved structures in presence of periodic elements and small-scale resonators. The aim of this approach is the complete description of the angle-dependent dispersion characteristics and the identification of the structural damping information of a vibrating structure, using the whole wave field of a vibrating structure as primary input. The basic idea of the approach is the same of the classical IWC method presented in section 1.2.3; this method estimates the complex wavenumber by maximization of

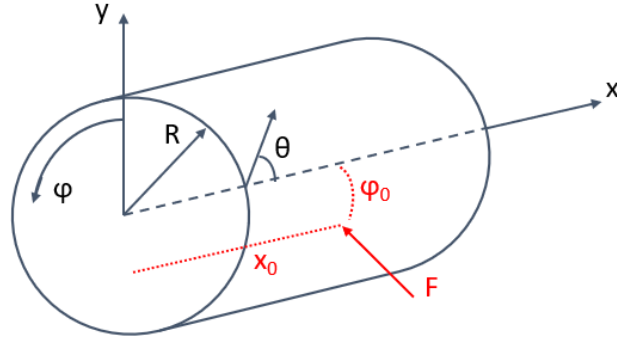


Figure 4.1 – Curved structure coordinates system.

the correlation function between the energy carried on by an inhomogeneous traveling wave and the total energy of the vibrational field.

Based on what is described in section 1.2.3, a new formulation for curved structures can be derived, which takes in account the curvature effect in the IWC formulation. The two components of the plane wave-vector are defined as:

$$k_x = k \cos \theta, \quad (4.1a)$$

$$k_y = k \sin \theta. \quad (4.1b)$$

From the notations and the coordinate system shown in Fig. 4.1, identifying with R the curvature radius of the structure and with φ the angular coordinate, the following relationships can be derived:

$$y = R \sin \varphi \approx R\varphi \quad \text{and} \quad k_\varphi = Rk_y, \quad (4.2)$$

where a small value of the angle φ is assumed (this value strictly depends on the discretization resolution) and k_φ is the circumferential component of the wave-vector, which is related to the k_y component by Eq. (4.2). The classical two-dimensional damped plane wave expressed in Eq. (1.26):

$$\hat{\sigma}_{k,\gamma,\theta}(x, y) = e^{-ik(\theta)(1+i\gamma(\theta))((x-x_0) \cos \theta + (y-y_0) \sin \theta)},$$

becomes a damped helical plane wave, which assumes the following form:

$$\tilde{w}_{k_{\mathbb{C}},\theta}(x, \varphi) = e^{-ik_{\mathbb{C}}(\theta)((x-x_0) \cos \theta + (\varphi-\varphi_0) \sin \theta)}. \quad (4.3)$$

where φ_0 is the angular position of the excitation point and $k_{\mathbb{C}} = k_{\mathbb{R}e} + ik_{\mathbb{I}m}$ is the complex wavenumber, which contains both propagation and attenuation informations.

Moving from the Cartesian coordinate system to the curved one (see Fig. 4.1), the correlation function of Eq. (1.24):

$$\text{IWC}(k, \gamma, \theta) = \frac{|\sum_{i=1}^N \hat{w}(x_i, y_i) \cdot \hat{\sigma}_{k,\gamma,\theta}^*(x_i, y_i) \rho_i S_i|}{\sqrt{\sum_{i=1}^N |\hat{w}(x_i, y_i)|^2 \rho_i S_i \cdot \sum_{i=1}^N |\hat{\sigma}_{k,\gamma,\theta}(x_i, y_i)|^2 \rho_i S_i}},$$

is modified as follows:

$$\mathcal{I}(k_{\mathbb{C}}, \theta) = \frac{|\sum_{j=1}^N \hat{w}(x_j, \varphi_j) \cdot \tilde{w}_{k_{\mathbb{C}}, \theta}^*(x_j, \varphi_j) h_j \Omega_j|}{\sqrt{\sum_{j=1}^N |\hat{w}(x_j, \varphi_j)|^2 h_j \Omega_j \cdot \sum_{j=1}^N |\tilde{w}_{k_{\mathbb{C}}, \theta}(x_j, \varphi_j)|^2 h_j \Omega_j}}, \quad (4.4)$$

where h_j is the coherence of the measured signal at each point, Ω_j is an estimation of the surface around point j and N is the total number of acquisition points.

The location of the maximum of the correlation function $\mathcal{I}(k_{\mathbb{C}}, \theta)$ gives the identified complex wavenumber in the specified direction. When the structure is complex, the correlation function could be characterized by an absolute maximum and some other local maxima, denoting the presence of different bending wave modes propagating at the same time. Following the evolution of the local maxima, the multi-modal behavior of the structure can be described, as shown in section 4.4.4.

4.3 Experimental sets-up

Three different structures have been experimentally investigated: an isotropic steel flat panel, a thick curved composite laminated sandwich panel and a thin aluminum aircraft sidewall panel, including frames and stringers (see Fig. 4.2). The considered structures are analyzed in the bare test case configuration and then with periodically distributed resonators. The structures have been analyzed under Diffuse Acoustic Field (DAF) and punctual mechanical excitations, as shown in Table 4.1. The concept of the resonators and their feasibility in reducing the bending wavenumber was demonstrated in [145]. The same concept was used in [144], in which they were also tested on the aluminum aircraft sidewall panel considered in the present work, with the aim of improving the sound insulation properties of the considered structure.

The single resonator is schematically represented in Fig. 4.3; the resonators are 3D-printed using polycarbonate polymer. The shape is similar to a cantilever beam, with a rectangular prismatic base of dimensions $10 \times 10 \times 8.0 \text{ mm}^3$ on which the beam and the stiffener are connected; the resonator main beam has dimensions $23 \times 10 \times 4 \text{ mm}^3$ and the stiffener element has section of $4 \times 3.5 \text{ mm}$. The resonator has a total dimensions of $33 \times 10 \times 8.0 \text{ mm}^3$ and a unit weight of 2.72 g. A magnet is glued on the opposite tip end, with the possibility to tune it by adding or removing neodymium magnets of known masses. A schematic representation of the resonator and its application on the host structure are shown in Fig. 4.3. A periodic distribution of the resonators on the surface of the structures is chosen to avoid any local and/or directional effect.

Table 4.1 – Experimentally tested configurations.

| | Bare | | Bare + resonators | |
|-----------------|--------|-----|-------------------|-----|
| | Shaker | DAF | Shaker | DAF |
| Steel panel | ✓ | × | ✓ | × |
| Composite shell | ✓ | ✓ | ✓ | ✓ |
| Aluminum shell | ✓ | ✓ | × | ✓ |

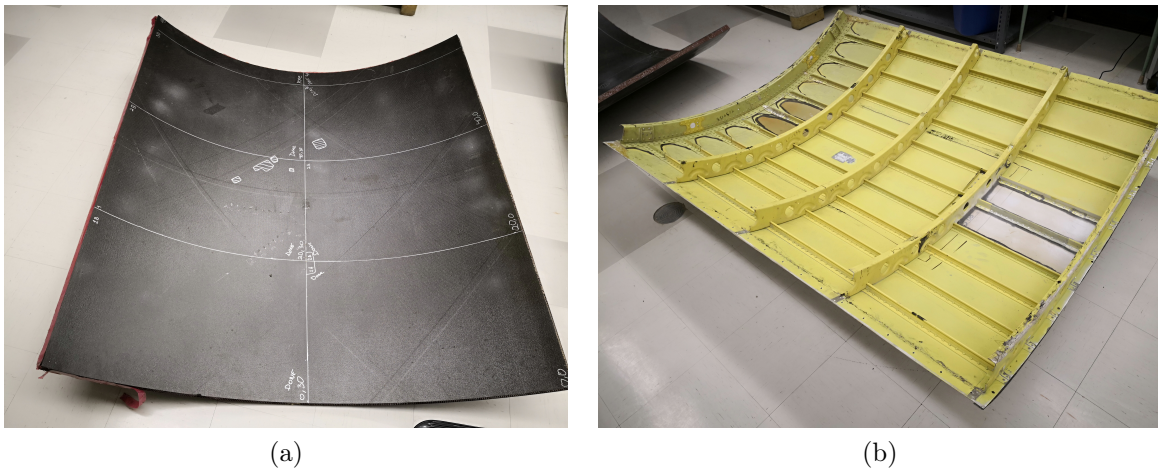


Figure 4.2 – Large-scale curved structures: composite sandwich honeycomb shell (a) and aluminum aircraft sidewall panel (b).

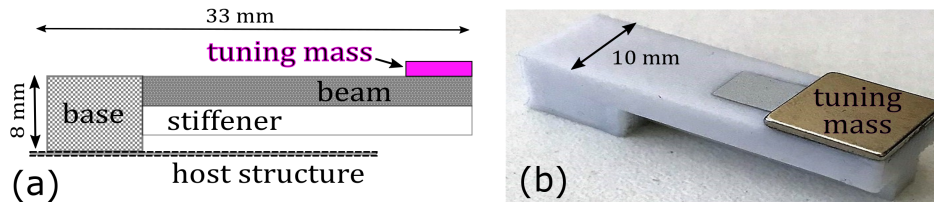


Figure 4.3 – Schematic representation of the resonator (a) and its application on the host structure (b).

4.3.1 Isotropic plate

An isotropic steel plate of dimensions $0.95\text{ m} \times 0.60\text{ m}$ and thickness of 2.0 mm is considered. The host structure has a total weight of 9.0 kg , approximatively. To simulate free boundary conditions, the structure was suspended at three points along the longer edge using Polylactic Acid filaments. The plate was excited by a point mechanical force using a Brüel & Kjær shaker attached to the host structure using an impedance head (see Fig. 4.4). The out of plane vibrational field was acquired using a Polytec PSV-500 Scanning Vibrometer. An acquisition window of $0.92\text{ m} \times 0.56\text{ m}$ was scanned, using a mesh of 60×24 along length and width, respectively, with a total number of 1440 acquisition points (see Fig. 4.4b). The bare structure was first tested, and then the effect of distributed resonators tuned at frequencies of 800 Hz and 1400 Hz were successively tested. The resonator working frequency being adjusted with varying tuning masses, the added weight was different for the two considered frequencies. For the first one (800 Hz), the added weight from the resonators represented 2.5% of the total panel weight, while for the second one (1400 Hz), the panel weight was increased by 1.5% .

The shaker and the resonators were mounted on the rear surface of the host structure while the front one was scanned by the Laser Doppler Velocimeter system. The excitation was generated using a white noise signal from 100 Hz to 2000 Hz . The acquisition was made with a frequency resolution of 1.25 Hz , resulting in 1521 acquisition frequencies; for each measured point, the signal was averaged over 10 acquisitions. A representation of the distributed resonators and a picture of the experimental set-up is

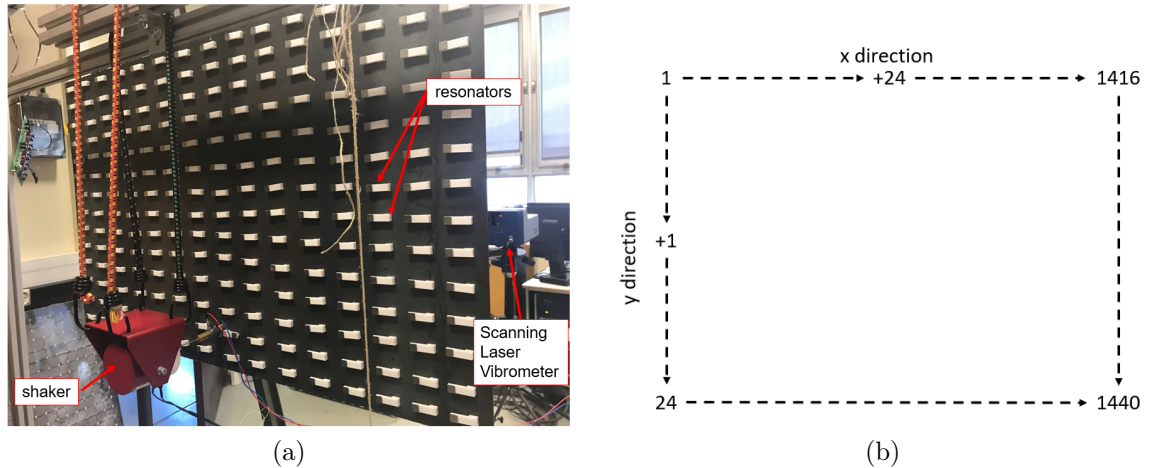


Figure 4.4 – Set-up of the steel plate with distributed resonators (a) and acquisition window (b).

Table 4.2 – Material properties of the curved composite sandwich panel.

| | Laminated skins | Honeycomb core |
|--|--------------------|---------------------|
| E_1 [MPa] | 46.0×10^3 | 0.01 |
| E_3 [MPa] | 46.0×10^3 | 0.179×10^3 |
| G_{12} [MPa] | 17.7×10^3 | 1.0 |
| G_{13} [MPa] | 17.7×10^3 | 26.0 |
| G_{23} [MPa] | 17.7×10^3 | 56.0 |
| ν_{12} [-] | 0.3 | 0.45 |
| ν_{13} [-] | 0.3 | 0.01 |
| ρ [$\text{kg}^3 \text{m}^{-1}$] | 1570.0 | 64.0 |
| Thickness [mm] | 0.98 | 25.5 |

shown in Fig. 4.4.

4.3.2 Curved composite sandwich panel

The composite panel dimensions are $1.54 \text{ m} \times 1.62 \text{ m}$, with a curvature radius approximately of 0.97 m , and thickness equal to 27.5 mm (see Fig. 4.5a). The material properties are listed in Table 4.2.

A preliminary experimental investigation of the dispersion characteristics of the composite laminated sandwich panel was first conducted. The panel has been simply hanged in the anechoic room assuming free boundary conditions. The tests were performed using an impact hammer and four accelerometers, placed in the circumferential and axial directions; the experimental data have been recorded using a Brüel & Kjær real-time, multichannel sound and vibration data acquisition card. The experimental wavenumbers were calculated using a technique based on the phase difference between consecutive accelerometers, placed along the specific direction [113, 146]. The recorded time domain data were filtered and truncated to measure only the first incident wave fronts.

The panel was then installed in the aperture between the coupled reverberant-anechoic rooms of the GAUS (*Groupe d'Acoustique de l'Université de Sherbrooke*) laboratory, at Université de Sherbrooke (see Fig. 4.5). The representative scheme of the coupled rooms is shown in Fig. 4.6. The reverberant room has dimensions $7.5 \times 6.2 \times 3.0 \text{ m}^3$ with an averaged reverberation time (T_{60}) of 5.5s in the frequency band [50 Hz - 1000 Hz]. The acoustic excitation was generated by a loudspeaker placed close to a corner of the room, with a white noise signal input from 100 Hz to 3000 Hz. Concerning the mechanical excitation, a Modal Shop Model 2025E shaker was installed in the reverberant room and attached to the test structure using an impedance head, as shown in Fig.4.5b; the excitation was generated using a white noise signal from 100 Hz to 3000 Hz. The full vibrational field was measured using a Polytec 3D Scanning Vibrometer (PSV-3D), installed in the anechoic room, with dimensions $6.0 \times 7.0 \times 3.0 \text{ m}^3$. The acquisition window was approximately of $1.2 \text{ m} \times 1.0 \text{ m}$, in order to be sufficiently far from the boundaries and to reduce the influence of the boundary conditions, with a total number of 3111 measured points (mesh grid of 61×51), with approximately 2.0 cm of spacing between two adjacent points; an illustration of the acquisition system is shown in Fig. 4.5c. In the frequency range of the excitation, 1857 frequency acquisitions were made, resulting in a resolution of 1.5625 Hz; for each point, the signals recorded by the LDV system were averaged over 10 acquisitions.

A regular pattern of 3D-printed small-scale resonators was then attached to the panel and compared to the bare test case (see Fig. 4.5b). The chosen tuning frequency was 1000 Hz; the panel weight was increased by 4% for a total number of 246 resonators. For each considered excitation (diffuse acoustic field (DAF) and point mechanical excitations), the bare structure was first tested, and then the effect of distributed resonators tuned at a frequency of 1000 Hz was tested. In the reverberant room, a control microphone was placed close to the surface of the excited structure to double check the incident pressure and normalize the FRFs (Frequency Response Functions).

For both configurations, the panel was installed on a plywood support with acoustic sealant made of neoprene adhesive and silicone applied on the four edges, to prevent any leakage while using the acoustic excitation. The boundary conditions can be assumed of the kind “clamped” for all the four edges.

4.3.3 Aluminum aircraft sidewall panel

The aluminum panel has dimensions $1.45 \text{ m} \times 1.70 \text{ m}$, with a curvature radius approximately of 1.30 m(see Fig. 4.2b). The main geometrical properties are listed in Table 4.3.

The panel was installed in the aperture between the coupled reverberant-anechoic rooms of the GAUS laboratory, already described in section 4.3.2. For the point mechanical excitation, the bare panel was tested with free boundary conditions, and in bare test case configuration only, as listed in Table 4.1. For the diffuse acoustic field excitation, the bare structure was first tested and then the effect of distributed resonators tuned at three different frequencies was evaluated. The resonators were tuned at three different frequencies, tuning 1/3 of the resonators at each frequency and attaching them regularly to avoid any local/directional effect. The chosen frequencies

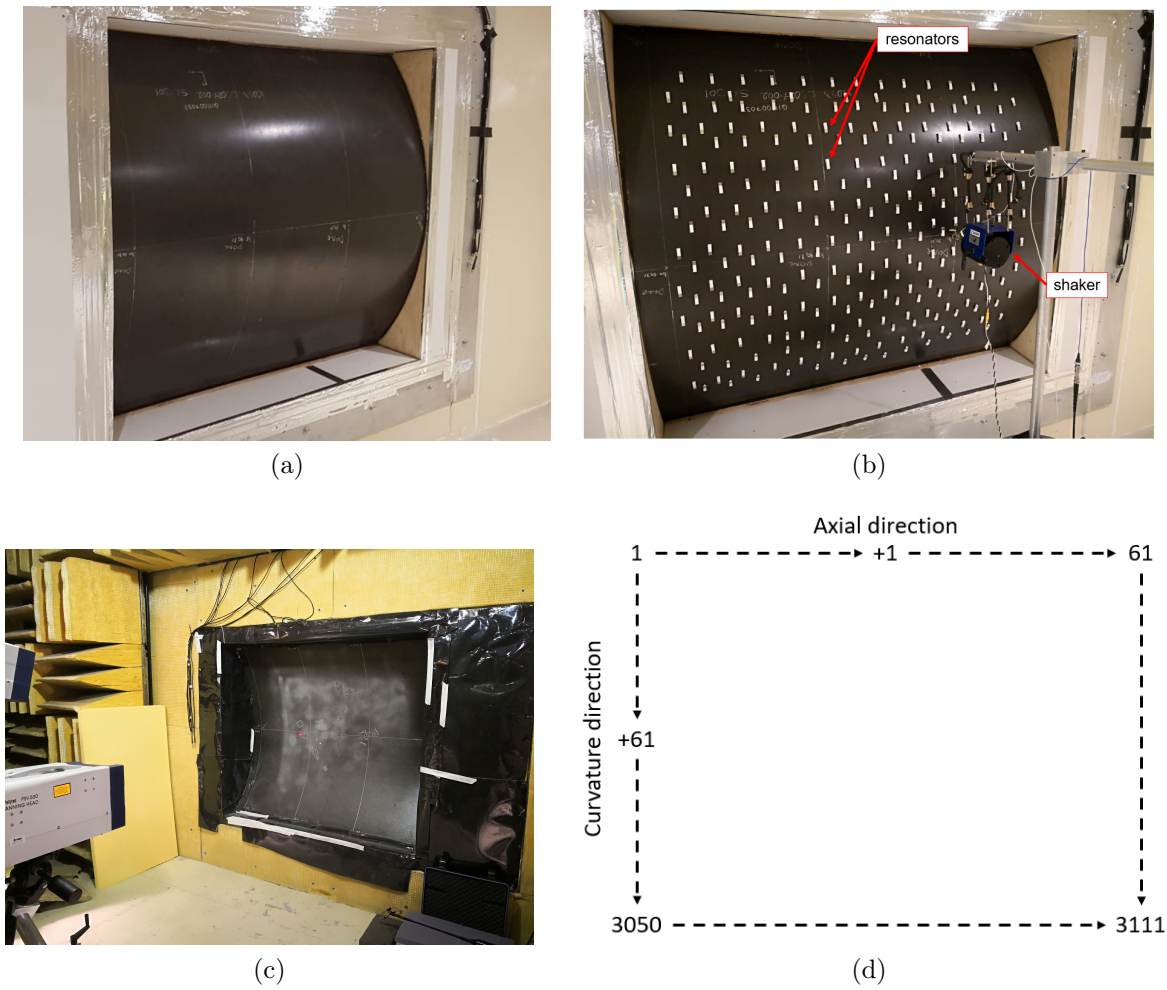


Figure 4.5 – Curved composite laminate sandwich panel: bare configuration (a), distributed resonators configuration (b), acquisition system (c) and acquisition window (d).

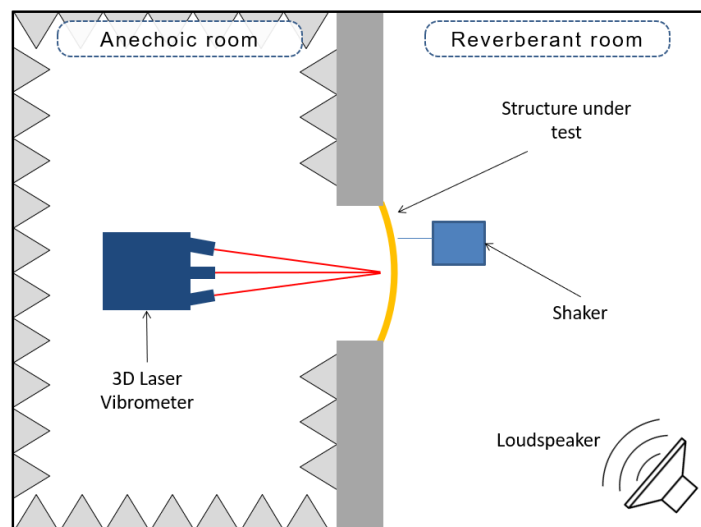


Figure 4.6 – Illustration of the coupled rooms.

Table 4.3 – Geometrical dimensions of the aluminum aircraft sidewall panel.

| | Frames (mm) | Stringers (mm) | Skin (mm) |
|-----------|----------------|-------------------|--------------|
| Thickness | 1.8 | 1.2 | 1.2 |
| Height | 72.0 | 28.0 | - |
| Spacing | 406.0 | 152.0 | - |



Figure 4.7 – Set-up and installation for mechanical excitation: shaker installation (a) and acquisition region (b).

were 670 Hz, 820 Hz and 980 Hz, in order to cover a relatively large frequency band around the ring frequency (estimated to be ≈ 670 Hz [147]). The presence of the 246 resonators increased the panel weight by 4.5% in this case.

The same Modal Shop Model 2025E shaker, described in the section 4.3.2, was used to excite the aluminum panel, using a white noise signal input from 50 Hz to 2000 Hz. The structure was freely suspended to simulate free boundary condition; the shaker was placed on an internal frame structure, as shown in Fig. 4.7a. The external surface was scanned using a Polytec 3D Scanning Vibrometer, with an acquisition window of approximately of $0.85 \text{ m} \times 0.95 \text{ m}$, with 5451 acquisition points (equivalent to a mesh grid of 69×79 , see Fig. 4.8a). A frequency resolution of 1.5625 Hz, resulting in 1255 acquisition frequencies.

To test the aluminum panel under diffuse acoustic field excitation, the panel was installed between the two rooms, as shown in Fig. 4.9. The panel was mounted using plywood frames of adapted sizes with acoustic sealant made of neoprene adhesive and silicone; the panel skin was clamped over approximately 2.0 cm in the mounting frame, while the stiffeners and frames were not clamped. The resonators were attached on the external surface (in the reverberant room) and the internal surface was scanned by a Polytec 3D Scanning Vibrometer, in the skin regions between stringers and frames, as shown in Fig. 4.10a; the total number of scanned points was 2916, with a mesh grid of 27×9 for each region (total mesh grid of 54×54), as shown in Fig. 4.8b. The structure was excited in the frequency range [100 Hz - 2000 Hz]; a frequency resolution of 0.625 Hz, resulting in 3040 acquisition frequencies.

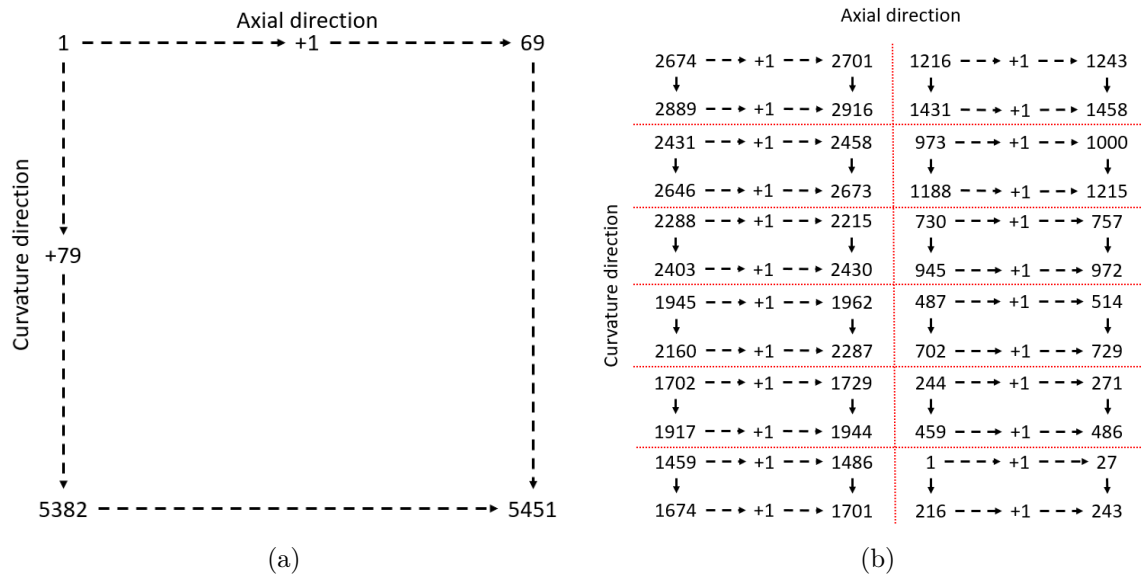


Figure 4.8 – Aluminum aircraft sidewall panel: acquisition windows for shaker (a) and DAF (b) excitations.

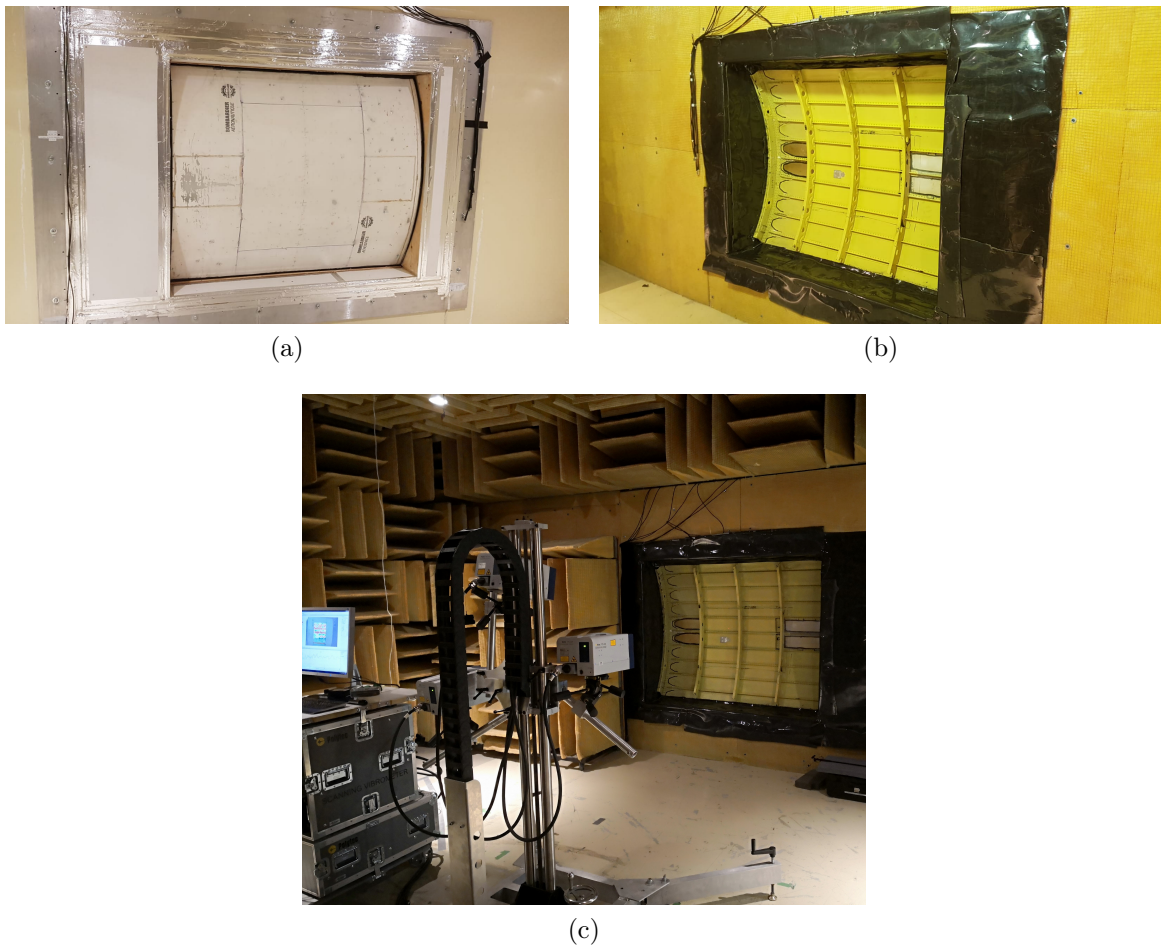


Figure 4.9 – Set-up and installation of the bare configuration: outer skin subjected to DAF excitation (a), inner surface (b) and acquisition system (c).

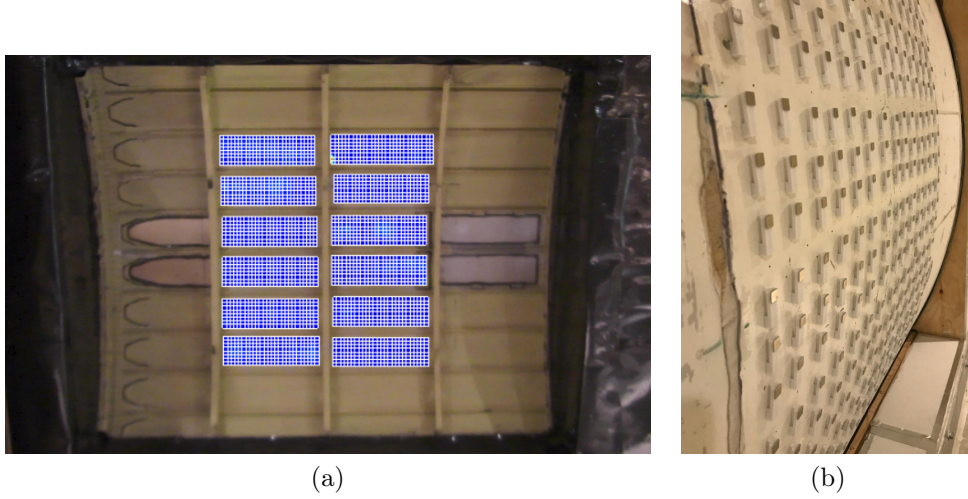


Figure 4.10 – DAF excitation: acquisition window (a) and detail of the host structure with the attached resonators (b).

4.4 Numerical validations and experimental results

In this section, the IWC method is applied to the experimental data to obtain the dispersion curves. The results are compared and validated with numerical simulations and analytical models.

4.4.1 Steel plate: experimental results and validation

In this case, the dispersion curves obtained with the IWC method are compared with the classical Kirchhoff's thin plate theory. The fundamental equations are here briefly reported. The differential equation of motion of a plate under pure bending is expressed as:

$$D\nabla^4 w + \rho \frac{\partial^2 w}{\partial t^2} = 0, \quad (4.5)$$

in which w is the transverse displacement, ρ is the mass density, D the bending stiffness and $\nabla^4 = \nabla^2 \nabla^2$, with ∇^2 the Laplacian operator, defined in Eq. (2.2):

$$\nabla^2 \nabla^2 = \frac{\partial^4}{\partial x_1^4} + 2 \frac{\partial^4}{\partial x_1^2 \partial x_2^2} + \frac{\partial^4}{\partial x_2^4}.$$

Assuming a free harmonic motion with amplitude W :

$$w = W \cos \omega t, \quad (4.6)$$

and substituting Eq. (4.6) into Eq. (4.5), the following expression can be obtained:

$$\frac{\partial^4 w}{\partial x_1^4} + 2 \frac{\partial^4 w}{\partial x_1^2 \partial x_2^2} + \frac{\partial^4 w}{\partial x_2^4} = \frac{\rho h \omega^2}{D} W = k^4 W, \quad (4.7)$$

obtaining the following expression for the flexural wavenumber:

$$k = \sqrt{\omega} \left(\frac{\rho h}{D} \right)^{1/4}. \quad (4.8)$$

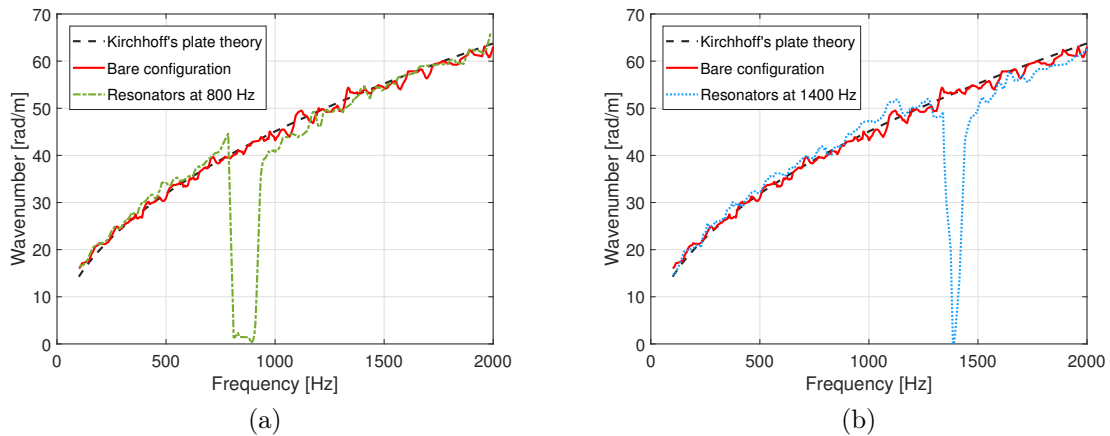


Figure 4.11 – Dispersion curves comparison for the steel plate, with and without the resonators: at 800 Hz (a) and at 1400 Hz (b).

The dispersion curves are estimated for all tested configurations and compared with the analytical solution, as shown in Fig. 4.11. The estimated dispersion curves are in agreement with the analytical solution in the whole frequency range. In Fig. 4.11a, the effect of the resonators tuned at 800 Hz is shown, giving a band-gap of approximately 200 Hz width; before and after the band gap, the dispersion curve follows the one of the bare configuration and the analytical solution. For what concerns the resonators tuned at 1400 Hz, the originated band gap is approximately 250 Hz wide, as shown in Fig. 4.11b. For both configuration, a strong attenuation is observed in the resonators tuning frequency regions.

The whole vibrational fields have been acquired for the three considered configurations. In Fig. 4.12 the normalized (respect to the maximum value of the amplitude) displacements fields are plotted at three different frequencies: before the first tuning frequency of the resonators (250 Hz), in the first band-gap region (820 Hz) and in the second band-gap interval (1375 Hz). At 250 Hz, the displacement fields are not affected by the resonators (see figures 4.12a, 4.12b and 4.12c). For the frequency value in the first band-gap, the bare test case panel and the panels with the resonators not tuned at this frequency exhibit a displacement fields similar to a global mode behavior (see figures 4.12d and 4.12f), while the panel with the resonators tuned at this frequency shows an attenuated vibration level (see Fig. 4.12e). At the last considered frequency, in the second band-gap, the bare test case panel and the panel with the resonators tuned at 800 Hz show a classical plate motions (see figures 4.12g and 4.12h), while the panel with the resonators correctly tuned exhibits an attenuated displacement field (see Fig. 4.12i).

Based on the acquired displacement values, the averaged (over 25 randomly chosen measurement points) FRFs of the three configurations are shown in Fig. 4.13, in which both drops due to the resonators are captured.

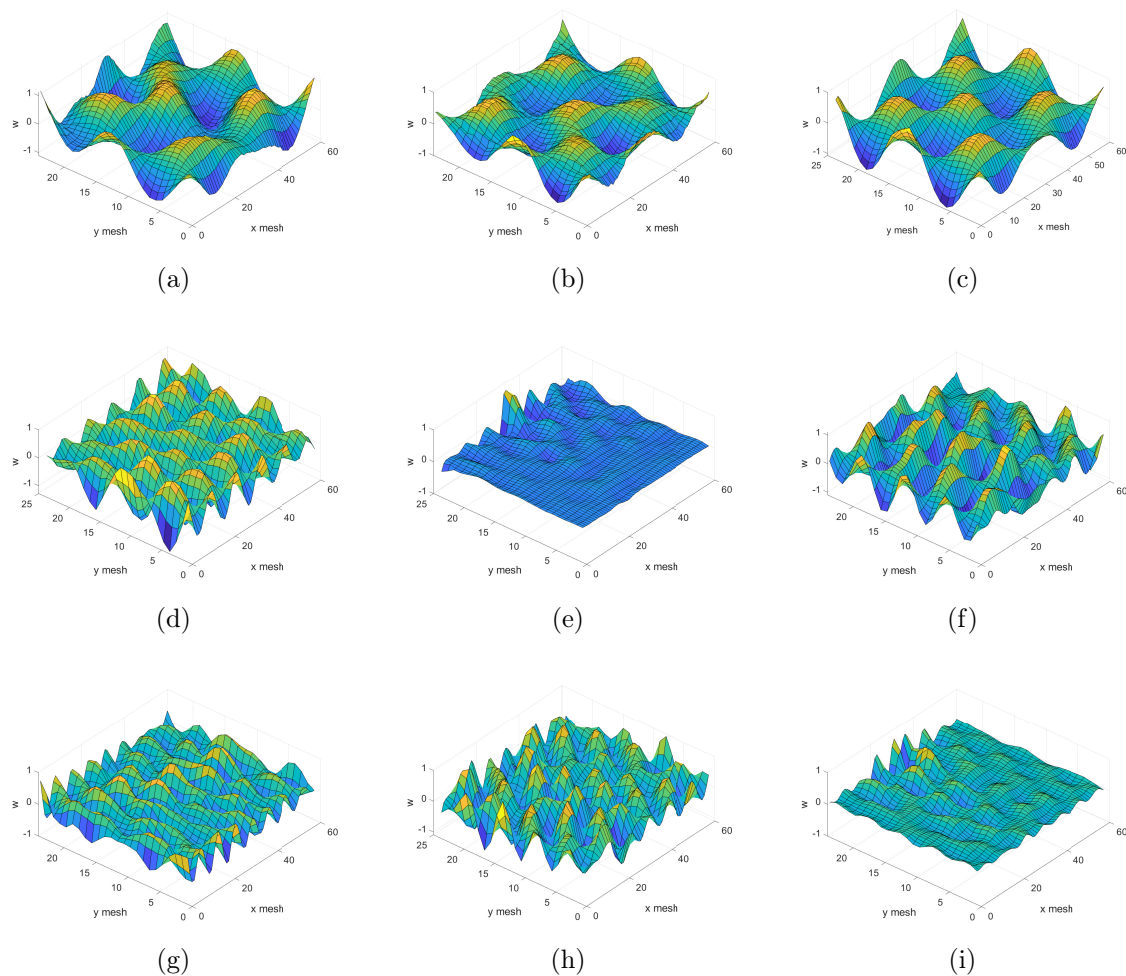


Figure 4.12 – Displacement fields of the steel plate, with and without the resonators. First frequency at 250 Hz: bare test case (a), first resonators configuration (b) and second resonators configurations (c). Second frequency at 820 Hz: bare test case (d), first resonators configuration (e) and second resonators configurations (f). Third frequency at 1375 Hz: bare test case (g), first resonators configuration (h) and second resonators configurations (i).

4.4.2 Isotropic curved panel: numerical simulation and validation

Firstly, the proposed IWC formulation for curved structures is numerically validated. The method is applied to an isotropic curved panel; the employed material is a standard aeronautical aluminum alloy, similarly to the experimentally measured case. The dimensions are $0.85\text{ m} \times 0.95\text{ m}$, thickness equal to 1.2 mm and curvature radius of 1.3 m . The finite element model of this structure, shown in Fig. 4.14a, is built using 13328 shell structural elements (ANSYS SHELL181), with a total number of degrees of freedom equal to 81560. A point mechanical force is positioned as it was made for experiments. The analysis is performed in the frequency range from 50 Hz to 2000 Hz. A frequency step of 5 Hz is chosen, resulting in 381 acquisition frequencies. The dispersion curve obtained with the proposed approach is validated by the Wave Finite Element Method (WFEM) for curved structures, based on the formulation described in section 1.4; the dispersion curves are in agreement on the whole frequency range, as

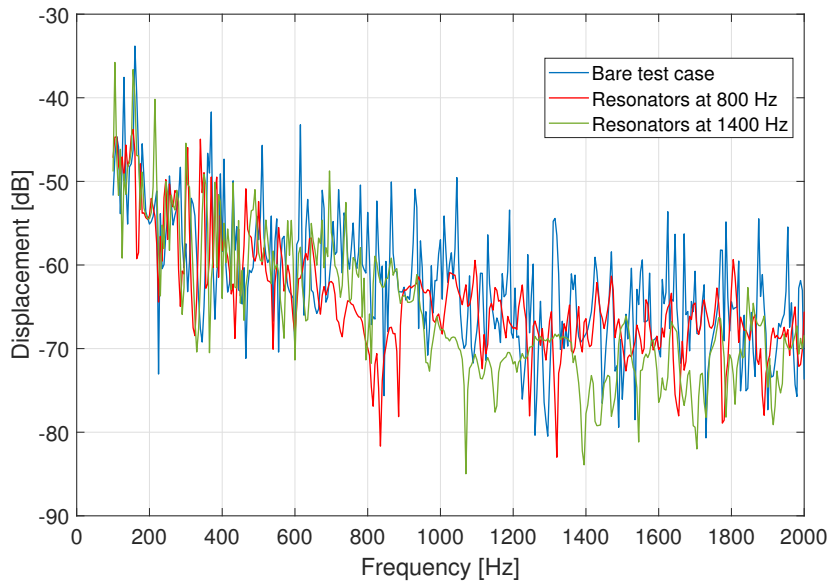


Figure 4.13 – Steel plate: averaged Frequency Response Functions comparison.

shown in Fig. 4.14b.

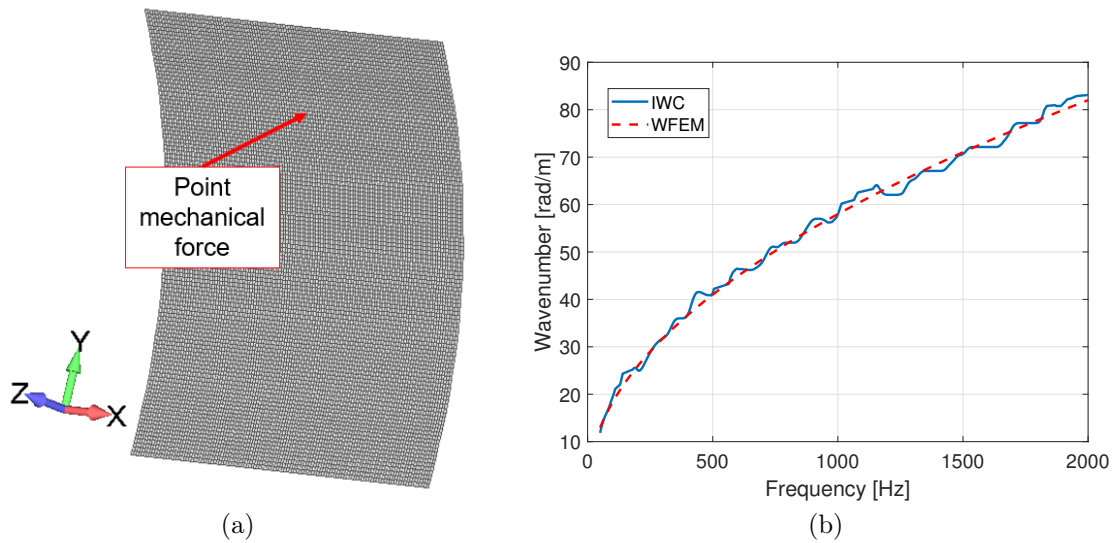


Figure 4.14 – FE model of the curved panel (a) and dispersion curves comparison (b).

4.4.3 Curved composite laminated sandwich panel: experimental results and validation

Firstly, the Frequency Response Functions (FRFs) of the two configurations of the panel are compared, for both excitations (see Fig. 4.15). For what concerns the FRF of the panel under diffuse acoustic field excitation, the natural modes are not well identified due to the high damping level; in any case, around the tuning frequency of the resonators a drop of the amplitude is observed (see Fig. 4.15a). Under mechanical excitation, the natural modes of the structure can be identified; the drop around the

tuning frequency of the resonators is captured (see Fig. 4.15b) and it is clearer compared to the one obtained in Fig. 4.15a.

The measured displacement fields for all four configurations and for both excitation condition are plotted in Fig. 4.16 and Fig. 4.17. Three different values of the frequency are chosen: before and after the tuning frequency of the resonators and in the region in which the resonators are tuned to work in. In Fig. 4.16, the displacement fields under DAF excitation are shown; for frequency values far from the tuning frequency of the resonators, the displacement fields of both configurations are similar showing that the resonators are not working at these frequencies (see figures 4.16a, 4.16b, 4.16e and 4.16f). Around the tuning frequency of the resonators, an attenuation of the vibration level is observed in Fig. 4.16d, compared to the bare test case configuration (see Fig. 4.16c).

A similar behavior is observed under shaker excitation, in which the location of the shaker is marked, allowing the identification of wave propagation (see Fig. 4.17). For frequency values very different from the tuning frequency of the resonators, the displacement fields for both configurations are very similar, as shown comparing Fig. 4.17a with Fig. 4.17b and Fig. 4.17e with Fig. 4.17f. Around the tuning frequency of the resonators, the vibration level is strongly attenuated, as shown in Fig. 4.17d.

Fig. 4.18 shows the bending dispersion curves under diffuse acoustic field excitation for both configurations, with and without resonators; the dispersion curves are computed in the two orthogonal directions, axial and circumferential. For both directions, the local dynamics of the resonators is well described.

The same comparison is done using the mechanical excitation, as shown in Fig. 4.19; the dispersion curves are calculated in both directions, with and without the resonators. The local dynamics of the resonators is well described in both directions.

From the estimation of the complex wavenumbers, a calculation of the damping loss factor is performed, using the following relationship between the real and imaginary parts of the flexural wavenumber, already expressed in Eq. (1.86), in section 1.5:

$$\eta = \left| \frac{\text{Im}(k^4)}{\text{Re}(k^4)} \right|.$$

The experimental damping loss factor is calculated for both configurations, the test case and the panel with distributed resonators, as shown in Fig. 4.20a, where the damping loss factor is expressed in one twelfth octave band. In the low frequency region, the damping loss factor appears very high, mainly due to the influence of the boundary conditions. Around the tuning frequency of the resonators an increase of the damping factor is present; this effect is correlated to the continuously increasing of the imaginary part of the wavenumber and decreasing of the real one, consequently to a strong reduction of the vibration level.

The estimated damping loss factor is then compared with a different method, the Power Input Method, already described in section 1.5. The damping loss factor is calculated using Eq. (1.89), as follows:

$$\eta_f = \frac{P_f}{\omega E_f},$$

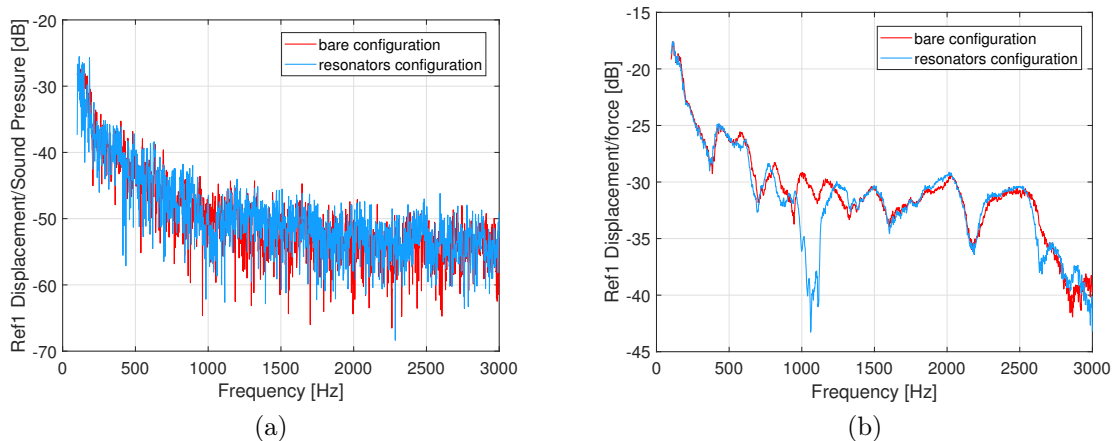


Figure 4.15 – FRFs comparison for both configurations and excitations: DAF excitation (a) and point mechanical excitation (b).

where P_f and the E_f are given by Eq. (1.90) and Eq. (1.91), respectively. The quadratic velocities and the force are averaged over 200 points. All these quantities are derived from the use of an impedance head.

4.4.4 Aluminum aircraft sidewall panel: experimental results and validation

The finite element model of the panel is shown together with the structure in Fig. 4.21; the numerical displacement field is obtained by a full FE analysis, using a point harmonic excitation at the same location of the shaker in the experimental test.

The material properties introduced in the numerical model are of a standard aluminum alloy for aeronautical application: Young's modulus $E = 73.1$ GPa, mass density $\rho = 2780.0$ kg m⁻³ and Poisson coefficient $\nu = 0.33$. The structure is not modeled with a very high degree of fidelity. For example, the all the joints and connections are not modeled, stringers and frame are considered rigidly connected; the small air-gap present in the real structure is neglected and some small holes in the frame structure are not present in the numerical model, because of their effect on the dispersion characteristics is considered small. The FE model is built using structural shell elements (ANSYS SHELL181); the total number of structural elements is approximatively of $3.2 \cdot 10^4$.

The normal displacements of the nodes of the external surface are used as primary input in Eq. (4.4); from the full-field measurements, the multi-modal behavior is well identified in the numerical simulation and experimental test, with shaker excitation and full-field acquisition, as shown in Fig. 4.22a. The two different modes of propagation are quite evident in the axial direction and they are well captured when the full-structure is scanned. The same behavior is not captured when the acquisition window is reduced to the internal bays (as shown in Fig. 4.10a), because the stringer vibration is not acquired. Two uncoupled wavenumber are identified at the same frequency: plate flexural and stringer flexural. Some discrepancy between the numerical

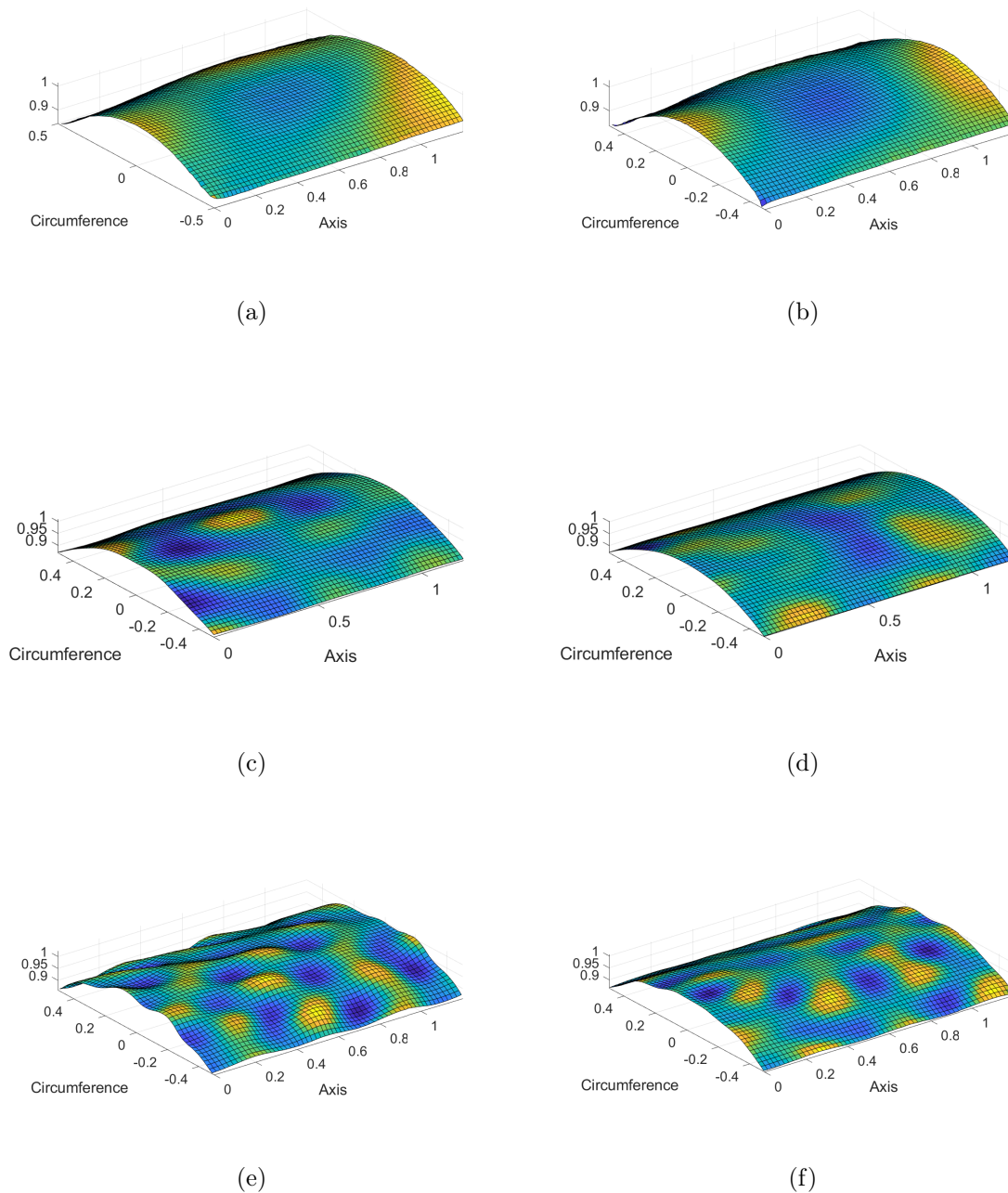


Figure 4.16 – Normalized displacement fields under DAF excitation for the composite shell at three different frequencies. At 325 Hz: bare test case (a) and resonating structure (b). At 1000 Hz: bare test case (c) and resonating structure (d). At 1675 Hz: bare test case (e) and resonating structure (f).

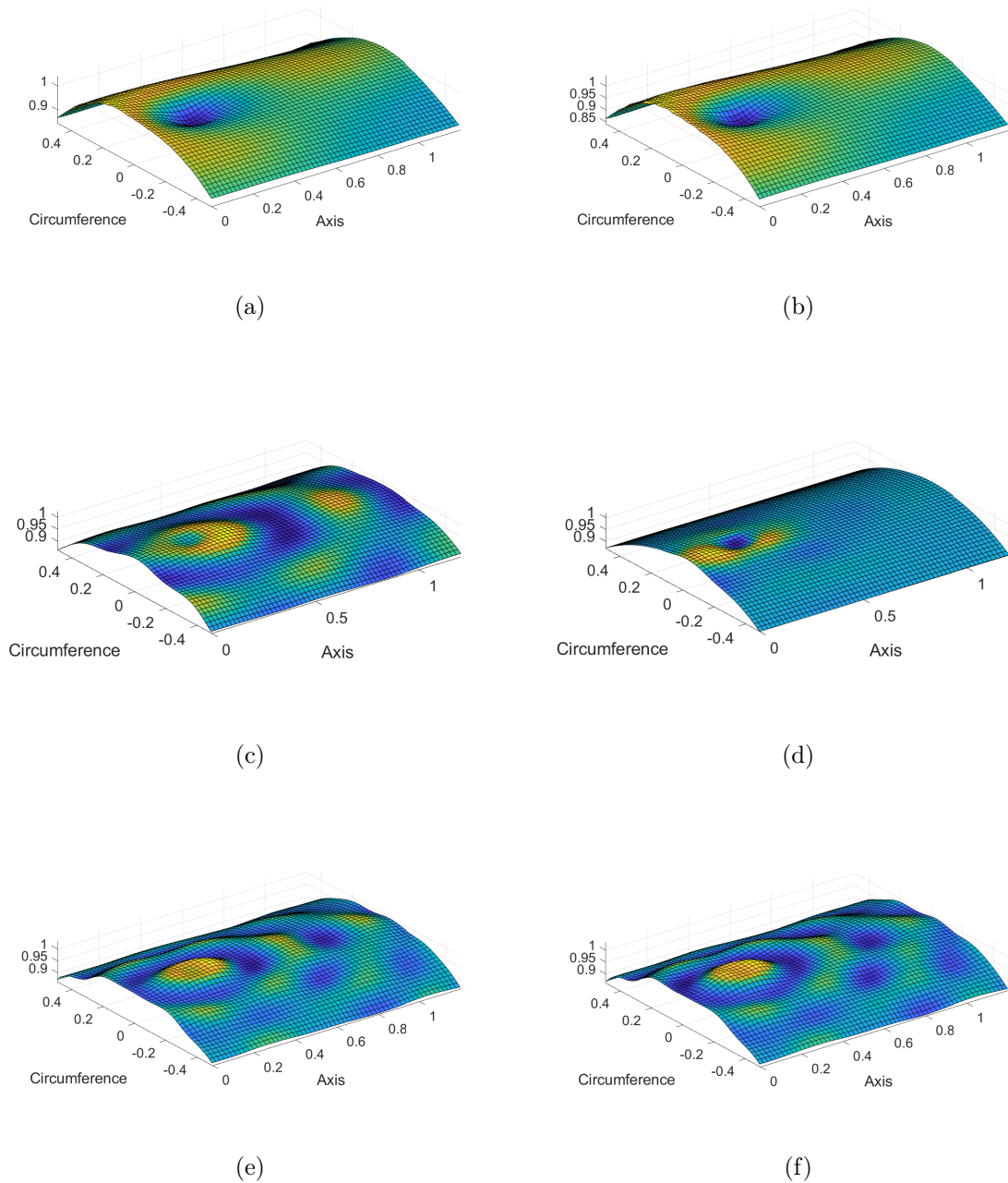


Figure 4.17 – Normalized displacement fields under shaker excitation for the composite shell at three different frequencies. At 325 Hz: bare test case (a) and resonating structure (b). At 1000 Hz: bare test case (c) and resonating structure (d). At 1675 Hz: bare test case (e) and resonating structure (f).

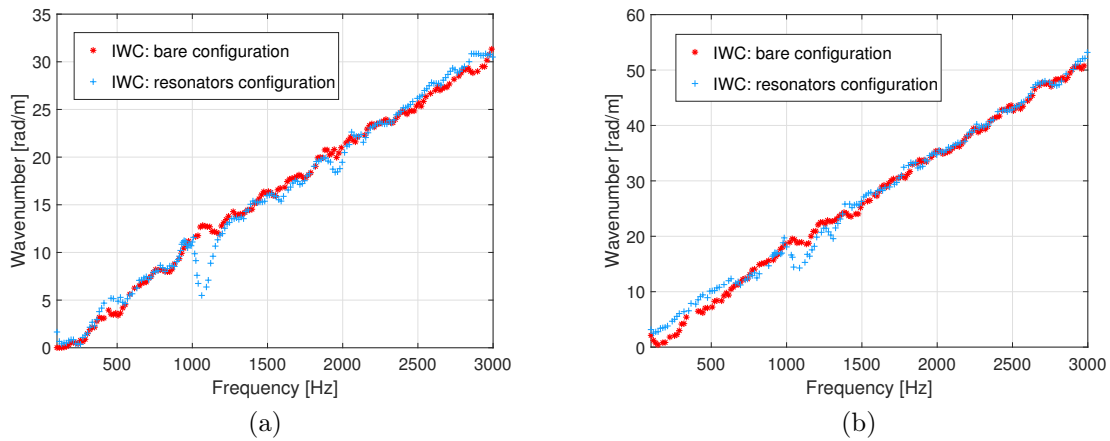


Figure 4.18 – Dispersion curves under DAF excitation, with and without resonators: axial (a) and circumferential (b) directions.

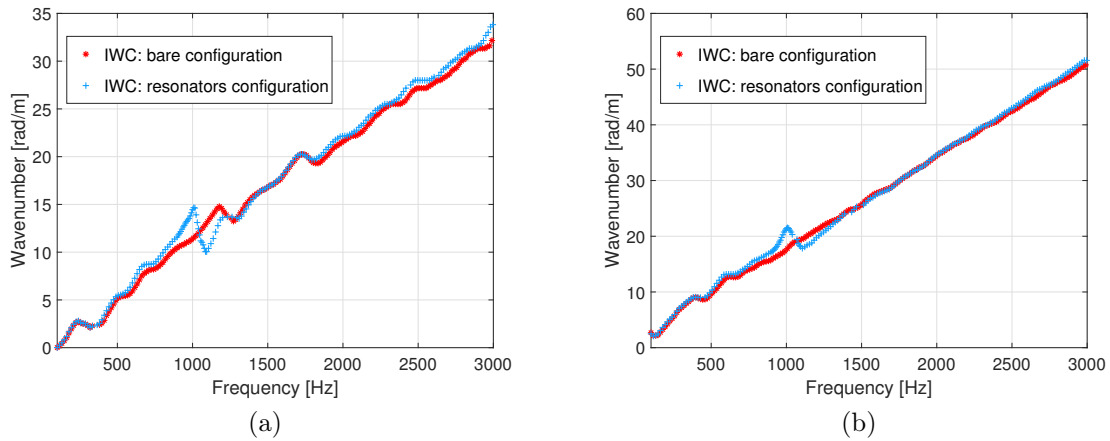


Figure 4.19 – Dispersion curves under shaker excitation, with and without resonators: axial (a) and circumferential (b) directions.

and experimental dispersion curves are present in Fig. 4.22a, mainly due to the modeling choices. A good agreement between the numerical dispersion curves and the experimental ones, under the two different loading conditions, is shown in Fig. 4.22, both in the axial and circumferential directions.

The effect of the resonators on the dispersion curves is remarkable, in both directions. In the axial direction (see Fig. 4.23a) the bending dispersion curve appears higher in frequency; in the circumferential one a band-gap between 500 Hz and 1000 Hz appears, as shown in Fig. 4.23b. In this frequency band, the energy flowing in structure is dissipated by the vibration of the resonators, showing a high apparent stiffening behavior (lower values of the wavenumbers compared to the bare test case).

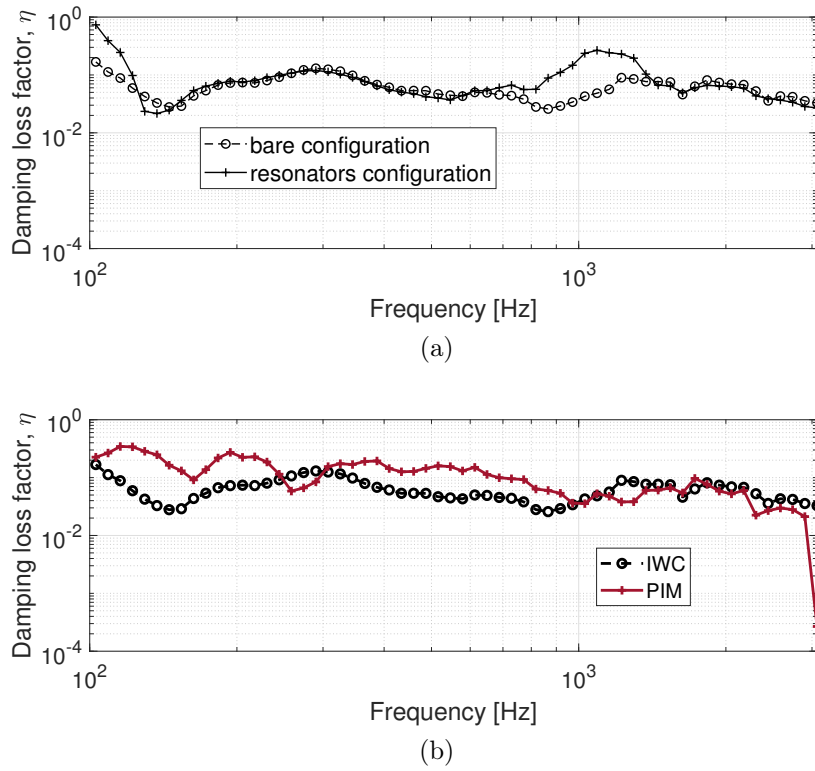


Figure 4.20 – Damping Loss Factor estimation: bare test case and resonators configuration comparison with Eq. (1.86) (a) and bare test case comparison between Eq. (1.86) and PIM (b).

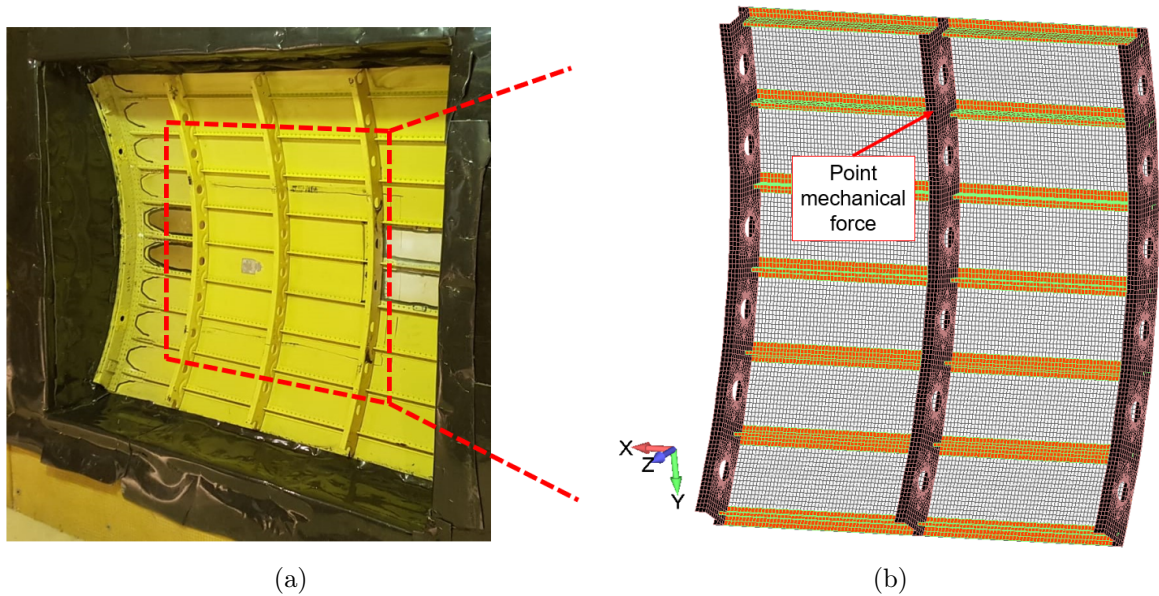


Figure 4.21 – Installation of the aluminum panel (a) and FE model (b).

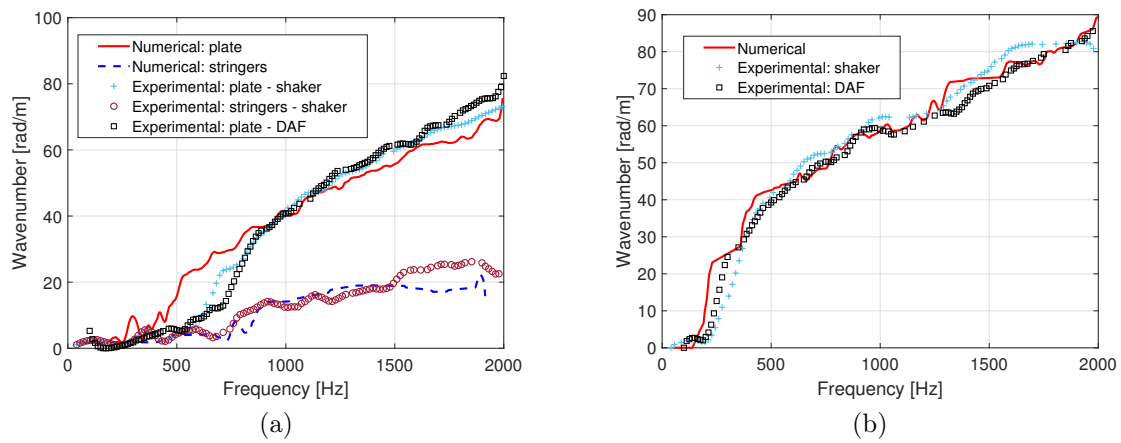


Figure 4.22 – Dispersion curves for the bare configuration and different loading conditions: axial (a) and circumferential (b) directions.

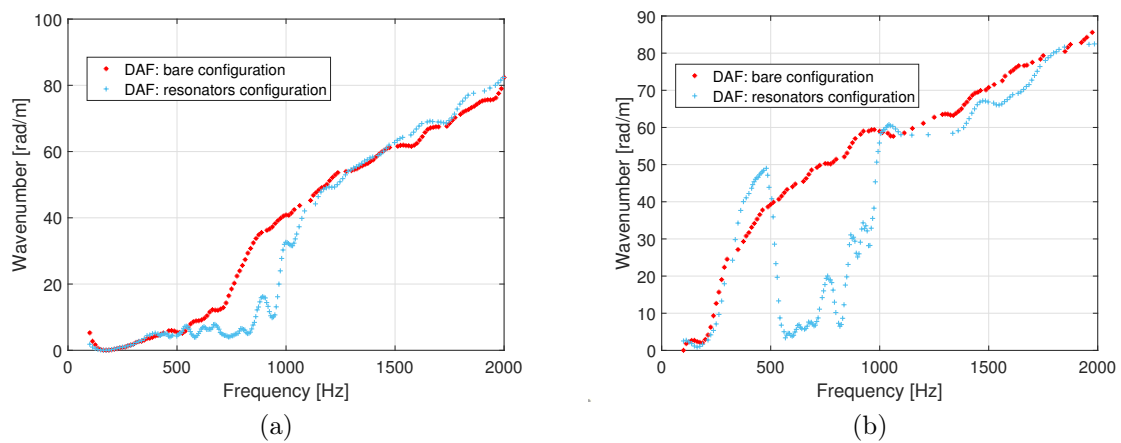


Figure 4.23 – Dispersion curves under DAF excitation, with and without resonators: axial (a) and circumferential (b) directions.

4.5 Conclusions

In this chapter, the feasibility of the Inhomogeneous Wave Correlation method on complex structures, in presence of a local dynamics effect and under diffuse acoustic field excitation has been demonstrated, giving an estimation of the dispersion curves for all tested configurations.

The global bending behavior of the aeronautical aluminum panel is well captured, even if the acquisition window is reduced to the bays between the stringers and the frames. At the same time, the local dynamics and the multi-modal behavior is not described. This is one of the main advantages of the proposed approach, which allows to describe the global behavior from a reduced acquisition window and a reduced number of points.

The efficiency of these 3D-printed small-scale resonators is also demonstrated, obtaining a reduction of the vibrational levels of the panels. For all tested configurations, in the frequency band the resonators are tuned to work in, a drop in the dispersion curves is observed. The method here developed is mainly an energetic approach, which makes a correlation between the energy carried on by the inhomogeneous wave and the total energy of the vibrating structure. The drops in the dispersion curves appear because the energy is dissipated by the motion of the resonators, resulting in a deformation of the main structure similar to the unloaded case.

This preliminary study on the industrial application of small-scale resonators on real aeronautic structures opens the possibility to attenuate the vibration levels in some specific frequency bands, working on the design of the resonators. A deep investigation about the design of the resonators can be done in order to increase the wave attenuation and to enlarge the band-gap and the resonance zone.

Chapter 5

Vibro-acoustic response of axially and ring stiffened curved structures

Abstract

A vibro-acoustic investigation on the effects of axially and circumferentially distributed stiffeners on curved panels is carried out in this chapter. The effect of the pitch between the stiffeners, of their cross-section shape and their orientation is investigated. The stiffeners are modeled using three different cross-sections: T shaped, H shaped and Ω shaped; the stiffened panels are then compared to the bare test case configuration. The dispersion characteristics in two orthogonal directions (axial and circumferential) are identified by the use of an Inhomogeneous Wave Correlation (IWC) based method. A periodic pattern of stiffeners is modeled in each studied case; the band-gaps related to the geometric periodicity are also well-captured. The structures are modeled using a commercial Finite Element (FE) package; the displacement field under punctual harmonic unit force is calculate by a full-FE analysis.

The effects of each configuration on the sound radiation are investigated by computing the sound transmission losses for each of the configurations tested. Both a purely diffuse acoustic excitation and a combination of turbulent boundary layer and acoustic diffuse load are simulated to approach real operational loading conditions.

5.1 Introduction

The presence of stringers and frames in the longitudinal and circumferential directions of aircraft fuselages and space launcher fairings is a very common design choice. To analyze and predict the vibro-acoustic behavior of stiffened plates, some analytical theories have been developed [148–150]. Many works investigating the vibro-acoustic behavior of stiffened cylindrical shells can be found in the literature [151–154]. Ribbed panels are widely used in many engineering applications, ensuring a compromise between weight and high apparent rigidity. The vibro-acoustic behavior of ribbed panels under point mechanical force or fluid-load excitation is intensively studied by different authors. Rumerman [155] used a plane wave excitation to obtain an explicit solution of the forced vibration of periodically ribbed plate. In the context of fluid-loaded plates, Mace [156, 157] developed a similar approach to investigate periodically stiffened plates.

The identification of the dispersion curves associated to transverse displacements are of fundamental interest since they contain informations directly related to the vibro-acoustic behavior of the structure. In this framework, k -space methods are growing in interest in the domain of wave propagation parameter identification. An application of the IWC method to identify the dispersion curves of a ribbed plate with inner resonance is presented in [158], in which the dispersion curves are compared with a homogenized analytical model. Maxit [134] investigated the vibro-acoustic behavior of a fluid-loaded periodically stiffened plate in the wavenumber domain; the out of plane displacement field is expressed in the wavenumber domain while the acoustic pressure in the fluid domain. He proposed also a discrete Fourier Transform to obtain the same information in the physical space. A vibro-acoustic analysis of stiffened composite panels is shown in [159], in which the influence of the shape and the position of the stiffening elements is analyzed.

Using the generalized nearfield acoustical holography, the calculation of the vibration and of the sound radiation of submerged cylinders excited by a point force is shown in [160]. Later, the same authors extended the analysis in the wavenumber domain [138]; in this domain, they identified the wavenumber diagrams and the contribution of each wave to the far-field radiation. Photiadis et al. [139] investigated the acoustic response of a ribbed shell in the wavenumber domain, identifying the flexural behavior in the mid-frequency range. Meyer et al. [141] experimentally investigated the influence of internal frames on the vibro-acoustic response of stiffened aluminum cylindrical shell. Their study was focused on the analysis of the effect of the non-axisymmetric frames on the radiation efficiency.

Some works analyzed the sound radiation of ring-stiffened shells as a function of the number of stiffeners and their pitch [161, 162]. For example, Laulagnet et al. [161] treated the sound radiation problem using stiffeners of hollow cross-section, to simulate real industrial case-studies; tangential and radial forces are applied on the skins and the stiffeners and the fluid-structure interaction modeled using a modal decomposition. Lee et al. [162] investigated the problem varying the angle of incidence of an acoustic plane wave excitation. The circumferential stiffeners induce an increased sound transmission loss before the ring frequency, that is simultaneously slightly reduced with respect to the one of the bare case.

On the contrary, shells with axial stiffeners are investigated in terms of acoustic radiation in [163]. The presence of axial stiffeners is studied only in terms of additional impedance and different configurations are analyzed by varying the number of axial stiffeners.

In this chapter, a full vibro-acoustic analysis is conducted, investigating both dispersion characteristics and sound radiation properties, extending the investigation to more realistic aero-acoustic loading conditions, using a unit cell approach developed in [164]. The dispersion curves of the unstiffened and stiffened shells are analyzed in section 5.4, while the STL results are shown in section 5.5.

5.2 Overview of the methodologies

In this section, an overview of the Donnell-Mushtary analytical theory for thin circular cylindrical shells, used to validate the dispersion curve for the bare configuration, and of the Inhomogeneous Wave correlation method for curved structures is proposed.

5.2.1 Donnell-Mushtary theory for thin cylindrical shells

This section is devoted to the derivation of the main equations of the Donnell-Mushtary theory for thin circular cylindrical shells. All the intermediate passages are skipped and they can be found in [165].

Based on Love's and Timoshenko's theories, the strain-displacement equations can be expressed as follows:

$$e_s = \varepsilon_s + z\kappa_s, \quad e_\theta = \varepsilon_\theta + z\kappa_\theta \quad \text{and} \quad \gamma_{s\theta} = \varepsilon_{s\theta} + z\tau, \quad (5.1)$$

where $s = x/R$ is the non-dimensional length, R is the radius of curvature of the cylinder and θ is the angular coordinate, as shown in Fig. 5.1. The expressions of the normal and shear strains in the middle surface (ε_s , ε_θ and $\varepsilon_{s\theta}$) and the mid-surface changes in curvature and twist (κ_s , κ_θ and τ) of Eq. (5.1) are listed below:

$$\begin{aligned} \varepsilon_s &= \frac{1}{R} \frac{\partial u}{\partial s} \\ \varepsilon_\theta &= \frac{1}{R} \frac{\partial v}{\partial \theta} + \frac{w}{R} \\ \varepsilon_{s\theta} &= \frac{1}{R} \frac{\partial u}{\partial \theta} + \frac{1}{R} \frac{\partial v}{\partial s} \\ \kappa_s &= -\frac{1}{R^2} \frac{\partial^2 w}{\partial s^2} \\ \kappa_\theta &= -\frac{1}{R^2} \frac{\partial^2 w}{\partial \theta^2} \\ \tau &= -\frac{1}{R^2} \frac{\partial^2 w}{\partial s \partial \theta} - \frac{1}{R^2} \frac{\partial^2 w}{\partial \theta \partial s} \end{aligned}, \quad (5.2)$$

where $\{u, v, w\}$ are the orthogonal components of displacements in the x , θ and radial directions, respectively. Skipping the derivation of the strain-displacement relations and the integration to find the stress resultants, the equations of motion can be written, in matrix notation, as:

$$[A]\mathbf{u} = \{0\}, \quad (5.3)$$

in which $[A]$ is the 3-by-3 matrix differential operator and $\{u\}$ is the displacement vector. This differential operator assumes the following expression:

$$[A] = \begin{bmatrix} \left[\frac{\partial^2}{\partial s^2} + \frac{1-\nu}{2} \frac{\partial^2}{R^2 \partial \theta^2} - \frac{\rho h}{K} \frac{\partial^2}{\partial t^2} \right] & \frac{1+\nu}{2} \frac{\partial^2}{R \partial x \partial \theta} & \nu \frac{\partial}{R \partial x} \\ \frac{1+\nu}{2} \frac{\partial^2}{R \partial x \partial \theta} & \left[\frac{1-\nu}{2} \frac{\partial^2}{\partial x^2} + \frac{\partial^2}{R^2 \partial \theta^2} - \frac{\rho h}{K} \frac{\partial^2}{\partial t^2} \right] & \frac{\partial}{R^2 \partial \theta} \\ \frac{12\nu}{h^2} \frac{\partial}{R \partial x} & \frac{12}{h^2} \frac{\partial}{R^2 \partial \theta} & \left[\frac{12}{h^2} \frac{1}{R^2} + \nabla^4 + \frac{\rho h}{D} \frac{\partial^2}{\partial t^2} \right] \end{bmatrix}, \quad (5.4)$$

where ν is the Poisson's coefficient, h is the thickness, K is the middle surface stiffness, D is the flexural rigidity and $\nabla^4 = \nabla^2 \nabla^2$, being ∇^2 the Laplacian operator. The quantities K , D and ∇^2 are defined as follows, respectively:

$$K = \frac{Eh}{1-\nu^2}, \quad D = \frac{Eh^3}{12(1-\nu^2)} \quad \text{and} \quad \nabla^2 = \frac{\partial^2}{\partial x^2} + \frac{\partial^2}{R^2 \partial \theta^2}. \quad (5.5)$$

The following expressions for the displacements can be assumed:

$$\begin{cases} u = U e^{\lambda \frac{x}{R}} \cos n\theta \cos \omega t \\ v = V e^{\lambda \frac{x}{R}} \sin n\theta \cos \omega t \\ w = W e^{\lambda \frac{x}{R}} \cos n\theta \cos \omega t \end{cases}, \quad (5.6)$$

in which U , V and W are the amplitudes of the displacement components, λ is the propagation constant in the axial direction, ω is the frequency in radians per second and n is the circumferential order. Substituting Eq. (5.6) into Eq. (5.3) and re-writing the resulting equations in matrix notations, we obtain:

$$\begin{bmatrix} B_{11} & \frac{1+\nu}{2} \frac{\lambda}{R^2} & \nu \frac{\lambda}{R^2} \\ -\frac{1+\nu}{2} \frac{\lambda n}{R^2} & B_{22} & -\frac{n}{R^2} \\ \nu \frac{\lambda}{R^2} & \frac{n}{R^2} & B_{33} \end{bmatrix} \begin{bmatrix} U \\ V \\ W \end{bmatrix} = \begin{bmatrix} 0 \\ 0 \\ 0 \end{bmatrix}, \quad (5.7)$$

in which:

$$\begin{aligned} B_{11} &= \frac{\lambda^2}{R^2} - \frac{1-\nu}{2} \frac{n^2}{R^2} + \frac{\rho h \omega^2}{K} \\ B_{22} &= \frac{1-\nu}{2} \frac{\lambda^2}{R^2} - \frac{n^2}{R^2} + \frac{\rho h \omega^2}{K} \\ B_{33} &= K \left(\frac{\lambda^4}{R^2} - 2 \frac{n^2 \lambda^2}{R^2} + \frac{n^4}{R^2} \right) + \frac{1}{R^2} - \frac{\rho h \omega^2}{K} \end{aligned}. \quad (5.8)$$

For non-trivial solution, the determinant of the coefficient matrix in Eq. (5.7) is set equal to zero, resulting in two eigenvalue problems:

- for a given value of the propagation constant λ , there is one or more values of the frequency such that the determinant is zero;
- for a given value of the frequency ω , there is one or more values of the propagation constant such that the determinant vanishes.

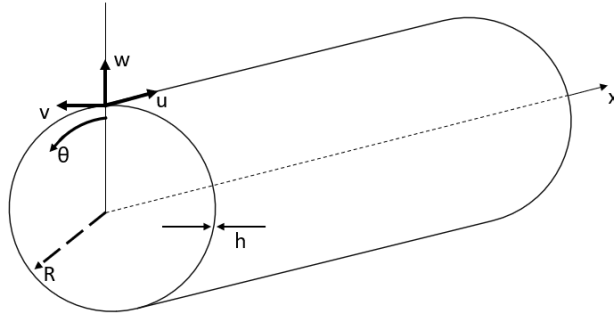


Figure 5.1 – Coordinates system for the Donnell-Mushtary theory

5.2.2 IWC method for curved structures

In this section an overview of the IWC method for curved structures is provided; this formulation is described in detail in Tufano et al. [166] and in chapter 4. The IWC method is applied to stiffened curved panels to identify the dispersion curves in two orthogonal directions, axial and circumferential.

Considering the reference system shown in Fig. 4.1, the inhomogeneous helical wave can be expressed as follows:

$$\tilde{w}_{k_C, \theta}(x, \varphi) = e^{-ik_C(\theta)((x-x_0) \cos \theta + (\varphi - \varphi_0) \sin \theta)}.$$

For a given direction θ and at a fixed value of the frequency f , the unknown complex wavenumber k_C is identified as the location of the maximum of the normalized correlation function, denoting the point where the measured signal \hat{w} correlates best with the inhomogeneous helical wave $\tilde{w}_{k_C, \theta}(x, \alpha)$:

$$\mathcal{I}(k_C, \theta) = \frac{|\sum_{j=1}^N \hat{w}(x_j, \varphi_j) \cdot \tilde{w}_{k_C, \theta}^*(x_j, \varphi_j) h_j \Omega_j|}{\sqrt{\sum_{j=1}^N |\hat{w}(x_j, \varphi_j)|^2 h_j \Omega_j \cdot \sum_{j=1}^N |\tilde{w}_{k_C, \theta}(x_j, \varphi_j)|^2 h_j \Omega_j}},$$

where $*$ denotes the complex conjugate, h_j is the coherence of the measured signal at each point, Ω_j is an estimation of the surface around the point j and N is the total number of acquisition points.

Firstly, a discrete value of the propagation angle θ_i is defined, then, for each frequency value, the maximum of the IWC correlation function is located at a value $(k_{\mathbb{R}e}, k_{\mathbb{I}m})$, creating two vectors $k_{\mathbb{R}e}(\theta_i)$ and $k_{\mathbb{I}m}(\theta_i)$ of the same length of the frequency vector. The location of the maximum of the correlation function $\mathcal{I}(k_C, \theta)$ gives the identified complex wavenumber in the specified direction. When the structure is complex, the correlation function could be characterized by an absolute maximum and some local maxima, denoting the presence of different bending waves propagating at the same time.

Table 5.1 – Cross-section properties of the stiffeners.

| | T shaped | H shaped | Ω shaped |
|---|-----------------------|-----------------------|-----------------------|
| Cross-section Area [m ²] | $3.46 \cdot 10^{-5}$ | $3.70 \cdot 10^{-5}$ | $2.78 \cdot 10^{-5}$ |
| Moment of Inertia, I_{xx} [m ⁴] | $2.54 \cdot 10^{-10}$ | $2.85 \cdot 10^{-10}$ | $2.61 \cdot 10^{-10}$ |
| Moment of Inertia, I_{yy} [m ⁴] | $8.01 \cdot 10^{-10}$ | $8.11 \cdot 10^{-10}$ | $7.87 \cdot 10^{-10}$ |

5.3 Numerical models of the considered configurations

A bare test case panel is considered, then a periodic distribution of stiffeners is applied in the axial and in the circumferential directions, separately. The effects of the spacing between the stiffeners and of their cross-section shape are then compared to the bare test case results. The panels have dimensions 0.60 m x 1.05 m, with a curvature radius $R = 1.0$ m and thickness equal to 1.2 mm (see Fig. 5.2a). The material properties are chosen to be similar to a standard aeronautical aluminum alloy, with Young's modulus $E = 70.0$ GPa, mass density $\rho = 2700.0$ kg m⁻³ and Poisson coefficient $\nu = 0.33$; the total weight is 19.91 kg.

From these properties, the ring frequency results equal to:

$$f_R = \frac{1}{2\pi R} \sqrt{\frac{E}{\rho}} = 800 \text{ Hz.} \quad (5.9)$$

The FE model is built using shell structural elements (ANSYS SHELL181); a total number of 6240 elements is used, resulting in 38430 degrees of freedom. For the stiffeners, three different cross-sections are analyzed: T , H and Ω shaped, as shown in Fig. 5.3; the cross-section properties are listed in Table 5.1. The stiffeners are modeled trying to keep constant the cross-section properties, in particular the Moments of Inertia, choosing the T shaped cross-section as reference. All the stiffeners are built using the same element property (ANSYS SHELL181) and the same material employed for the skin.

The periodic stiffeners are placed in the axial and in the circumferential direction, as shown in Fig. 5.4a-5.4b, respectively. Keeping the T shaped design for the stiffeners, two different inter-spacings are chosen: 6 cm and 10 cm (see Fig. 5.4). The effect of the shape on the vibro-acoustic response is analyzed keeping the stiffener inter-spacing equal to 6 cm. The information about the FE models of the stiffened panels is listed in Table 5.2.

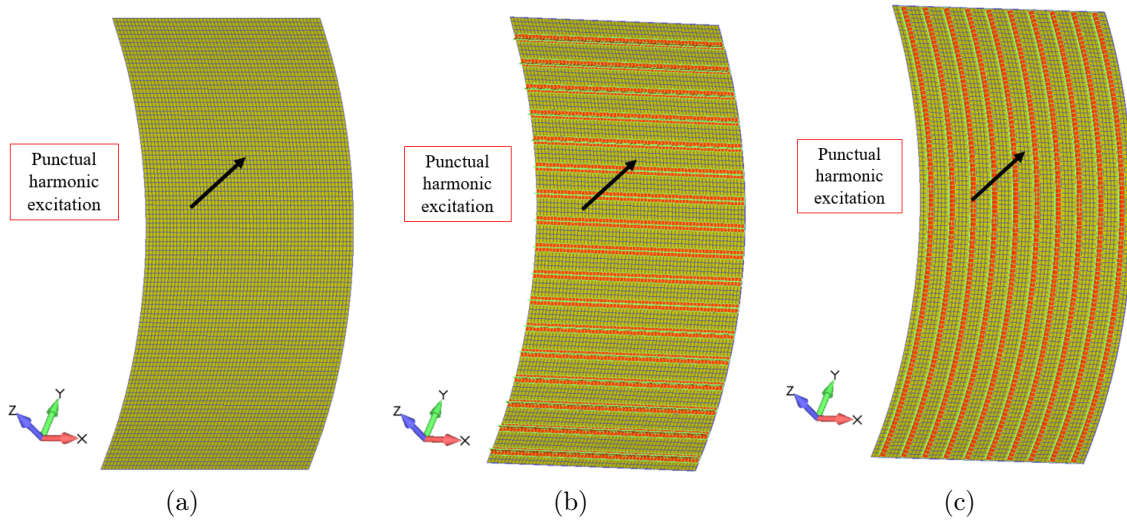


Figure 5.2 – FE models of the bare test case panel (a) and of the stiffened panels with T shaped stiffeners in axial (b) and circumferential (c) directions.

Table 5.2 – FE models details of the stiffened panels

| | Axial stiffeners | | | Circumferential stiffeners | | |
|-----------------------------|------------------|-------|--------|----------------------------|-------|--------|
| | Elements | DoF | Weight | Elements | DoF | Weight |
| | [-] | [-] | [kg] | [-] | [-] | [kg] |
| T shaped, 10 cm pitch | 8040 | 42090 | 25.8 | 8112 | 42210 | 26.1 |
| T shaped, 6 cm pitch | 9300 | 44652 | 29.9 | 9360 | 44730 | 30.1 |
| H shaped, 6 cm pitch | 11340 | 57096 | 30.8 | 11440 | 57330 | 31.0 |
| Ω shaped, 6 cm pitch | 11340 | 50874 | 30.4 | 11440 | 51030 | 30.6 |

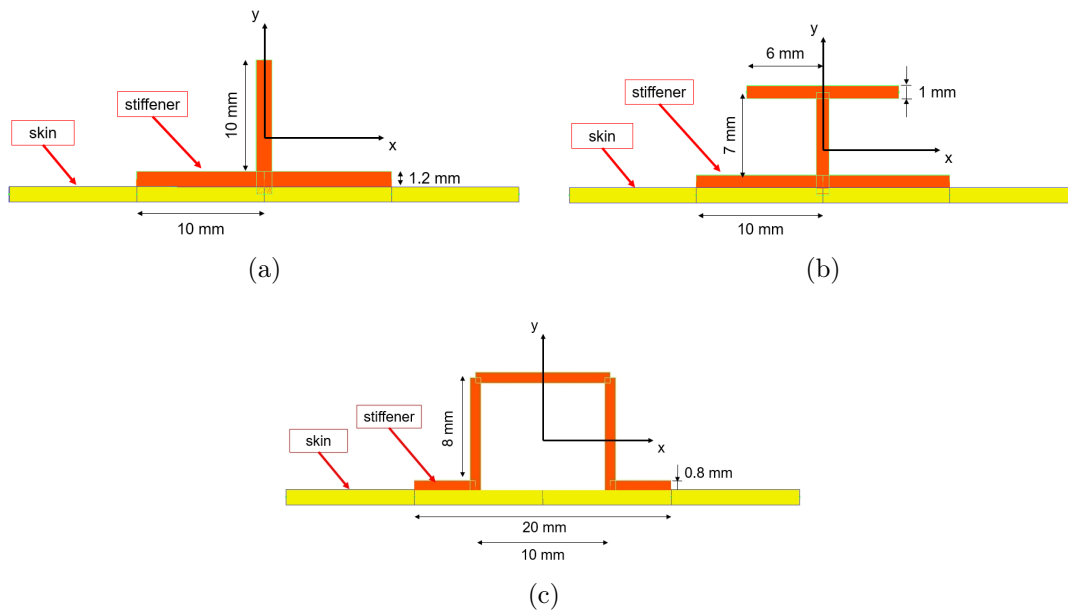


Figure 5.3 – Front view of the stiffeners cross-section: T shaped (a), H shaped (b) and Ω shaped (c).

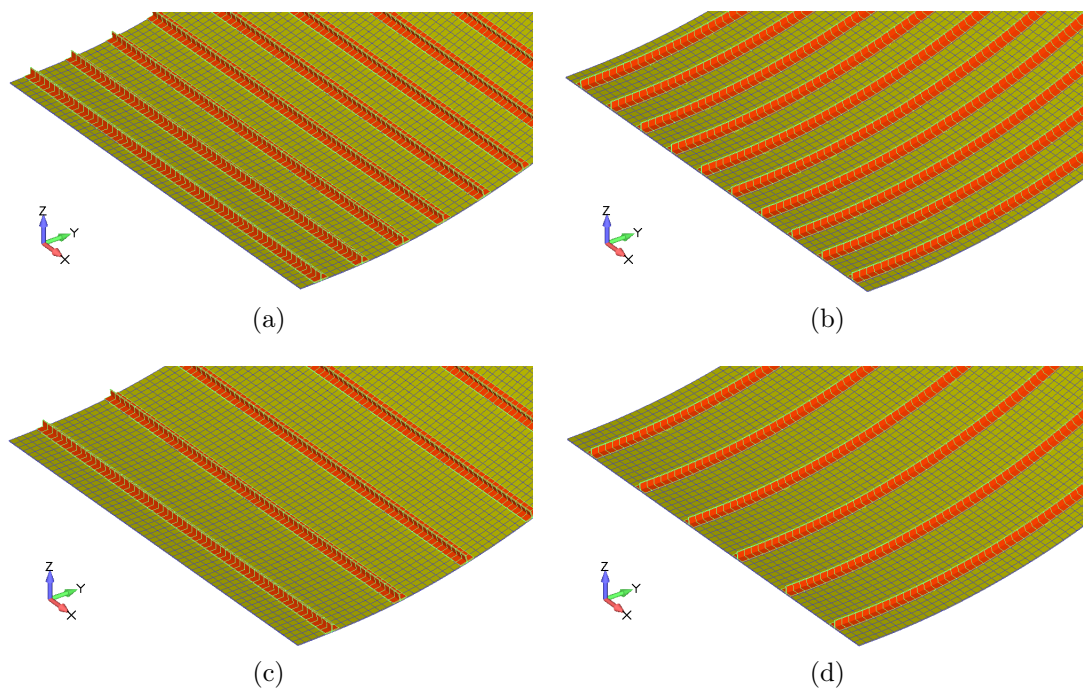


Figure 5.4 – FE models of the panels with T shaped stiffeners: 6 cm pitch in the axial (a) and circumferential (b) directions, 10 cm pitch in the axial (c) and circumferential (d) directions.

5.4 Wavenumber analysis

In this section, a wavenumber analysis is conducted. The aim is to evaluate the effects of both the stiffener inter-spacing and the stiffener shape in the wavenumber domain, making a comparison between the dispersion curves of the bare test case and the stiffened panel ones.

The dispersion curves are calculated in two orthogonal directions: axial and circumferential. In case of curved structures, the curvature effect on the dispersion curves is present when evaluating the axial wavenumber, while in the curvature direction the response of the structure is equivalent to the one of an infinite flat plate. The axial dispersion curve of the bare test case panel is compared to the one calculated with the Donnell-Mushtary theory (by solving the second kind of eigenvalue problem which comes from Eq. (5.7)). The dispersion curve in the circumferential direction is validated by using the Kirchhoff's thin plate theory, in which the flexural wavenumber is given by Eq. (4.8) and here rewritten:

$$k_f = \sqrt{\omega} \left(\frac{\rho h}{D} \right)^{1/4}.$$

The displacement fields are obtained by a full-FE analysis using an *in-home* MATLAB[®] code script; a punctual harmonic unit force is applied to excite the structure in the frequency range [50 Hz - 2000 Hz], with a frequency resolution of 5 Hz. A schematic representation of the punctual force is shown in Fig. 5.2. The location of the force is the same for all the considered configurations. The displacement field is introduced in Eq. (4.4) and correlated with the inhomogeneous propagating wave.

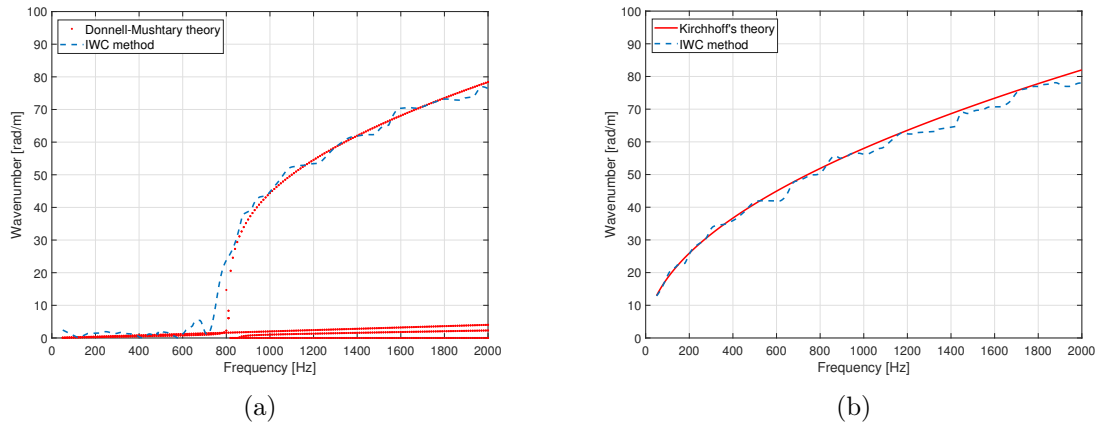


Figure 5.5 – Dispersion curves comparisons between the IWC method and the analytical theories: axial direction (a) and circumferential direction (b).

5.4.1 Bare test case configuration

The dispersion curves of the bare test case panel are plotted in Fig. 5.5. In Fig. 5.5a, a comparison with the Donnell-Mushtary theory is made; this analytical theory allows estimating all the propagating wavenumbers (longitudinal, shear and flexural wavenumber), while the IWC method allows to calculate the flexural wavenumber only. The Donnell-Mushtary theory predicts exactly the same value of the ring frequency estimated in Eq. (5.9) (800 Hz); the IWC method estimates a lower value for f_R , which is 770 Hz. This discrepancy is due to several reasons; first of all, the IWC method works better in the mid-high frequency range. Below the ring frequency, the evanescent flexural wave is dominant in terms of wavenumber amplitude, while the longitudinal and shear propagating wavenumbers are always present; estimating the flexural wavenumber, the IWC method is not precise enough in this region, in which the amplitude of the real part of the longitudinal, shear and bending wavenumbers are comparable. Starting from the ring frequency value and until the upper limit of the considered frequency range a good agreement is observed, as shown in Fig. 5.5a. The dispersion curve in the curvature direction is shown in Fig. 5.5b; a good agreement between the IWC method and the Kirchhoff's thin plate theory is observed in the whole frequency range.

5.4.2 Stiffened panels with T shaped stiffeners: inter-spacing effect

To evaluate the effect of the stiffener inter-spacing, a single shape of the stiffener cross-section is chosen as reference: T shaped. The dispersion curves in the two orthogonal directions are shown in Fig. 5.6 and compared with the bare test case configuration. Two different stiffened panels are analyzed: stiffeners placed along the axial direction and then along the circumferential one.

Firstly, the results of the stiffened panels with the stiffener inter-spacing of 6 cm are analysed. For what concerns the axially stiffened panel, when evaluating the wave propagation in the axial direction (along the stiffeners direction) the behavior of the

structure is dominated by the bending motion of the stiffeners, as shown in Fig. 5.6a. On the other hand, when the inhomogeneous wave travels in the circumferential direction the periodic distribution of stiffeners is encountered; the global behavior is dominated by the bending motion of the skin, but a band-gap is observed in the frequency range [720 Hz - 920 Hz] (see Fig. 5.6b).

The opposite behavior is observable for the circumferentially stiffened panel. The dispersion curve calculated in the orthogonal direction respect to the stiffeners main dimension presents a band-gap from 1030 Hz to 1380 Hz; the presence of the stiffeners has an influence on the ring frequency, which is identified at 550 Hz, as shown in Fig. 5.6a. The dispersion curve in the same direction of the stiffeners is shown in Fig. 5.6b; the structural behavior is dominated by the flexural motion of the stiffeners.

A similar behavior is obtained considering the stiffened panels with an inter-spacing of 10 cm, as reported in Fig. 5.6. In this case, the band-gap occurs in the low-frequency region; in Fig. 5.6a any band-gap is observable while in the circumferential direction the band-gap appears in the frequency range [250 Hz - 350 Hz] (see Fig. 5.6b). From the dispersion curves in the axial direction, the ring frequency can be identified around 600 Hz.

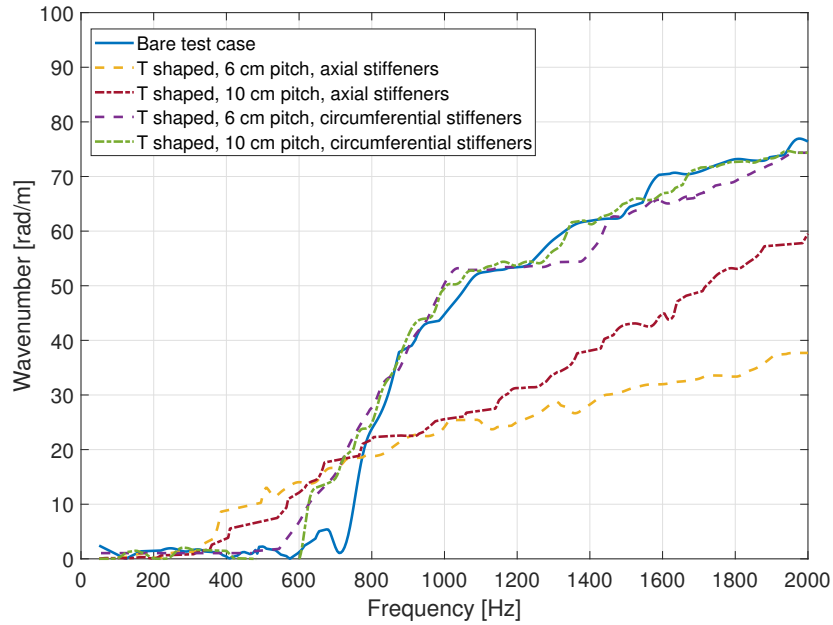
A similar global behavior is observed for both inter-spacings and compared to the bare test case. For what concerns the band-gaps, they are wider for the stiffened panels with 6 cm pitch between the stiffeners. The panels with an inter-spacing of 6 cm are stiffer than the others, as shown in Fig. 5.6, in which the dispersion curves have a smaller amplitude compared to the others, in the whole frequency range.

5.4.3 Effect of the stiffener cross-section shape on the dispersion curves

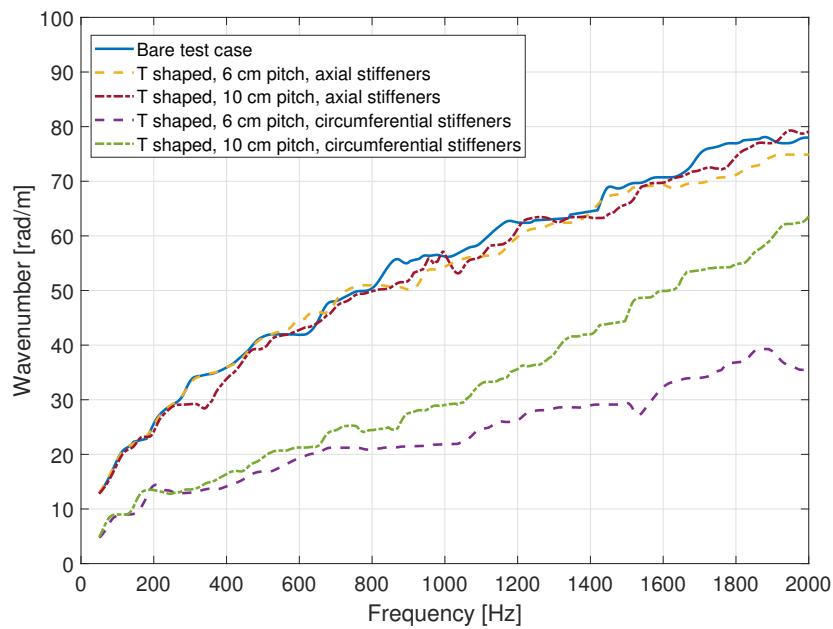
The effect of the stiffener cross-section shape on the dispersion curves is evaluated in this section. The pitch between the stiffeners is 6 cm for all the considered configurations. Three different stiffener cross-sections are analyzed and compared to the bare test case. The stiffened panels with the T shaped stiffeners have already been analyzed and discussed in section 5.4.2, and the dispersion curves shown in Fig. 5.6.

The second stiffener cross-section shape which has been analyzed is the H shape. The dispersion curves are shown in Fig. 5.7. When evaluating the dispersion curves in same direction of the stiffeners, the global structural behavior is dominated by the bending mode of the stiffeners for both axially and circumferentially stiffened panels. In Fig. 5.7a the dispersion curves in the axial direction are shown; for what concerns the circumferentially stiffened panels, a band-gap is open in the frequency range [900 Hz - 1150 Hz]. For the axially stiffened panel, the band-gap occurs when the dispersion curve is calculated in the circumferential direction, as shown in Fig. 5.7b; in this case, the band-gap is from 580 Hz to 725 Hz.

The third stiffener cross-section shape that has been investigated is the Ω shape; the corresponding dispersion curves are shown in Fig. 5.7. The dispersion curves of the axially stiffened panel exhibit a band-gap in the direction orthogonal to the stiffeners, as shown in Fig. 5.7b; the band-gap is present in the frequency range [480 Hz - 680 Hz]. The dispersion curve calculated in the same direction of the stiffeners is representative



(a)

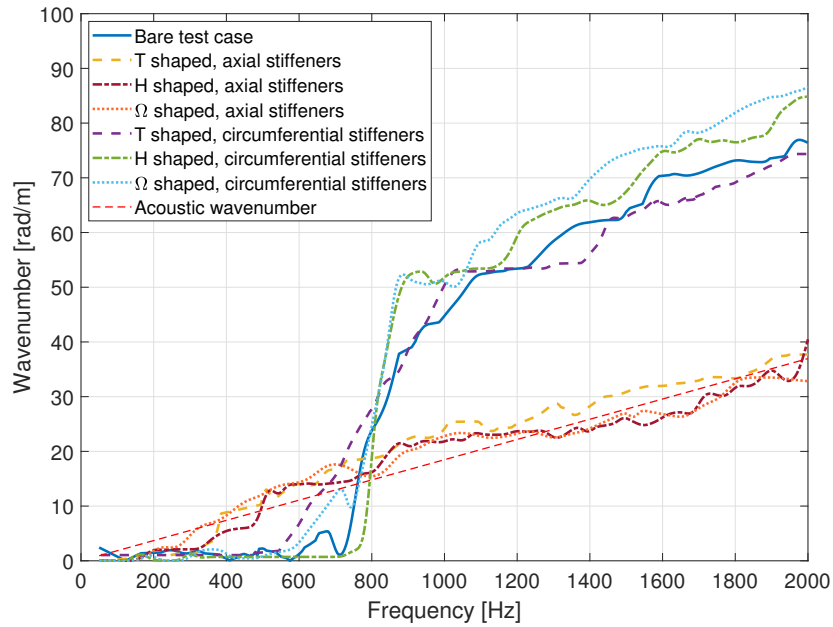


(b)

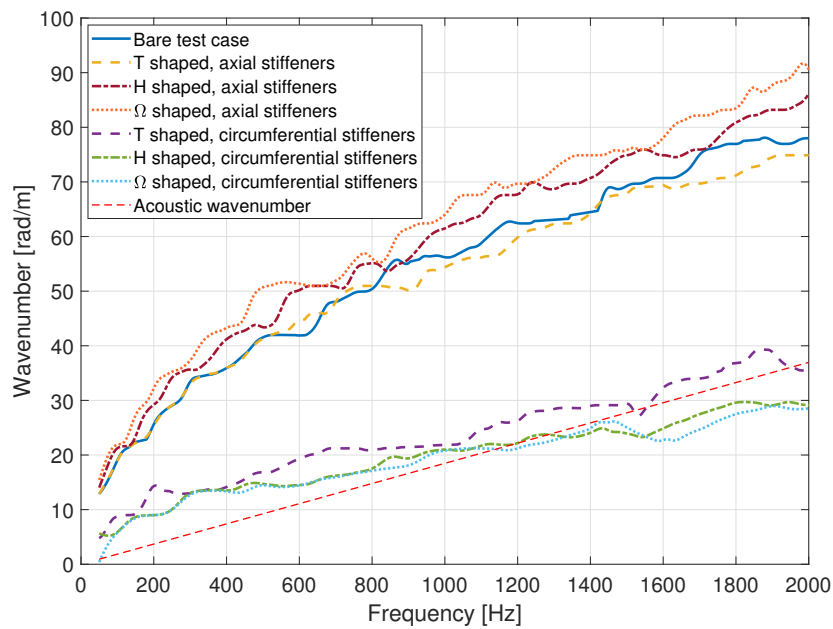
Figure 5.6 – Effect of stiffeners inter-spacing on the dispersion curves of the stiffened panels with T shaped stiffeners: axial direction (a) and circumferential direction (b).

of the dominating global bending mode of the stiffeners on the structural behavior (see Fig. 5.7a). For what concerns the circumferentially stiffened panel, a band-gap appears in the dispersion curve calculated in the axial direction; the band-gap is from 850 Hz to 1050 Hz, as shown in Fig. 5.7a. For this configuration, the estimated ring frequency is approximately 550 Hz. The dispersion curve in the curvature direction is influenced by the presence of the stiffeners in the same direction (see Fig. 5.7b).

The dispersion curves of all the considered configurations are summarized in Fig. 5.7. A similar behavior is observed for the different cross-section shapes of the stiffeners. When evaluating the waves propagation in the stiffener direction, the global behavior of the stiffened panels is dominated by the bending of the stiffeners themselves. Considering the dispersion curves in the axial direction for the circumferentially stiffened panels, the band-gaps are slightly dependent of the stiffener shape; the frequency range is larger in the case of T shaped stiffeners, while it is comparable for the other two shapes. The band-gap starts at a lower frequency value for the H and Ω shaped stiffeners and it shifts to a higher value for the T shaped stiffener. For what concerns the dispersion curves in the circumferential direction, a similar global trend is observed (see Fig. 5.7b). The dispersion curves of the circumferentially stiffened panels are very close to each other, denoting similar equivalent stiffness properties. For the axially stiffened panels, the dispersion curves follow the same trend of the bare test case panel; the band-gaps appear in three different frequency regions, but with a similar width of approximately 200 Hz.



(a)



(b)

Figure 5.7 – Dispersion curves of the stiffened panels: axial direction (a) and circumferential direction (b).

5.5 Sound transmission Loss calculations

In this section the effects of the different stiffeners are evaluated in terms of sound transmission. The numerical approach adopted for the acoustic simulations is given in [147, 164]. The structure is modeled using a periodic cell approach and using ANSYS SOLID45 elements. The calculations are carried out considering two excitation models: a purely diffuse acoustic field (DAF) and a simultaneous presence of a diffuse acoustic field and a turbulent boundary layer (DAF + TBL) to simulate more realistic loading conditions in some practical applications. The hypothesis of semi-infinite fluid termination is applied in the internal radiating domain and thus single acoustic cavity modes are not considered while a band-averaged result (in the classic SEA definition) is given [164]. This numerical approach is validated with measurements of real ribbed aircraft panels by Errico et al. [147].

The configurations described in Fig. 5.3 are analyzed under a diffuse acoustic field in Fig. 5.8. All the configurations with axial and circumferential stiffeners are considered. In all cases, two phenomena are observed. First, as before, the ring frequency of the shell is reduced and thus the first drop of sound transmission loss is shifted to a lower frequency. At the same time, an increase of transmission loss is evident in the region before the ring frequency because of the strong stiffening of the structure compared to the bare test case.

Among all the configurations, the main differences between the axial and circumferential stiffening are observed for the H shaped, in the whole frequency band after the ring frequency. Even though the differences are not important, the circumferential stiffening provides a slightly reduced sound radiation. Comparing the three shapes the T shaped seems to provide a higher sound transmission loss than the other configurations in the band between 1000 Hz and 2000 Hz.

Differently, when changing the excitation model as in Fig. 5.9, the differences between structures with axial and circumferential stiffeners become more important. The TBL model used is the one of Corcos [167], with flow direction always along the axis of the shell: $U_c = 190 \text{ m s}^{-1}$; stream-wise and cross-wise correlation coefficients equal to 0.125 and 0.81.

In contrast with the diffuse acoustic excitation, the convective nature of the TBL load requires stiffening elements in the direction of the flow; the axial stiffening provides a sound transmission loss at least 5 dB higher in the whole frequency band, as observable from Fig. 5.9. This can be explained by looking at the wavenumber transforms (see Fig. 5.10) of the structures in bare, axially-stiffened and ring-stiffened configurations. The response to turbulent boundary layer load, in fact, can be calculated starting from the product of the wavenumber transforms of the structure and the load model; the joint-acceptance is a fundamental parameter [168]. In Fig. 5.10 the wavenumber transforms show how the bare configuration is characterized by axially propagating waves (see Fig. 5.10a) with almost the same wavenumber as the convective ridge of the load model in Fig. 5.10d. At the same frequency, the ring stiffeners reduce the peaks of the circumferential wavenumbers in the circumferential direction by stiffening the structure (see Fig. 5.10c); only small changes are present on the ones in the axial direction, that couple very well with the convective load. Differently, when axial stiffeners are adopted

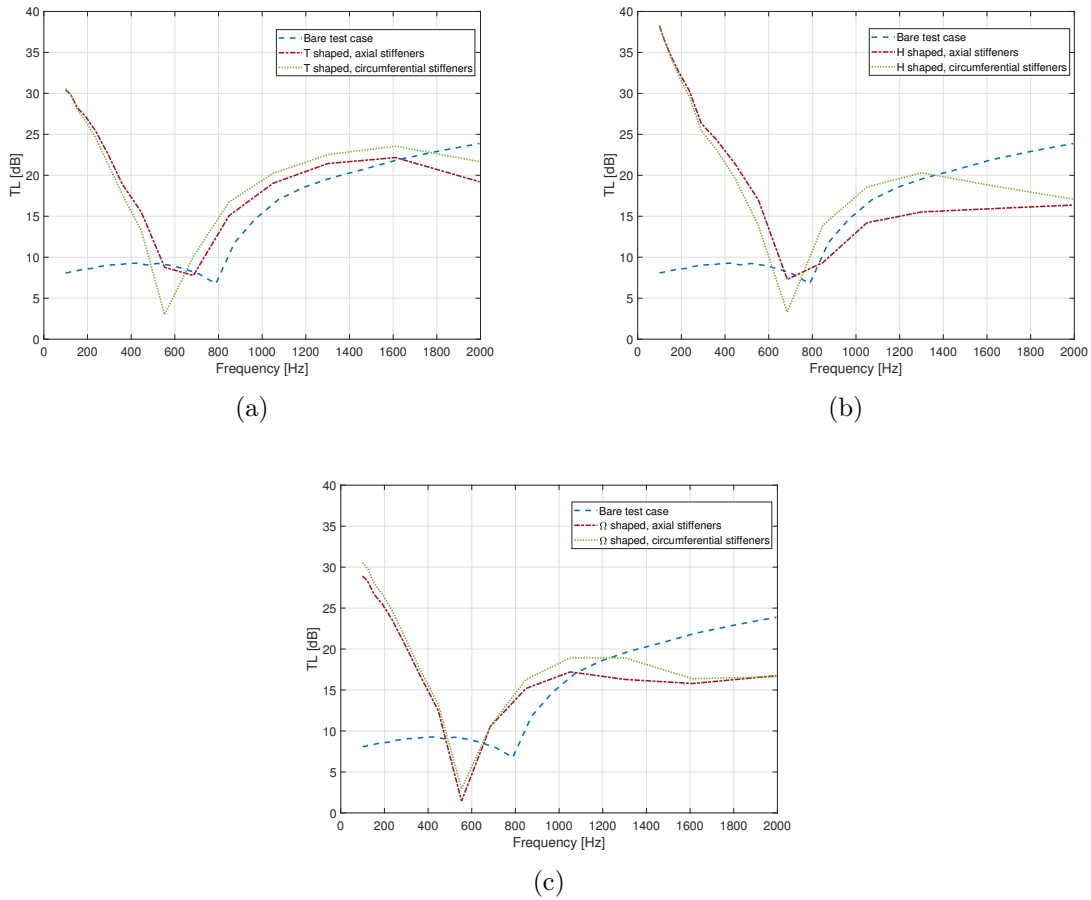


Figure 5.8 – Sound Transmission Loss for the stiffened panels under DAF excitation: T shaped (a), H shaped (b) and Ω shaped (c) stiffeners.

(see Fig.5.10b), the axial wavenumber peaks shift to lower frequencies (stiffer structure in this direction) and thus distance from the convective ridge of the TBL model at that frequency; the result is a reduced vibration and sound radiation of the shell.

It is also worth to observe how, with a convective load, the Ω shaped stiffeners give better results, in Fig. 5.9, due to their higher torsional stiffness, which induced a reduced local bending of the skins that contributes to the sound radiation.

5.5.1 The effect of pitch distance on sound radiation

The effect of the pitch distance on the sound radiation is analysed here for the T shaped stiffeners. Again, both a pure diffuse acoustic excitation and turbulent boundary layer load are considered. The main differences observed are in the low-frequency region. A slight variation of the ring frequency is followed by a global reduction of sound transmission loss that eventually approaches the one of the un-stiffened shell for increasing pitch. This is of course given by the reduced stiffening of the global structure compared to the cases with small pitch, as observed also in [162].

In particular, the axial stiffening being important when a turbulent boundary layer

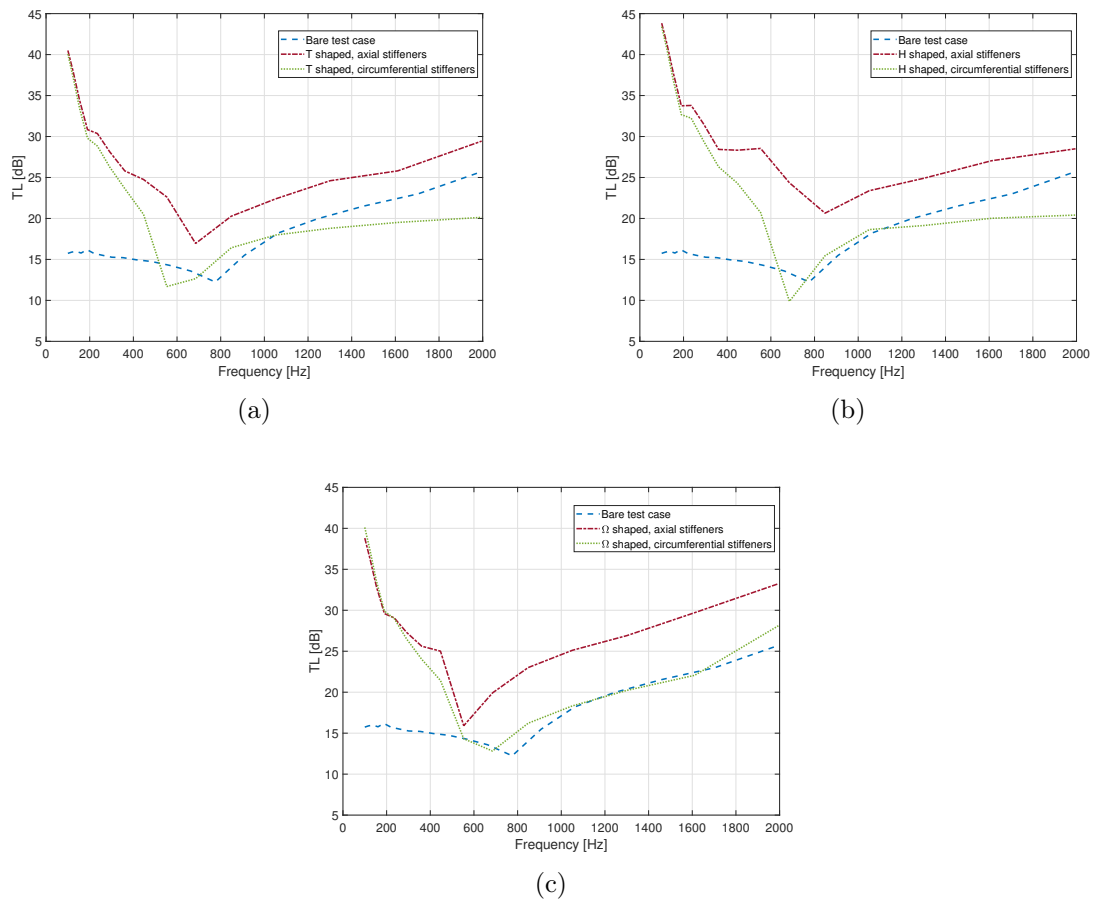


Figure 5.9 – Sound Transmission Loss for the stiffened panels under DAF and TBL excitations: T shaped (a), H shaped (b) and Ω shaped (c) stiffeners.

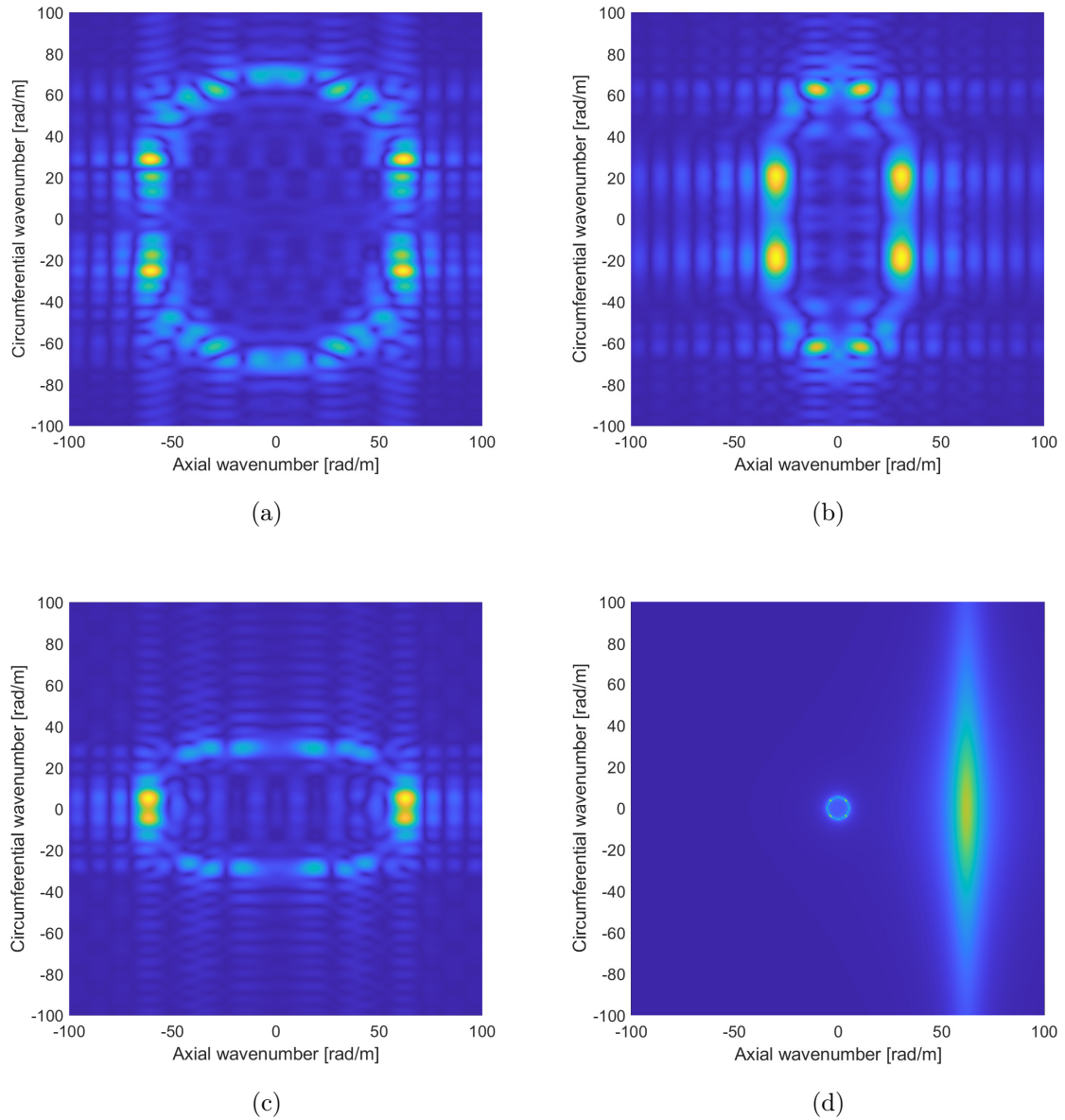


Figure 5.10 – Wavenumber transforms for the structures and the load model at 1.5 kHz: unstiffened shell (a), shell with axial T shaped stiffeners (b), shell with circumferential T shaped stiffeners (c) and DAF and TBL load spectra (d).

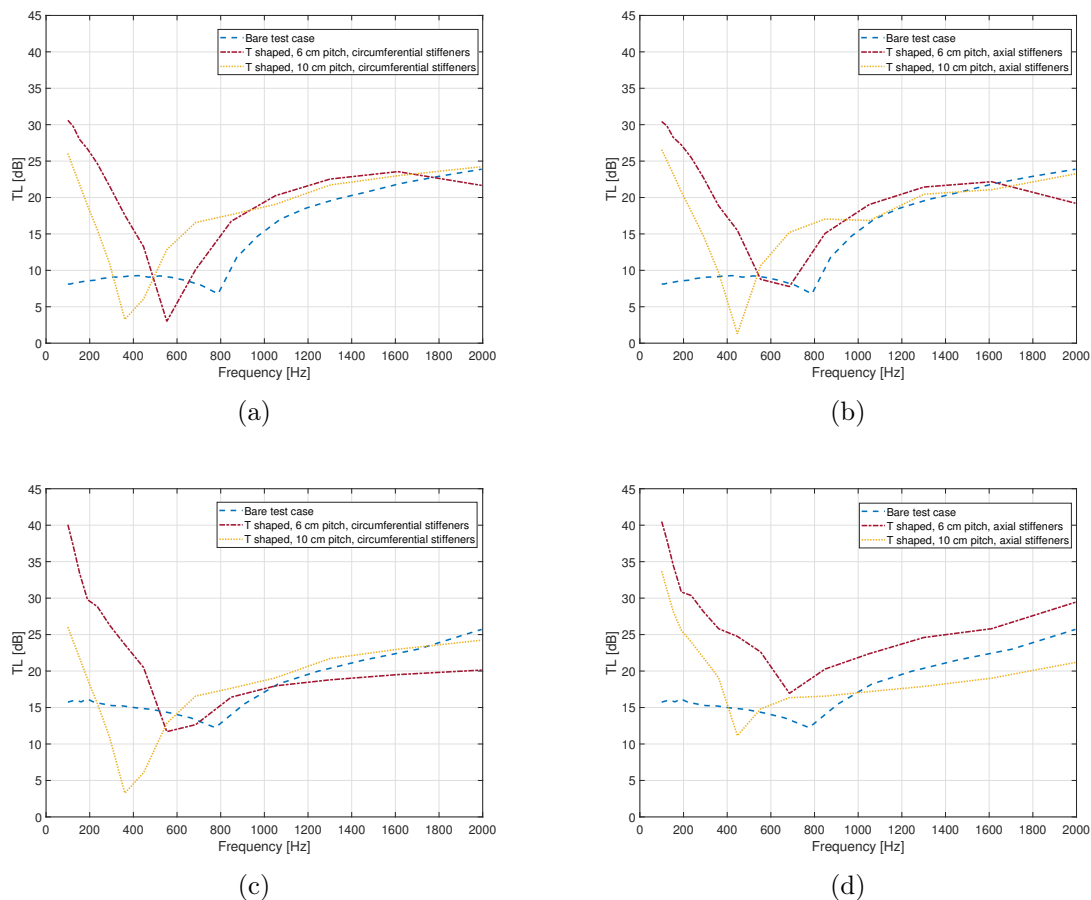


Figure 5.11 – Sound Transmission Loss for the T shaped stiffened panels with different pitch distances: circumferential stiffeners and DAF load (a), axial stiffeners and DAF load (b) circumferential stiffeners and DAF + TBL load (c) and axial stiffeners and DAF + TBL load (d).

excitation is applied, the different pitches induce a frequency broadband variation of the sound transmission loss (see Fig. 5.11d), in contrast to the mainly low-frequency effects in the cases of pure acoustic excitation (see Fig. 5.11b).

5.6 Conclusions

In this chapter, a vibroacoustic investigation of periodically stiffened shells is conducted, highlighting the effect of both stiffener cross-section shape and stiffener pitch.

For what concerns the wavenumber domain, an increase of the stiffness of the shells is observed when evaluating the dispersion curves in the same direction of the wave propagation, represented by a smaller amplitude of the estimated wavenumbers compared to the bare test case. The dispersion curves calculated in the orthogonal direction respect to the stiffeners main dimension follow the same global behavior of the unstiffened shell, except for the band-gaps frequency regions. A reduction of the ring frequency is observed in the dispersion curves of the stiffened shells. A reduction of the stiffeners inter-spacing reduces the amplitude of the estimated wavenumbers, showing

an increase of the global stiffness of the structure.

In terms of sound transmission loss, the main differences between axial and circumferential stiffening are observed with convective loads. While a reduction of the ring frequency is always present, the presence of axial stiffeners strongly reduces the sound radiation under turbulent boundary layer loads, while is giving a negligible difference for a diffuse acoustic field. The physical explanation is given by looking at the wave propagation in the structures and comparing it to the wavenumber spectra of the load model.

The results show that a reduction of pitch distance is beneficial for the sound transmission loss in the lowest frequency bands, due to the increased stiffness of the global structural system. When a convective load is considered, this effect is beneficial in the whole band and not just in the low frequencies.

Concluding remarks and perspectives

The main purpose of the presented work is addressed to the development of k -space based methods for vibro-acoustic problems. The guideline is to give a tool for the analysis and design of industrial structures and for a fast estimation of vibro-acoustic indicators. The main findings can be summarized as follows:

- The Inhomogeneous Wave Correlation method is successfully implemented to obtain the angle-dependent dispersion curves. The orthotropic behavior is described in both dispersion curves and k -space plots at fixed frequencies. The IWC method is applied to the experimental vibrational field of a 3D-printed sandwich panel, showing a good agreement with the predicted numerical dispersion curves. The dynamic behavior of the structure is fully-described by a reduced number measurement points, as shown in chapter 3.
- To avoid some limitations related to the plane wave assumption, an extended formulation of the IWC method is proposed in chapter 2, using a combination of Green's and Hankel's functions. The extended IWC approach shows a good prediction of the complex dispersion relations for both periodic narrow plates and laminated structures. The estimations of the damping loss factor are obtained for the considered configurations; the calculated values of η rapidly converge to the structural damping introduced in the FE models as the frequency increases. The feasibility of this method in estimating the wave attenuation in a structure is successfully demonstrated.
- The proposed approach allows to identify the local resonance frequency bands (stop-bands) due to the geometric periodicity of the structure, including the apparent stiffening or softening behavior of the structures in presence of mechanical stiffeners.
- A vibro-acoustic investigation of periodically stiffened shells is conducted, highlighting the effect of both the stiffener cross-section shape and the stiffener pitch. The IWC method allows to identify the global bending behavior and the stiffener effect on the dynamic response of the considered curved structures. The dispersion curves calculated in the orthogonal direction with respect to the stiffener main dimension follow the same global behavior of the unstiffened shell, except for the band-gap frequency regions. A reduction of the ring frequency is also captured in the dispersion curves of the stiffened shells, as expected. A reduction of the stiffener inter-spacing reduces the amplitude of the estimated wavenumbers, showing an increase of the global stiffness of the structure. This investigation on the stiffener cross-sections and stiffener pitch shows the feasibility of the proposed approach as a tool to compare different design choices.

- The applicability of 3D-printed small-scale resonators is demonstrated on relevant industrial structures. For all tested configurations, in the frequency band the resonators are tuned to work in, a drop in the dispersion curves is observed. The drops in the dispersion curves appear because the energy flow in the structure is strongly reduced and dissipated by the resonators. In chapter 4, a preliminary study on the industrial application of small-scale resonators on real aeronautic structures opens the possibility of attenuating the vibration levels in some specific frequency bands, working on the design of the resonators.
- The multi-modal behavior in terms of uncoupled flexural skin and flexural stiffener motions is described in the dispersion curves. This aspect allows to identify preferred propagation directions and the energy flows in the structures.
- The proposed approach can be used in an inverse way to estimate the frequency-dependent equivalent material properties of complex structures, when analytical models are not available or difficult to obtain.

The presented work touches several key points in the vibro-acoustic domain. The work has the potential to be implemented in an industrial environment in order to give an immediate comparison between different design choices. Some perspectives can be summarized in the next bullets in the hope of opening new scenarios and further developments in the near future.

- The inclusion of orthotropic Green's function in the new proposed approach for the IWC method to investigate any kind of structure and not only isotropic or slightly orthotropic media.
- Generalization of the IWC formulation for curved structures to conical shells, in order to cover any kind of geometry in the aerospace field.
- The IWC method can be used as a design tool. The proposed approach can be included in a parametric study in order to achieve an optimal design in the vibro-acoustic framework.
- This preliminary study on the industrial application of small-scale resonators on real aeronautic structures opens the possibility to attenuate the vibration level in some specific frequency bands, working on the design of the resonators. A deep investigation about the design of the resonators can be done in order to increase the wave attenuation and to enlarge both band-gaps and resonance zones.

Bibliography

Bibliography

- [1] R. Cherif, J.-D. Chazot, N. Atalla, Damping loss factor estimation of two-dimensional orthotropic structures from a displacement field measurement, *Journal of Sound and Vibration* 356 (2015) 61–71. doi:10.1016/j.jsv.2015.06.042.
- [2] C. Droz, O. Bareille, M. Ichchou, A new procedure for the determination of structural characteristics of sandwich plates in medium frequencies, *Composites Part B* 112 (2017) 103–111. doi:10.1016/j.compositesb.2016.12.023.
- [3] F. Ablitzer, C. Pézerat, J. M. Génevaux, J. Bégué, Identification of stiffness and damping properties of plates by using the local equation of motion, *Journal of Sound and Vibration* 333 (2014) 2454–2468. doi:10.1016/j.jsv.2013.12.013.
- [4] N. B. Roozen, L. Labelle, Q. Leclère, K. Ege, S. Alvarado, Non-contact experimental assessment of apparent dynamic stiffness of constrained-layer damping sandwich plates in a broad frequency range using a Nd:YAG pump laser and a laser doppler vibrometer, *Journal of Sound and Vibration* 395 (2017) 90–101. doi:10.1016/j.jsv.2017.02.012.
- [5] N. B. Roozen, Q. Leclère, K. Ege, Y. Gerges, Estimation of plate material properties by means of a complex wavenumber fit using Hankel’s functions and the image source method, *Journal of Sound and Vibration* 390 (2017) 257–271. doi:10.1016/j.jsv.2016.11.037.
- [6] D. Chronopoulos, B. Troclet, O. Bareille, M. Ichchou, Modeling the response of composite panels by a dynamic stiffness approach, *Composite Structures* 96 (2013) 111–120. doi:10.1016/j.compstruct.2012.08.047.
- [7] D. Chronopoulos, M. Ichchou, B. Troclet, O. Bareille, Efficient prediction of the response of layered shells by a dynamic stiffness approach, *Composite Structures* 97 (2013) 401–404. doi:10.1016/j.compstruct.2012.10.012.
- [8] J. G. McDaniel, W. S. Shepard-Jr., Estimation of structural wave numbers from spatially sparse response measurements, *The Journal of the Acoustical Society of America* 108 (2000) 1674. doi:10.1121/1.1310668.
- [9] J. McDaniel, P. Dupont, L. Savino, A wave approach to estimating frequency-dependent damping under transient loading, *Journal of Sound and Vibration* 231 (2000) 433–449. doi:10.1006/jsvi.1999.2723.
- [10] E. Nilsson, A. C. Nilsson, Prediction and measurement of some dynamic properties of sandwich structures with honeycomb and foam cores, *Journal of Sound and Vibration* 251 (2002) 409–430. doi:10.1006/jsvi.2001.4007.

- [11] J. Berthaut, M. N. Ichchou, L. Jezequel, *K*-space identification of apparent structural behavior, *Journal of Sound and Vibration* 280 (2005) 1125–1131. doi:10.1016/j.jsv.2004.02.044.
- [12] M. N. Ichchou, J. Berthaut, M. Collet, Multi-mode wave propagation in ribbed plates: Part I, wavenumber-space characteristics, *International Journal of Solids and Structures* 45 (2008) 1179–1195. doi:10.1016/j.ijsolstr.2007.09.032.
- [13] R. H. Lyon, R. G. DeJong, *Theory and Application of Statistical Energy Analysis*, Butterworth Heinemann, 1995.
- [14] S. Langley, Some perspective on wave-mode duality in SEA, *Proceeding of the IUTAM symposium on statistical energy analysis; 1997* (1997) 1–12doi:10.1007/978-94-015-9173-7_1.
- [15] D. Chronopoulos, M. Ichchou, B. Troclet, O. Bareille, Predicting the broadband response of a layered cone-cylinder-cone shell, *Composite Structures* 107 (2014) 149–159. doi:10.1016/j.compstruct.2013.07.055.
- [16] K. Grosh, E. J. Williams, Complex wave-number decomposition of structural vibrations, *The Journal of the Acoustical Society of America* 93 (1993) 836–848. doi:10.1121/1.405445.
- [17] S. A. Hambric, A. R. Barnard, *Tutorial on Wavenumber Transforms of Structural Vibration Fields*, *Proceeding of Internoise 2018*.
- [18] J. Berthaut, *Contribution à l'identification large bande des structures anisotropes: application aux tables d'harmonie des pianos*, PhD Thesis, 2004, École Centrale de Lyon, France.
- [19] M. N. Ichchou, J. Berthaut, M. Collet, Multi-mode wave propagation in ribbed plates. Part II: predictions and comparisons, *International Journal of Solids and Structures* 45 (2008) 1196–1216. doi:10.1016/j.ijsolstr.2007.08.020.
- [20] G. Inquiétude, *Numerical simulation of wave propagation in laminated composite plates*, PhD Thesis, 2008, École Centrale de Lyon, France.
- [21] D. J. Ewins, *Modal Testing: Theory and Practice*, Research Studies Press, London, 1984.
- [22] M. N. Ichchou, O. Bareille, J. Berthaut, Identification of effective sandwich structural properties via an inverse wave approach, *Engineering Structures* 30 (2008) 2591–2604. doi:10.1016/j.engstruct.2008.02.009.
- [23] R. Lajili, O. Bareille, M. L. Bouazizi, M. Ichchou, N. Bouhaddi, Composite beam identification using a variant of the inhomogeneous wave correlation method in presence of uncertainties, *Engineering Computations* 35 (2018) 2126–2164. doi:10.1108/EC-03-2017-0072.
- [24] L. Van Belle, C. Claeys, E. Deckers, W. Desmet, On the impact of damping on the dispersion curves of a locally resonant metamaterial: Modeling and experimental validation, *Journal of Sound and Vibration* 409 (2017) 1–23. doi:10.1016/j.jsv.2017.07.045.

-
- [25] B. Van Damme, A. Zemp, Measuring Dispersion Curve for Bending Waves in Beams: A Comparison of Spatial Fourier Transform and Inhomogeneous Wave Correlation, *Acta Acustica United with Acustica* 104 (2018) 228–234. doi:10.3813/AAA.919164.
- [26] B. Van Damme, A. Zemp, Energy Distribution and Exchange Between Spatial Harmonics in Bending Wave Phononic Crystals, *Physical Review Applied* 10 (2018) 014001. doi:10.1103/PhysRevApplied.10.014001.
- [27] L. Liu, M. I. Hussein, Wave motion in periodic flexural beams and characterization of the transition between bragg scattering and local resonance, *Journal of Applied Mechanics* 79 (2011) :011003. doi:10.1115/1.4004592.
- [28] A. Geslain, S. Raetz, M. Hiraiwa, M. Abi Ghanem, S. P. Wallen, A. Khanolkar, N. Boechler, J. Laurent, C. Prada, A. Duclos, P. Leclaire, J.-P. Groby, Spatial Laplace transform for complex wavenumber recovery and its application to the analysis of attenuation in acoustic systems, *Journal of Applied Physics* 120 (2016) 135107. doi:10.1063/1.4963827.
- [29] L. Schwan, A. Geslain, R. G. Vicente, J. P. Groby, Complex dispersion relation of surface acoustic waves at a lossy metasurface, *Applied Physics Letters* 110 (2017) 051902. doi:10.1063/1.4975120.
- [30] A. Cebrecos, R. G. Vicente, J. P. Groby, Complex dispersion relation recovery from 2d periodic resonant systems of finite size, *Applied Sciences* 9. doi:10.3390/app9030478.
- [31] J. Prisutova, K. Horoshenkov, J. P. Groby, B. Brouard, A method to determine the acoustic reflection and absorption coefficients of porous media by using modal dispersion in a waveguide, *The Journal of the Acoustical Society of America* 136 (2014) 2947–2958. doi:10.1121/1.4900598.
- [32] P. Margerit, A. Lebé, J.-F. Caron, X. Boutillon, High Resolution Wavenumber Analysis (HRWA) for the mechanical characterization of viscoelastic beams, *Journal of Sound and Vibration* 433 (2018) 198–211. doi:10.1016/j.jsv.2018.06.062.
- [33] P. Margerit, A. Lebé, J.-F. Caron, K. Ege, X. Boutillon, The high-resolution wavevector analysis for the characterization of the dynamic response of composite plates, *Journal of Sound and Vibration* 458 (2019) 177–196. doi:10.1016/j.jsv.2019.06.026.
- [34] R. Prony, *Essai experimental et analytique*, *Journal de École Polytechnique de Floréal et Plairial*.
- [35] Y. Hua, T. K. Sarkar, Matrix pencil method for estimating parameters of exponentially damped/undamped sinusoids in noise, *IEEE Transactions on Acoustics, Speech, and Signal Processing* 38 (1990) 814–824. doi:10.1109/29.56027.
- [36] V. F. Pisarenko, The retrieval of harmonics from a covariance function, *Geophysical Journal International* 33 (1973) 347–366. doi:10.1111/j.1365-246X.1973.tb03424.x.
- [37] R. O. Schimdt, A signal subspace approach to multiple emitter location and spectral estimation, PhD Thesis, 1981, Stanford University.
- [38] S. Shahbazpanahi, S. Valaee, M. H. Bastani, Distributed source localization using esprit algorithm, *IEEE Transactions on Acoustics, Speech, and Signal Processing* 49 (2001) 2169–2178. doi:10.1109/78.950773.

- [39] S. Rouquette, M. Najim, Estimation of frequencies and damping factors by two-dimensional esprit type methods, *IEEE Transactions on Acoustics, Speech, and Signal Processing* 49 (2001) 237–245. doi:10.1109/78.890367.
- [40] V. Emiya, B. David, R. Badeau, A parametric method for pitch estimation of piano tones, *IEEE International Conference of Acoustics and Signal Processing Proceeding* 1.
- [41] R. Badeau, R. Boyer, B. David, EDS parametric modeling and tracking of audio signals, *Proc. of the 5th International Conference on Digital Audio Effects (DAFx)* (2002) 139–144.
- [42] R. Badeau, B. David, G. Richard, High-resolution spectral analysis of mixtures of complex exponentials modulated by polynomials, *IEEE Transactions on Signal Processing* 54 (2006) 1341–1350.
- [43] L. Qiu, B. Liu, S. Yuan, Z. Su, Impact imaging of aircraft composite structure based on a model-independent spatial-wavenumber filter, *Ultrasonics* 64 (2016) 10–24. doi:10.1016/j.ultras.2015.07.006.
- [44] T. J. Plona, B. K. Sinha, S. Kostek, S.-K. Chang, Axisymmetric wave propagation in fluid-loaded cylindrical shells. ii: Theory versus experiment, *The Journal of the Acoustical Society of America* 92 (1992) 1144–1155. doi:10.1121/1.404041.
- [45] J. Vollmann, R. Breu, J. Dual, High-resolution analysis of the complex wave spectrum in a cylindrical shell containing a viscoelastic medium. part ii. experimental results versus theory, *The Journal of the Acoustical Society of America* 102 (1997) 909–920. doi:10.1121/1.419957.
- [46] R. Roy, T. Kailath, ESPRIT Estimation of Signal Parameters via Rotational Invariance Technique, *IEEE Transactions on Acoustics, Speech, and Signal Processing* 37 (1989) 984–995. doi:10.1109/29.32276.
- [47] R. Badeau, B. David, G. Richard, A new perturbation analysis for signal enumeration in rotational invariance techniques, *IEEE Transactions on Signal Processing* 54 (2006) 450–458. doi:10.1109/TSP.2005.861899.
- [48] K. Ege, X. Boutillon, B. David, High-resolution modal analysis, *Journal of Sound and Vibration* 325 (2009) 852–869. doi:10.1016/j.jsv.2009.04.019.
- [49] V. Fréour, F. Gautier, B. David, M. Curtit, Extraction and analysis of body-induced partials of guitar tones, *The Journal of the Acoustical Society of America* 138 (2015) 3930–3940. doi:10.1121/1.4937749.
- [50] R. Badeau, B. David, G. Richard, A new perturbation analysis for signal enumeration in rotational invariance techniques, *IEEE Transactions on Signal Processing* 54 (2006) 450–458. doi:10.1109/TSP.2005.861899.
- [51] P. J. Shorter, Wave propagation and damping in linear viscoelastic laminates, *The Journal of the Acoustical Society of America* 115 (2004) 1917–1925. doi:10.1121/1.1689342.
- [52] I. Bartoli, A. Marzani, F. Lanza di Scalea, E. Viola, Modeling wave propagation in damped waveguides of arbitrary cross-section, *Journal of Sound and Vibration* 295 (2006) 685–707. doi:10.1016/j.jsv.2006.01.021.

-
- [53] E. Barbieri, A. Cammarano, S. De Rosa, F. Franco, Waveguides of a composite plate by using the spectral finite element approach, *Journal of Vibration and Control* 15 (2009) 347–367. doi:10.1177/1077546307087455.
- [54] J. Cuenca, F. Gautier, L. Simon, The image source method for calculating the vibrations of simply supported convex polygonal plates, *Journal of Sound and Vibration* 322 (2009) 1048–1069. doi:10.1016/j.jsv.2008.11.018.
- [55] P. M. Morse, H. Feshbach, *Methods of Theoretical Physics*, McGraw-Hill, 1953.
- [56] R. Gunda, S. M. Vijayakar, R. Singh, Method of images for the harmonic response of beams and rectangular plates, *Journal of Sound and Vibration* 185 (1995) 791–808. doi:10.1006/jsvi.1995.0418.
- [57] A. W. Leissa, *Vibration of plates*, Acoustical Society of America, 1993.
- [58] K. F. Graff, *Wave Motion in Elastic Solids*, Oxford University Press, 1975.
- [59] J. B. Allen, D. A. Berkley, Image method for efficiently simulating small-room acoustics, *The Journal of the Acoustical Society of America* 65 (1979) 943–950. doi:10.1121/1.382599.
- [60] J. Cuenca, F. Gautier, L. Simon, Measurement of the complex bending stiffness of a flat panel covered with a viscoelastic layer using the image source method, *Proceeding of EURONOISE 2009*.
- [61] E. G. Williams, *Fourier Acoustics: Sound Radiation and Nearfield Acoustic Holography*, Academic Press, New York, 1999.
- [62] J. Cuenca, B. R. Mace, N. S. Ferguson, High-frequency vibrations of uncertain coupled beams using an image source approach, *Proceeding of NOVEM 2012*.
- [63] S. H. Yoon, P. A. Nelson, Estimation of acoustic source strength by inverse methods: Part II, experimental investigation of methods for choosing regularization parameters, *Journal of Sound and Vibration* 233 (2000) 665–701. doi:10.1006/jsvi.2000.2836.
- [64] J. Antoni, A bayesian approach to sound source reconstruction: Optimal basis, regularization, and focusing, *The Journal of the Acoustical Society of America* 131 (2012) 2873–2890. doi:10.1121/1.3685484.
- [65] A. Pereira, J. Antoni, Q. Leclère, Empirical bayesian regularization of the inverse acoustic problem, *Applied Acoustics* 97 (2015) 11–29. doi:10.1016/j.apacoust.2015.03.008.
- [66] C. Pézerat, J.-L. Guyader, Two inverse methods for localization of external sources exciting a beam, *Acta Acustica* 3 (1995) 1–10.
- [67] C. Pézerat, J.-L. Guyader, Force analysis technique: reconstruction of force distribution on plates, *Acta Acustica united with Acustica* 86 (2000) 322–332.
- [68] M. C. Djamaa, N. Ouelaa, C. Pézerat, J.-L. Guyader, Reconstruction of a distributed force applied on a thin cylindrical shell by an inverse method and spatial filtering, *Journal of Sound and Vibration* 301 (2007) 560–575. doi:10.1016/j.jsv.2006.10.021.

- [69] C. Renzi, C. Pézerat, J.-L. Guyader, Vibratory source identification by using the finite element model of a subdomain of a flexural beam, *Journal of Sound and Vibration* 332 (2013) 545–562. doi:10.1016/j.jsv.2012.09.003.
- [70] F. Chevillotte, Q. Leclère, N. Totaro, C. Pézerat, P. Souchotte, Identification d'un champ de pression pariétale induit par un écoulement turbulent à partir de mesures vibratoires, 10ème Congrès Français d'Acoustique, 2010, Lyon, France.
- [71] C. Pézerat, J.-L. Guyader, Identification of vibration sources, *Applied Acoustics* 61 (2000) 309–324. doi:10.1016/S0003-682X(00)00036-0.
- [72] O. Grosset, C. Pézerat, J.-H. Thomas, F. Ablitzer, Introduction of the fluid-structure coupling into the force analysis technique, *International Journal of Mechanical and Mechatronics Engineering* 11 (2017) 342–346. doi:10.5281/zenodo.1128775.
- [73] Q. Leclère, C. Pézerat, Vibration source identification using corrected finite difference schemes, *Journal of Sound and Vibration* 331 (2012) 1366–1377. doi:10.1016/j.jsv.2011.11.002.
- [74] F. Ablitzer, C. Pézerat, B. Lascoup, J. Brocaïl, Identification of the flexural stiffness parameters of an orthotropic plate from the local dynamic equilibrium without a priori knowledge of the principal directions, *Journal of Sound and Vibration* 404 (2017) 31–46. doi:10.1016/j.jsv.2017.05.037.
- [75] V. Koloušek, R. F. McLean, *Dynamics in engineering structures*, Butterworths, 1973.
- [76] W. T. Thomson, Transmission of elastic waves through a stratified solid medium, *Journal of Applied Physics* 21 (1950) 89–93. doi:10.1063/1.1699629.
- [77] B. R. Mace, D. Duhamel, M. J. Brennan, L. Hinke, Finite element prediction of wave motion in structural waveguides, *Journal of the Acoustical Society of America* 117 (2005) 2835–2843. doi:10.1121/1.1887126.
- [78] D. Duhamel, B. R. Mace, M. J. Brennan, Finite element analysis of the vibrations of waveguides and periodic structures, *Journal of Sound and Vibration* 294 (2006) 205–220. doi:10.1016/j.jsv.2005.11.014.
- [79] L. Brillouin, *Wave Propagation in Periodic Structures: Electric Filters and Crystal Lattices*, Dover Publications, 1953.
- [80] R. M. Orris, M. Petyt, A finite element study of harmonic wave propagation in periodic structures, *Journal of Sound and Vibration* 33 (1974) 223–236. doi:10.1016/S0022-460X(74)80108-2.
- [81] A. Abdel-Rahman, *Matrix analysis of wave propagation in periodic systems*, PhD Thesis, 1979, University of Southampton.
- [82] D. J. Thompson, Wheel-rail noise generation, Part I: Introduction and interaction model, *Journal of Sound and Vibration* 161 (1993) 387–400. doi:10.1006/jsvi.1993.1082.
- [83] D. J. Thompson, Wheel-rail noise generation, Part II: Wheel vibration, *Journal of Sound and Vibration* 161 (1993) 401–419. doi:10.1006/jsvi.1993.1083.

-
- [84] D. J. Thompson, Wheel-rail noise generation, Part III: Rail vibration, *Journal of Sound and Vibration* 161 (1993) 421–446. doi:10.1006/jsvi.1993.1084.
- [85] L. Gry, Dynamic modelling of railway track based on wave propagation, *Journal of Sound and Vibration* 195 (1996) 477–505. doi:10.1006/jsvi.1996.0438.
- [86] B. P. Silva, J.-M. Mencik, J. R. F. Arruda, Wave finite element-based superelements for forced response analysis of coupled systems via dynamic substructuring, *International Journal for Numerical Methods in Engineering* 108 (2016) 453–476. doi:10.1002/nme.5176.
- [87] L. Houillon, M. N. Ichchou, L. Jezequel, Wave motion in thin-walled structures, *Journal of Sound and Vibration* 281 (2005) 483–507. doi:10.1016/j.jsv.2004.01.020.
- [88] J. M. Mencik, M. N. Ichchou, Multi-mode propagation and diffusion in structures through finite elements, *European Journal of Mechanics - A/Solids* 24 (2005) 877–898. doi:10.1016/j.euromechsol.2005.05.004.
- [89] M. N. Ichchou, S. Akrouf, J.-M. Mencik, Guided waves group and energy velocities via finite elements, *Journal of Sound and Vibration* 305 (2007) 931–944. doi:10.1016/j.jsv.2007.05.007.
- [90] J. M. Mencik, M. N. Ichchou, Wave finite elements in guided elastodynamics with internal fluid, *International Journal of Solids and Structures* 44 (2007) 2148–2167. doi:10.1016/j.ijsolstr.2006.06.048.
- [91] J. M. Mencik, M. N. Ichchou, A substructuring technique for finite element wave propagation in multi-layered systems, *Computer Methods in Applied Mechanics and Engineering* 197 (2008) 505–523. doi:10.1016/j.cma.2007.08.002.
- [92] W. J. Zhou, M. N. Ichchou, J. M. Mencik, Analysis of wave propagation in cylindrical pipes with local inhomogeneities, *Journal of Sound and Vibration* 319 (2009) 335–354. doi:10.1016/j.jsv.2008.05.039.
- [93] F. Errico, M. Ichchou, S. D. Rosa, O. Bareille, F. Franco, The modelling of the flow-induced vibrations of periodic flat and axial-symmetric structures with a wave-based method, *Journal of Sound and Vibration* 424 (2018) 32–47. doi:10.1016/j.jsv.2018.03.012.
- [94] Y. Waki, B. R. Mace, M. J. Brennan, Flexural wave propagation in a plate stripe with free boundaries using a Wave Finite Element method, *Proc. of the 36th International Congress and Exposition on Noise Control Engineering (INTER-NOISE 2007)*, Istanbul, Turkey.
- [95] Y. Waki, B. R. Mace, M. J. Brennan, Vibration analysis of a tyre using the Wave Finite Element method, *Proc. of the 19th International Congress on Acoustics (ICA 2007)*, Madrid, Spain.
- [96] Y. Waki, B. R. Mace, M. J. Brennan, Numerical issues concerning the wave and finite element method for free and forced vibrations of waveguides, *Journal of Sound and Vibration* 327 (2009) 92–108. doi:10.1016/j.jsv.2009.06.005.

- [97] B. R. Mace, E. Manconi, Modelling wave propagation in two-dimensional structures using a wave/finite element technique, Proc. of COMPDYN 2007: Computational Methods in Structural Dynamics and Earthquake Engineering (COMPDYN 2007), Crete, Greece.
- [98] E. Manconi, B. R. Mace, Modelling wave propagation in two dimensional structures using finite element analysis, Journal of Sound and Vibration 318 (2008) 884–902. doi:10.1016/j.jsv.2008.04.039.
- [99] E. Manconi, Modelling wave propagation in two-dimensional structures using a wave/finite element method, PhD Thesis, 2008, Department of Industrial Engineering, University of Parma.
- [100] E. Manconi, B. R. Mace, Wave propagation in axisymmetric structures from finite element analysis, Proc. of COMPDYN 2009: Computational Methods in Structural Dynamics and Earthquake Engineering (COMPDYN 2009), Rhodes, Greece.
- [101] E. Manconi, B. R. Mace, Wave characterization of cylindrical and curved panels using a finite element method, The Journal of the Acoustical Society of America 125 (2009) 154–163. doi:10.1121/1.3021418.
- [102] E. Manconi, B. R. Mace, Estimation of the loss factor of viscoelastic laminated panels from finite element analysis, Journal of Sound and Vibration 329 (2010) 3928–3939. doi:10.1016/j.jsv.2010.04.014.
- [103] E. Manconi, B. R. Mace, R. Garziera, The loss-factor of pre-stressed laminated curved panels and cylinders using a wave and finite element method, Journal of Sound and Vibration 332 (2013) 1704–1711. doi:10.1016/j.jsv.2012.09.039.
- [104] J. M. Renno, B. R. Mace, On the forced response of waveguides using the wave and finite element method, Journal of Sound and Vibration 329 (2010) 5474–5488. doi:10.1016/j.jsv.2010.07.009.
- [105] J. M. Renno, B. R. Mace, Calculating the forced response of two-dimensional homogeneous media using the wave and finite element method, Journal of Sound and Vibration 330 (2011) 5913–5927. doi:10.1016/j.jsv.2011.06.011.
- [106] J. M. Renno, B. R. Mace, Calculation of reflection and transmission coefficients of joints using a hybrid finite element/wave and finite element approach, Journal of Sound and Vibration 332 (2013) 2149–2164. doi:10.1016/j.jsv.2012.04.029.
- [107] M. Ruzzene, F. Scarpa, F. Soranna, Wave beaming effects in two-dimensional cellular structures, Smart Materials and Structures 12 (2003) 363–372. doi:10.1088/0964-1726/12/3/307.
- [108] V. D’Alessandro, Investigation and assessment of the Wave and Finite Element method for structural waveguides, PhD Thesis, 2014, Department of Industrial Engineering, University of Naples.
- [109] F. Bloch, Über die quantenmechanik der elektronen in kristallgittern, Zeitschrift für Physik 52 (1929) 555–600. doi:10.1007/BF01339455.
- [110] G. Floquet, Sur les équations différentielles linéaires à coefficients périodiques, Annales scientifiques de l’École normale supérieure 12 (1883) 47–88.

-
- [111] H. Oberst, Über die dämpfung der biegeschwingungen dünner bleche durch fest haftende beläge, *Acta Acustica united with Acustica* 2 (1952) 181–194.
- [112] H. Oberst, Über die dämpfung der biegeschwingungen dünner bleche durch fest haftende beläge II, *Acta Acustica united with Acustica* 4 (1954) 433–444.
- [113] S. Thwaites, N. H. Clark, Non-destructive testing of honeycomb sandwich structures using elastic waves, *Journal of Sound and Vibration* 187 (1995) 253–269. doi:10.1006/jsvi.1995.0519.
- [114] G. Papagiannopoulos, G. Hatzigeorgiou, On the use of the half-power bandwidth method to estimate damping in building structures, *Soil Dynamics and Earthquake Engineering* 31 (2011) 1075–1079. doi:10.1016/j.soildyn.2011.02.007.
- [115] B. C. Bloss, M. D. Rao, Estimation of frequency-averaged loss factor by the power injection method and the impulse response decay methods, *Journal of the Acoustical Society of America* 117 (2005) 240–249. doi:10.1121/1.1835512.
- [116] D. Bies, S. Hamid, In situ determination of loss and coupling loss factors by the power injection method, *Journal of Sound and Vibration* 70 (1980) 187–204. doi:10.1016/0022-460X(80)90595-7.
- [117] J. Ormondroyd, J. P. Den Hartog, The theory of the vibration absorber, *Transactions of the Americal Society of Mechanical Engineers* 49 (1928) 9–22.
- [118] J. C. Snowdon, Steady-state behavior of the dynamic absorber, *The Journal of the Acoustical Society of America* 31 (1959) 1096–1103. doi:10.1121/1.1907832.
- [119] A. G. Thompson, Optimum tuning and damping of a dynamic vibration absorber applied to a force excited and damped primary system, *Journal of Sound and Vibration* 77 (1981) 403–415. doi:10.1016/S0022-460X(81)80176-9.
- [120] R. Rana, T. Soong, Parametric study and simplified design of tuned mass dampers, *Engineering Structures* 20 (1998) 193–204. doi:10.1016/S0141-0296(97)00078-3.
- [121] M. A. Lang, C. L. Dym, Optimal acoustic design of sandwich panels, *The Journal of the Acoustical Society of America* 57 (1975) 1481–1487. doi:10.1121/1.380588.
- [122] F. Franco, K. A. Cunefare, M. Ruzzene, Structural-acoustic optimization of sandwich panels, *Journal of Vibration and Acoustics* 129 (2006) 330–340. doi:10.1115/1.2731410.
- [123] B. L. Clarkson, M. F. Ranky, Modal density of honeycomb plates, *Journal of Sound and Vibration* 91 (1983) 103–118. doi:10.1016/0022-460X(83)90454-6.
- [124] J. N. Reddy, *Mechanics of laminated composite plates and shells: theory and analysis*, CRC press, 2003.
- [125] K. Renji, P. S. Nair, S. Narayanan, Modal density of composite honeycomb sandwich panels, *Journal of Sound and Vibration* 195 (1996) 687–699. doi:10.1006/jsvi.1996.0456.
- [126] S. Ghinet, N. Atalla, Vibro-acoustic behaviors of flat sandwich composite panels, *Transactions of the Canadian Society for Mechanical Engineering* 30 (2006) 473–493. doi:10.1139/tcsme-2006-0030.

- [127] S. Ghinet, N. Atalla, Modeling thick composite laminate and sandwich structures with linear viscoelastic damping, *Computers & Structures* 89 (2011) 1547–1561. doi:10.1016/j.compstruc.2010.09.008.
- [128] L. Guillaumie, Vibroacoustic flexural properties of symmetric honeycomb sandwich panels with composite faces, *Journal of Sound and Vibration* 343 (2015) 71–103. doi:10.1016/j.jsv.2014.12.026.
- [129] D. Chronopoulos, M. Ichchou, B. Troclet, O. Bareille, Computing the broadband vibroacoustic response of arbitrarily thick layered panels by a wave finite element approach, *Applied Acoustics* 77 (2014) 89–98. doi:10.1016/j.apacoust.2013.10.002.
- [130] C. Droz, Z. Zergoune, R. Boukadia, O. Bareille, M. N. Ichchou, Vibro-acoustic optimisation of sandwich panels using the wave/finite element method, *Composite Structures* 156 (2016) 108–114. doi:10.1016/j.compstruct.2016.01.025.
- [131] J. S. R. Marple, *Digital Spectral Analysis with Applications*, Prentice-Hall, Englewood Cliffs, NJ, 1987.
- [132] N. S. Ferguson, C. R. Halkyard, B. G. Mace, K. H. Heron, The estimation of wavenumbers in two dimensional structures, *Proceeding of ISMA 2002 2* (2002) 799–806.
- [133] U. Orrenius, S. Finnveden, Calculation of wave propagation in rib-stiffened plate structures, *Journal of Sound and Vibration* 198 (1996) 203–224. doi:10.1006/jsvi.1996.0565.
- [134] L. Maxit, Wavenumber space and physical space responses of a periodically ribbed plate to a point drive: A discrete approach, *Applied Acoustics* 70 (2009) 563–578. doi:10.1016/j.apacoust.2008.06.012.
- [135] G. Tufano, C. Droz, O. Bareille, A.-M. Zine, B. Pluymers, W. Desmet, M. Ichchou, Wavenumber identification technique for axial-symmetric structures, *Proceeding of ISMA 2018* (2018) 4499–4508.
- [136] C. Claeys, K. Vergote, P. Sas, W. Desmet, On the potential of tuned resonators to obtain low-frequency vibrational stop bands in periodic panels, *Journal of Sound and Vibration* 332 (2013) 1418–1436. doi:10.1016/j.jsv.2012.09.047.
- [137] C. Claeys, P. Sas, W. Desmet, On the acoustic radiation efficiency of local resonance based stop band materials, *Journal of Sound and Vibration* 333 (2014) 3203–3213. doi:10.1016/j.jsv.2014.03.019.
- [138] E. G. Williams, B. H. Houston, J. A. Bucaro, Experimental investigation of the wave propagation on a point-driven, submerged capped cylinder using k-space analysis, *The Journal of the Acoustical Society of America* 87 (1990) 513–522. doi:10.1121/1.398922.
- [139] D. M. Photiadis, B. H. Houston, E. G. Williams, Wave-number space response of a near periodically ribbed shell, *The Journal of the Acoustical Society of America* 101 (1997) 877–886. doi:10.1121/1.418108.
- [140] D. M. Photiadis, J. A. Bucaro, B. H. Houston, The effect of internal oscillators on the acoustic response of a submerged shell, *The Journal of the Acoustical Society of America* 101 (1997) 895–899. doi:10.1121/1.418048.

-
- [141] V. Meyer, L. Maxit, Y. Renou, C. Audoly, Experimental investigation of the influence of internal frames on the vibroacoustic behavior of a stiffened cylindrical shell using wavenumber analysis, *Mechanical Systems and Signal Processing* 93 (2017) 104–117. doi:10.1016/j.ymssp.2017.01.039.
- [142] A. Nateghi, L. Van Belle, C. Claeys, E. Deckers, B. Pluymers, W. Desmet, Wave propagation in locally resonant cylindrically curved metamaterial panels, *International Journal of Mechanical Sciences* 127 (2017) 73–90. doi:10.1016/j.ijmecsci.2016.07.003.
- [143] A. Nateghi, L. Sangiuliano, C. Claeys, E. Deckers, B. Pluymers, W. Desmet, Design and experimental validation of a metamaterial solution for improved noise and vibration behavior of pipes, *Journal of Sound and Vibration* 455 (2019) 96–117. doi:10.1016/j.jsv.2019.05.009.
- [144] C. Droz, O. Robin, M. Ichchou, N. Atalla, Improving sound transmission loss at ring frequency of a curved panel using tunable 3D-printed small-scale resonators, *Journal of Acoustical Society of America* 145(1) (2019) 72–78. doi:10.1121/1.5088036.
- [145] C. Droz, R. F. Boukadia, M. Ichchou, W. Desmet, Diffusion-based design of locally resonant sub-systems using a reduced wave finite element framework, *Proceeding of ISMA 2018* (2018) 2983–2995.
- [146] J. H. Rindel, Dispersion and absorption of structure-born sound in acoustically thick plates, *Applied Acoustics* 41 (1994) 97–111. doi:10.1016/0003-682X(94)90063-9.
- [147] F. Errico, G. Tufano, O. Robin, N. Guenfoud, M. Ichchou, N. Atalla, Simulating the sound transmission loss of complex curved panels with attached noise control materials using periodic cell wavemodes, *Applied Acoustics* 156 (2019) 21–28. doi:10.1016/j.apacoust.2019.06.027.
- [148] J.-H. Lee, J. Kim, Analysis of sound transmission through periodically stiffened panels by space harmonic expansion, *Journal of Sound and Vibration* 251 (2002) 349–366. doi:10.1006/jsvi.2001.4008.
- [149] A. Mejdji, N. Atalla, Dynamic and acoustic response of bidirectionally stiffened plates with eccentric stiffeners subject to airborne and structure-borne excitations, *Journal of Sound and Vibration* 329 (2010) 4422–4439. doi:10.1016/j.jsv.2010.04.007.
- [150] T. R. Lin, J. Pan, A closed form solution for the dynamic response of finite ribbed plates, *The Journal of the Acoustical Society of America* 119 (2010) 917–925. doi:10.1121/1.2146111.
- [151] R. N. Arnold, G. B. Warburton, M. Born, Flexural vibrations of the walls of thin cylindrical shells having freely supported ends, *Proceedings of the Royal Society of London. Series A. Mathematical and Physical Sciences* 197 (1949) 238–256. doi:10.1098/rspa.1949.0061.
- [152] W. H. Hoppmann, Some characteristics of the flexural vibrations of orthogonally stiffened cylindrical shells, *The Journal of the Acoustical Society of America* 30 (1958) 77–82. doi:10.1121/1.1909392.
- [153] B. A. J. Mustafa, R. Ali, Prediction of natural frequency of vibration of stiffened cylindrical shells and orthogonally stiffened curved panels, *Journal of Sound and Vibration* 113 (1987) 317–327. doi:10.1016/S0022-460X(87)80218-3.

- [154] B. A. J. Mustafa, R. Ali, Sound transmission through curved aircraft panels with stringer and ring frame attachments, *Journal of Sound and Vibration* 300 (2007) 949–973. doi:10.1016/j.jsv.2006.09.008.
- [155] M. L. Rumerman, Vibration and wave propagation in ribbed plates, *The Journal of the Acoustical Society of America* 57 (1975) 370–373. doi:10.1121/1.380450.
- [156] B. R. Mace, Periodically stiffened fluid-loaded plates, i: Response to convected harmonic pressure and free wave propagation, *Journal of Sound and Vibration* 73 (1980) 473–486. doi:10.1016/0022-460X(80)90662-8.
- [157] B. R. Mace, Periodically stiffened fluid-loaded plates, ii: Response to line and point forces, *Journal of Sound and Vibration* 73 (1980) 487–504. doi:10.1016/0022-460X(80)90663-X.
- [158] P. Fossat, C. Boutin, M. Ichchou, Dynamics of periodic ribbed plates with inner resonance: Analytical homogenized model and dispersion features, *International Journal of Solids and Structures* 152-153 (2018) 85–103. doi:10.1016/j.ijsolstr.2018.06.012.
- [159] A. Mejdí, N. Atalla, Vibroacoustic analysis of laminated composite panels stiffened by complex laminated composite stiffeners, *International Journal of Mechanical Sciences* 58 (2012) 13–26. doi:10.1016/j.ijmecsci.2012.02.003.
- [160] E. G. Williams, B. H. Houston, J. A. Bucaro, Broadband nearfield acoustical holography for vibrating cylinders, *The Journal of the Acoustical Society of America* 86 (1990) 674–679. doi:10.1121/1.398245.
- [161] B. Laulagnet, J. L. Guyader, Sound radiation by finite cylindrical ring stiffened shells, *Journal of Sound and Vibration* 138 (1990) 173–191. doi:10.1016/0022-460X(90)90536-9.
- [162] J. H. Lee, J. Kim, Sound transmission through periodically stiffened cylindrical shells, *Journal of Sound and Vibration* 251 (2002) 431–456. doi:10.1006/jsvi.2001.4009.
- [163] C. J. Liao, W. K. Jiang, H. Duan, Y. Wang, Vibration and sound radiation from submerged finite cylindrical shells reinforced with axially periodic stiffeners, *Journal of Vibration and Control* 17 (2011) 1472–1480. doi:10.1177/1077546310380515.
- [164] F. Errico, M. Ichchou, F. Franco, S. De Rosa, O. Bareille, C. Droz, Schemes for the sound transmission of flat, curved and axisymmetric structures excited by aerodynamic and acoustic sources, *Journal of Sound and Vibration* 476 (2019) 221–238. doi:10.1016/j.jsv.2019.05.041.
- [165] A. W. Leissa, *Vibration of shells*, NASA-SP-288, 1973.
- [166] G. Tufano, F. Errico, O. Robin, C. Droz, M. Ichchou, B. Pluymers, W. Desmet, N. Atalla, K-space analysis of large-scale complex meta-structures using the inhomogeneous wave correlation method, *Mechanical Systems and Signal Processing* 135 (2020) 106407. doi:10.1016/j.ymsp.2019.106407.
- [167] G. Corcos, Resolution of pressure in turbulence, *Journal of the Acoustical Society of America* 35 (1963) 192–199. doi:/10.1121/1.1918431.
- [168] M. Ichchou, B. Hiverniau, B. Troclet, Equivalent ‘rain on the roof’ loads for random spatially correlated excitations in the mid frequency range, *Journal of Sound and Vibration* 322 (2009) 926–940. doi:/10.1016/j.jsv.2008.11.050.

List of Publications

- G. Tufano, F. Errico, O. Robin, C. Droz, M. Ichchou, B. Pluymers, W. Desmet and N. Atalla, *K-space analysis of complex large-scale meta-structure using the Inhomogeneous Wave Correlation method*, Mechanical Systems and Signal Processing 135, 106407, 2020
- G. Tufano, F. Errico, M. Ichchou, W. Desmet, O. Bareille and B. Pluymers, *On the effect of axial and ring stiffeners on the vibro-acoustic response of curved structures*, submitted to Journal of Sound and Vibration
- F. Errico, G. Tufano, O. Robin, N. Guenfoud, M. Ichchou and N. Atalla, *Simulating the sound transmission loss of complex curved panels with attached noise control materials using periodic cell wavemodes*, Applied Acoustics 156, 21-28, 2019
- G. Tufano, M. Ichchou, W. Desmet and N. Atalla, *K-space analysis of composite sandwich shell with small-scale resonators*, *Book of Proceeding of 3rd Euro-Mediterranean Conference on Structural Dynamics and Vibroacoustics*, MEDYNA 2020, Naples, Italy
- G. Tufano, O. Bareille, B. Pluymers, A.-M. Zine, W. Desmet and M. Ichchou, *On the multi-modal behavior and inner resonance of stiffened shells*, *Book of Proceeding of 3rd Euro-Mediterranean Conference on Structural Dynamics and Vibroacoustics*, MEDYNA 2020, Naples, Italy
- G. Tufano, C. Droz, M. Ichchou, O. Bareille, A.-M. Zine, B. Pluymers and W. Desmet, *On the structural characterization through k-space methods: assessments and validations*, *Book of Proceeding of 9th ECCOMAS Thematic Conference on Smart Structures and Materials*, SMART 2019, Paris, France
- G. Tufano, C. Droz, O. Bareille, A.-M. Zine, B. Pluymers, W. Desmet and M. Ichchou, *Wavenumber identification technique for axial-symmetric structures*, *Proceedings of ISMA 2018 - International Conference on Noise and Vibration Engineering and USD 2018 - International Conference on Uncertainty in Structural Dynamics*, ISMA 2018, Leuven, Belgium
- G. Tufano, M. Ichchou, O. Bareille, A.-M. Zine, B. Pluymers and W. Desmet, *Industrial application of periodic structures to aircraft/launchers*, *Book of Proceeding of 2nd Euro-Mediterranean Conference on Structural Dynamics and Vibroacoustics*, MEDYNA 2017, Seville, Spain

List of Figures

| | | |
|------|---|----|
| 0.1 | Honeycomb sandwich panel | 2 |
| 0.2 | Periodic structures: part of the fuselage of an AIRBUS A350 aircraft (a) and a rail (b). | 2 |
| 0.3 | Tuned mass damper used in the <i>Taipei 101</i> skyscraper. | 3 |
| 0.4 | Flowchart of the optimization process. | 4 |
| 1.1 | Structural mode shape (a) and wavenumber transform (b) [17]. | 10 |
| 1.2 | Normalized dispersion curve (a) and estimation error in the real and imaginary parts of the normalized wavenumbers (b) [8]. | 13 |
| 1.3 | Damping loss factor estimation for the finite element model: exact solution $\cdot - \cdot -$, noise-free simulated data $--$, noisy-simulated data $—$ (a) and normalized error: noise-free simulated data $--$, noisy-simulated data $—$ (b). [9]. | 14 |
| 1.4 | Schematic representation of the basis of the IWC method: vibrational field of a plane structure (a) and the representation of an inhomogeneous damped wave (b). | 15 |
| 1.5 | Identified maximum values of the wavenumber (a) and of the attenuation factor γ (b) for a fixed frequency f_0 | 16 |
| 1.6 | Set-up of the one-side clamped ribbed panel [12]. | 16 |
| 1.7 | IWC results for a ribbed panel with different boundary conditions: free (a) and one-side clamped (b) [12]. | 17 |
| 1.8 | Multi-modal dispersion curves [19]. | 18 |
| 1.9 | Multi-modal propagation at different frequencies [12]. | 18 |
| 1.10 | Dispersion curve for the composite beam [22]. | 19 |
| 1.11 | Angle-dependent wavenumbers at fixed frequencies (a) and inverse estimation of the dynamic stiffness (b) [22]. | 19 |
| 1.12 | Unit cell of the locally resonant meta-structure (a), full-scale resonant plate (b) and close-up view (c) [24]. | 20 |
| 1.13 | Numerically predicted dispersion curves compared with the measured one by using the extended IWC method: $\theta = 0$ deg (a), $\theta = 45$ deg (b) and $\theta = 90$ deg (c)[24]. | 20 |
| 1.14 | Experimental set-up of the beam with varying cross-section (a) and analytical dispersion curves in the first Brillouin zone (b) [26]. | 21 |
| 1.15 | Dispersion curves of the polyamid beam with periodically varying thickness with the spacial Fourier transform (a) and the IWC method (real part (b) and imaginary part (c)) [25]. | 22 |
| 1.16 | Set-up of the experimental test (a), Laplace transform at 2453 Hz (b), real part (c) and imaginary part (d) of the estimated wavenumbers [28]. | 24 |

| | | |
|------|--|----|
| 1.17 | HRWA method on a PVC beam: torsional and bending wavenumbers (a), spatial decay γ (b), apparent complex moduli (c) and damping loss factor (d) [32]. | 27 |
| 1.18 | Set-up of the experimental tests, with excitation and acquisition systems, for the 2D application of the HRWA method [33]. | 28 |
| 1.19 | 2D application of the HRWA method on a sandwich plate with CFRP skins and PVC core: phase velocity-frequency relation (a) and phase velocity angle dependency (b) [33]. | 28 |
| 1.20 | 2D application of the HRWA method on a sandwich plate with CFRP skins and honeycomb core: frequency and angle dependency of the real (a) and imaginary (b) parts of the estimated wavenumbers; real (c) and imaginary (d) discrete dispersion surfaces [33]. | 29 |
| 1.21 | Image of a source point (x_0, y_0) in the plane $x = 0$ [55]. | 31 |
| 1.22 | Polygonal plate with inside domain Ω and boundaries $\partial\Omega$, with source (+) and receiver (\times) locations [54]. | 32 |
| 1.23 | Experimental set-up of the plate with viscoelastic layer (a) and shaker excitation (b) [60]. | 33 |
| 1.24 | Experimental estimation of the bending stiffness D (a), the Young's modulus E (b) and the damping loss factor (c) [60]. | 34 |
| 1.25 | Isotropic plate and measurement area [5]. | 36 |
| 1.26 | Real part of the dispersion curve (a), damping loss factor estimation (b), equivalent stiffness modulus (c) and equivalent Young's modulus (d) [5]. | 36 |
| 1.27 | FAT on isotropic plate: exact motion (a), noisy displacement (b), SVD filtering (c), low-pass wavenumber filtering (d), spatial windowing (e) and filtered force distribution (f) [67]. | 39 |
| 1.28 | Points needed to estimate the fourth derivatives with the finite difference scheme [72]. | 39 |
| 1.29 | Fluid-loaded plate (a) and dispersion curves (b) [72]. | 40 |
| 1.30 | Periodicity conditions between two adjacent cells [108]. | 41 |
| 1.31 | FE models of the 2D unit cells with corners nodes (a) and mid-side nodes (b) [99]. | 41 |
| 1.32 | Wave Finite Element method for curved structures: cylindrical coordinates (a), curved element (b) and FE model of the unit periodic cell (c) [99]. | 43 |
| 1.33 | Experimental estimation of the damping loss factor [8]. | 44 |
| 1.34 | Damping loss factor estimation for flat panels: isotropic aluminum (a), isotropic aluminum with viscoelastic layer (b), thin composite (c) and thick composite (d), with 3 dB method (Δ), decay rate method (+), power injected method (\times) and IWC method ($-$) [1]. | 46 |
| 2.1 | Finite element models of the isotropic narrow plate: full-scale (a) and periodic unit cell (b). | 54 |
| 2.2 | Isotropic beam: propagative part of the dispersion curve calculated with proposed approach compared with the analytical model and the WFE method (a) and damping loss factor estimation (b). | 54 |
| 2.3 | Finite element models of the periodic narrow plate: full-scale (a) and periodic unit cell (b). | 55 |
| 2.4 | Periodic beam: WFE method (a) and proposed approach (b) complex dispersion curve estimation. | 56 |

| | | |
|------|--|----|
| 2.5 | FE models of the isotropic narrow plate with distributed TMDs: full-size (a) and front view of the unit periodic cell (b). | 56 |
| 2.6 | FRFs comparison of the isotropic narrow plate with distributed TMDs: resonators tuned at 1500 Hz (a) and at 3500 Hz (b). | 58 |
| 2.7 | Dispersion curves of the isotropic narrow plate with distributed TMDs. | 59 |
| 2.8 | Dispersion curve (a) and damping loss factor estimation (b) for the isotropic narrow plate with distributed TMDs tuned at 1500 Hz. | 59 |
| 2.9 | Dispersion curve (a) and damping loss factor estimation (b) for the isotropic narrow plate with distributed TMDs tuned at 3500 Hz. | 59 |
| 2.10 | Finite element models of the full-size (a) and of the periodic unit cell (b) of the homogeneous plate. | 60 |
| 2.11 | Homogeneous plate: dispersion curve comparison (a) and damping loss factor estimation (b). | 61 |
| 2.12 | Finite element models of the full-size (a) and of the periodic unit cell (b) of the laminated composite plate. | 62 |
| 2.13 | Dispersion curve (a) and damping loss factor estimation (b) for the laminated composite plate. | 62 |
| 2.14 | Equivalent mechanical properties of the laminated composite panel: bending stiffness modulus (a) and Young's modulus (b). | 63 |
| 2.15 | FE models of the homogeneous panel with distributed TMDs: full-size (a) and front view of the unit periodic cell (b). | 63 |
| 2.16 | FRFs comparison of the homogeneous panel with distributed TMDs. | 64 |
| 2.17 | Dispersion curve (a) and damping loss factor estimation (b) for the homogeneous panel with distributed TMDs. | 64 |
| | | |
| 3.1 | FE model of the isotropic panel with the punctual harmonic excitation. | 70 |
| 3.2 | Angle-dependent dispersion curves for the isotropic panel. Comparison with the Kirchhoff's theory and the FFT at three different frequencies: at 500 Hz (a-b), at 700 Hz (c-d) and at 1100 Hz (e-f). | 71 |
| 3.3 | Isotropic panel: angle-dependent dispersion curves (a) and damping loss factor estimation (b). | 72 |
| 3.4 | FE model of the orthotropic panel with the punctual harmonic excitation. | 72 |
| 3.5 | Orthotropic panel: angle-dependent dispersion curves (a) and damping loss factor estimation (b). | 72 |
| 3.6 | Double-wall panel with 1.0 cm of inter-spacing between the mechanical links: full view (a) and periodic unit cell (b). | 74 |
| 3.7 | 3D-printed sandwich panel: full-size (a) and close up (b) views. | 74 |
| 3.8 | 3D-printed sandwich panel: reflective tape (a) and installation for shaker excitation (b). | 75 |
| 3.9 | Double-wall panel with 1.0 cm of inter-spacing. K-space obtained using the FFT (a) and the IWC (b) methods, and angle-dependent wavenumbers (c) at 1500 Hz. | 75 |
| 3.10 | Numerical-experimental dispersion curves of the double-wall panel with 1.0 cm of inter-spacing between the mechanical links. | 76 |
| 3.11 | Double-wall panel with 2.0 cm of inter-spacing between the mechanical links: full view (a) and periodic unit cell (b). | 77 |
| 3.12 | Numerical dispersion curves of the double-wall panel with 2.0 cm of inter-spacing between the mechanical links. | 77 |

| | | |
|------|--|-----|
| 4.1 | Curved structure coordinates system. | 84 |
| 4.2 | Large-scale curved structures: composite sandwich honeycomb shell (a) and aluminum aircraft sidewall panel (b). | 86 |
| 4.3 | Schematic representation of the resonator (a) and its application on the host structure (b). | 86 |
| 4.4 | Set-up of the steel plate with distributed resonators (a) and acquisition window (b). | 87 |
| 4.5 | Curved composite laminate sandwich panel: bare configuration (a), distributed resonators configuration (b), acquisition system (c) and acquisition window (d). | 89 |
| 4.6 | Illustration of the coupled rooms. | 89 |
| 4.7 | Set-up and installation for mechanical excitation: shaker installation (a) and acquisition region (b). | 90 |
| 4.8 | Aluminum aircraft sidewall panel: acquisition windows for shaker (a) and DAF (b) excitations. | 91 |
| 4.9 | Set-up and installation of the bare configuration: outer skin subjected to DAF excitation (a), inner surface (b) and acquisition system (c). | 91 |
| 4.10 | DAF excitation: acquisition window (a) and detail of the host structure with the attached resonators (b). | 92 |
| 4.11 | Dispersion curves comparison for the steel plate, with and without the resonators: at 800 Hz (a) and at 1400 Hz (b). | 93 |
| 4.12 | Displacement fields of the steel plate, with and without the resonators. First frequency at 250 Hz: bare test case (a), first resonators configuration (b) and second resonators configurations (c). Second frequency at 820 Hz: bare test case (d), first resonators configuration (e) and second resonators configurations (f). Third frequency at 1375 Hz: bare test case (g), first resonators configuration (h) and second resonators configurations (i). | 94 |
| 4.13 | Steel plate: averaged Frequency Response Functions comparison. | 95 |
| 4.14 | FE model of the curved panel (a) and dispersion curves comparison (b). | 95 |
| 4.15 | FRFs comparison for both configurations and excitations: DAF excitation (a) and point mechanical excitation (b). | 97 |
| 4.16 | Normalized displacement fields under DAF excitation for the composite shell at three different frequencies. At 325 Hz: bare test case (a) and resonating structure (b). At 1000 Hz: bare test case (c) and resonating structure (d). At 1675 Hz: bare test case (e) and resonating structure (f). | 98 |
| 4.17 | Normalized displacement fields under shaker excitation for the composite shell at three different frequencies. At 325 Hz: bare test case (a) and resonating structure (b). At 1000 Hz: bare test case (c) and resonating structure (d). At 1675 Hz: bare test case (e) and resonating structure (f). | 99 |
| 4.18 | Dispersion curves under DAF excitation, with and without resonators: axial (a) and circumferential (b) directions. | 100 |
| 4.19 | Dispersion curves under shaker excitation, with and without resonators: axial (a) and circumferential (b) directions. | 100 |
| 4.20 | Damping Loss Factor estimation: bare test case and resonators configuration comparison with Eq. (1.86) (a) and bare test case comparison between Eq. (1.86) and PIM (b). | 101 |
| 4.21 | Installation of the aluminum panel (a) and FE model (b). | 101 |

| | | |
|------|---|-----|
| 4.22 | Dispersion curves for the bare configuration and different loading conditions: axial (a) and circumferential (b) directions. | 102 |
| 4.23 | Dispersion curves under DAF excitation, with and without resonators: axial (a) and circumferential (b) directions. | 102 |
| 5.1 | Coordinates system for the Donnell-Mushtary theory | 109 |
| 5.2 | FE models of the bare test case panel (a) and of the stiffened panels with T shaped stiffeners in axial (b) and circumferential (c) directions. | 111 |
| 5.3 | Front view of the stiffeners cross-section: T shaped (a), H shaped (b) and Ω shaped (c). | 111 |
| 5.4 | FE models of the panels with T shaped stiffeners: 6 cm pitch in the axial (a) and circumferential (b) directions, 10 cm pitch in the axial (c) and circumferential (d) directions. | 112 |
| 5.5 | Dispersion curves comparisons between the IWC method and the analytical theories: axial direction (a) and circumferential direction (b). | 113 |
| 5.6 | Effect of stiffeners inter-spacing on the dispersion curves of the stiffened panels with T shaped stiffeners: axial direction (a) and circumferential direction (b). | 115 |
| 5.7 | Dispersion curves of the stiffened panels: axial direction (a) and circumferential direction (b). | 117 |
| 5.8 | Sound Transmission Loss for the stiffened panels under DAF excitation: T shaped (a), H shaped (b) and Ω shaped (c) stiffeners. | 119 |
| 5.9 | Sound Transmission Loss for the stiffened panels under DAF and TBL excitations: T shaped (a), H shaped (b) and Ω shaped (c) stiffeners. | 120 |
| 5.10 | Wavenumber transforms for the structures and the load model at 1.5 kHz: unstiffened shell (a), shell with axial T shaped stiffeners (b), shell with circumferential T shaped stiffeners (c) and DAF and TBL load spectra (d). | 121 |
| 5.11 | Sound Transmission Loss for the T shaped stiffened panels with different pitch distances: circumferential stiffeners and DAF load (a), axial stiffeners and DAF load (b) circumferential stiffeners and DAF + TBL load (c) and axial stiffeners and DAF + TBL load (d). | 122 |

List of Tables

| | | |
|-----|---|-----|
| 4.1 | Experimentally tested configurations. | 85 |
| 4.2 | Material properties of the curved composite sandwich panel. | 87 |
| 4.3 | Geometrical dimensions of the aluminum aircraft sidewall panel. | 90 |
| 5.1 | Cross-section properties of the stiffeners. | 110 |
| 5.2 | FE models details of the stiffened panels | 111 |

AUTORISATION DE SOUTENANCE

Vu les dispositions de l'arrêté du 25 mai 2016,

Vu la demande des directeurs de thèse

Messieurs M. ICHCHOU et W. DESMET

et les rapports de

M. J-R. ARRUDA

Professeur - Université de Campinas - Cidade Universitária Zeferino Vaz
Barão Geraldo, Campinas - SP, 13083-970, Brésil

et de

M. M-A. HAMDI

Professeur - Université de Technologie de Compiègne - Rue Roger Couttolenc
60200 Compiègne

Monsieur TUFANO Giovanni

est autorisé à soutenir une thèse pour l'obtention du grade de **DOCTEUR**

Ecole doctorale MECANIQUE, ENERGETIQUE, GENIE CIVIL ET ACOUSTIQUE

Fait à Ecully, le 6 février 2020

P/Le directeur de l'E.C.L.
Le directeur des Etudes



